X-ray Scattering

Edited by Alicia Esther Ares

X-RAY SCATTERING

Edited by **Alicia Esther Ares**

Contributors

Margareth Kazuyo Kobayashi Dias Franco, Daniele Ribeiro De Araújo, Eneida De Paula, Leide Cavalcanti, Fabiano Yokaichiya, Ahmed Rebey, Hédi Fitouri, Mohamed Mourad Habchi, Shinichi Sakurai, Jakub Szlachetko, Joanna Czapla-Masztafiak, Jacinto Sa, Alessandro Cunsolo, Gonzalo Santoro, Shun Yu, Katsuhiro Yamamoto, Claudine Mayer, Renwick Dobson, F. Grant Pearce, Serena A. J. Watkin, Volker Nock, Timothy M. Ryan, Nigel Kirby, Antonia G. Miller

Notice

Statements and opinions expressed in the chapters are these of the individual contributors and not necessarily those of the editors or publisher. No responsibility is accepted for the accuracy of information contained in the published chapters. The publisher assumes no responsibility for any damage or injury to persons or property arising out of the use of any materials, instructions, methods or ideas contained in the book.

We are IntechOpen, the first native scientific publisher of Open Access books

3,250+
Open access books available

106,000+
International authors and editors

112M+
Downloads

151
Countries delivered to

Our authors are among the
Top 1%
most cited scientists

12.2%
Contributors from top 500 universities

Interested in publishing with us?
Contact book.department@intechopen.com

Numbers displayed above are based on latest data collected.
For more information visit www.intechopen.com

Meet the editor

Alicia Esther Ares is a headline professor of Materials Science at the Chemical Engineering Department, School of Sciences (FCEQyN), National University of Misiones (UNaM), Posadas, Misiones, Argentina, since December 2013. Also, she is an independent researcher at the National Scientific and Technical Research Council (CONICET), Argentina, since January 2015. Previously, she has been a research associate at CONICET (2008–2014) and an associate professor at UNaM (2007–2013). She has also been an assistant professor at UNaM (1989–2007). She graduated at the University of Misiones in 1992 and completed a PhD degree in Materials Science at the Institute of Technology "Jorge Sabato," UNSAM–CNEA, Buenos Aires, Argentina. Later, she made a postdoctoral stays at the following institutions: Faculdade de Engenharía Mecânica, Departamento de Engenharía de Materiais, Universidade Estadual de Campinas, Campinas, São Paulo, Brazil (2001 and 2005–2006); Department of Materials Science and Engineering, University of Florida, Gainesville, Florida, United States (2002–20003); and Faculty of Sciences, National University of Misiones, Posadas, Misiones, Argentina (2003–2004). She has a 27-year teaching experience both at the undergraduate and at the graduate level.

Her research interests lie in the following areas:
- Solidification thermal parameters, mechanical properties, and corrosion resistance of different alloys and composite materials
- Solidification structures and properties of alloys for hard tissue replacement
- Metallic materials selection for the management of biofuels
- Synthesis and characterization of nanostructured coatings, membranes, and templates of aluminum and zinc oxides
- Fabrication and characterization of nanostructured titanium and iron oxide coatings for water treatment systems based on advanced oxidative and reductive processes
- Natural products as corrosion inhibitors of metallic materials

Her articles are published in well-established international and Argentinean journals.

Contents

Preface

X-ray scattering techniques are a family of nondestructive analytical techniques. Using these techniques, scientists obtain information about the crystal structure and chemical and physical properties of materials. Nowadays, different techniques are based on observing the scattered intensity of an X-ray beam hitting a sample as a function of incident and scattered angle, polarization, and wavelength.

This book is intended to give overviews of the relevant X-ray scattering techniques, particularly about inelastic X-ray scattering, elastic scattering, grazing-incidence small-angle X-ray scattering, small-angle X-ray scattering, high-resolution X-ray diffraction (XRD), and, finally, applications of X-ray spectroscopy to study different biological systems.

Section I: Inelastic X-ray Scattering

Chapter 1 reviews some relevant experimental contributions brought about by inelastic X-ray scattering (IXS). The development of inelastic X-ray scattering (IXS) has substantially expanded the potentialities of modern spectroscopy, thus providing an unprecedented detailed mapping of such a crossover. A better understanding of the line-shape evolution is deemed to improve our knowledge of all dynamical processes occurring in a fluid from macroscopic to microscopic scales.

Section II: Grazing-Incidence Small-Angle X-ray Scattering

Chapter 2 reviews the current trends of time-resolved grazing-incidence small-angle X-ray scattering (GISAXS) studies. After an introduction to the GISAXS technique, the authors present exemplary results of metallic and organic thin-film preparation, wet deposition of polymer thin films, and self-assembly of colloidal thin films, as well as examples of thin-film modification in, e.g., microfluidic channels and within working devices. Finally, they provide an overview of the future perspectives in the field.

Chapter 3 introduces recent advances in grazing-incident small-angle X-ray scattering (GISAXS) experiment utilizing low-energy X-rays. GISAXS probes the complex nano- and micro-phase-separated structure in polymer thin films. Especially, tuning the energy of GISAXS in the tender and soft X-ray regime allows the tailoring of X-ray penetration depth and contrast and thereby the probing of more complex morphologies in polymer thin films. Grazing-incidence-resonant soft X-ray scattering (GI-RSoXS) is applied for polymer blend thin films with low contrast in the real part of the refractive index for the hard X-rays but with significant differences in the soft X-ray regime. Furthermore, the X-ray penetration depth is drastically affected by the changes in the X-ray photon energy across the K-edge. The surface- and volume-sensitive structure of polymer blend films is analyzed using this technique.

Chapter 4 provides practical design considerations for X-ray based on microfluidic systems and examines some of the existing microfluidic platforms used in conjunction with small-angle X-ray scattering (SAXS). As the exclusive advantages of microfluidics become recognized

and accessible, the prevalence of microfluidic sample environments in X-ray scattering measurements will hopefully increase.

Section III: Small-Angle X-ray Scattering

Chapter 5 focuses on the study of form factor of a variety of nanostructures (spheres, prolates, core-shell spheres, core-shell cylinders, and lamellae) using the small-angle X-ray scattering (SAXS) technique, getting started with a monodisperse distribution of the size of the nanostructure, to unimodal distribution with a narrow standard deviation or widespreading distribution and finally to the discrete distribution that can be evaluated by the computational parameter fitting to the experimentally obtained SAXS profile.

Chapter 6 presents theoretical aspects, experiment design, and applications of both techniques for the development of delivery systems for bioactive molecules. Small-angle X-ray scattering (SAXS) and X-ray diffraction (XRD) have presented important contribution to the study of organization phase of nanocarriers such as organic/inorganic nanoparticles, micelles, liposomes, cyclodextrins, polymers, and their interaction with drugs and other bioactive molecules.

Section IV: High-Resolution X-ray Diffraction

Chapter 7 gives an overview on the basic experimental apparatus and theory element of high-resolution X-ray diffraction method applied to III–V semiconductor thin films. Also, treat several examples in order to determine the effect of doping, composition, and strain on structural properties of crystal. Analyzed layers were grown by metal-organic vapor-phase epitaxy (MOVPE). Films treated as examples are selected in order to bring the utility of characterization technique. The authors investigate GaAs/GaAs(001), GaAs:C/GaAs(001), GaN/Si(111), GaN:Si/Al2O3(00.1), GaAsBi/GaAs(001), and InGaAs/GaAs(001) heterostructures by using different scans for studying numerous structural layer and substrate parameters.

Section V: Applications of X-ray Spectroscopy to Study Different Biological Systems

Chapter 8 summarizes the latest efforts in applying X-ray spectroscopy to study different biological systems starting from the impact of different damaging agents on the model of DNA molecule, followed by the chemical speciation in the studies of cancerous cell lines and human tissues. Chosen topics show the variety of medically important subjects that can be studied with X-ray spectroscopy and its undeniable role as a technique complementary to classical methods.

Chapter 9 presents the principle, methodology, and limitations of solving biological structures by crystallography. Knowing the three-dimensional structure of biological macromolecules, such as proteins and DNA, is crucial for understanding the functioning of life. Biological crystallography, the main method of structural biology, which is the branch of biology that studies the structure and spatial organization in biological macromolecules, is based on the study of X-ray diffraction by crystals of macromolecules.

Prof. Dr. Alicia Esther Ares
Materials Institute of Misiones (CONICET–UNaM)
Posadas, Misiones
Argentina

Inelastic X-ray Scattering

Inelastic X-Ray Scattering as a Probe of the Transition Between the Hydrodynamic and the Single Particle Regimes in Simple Fluids

Alessandro Cunsolo

Additional information is available at the end of the chapter

http://dx.doi.org/10.5772/66126

Abstract

In the last few decades, the study of the spectrum of density fluctuations in fluids at the transition from the continuous to the single particle regimes has attracted an increasing interest. Although the shape of the spectrum is well known in these two extreme limits, no theory firmly predicts its evolution in the broad crossover region. However, the development of inelastic X-ray scattering (IXS) has substantially expanded the potentialities of modern spectroscopy, thus, providing an unprecedented detailed mapping of such a crossover. A better understanding of the line-shape evolution in this intermediate regime is deemed to improve our knowledge of all dynamical processes occurring in a fluid from macroscopic to microscopic scales. The aim of this chapter is to review some relevant experimental contributions brought about by IXS in this field since its development toward the end of past millennium.

Keywords: inelastic X-ray scattering, simple fluids, hydrodynamics, single particle limit, collective excitations

1. Introduction

In the last 50 years, the short-time collective dynamics of molecules in fluid and glassy systems has been in the focus of a thorough experimental, theoretical, and computational scrutiny, yet it still has many unsettled aspects. This mostly owes to the lack of a large-scale symmetry in the structure of these systems and to the often exceptionally complex movements of their microscopic constituents. Among various variables providing insight into the dynamic behavior of a disordered system, density fluctuations are a particularly well-suited subject to

study, as they can be directly accessed by several independent investigation methods. Indeed, the most significant advances made in the field of dynamics of liquids have been achieved thanks to the critical comparison of parallel experimental and computational results. In fact, both spectroscopy experiments and molecular dynamics simulations provide direct access to the Fourier transform of correlation functions between density fluctuations, i. e., the dynamic structure factor, $S(Q,\omega)$. This variable is a unique function of the energy, $\hbar\omega$, and the momentum $\hbar\vec{Q}$ exchanged between the probe and the sample in a scattering event; here $\hbar = h/2\pi$ with h being the Planck constant.

In general, the shape of $S(Q,\omega)$ is reasonably understood both at quasi-macroscopic distances, over which the fluid appears as a continuum, and at truly microscopic scales where instead the single particle dynamics is probed.

The evolution of the $S(Q,\omega)$ shape in the whole crossover between these two limits still represents a theoretical challenge. This particularly applies to the so-called "mesoscopic" regime, corresponding to distances and timescales roughly matching first neighboring molecules' separations and cage oscillations periods, respectively. From the experimental side, the study of $S(Q,\omega)$ in liquids at mesoscopic scales has been for long time an exclusive domain of inelastic neutron scattering (INS), a technique already in its mature phase, having been developed in the mid-1950s [1]. The complementary mesoscopic technique, inelastic X-ray scattering (IXS), is instead relatively young, since its first demonstration dates back to the last decade of the past millennium [2, 3]. Its implementation was enabled by the advent of synchrotron sources with unprecedented brilliance and by parallel advances in crystal optics fabrication. Furthermore, the improved performance of X-ray sources has greatly increased the level of statistical accuracy typically achieved by inelastic scattering measurements, thus enabling more detailed and physically informative modeling of the spetral shape. Across the years, this new spectroscopic tool allowed the scientific community to gain a deep-seated knowledge of the mesoscopic dynamics of disordered systems. Nowadays, IXS experiments have reached the level of statistical accuracy required for extremely detailed and informative line-shape analyses, thus representing a valuable test for the most advanced theories of liquid dynamics.

As a simple example of possible IXS applications, this chapter will provide a concise overview of relevant IXS investigations of the $S(Q,\omega)$ across the transition from the hydrodynamic to the single particle regimes. Looking at the available literature results from a global perspective has a relevant scientific interest since a better understanding of this crossover can shed further insight into the various dynamic events occurring in a fluid from macroscopic to microscopic scales.

2. Generalities on an inelastic scattering experiment

In a scattering experiment, a beam impinges on the sample exchanging with it, an energy of $\hbar\omega$ and a momentum of $\hbar\vec{Q}$. It can be shown that intensity measured in a spectroscopy

experiment from GHz frequencies [4] to THz ones [5–7] is proportional to the spectrum of density fluctuations, or dynamic structure factor:

$$S(Q,\omega) = \int_V d\vec{r} \int_{-\infty}^{+\infty} \left\langle \delta\rho(\vec{r},t)\delta\rho^*(\vec{r},0) \right\rangle \exp\left[i(\vec{Q}\cdot\vec{r} - \omega t) \right] dt \qquad (1)$$

with $\delta\rho(\vec{r},t)$ being the space $(\vec{r})$ and time (t) dependent density fluctuation of the target sample within the volume V. The term $\delta\rho(\vec{r},t)$ appearing in Eq. (1) may represent either a spontaneous or a scattering-induced density fluctuation, in either case its amplitude is assumed small enough to induce a linear response on the target sample. Under this condition, the response of the latter can be expressed in terms of correlation functions calculated at its equilibrium. Note that for isotropic systems as liquids and glasses, only the amplitude $Q = |\vec{Q}|$ of the exchanged wave-vector $\vec{Q}$ counts, the actual direction being irrelevant. For this reason, while dealing with these systems, it is customary to express the dynamic structure factor as $S(Q,\omega)$ rather than $S(\vec{Q},\omega)$.

Typically, in a scattering experiment the sample is kept at a constant temperature T and therefore the correlation function, defined by the symbol $\langle ......\rangle$, can be calculated as a thermal average over the initial states of the target atoms. For a classical system, this sum can be performed using the counting factor $n(E_I) = \exp(-\beta E_I) \big/ \sum_I \exp(-\beta E_I)$, with $\beta = 1/k_B T$, where E_I is the energy of the I-th initial state and k_B, the Boltzmann constant. From the above formula, one readily recognizes that the scattering of a plane wave at an energy (frequency) and a direction (wavevector) different from the initial ones is caused by a density fluctuation $\delta\rho(\vec{r},t)$. If, for instance, if the probe is visible light, the occurrence of a density fluctuation causes a local variation of the index of refraction, thereby disrupting the optical homogeinity of the medium. By virtue of the scattering event, according to the Huygens principle (see, e.g., [8]), the target sample becomes the source of spherical wave: $\psi_{sc} \propto e^{ikr}/r$ with r being the distance from the origin, that is the location of the probe-sample collision.

The photoms deviated at an angle 2θ, after passing through an analyzer filter are ultimately counted by the detector. If the latter intercepts only a very small portion of the solid angle, it can be safely assumed that the wavevector of photons impinging on its sensitive area is constant and orthogonal to the front wave (plane wave approximation). Consequently, the scattering process can be treated as a transition between two distinct plane waves.

Given the above general considerations, we can now attempt a course derivation of the frequency distribution of the scattering from a density wave to achieve a rough estimate of the shape of $S(Q,\omega)$.

As apparent from Eq. (1), $S(Q,\omega)$ is connected to density fluctuations through the space and time Fourier transform of their correlation function. Its determination thus provides a snapshot of this correlation function over timescale $\sim \omega^{-1}$ and distances $\sim Q^{-1}$. For small Q and ω, the target system is "perceived" by the probe as a continuous and homogeneus medium, whose dynamic response is averaged over long times. This continuous limit can be probed, for

instance, by illuminating the sample with the visible light beam emitted by a laser. In fact, Q values typical of visible light scattering measurements span the 10^{-3}–10^{-2} nm^{-1} range, corresponding to sub-μm to μm lengthscales. These distances are sufficiently smaller than the sample size, yet still much larger than first neighboring atoms' separations. Clearly, at these scales the detail of the microscopic structure and dynamics cannot be directly observed, since only long distances and times effects on the dynamics can be captured by the probe.

Over long distances density fluctuations in a liquid can, for instance, have the form of density (acoustic) waves propagating throughout the medium with the speed of sound, c_s. Since c_s is much smaller the speed of light in the medium a given density wave is "seen" by the incident photons as essentially static, i. e., stationary, perturbation.

We can now focus on the intensity scattered, e.g., by successive crests of the density wave, as illustrated in **Figure 1**. The interference between these successive reflections is constructive whenever the difference in their optical paths (namely, the two red segments in the scheme of **Figure 1**) equals an integer multiple of the incident wavelength in the medium. Considering the smallest of these integer numbers, one has:
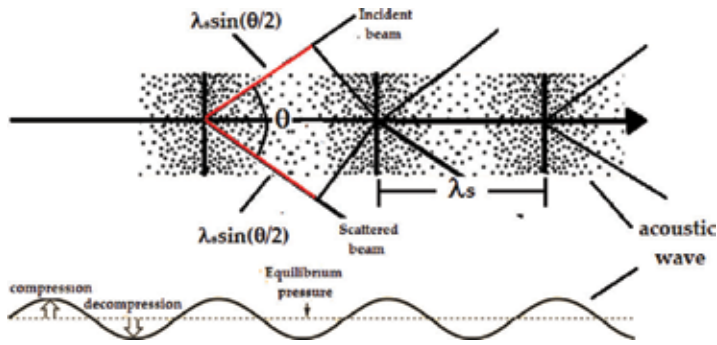
Figure 1. Schematics of the interaction between a density wave and a photon beam (see text) causing a scattering at an angle 2θ.

$$\frac{\lambda}{n} = 2\lambda_s \sin \vartheta = 4\pi \frac{c_s}{\omega_s} \sin \vartheta \tag{2}$$

where λ and λ/n are, respectively, the wavelength of light in vacuum and in the target medium, with n being the refractive index of the sample; furthermore, λ_s, c_s, and ω_s are the wavelength, the speed and the angular frequency of the acoustic wave with $\lambda_s = 2\pi c_s/\omega_s$. The scattering-genearted acoustic wave has a wavevector of amplitude amplitude $= Q$, therefore it propagates at a frequency $\omega_s = c_s Q$. From Eq. (2) it follows that the amplitude of the exchanged wavevector is $Q = (4\pi n/\lambda) \sin\theta$.

From a physical point of view, the acoustic wave can be considered as a source of scattered radiation traveling with a velocity c_s. As well known from Physics textbooks, the frequency of

the radiation emitted by a moving source is frequency-shifted by the Doppler effect. This ultimately causes $a \pm c_s Q$ offset of the frequency of scattered wave with respect to the one of the incident beam; here the signs "+" and "−" refer to the acoustic wave propagating toward or away from the detector, respectively. From these very general arguments, one can expect the frequency distribution of the scattered intensity, i.e., the spectrum, to be dominated by two peaks symmetrically shifted by an amount $\pm c_s Q$ from the center of the spectrum, $\omega = 0$.

These peaks are customarily quoted as "inelastic" insofar their energy is either lower or higher (by an amount $E = \hbar c_s Q$) than the energy of the impinging beam.

The two symmetric side peaks are named Brillouin peaks after their prediction by L. Brillouin in the early 1920s [9] and, as discussed in the following, their position and width convey insight, on the frequency and the lifetime of acoustic waves, respectively.

Let us now consider the case of diffusive, rather than propagating, density fluctuations. These can be for instance those generated by local temperature gradients causing transient density inhomogeneities. Their time evolution can be described by the Fick's law [10], which predicts a simple exponential time decay. The corresponding spectral shape is the Fourier transform of such an exponential law, namely a Lorentzian centered at $w = 0$. Since this position corresponds to the absence of energy-transfer, the corresponding peak is thus customarily referred to as quasi-elastic. Here the prefix "quasi-" alludes to the nonvanishing width of the peak and to its wings extending to the inelatic region of the spectrum ($w \neq 0$).

Since in general density fluctuations in a fluid can have either a diffusive, or a propagating character, one can anticipate that the spectrum of density fluctuations has a triplet shape composed by a quasi-elastic peak—connected to internal diffusive motions—and two symmetric side peaks— arising from acoustic modes.

A physically more informative description of the spectral shape in the continuous limit requires a detailed knowledge of the thermodynamic and transport properties of the sample. As well assessed both experimentally and computationally, the hydrodynamic theory for continuous media can be consistently used to describe the spectral shape in this limit.

This theory stems from an explicit expression of the conservation laws of the density of mass, momentum, and energy of the target sample [4, 11]. These can be described by few independent equations, which, however, do not form a complete set unless complemented by two so-called constitutive equations: the Navier-Stokes equation and the heat transfer one. The spectrum of density fluctuation can be ultimately obtained through Fourier and Laplace transforms of this set of equations. The result can be conveniently expressed in terms of a hydrodynamic matrix, whose eigenvalues define the modes dominating the spectral shape. As shown in Ref. [4] these long-lived, or quasi-conserved, collective modes are customarily referred to as "hydrodynamic modes," and appear in the spectrum as a triplet, well approximated by the following expression:

$$S(Q,\omega) \propto A_h \frac{z_h}{\omega^2 + z_h^2} + A_S\left[\frac{z_S}{(\omega - \omega_S)^2 + z_S^2} + \frac{z_S}{(\omega + \omega_S)^2 + z_S^2}\right] +$$
$$+ A_S b\left[\frac{(\omega - \omega_S)}{(\omega - \omega_S)^2 + z_S^2} - \frac{(\omega + \omega_S)}{(\omega + \omega_S)^2 + z_S^2}\right] \tag{3}$$

where the shape parameters ω_s, z_h and z_s represent the acoustic frequency and the inverse lifetime of the quasi-elastic and inelastic modes, respectively. All shape parameters in Eq. (3) are in general Q dependent, even if such dependence is not explicitly mentioned in the notation.

At low Q values, such a Q-dependence can be made explicit using a polynomial Q-expansion (see, e.g., [12]), which to the lowest order yields:

$$\omega_s \approx \omega_s^{hyd} = c_s Q \tag{4a}$$

$$z_s \approx z_s^{hyd} = \left[(\gamma - 1)D_T + \nu_L\right]Q^2/2 \tag{4b}$$

$$z_h \approx z_h^{hyd} = D_T Q^2 \tag{4c}$$

with c_s, D_T, and ν_L being, respectively, the adiabatic sound velocity, the thermal diffusivity, and the longitudinal kinematic viscosity.

One readily recognizes that Eq. (3) consists of these components (from left):

1. The so-called Rayleigh, or central, peak (term $\propto A_h$) which relates to entropy (heat) fluctuations diffusing at constant pressure (P).

2. The two Brillouin side peaks (term $\propto A_S$), connected to P-fluctuations propagating at constant entropy, and

3. An additional contribution (term $\propto A_s b$) asymmetric around the Brillouin peaks position having negative tails. This term distorts the Lorentzian terms (1) and (2) ultimately enabling the convergence of spectral moments $\int_{-\infty}^{+\infty} \omega^n S(Q, \omega)d\omega$ for $n \leq 2$. The latter imposes the following constraint: $b = [A_h z_h/(1 - A_h) + z_s]/\omega_s$.

The Rayleigh-Brillouin triplet in Eq. (3) is customarily quoted to as either generalized or simple hydrodynamic spectrum, respectively with or without the lowest order Q approximation in Eqs. (4a)–(4c).

It is worth stressing that the shape in Eqs. (3) and (4a)–(4c) provides an accurate description of the spectrum only when $D_T Q^2$, $\Gamma Q^2 << c_s Q$, or, equivalently, as long as the lifetime of hydrodynamic modes is much longer than the acoustic period. In this regime the spectrum is

dominated by three sharp peaks, forming the so-called Rayleigh-Brillouin triplet, typically measured in Brillouin light scattering (BLS) experiments.

Figure 2 displays the generic shape of the Rayleigh-Brillouin triplet from a liquid along with its three individual spectral components.
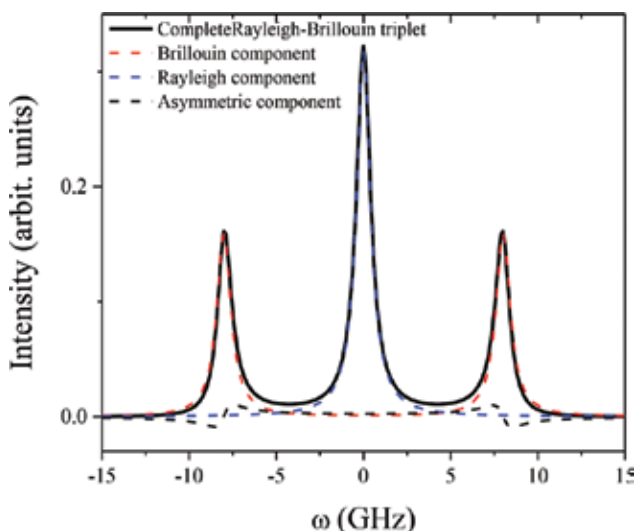
Figure 2. Typical shape of the Rayleigh-Brillouin triplet measured by Brillouin light scattering. The separate contributions to the total shape are represented by lines of different color, as indicated in the legend.

In general, the shape of the spectrum determined by a scattering experiment strongly depends on the probed space and time (or, equivalently, Q and ω) window, however the analytical form of such a dependence is generally unknown. Indeed, this is exactly known only at extreme Q and ω values: either extremely small (hydrodynamic limit-discussed above) or extremely large (single particle limit, to be discussed in Section 5).

At the crossover between these two limits, the shape of $S(Q,\omega)$ becomes highly sensitive complex dynamical processes involving inter and intramolecular degrees of freedoms. The coupling of density fluctuation with the mesoscopic dynamics of fluids makes the investigation of their spectrum of prominent interest.

3. The persistence of hydrodynamic modes beyond the continuous limit: first INS results

In principle, a "bare" extension of the hydrodynamic description of $S(Q,\omega)$ to the so-called mesoscopic regime would appear suspicious, since at those scales the matter can no longer be considered as continuous, or stationary. In fact, this regime corresponds to distances and times comparable with atomic separations and cage oscillations periods, respectively. Nonetheless,

sound arguments can still be used in support of a suitably generalized hydrodynamic description in this range. To understand this point, it is useful to recognize that for a dense liquid the mean free path can span the (10^{-1} nm) window, thus possibly becoming even smaller than interatomic separations. Under these conditions, the movements permitted to the atoms mainly resemble rapid, vibration-like, cage oscillations in the 0.1 ps window.

Consequently, even at mesoscopic (nm, ps) scales the response of the system is still "averaged" over a large number of elementary dynamic interactions, as required by a suitably generalized hydrodynamic description to hold validity. Based upon the above argument, possible reminiscences of Brillouin peaks in the THz spectrum of fluids appeared as an intriguing, yet somehow realistic, possibility since the early development of INS methods, which motivated several pioneering INS investigations in the mid-1960s.
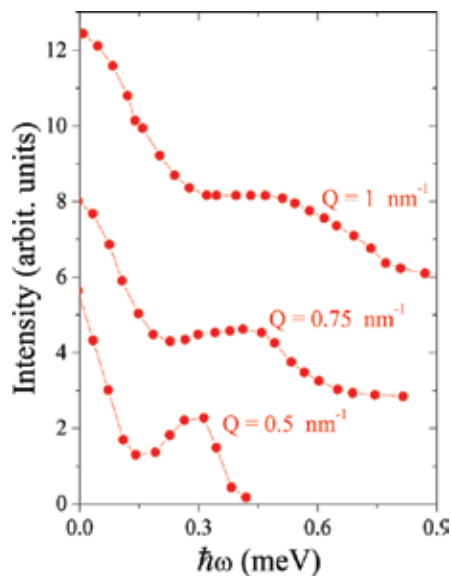
Figure 3. Few representative INS spectral line shapes of Ar measured by Bafile et al. [19] at low exchanged wave-vectors. Reported spectra have a mutual vertical offset for clarity.

Unfortunately, the first results reported in the literature were mutually inconsistent. In fact, the persistence in the spectrum of side shoulders reminiscent of hydrodynamic modes was suggested by Chen et al. [13] and successively confuted by Kroô et al. [14]. The former INS work focused on several samples having a strongly coherent neutron-scattering cross-section, as Ne, Ar, and D_2, and showed that, at low Qs, the frequency shift of side peaks approached from the above linear hydrodynamic law predicted by Eq. (4a) This pinpointed a link between these high frequency spectral features and the Brillouin peaks dominating the spectrum at much lower Qs. In a further INS work on Ar in both liquid (at T = 94 and 102 K) and solid (at T = 68 and 78 K) phases, Sköld et al. [15] found close resemblances between the phonon dispersion curves of a liquid and the one of a solid, thus suggesting that the local pseudo-periodicity of the liquid structure gives rise to quasiperiodic zones reminiscent of the Brillouin

zones of a crystal. A similar conclusion was previously reached by an INS investigation on liquid Pb [16], as well as a computer simulation on liquid Rb [17].

Coming back to noble gases, the first convincing evidence of well-defined inelastic peaks beyond the hydrodynamic regime is suggested by an INS measurement of Bell and collaborators on supercritical neon [18]. The low Q values explored in such a work (0.6 nm^{-1} ≤ Q ≤ 1.4 nm^{-1}) substantially reduced the dynamic gap between neutron and visible light Brillouin scattering techniques. The results demonstrated that the simple hydrodynamic theory consistently describes the spectral shapes well beyond the continuous limit and at least down to few nanometers distances. In particular, the inelastic shift of side peaks had, reportedly, a linear Q-dependence, whose slope is consistent with the adiabatic sound velocity.

Almost two decades after the measurement by Bell et al. on Ne, further low Q INS measurements were performed by Bafile et al. on supercritical Ar [19]. Again, the spectral line-shape measured in this work clearly confirmed the persistence of extended Brillouin peaks beyond the hydrodynamic limit (see **Figure 3**).
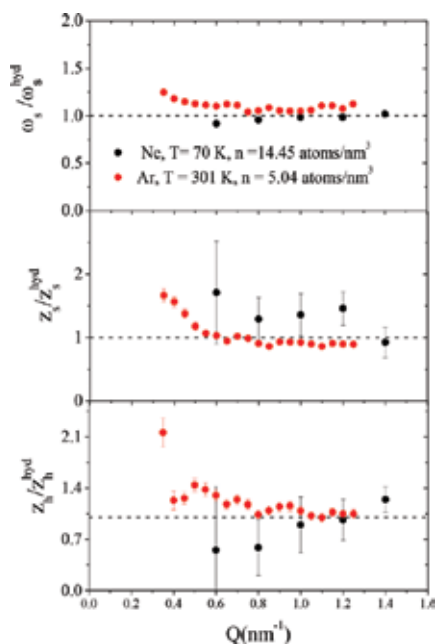
Figure 4. Shape parameters of the $S(Q,\omega)$ reported by Refs. [18, 19] for Ne and Ar, respectively, under the indicated thermodynamic conditions. Data are normalized to the corresponding hydrodynamic values as derived from Eqs. (4a)–(4c). Transport parameters in Eqs. (4a)–(4c) were extracted either from original works or from the database of the National Institute of Standards and Technology (NIST).

The extremely low Q range explored by this work (0.35 nm^{-1} ≤ Q ≤ 1.25 nm^{-1}) further reduced the gap separating standard INS measurements from light scattering ones. The INS investigation of Bafile and collaborators took full advantage of the improved statistical accuracy in

the beam counting and the unprecedented fine Q-grid. Both these assets enabled a very precise determination of the Q-dependence of line-shape parameters in Eq. (3).

Best-fit values of such parameters derived from [19] are reported in **Figure 4** after normalizations to the respective simple hydrodynamic predictions, expressed by Eqs. (4)–(4). The corresponding quantities derived by Bell and collaborators for neon [18] are also reported for comparison.

Data reported in **Figure 4** demonstrate that the simple hydrodynamic laws in Eqs. (4a)–(4c) derived for continuous media hold validity up to the ≈ 1 nm^{-1} mesoscopic Q-range. This result is certainly surprising since at these Q's the spectral peaks gradually transform into broad features (see, e.g., **Figure 3**) for which the simple hydrodynamic approximation ($D_T Q^2$, $\Gamma Q^2 << c_s Q$) becomes clearly inaccurate. In Ref. [19] these high frequency inelastic features are quoted to as "extended hydrodynamic modes," which emphasizes their hydrodynamic-like behavior persistent well beyond the continuous limit.

4. The advent of inelastic X-ray scattering

The only THz spectroscopic technique available until the mid-1990s, INS, is intrinsically hampered by kinematic limitations (see, e.g., [5] pp. 63–101). These shrink the accessible portion of dynamic plane (Q,ω) especially at low Qs, where the collective modes dominate. This problem was successfully addressed by the development of IXS, a technique virtually free from kinematic limitations [2, 3], apart from, of course, those arising from finite energy resolution width. Toward the end of past millennium, the availability of this new spectroscopic tool revitalized the interest toward experimental studies of the transition from the continuous to the mesoscopic regime. It is important to stress that noble gases present undoubted advantages in this kind of studies. In fact, at variance of molecular fluids, their microscopic components lack internal degrees of freedom and contrary to, e.g., metallic liquids, microscopic interactions are simpler and shorter-ranged. These, for instance, are key assets to reliably approximate the interatomic potential when performing molecular dynamics (MD) simulation studies [20]. Another advantage of gaseous systems in general is the large compressibility, which permits substantial variations of density, that is the strength of atomic interactions, even with moderate thermodynamic changes.

The first IXS measurement on a dense noble gas was performed on deeply supercritical neon (T = 295 K, n = 29.1 atoms/nm³) in 1998. Experimental results were discussed in combination with the outcome of a parallel MD simulation on a Lennard-Jones model representative of the same sample [21]. In **Figure 5**, some of the IXS spectra discussed in this work (and, successively in Ref. [22]) are compared with the best-fitting line-shape obtaining using Eq. (3) as a model, without any constraint on the Q dependence of shape parameters. In this case the persistence of a triple peak structure at mesoscopic scale can be inferred at least up to Q = 6 nm^{-1}, while at Q = 10 nm^{-1} or higher the two shoulder can be no longer easily discerned in the IXS spectral shape.
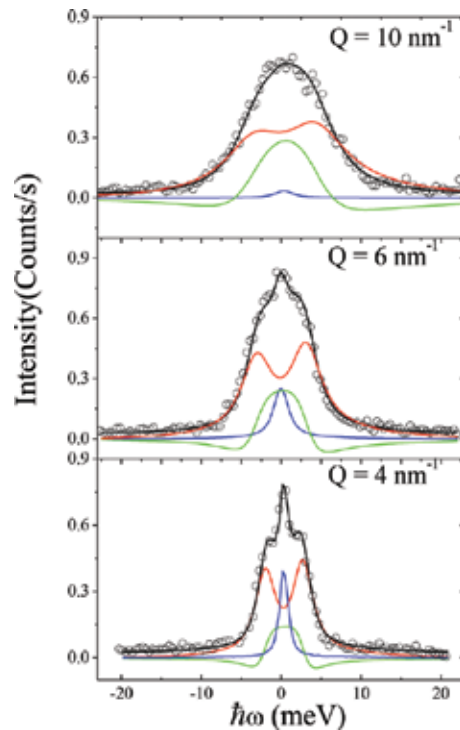
Figure 5. Some representative spectral shapes (circles) of deeply supercritical neon at $P = 3$ kbar and ambient temperature reported in [22] are compared with corresponding best-fitting line shapes (black lines) and their quasi-elastic (blue), inelastic (red) and "negative tails" (green line) components. These are obtained using Eq. (3) as a model for the spectral shape.

4.1. The Q-dependence of the spectral shape parameters

At this stage a question may arise on the Q dependence of inelastic peaks beyond the extremely low Q (<1nm^{-1}) extended hydrodynamic regime probed by Brillouin neutron scattering. A meaningful answer to this question is provided by the IXS results displayed in **Figure 6**, which illustrates the results reported in [21] and also discussed in [22]. These data refer to deeply supercritical neon at room temperature and 3 Kbar pressure. Plotted data appear paradigmatic of an IXS measurement on a simple, hard sphere-like, system of a supercritical dense gas. The curves are compared with the trends expected in the simple hydrodynamic limit, as obtained by inserting in Eqs. (4a)–(4c) the transport parameters derived from the National Institute of Standards and Technology (NIST). It can be readily noticed that the Q-dependence of ω_s is linear within a Q range extending up to $Q \approx 10$ nm^{-1}, the slope being consistent with the adiabatic sound velocity of the sample (1050 m/s). The Q-interval spanned by this linear trend corresponds to distances larger than about .6 nm, a value higher, yet comparable, with first neighboring atoms separations. This indicates that an extended hydrodynamic behavior can be still observed at Q higher by a decade than those previously investigated by Bell et al. [18] and Bafile et al. [19].
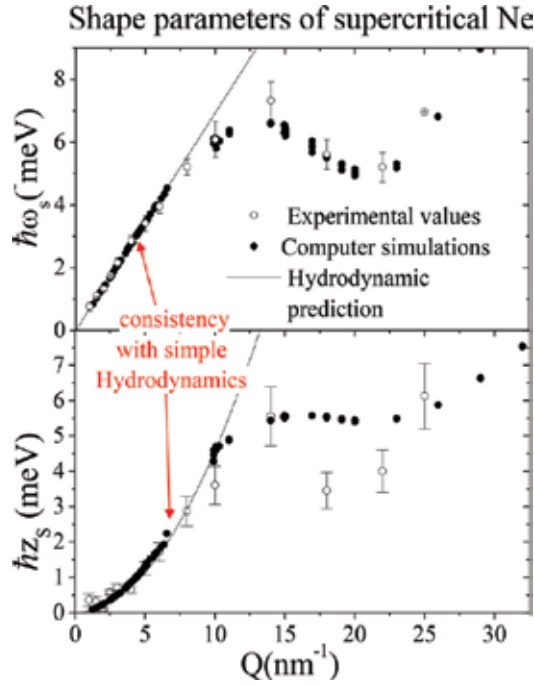
Figure 6. Shape parameters of the inelastic modes of $S(Q,\omega)$, as derived for supercritical Ne by IXS (circles [22]) and MD simulations (dots [21]). The solid lines represent the hydrodynamic predictions derived from Eqs. (4a) and (4b), while inserting in them thermodynamic and transport parameters from [28] and from [29], respectively.

4.1.1. The role of the static structure factor

From **Figure 6** one readily notices that beyond $Q = 10$ nm^{-1} the extended acoustic frequency ω_s bends down to a minimum at about 22.5 nm^{-1}. This turns out to be the same Q value where the structure factor $S(Q)$ (not reported in the plot) reaches its first maximum. We recall here that the static structure factor is related to the $S(Q,\omega)$ by the simple relation:

$$S(Q) = \int_{-\infty}^{\infty} S(Q,\omega)d\omega \tag{5}$$

Upon inserting Equation (1) i the formula above, it readily appears that the ω-integration of $S(Q,\omega)$ introduces a term $\propto \delta(t) = 1/2\pi \int_{-\infty}^{\infty} \exp[i\omega t]dt$, which, as well known, is nonvanishing only for $t = 0$. It follows that $S(Q)$ essentially measures the "static" ($t = 0$) value of density correlations, rather than the dynamic one probed by $S(Q,\omega)$. Therefore, $S(Q)$ carries direct insight into time-independent or structural properties of the fluid, which justify the name "static structure factor," customarily used for this variable. Alternatively, $S(Q)$ is often referred to as diffraction

profile as directly determined by diffraction measurements. These are frequency integrated measurements of the scattering and, as such, not directly sensitive to the dynamic (*t*-dependent) properties of the sample.
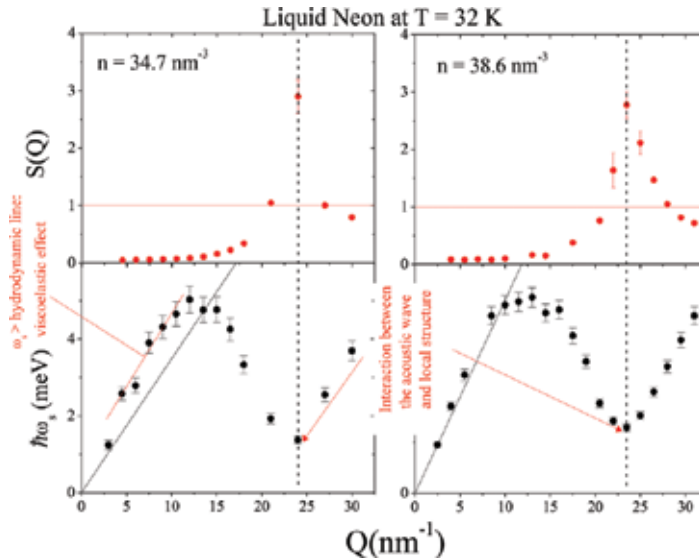
Figure 7. The dispersion liquid neon (bottom panels) are compared with the diffraction profiles *S(Q)* (upper panels), both being derived from IXS measurements discussed in Ref. [24] The vertical dashed lines indicates the essentially coincident *Q*-position of minima and maxima of ω_s and *S(Q)*, respectively. Horizontal lines in the upper plots indicate the asymptotic large *Q* unit value. The dispersive effects discussed in the text are labeled and indicated by arrows.

Typical *S(Q)* profiles of a liquid are reported in **Figures 7** and **9**. In all reported curve one readily notices the presence of a sharp maximum at some exchanged wavevector, $Q = Q_m$ for which $Q_m = 2\pi/a$, with a being the average distance between first neighboring atoms. Furthermore, it clearly appears from **Figure 9** that beyond the first diffraction peak the *S(Q)* displays oscillations from the unit limiting value, which is reached at extremely high *Q*'s. As discussed in Section 5 in further detail, these oscillations are induced by coherent or "pair" interactions. In crystalline solid pair, interactions are much stronger and this is reflected by the circumstance that the diffraction profile, rather than highly damped oscillations, displays narrow and exceptionally intense spots (Bragg peaks) [23].

4.2. The physical meaning of the dispersion minimum

The coincidence between the positions of the first *S(Q)* maximum and the ω_s minimum is an ubiquitous feature of liquids, clearly exemplified in **Figure 7**. There, the dispersion curve and corresponding static structure factor are compared as derived from the modeling of IXS spectra of liquid Ne [24]. The vertical dashed line shows unambiguously the coincidence between the *S(Q)* maximum and ω_s minimum. Indeed, both effects appear as a manifestation of the interference between the density fluctuations and the pseudo-periodicity of the local structure.

Specifically, a maximum in $S(Q)$ is observed when the probed distance, Q^{-1}, roughly matches the first neighboring atoms' separation. Under this condition, the presence of an "interference node" (the first neighboring atom) causes a sharp minimum in the density wave dispersion.

This minimum arises from the coexistence of an acoustic wave "transmitted" through the node — for which $\partial \omega_s / \partial Q > 0$ (positive group velocity)—and one reflected by it— for which $\partial \omega_s / \partial Q < 0$ (negative group velocity). It is commonly observed that the sharpness of this minimum deeply enhances upon approaching the solid phase. This suggests that, at mesoscopic scales, dispersion of a dense liquid resembles the one of its crystalline counterpart.

4.3. The slowing down of the dynamics

Figure 6 clearly shows that beside the extended sound frequency ω_s, also the half-width of the sound mode, z_s, reaches a local minimum at Q_m and, although non reported in the figure, a similar behavior is observed for the quasielastic half-width z_h [25]. The occurrence of a minimum in z_h was predicted by De Gennes [26], the effect having been named after him the "De Gennes narrowing." More in general, a large body of IXS results on liquids demonstrates that all relevant timescales defining the dynamics of density fluctuations undergo a clear enhancement at Q_m. This global slowing down of the dynamics stems from the higher correlation between the movements of the atoms and those of the respective first neighbor cages for $Q = Q_m$. As noticed by Sköld [27] $S(Q)$ yields a measure of the effective number of atoms contributing to the scattered intensity at a given exchanged wave vector Q. It seems thus natural to ascribe the slowing down at Q_m to the higher inertia of the target system due to the larger number of atoms participating to the collective response of the target system. In particular, first neighbor movements become more correlated when Q matches the inverse of first neighbor's separations and $S(Q)$ approaches its first maximum. One can thus identify the quantity $Q^* = Q / \sqrt{S(Q)}$ as the momentum "effectively" transferred, where the factor $\sqrt{S(Q)}$ embodies the inertia of the target system [27]. For a perfect crystal, owing to the global periodicity of first neighbors' arrangement, such a factor diverges when Bragg conditions are met. Here the whole target system coherently participates to density fluctuations and, correspondingly, an infinitely narrow intrinsic spectral linewidth is to be expected. Furthermore, the effective inelastic shift, proportional to Q^*, tends to vanish as $1 / \sqrt{S(Q)}$.

4.4. The onset of viscoelastic effects

A noticeable feature displayed by the left bottom plot of **Figure 7** is the clear inconsistency between the low-intermediate Q region of the dispersion curve and the corresponding linear hydrodynamic prediction.

Although a detailed description of this effect goes beyond the scope of this chapter, it is useful to recall here that this is a manifestation of the viscoelastic response induced by the coupling with a relaxation process.

To better illustrate this point, it is useful to recall that scattering-excited density fluctuation causes a time-dependent perturbation of the local equilibrium of the target sample. As a

response, decay channels redistribute the energy from the density fluctuation toward some internal degrees of freedom, thus ultimately driving the sample to relax into a new local equilibrium within a timescale τ.

Two limiting scenarios can thus occur:

1. the time-dependent acoustic perturbation has a timescale much longer than any internal degrees of freedom of the system. Under these conditions, the latter relaxes to equilibrium "instantaneously" and the density fluctuation propagates or diffuses over successive equilibrium states (**viscous**, or liquid-like, limit);

2. If the density fluctuation is instead extremely rapid, it "perceives" internal rearrangements as frozen-like and does not couple with them thus virtually evolving with no energy losses (**elastic** or solid-like limit).

If such considered perturbation has the form of an acoustic wave, its transition from the viscous to the elastic limit is accompanied by a decrease of dissipation and a consequent increase in the propagation speed. Therefore a **viscoelastic** transition manifests itself through a systematic increase of sound velocity with Q. While the hydrodynamic theory correctly predicts (through Eq. (4a)) the Q-dependence of ω_s in the viscous limit, it fails to predict its elastic value at intermediate Qs. This explains the discrepancy between the hydrodynamic straight line and the actual value of the inelastic shift in the 5 nm^{-1} < Q < 14 nm^{-1} range, as evidenced in the bottom left plot of **Figure 7**.

5. Moving toward the single particle limit

Upon reaching extremely high Q values, the probed dynamic event gradually reduces to the free recoil of the single particle after the collision with the probe particle and before any successive interactions with the first neighbors' cage.

Within these short times, the struck atom can be assumed to freely stream without interacting with the neighboring cage, its equation of motion being thus expressed as $\vec{R}_j(t)=\vec{v}_j t$.

This merely "ballistic" behavior can be easily understood for a system of hard spheres, in which microscopic interactions essentially consists of atomic collisions, i.e., interactions instantaneous and localized in space. For a more realistic system, atomic interactions can no longer be considered as "close contact", rather spanning finite distance and time lapses. However, if the energy transferred in the scattering event is much larger than any local interaction, the struck particle can still be "perceived" as freely recoiling from the collision with the probe. In this so-called impulse approximation (IA) regime it can be safely assumed that no sizable external force acts on the isolated system formed by the incident photon and the struck atom.

Within the unrealistic hypothesis that the target atom is exactly at rest, its response function would reduce to a delta function centered at the recoil energy. More realistically, one can assume that the initial state of the system is characterized by a distribution of initial momenta, and the spectrum scattered by this moving source therefore becomes "Doppler broadened."

Each possible initial momentum provides a contribution to the scattering intensity and the shape of the spectrum is directly connected to the momentum distribution of the struck particle.

For a classical particle this can be assumed to have the form of a Maxwell-Boltzmann distribution $\propto \exp\left(-Mv^2/2k_BT\right)$, where M is the atomic mass. Disregarding the analytical details of the derivation (thoroughly discussed, for instance, in Ref. [5]), it is here important to mention that the use of the Boltzmann distribution ultimately yields the following Gaussian shape for the dynamic structure factor:

$$S_{IA}(Q,\omega) = \left(\frac{M}{2\pi k_B T Q^2}\right)^{1/2} \exp\left[\frac{M\hbar}{2\pi k_B T Q^2}(\omega - \omega_r)^2\right] \qquad (6)$$

where the suffix "IA" labels the impulse approximation value of $S(Q,\omega)$. One readily recognizes that profile in Eq. (8) is a Gaussian centered at $\omega=0$ and its variance, $k_B T Q^2/M$, can be simply related to the mean kinetic energy of the struck particle ($\langle K.E.\rangle = 3/2k_BT$ for a monatomic system). It can be shown that for a quantum system, the *IA* spectrum preserves the Gaussian shape; however, its variance deviates from the classically expected values being instead simply determined by the quantum value of $\langle K.E.\rangle$. Since the latter is in general unknown, a useful application of extremely high Q measurements is to achieve a direct determination of its value (see, e.g., Ref. [30]). Another interesting application is the determination of actual shape of the momentum distribution, e.g., in intriguing quantum system as Bose condensates [31].

The study of the spectrum of simple fluids in the IA regime [32] has been for decades an essentially exclusive domain of deep inelastic neutron scattering (DINS). The first deep inelastic X-ray scattering (DIXS) investigations of the IA spectrum of liquids were pioneered by a work on liquid neon at the onset of the new millennium [33].

In this work, it was found that the single particle kinetic energy extracted from the spectral shape provided clear evidence for quantum deviations.

An example of the gradual evolution of the IXS spectrum toward the single particle Gaussian shape predicted by Eq. (6) is illustrated in **Figure 8**.

DIXS experiments are not common in the literature since this technique suffers from major intensity penalties due to the high Q decay of the form factor. Furthermore, these studies often deal with samples having a light atomic mass (as He, D_2 and H_2, and Ne), as better suited to observe quantum effects. Unfortunately, these systems have also a small atomic number which makes their IXS cross-section rather weak. Finally, the highest Q's reachable by DIXS are still below typical values covered by DINS measurements by more than an order of magnitude. These intrinsic and practical difficulties explain why DIXS experiments are still sporadic and this technique is still in its "infancy."
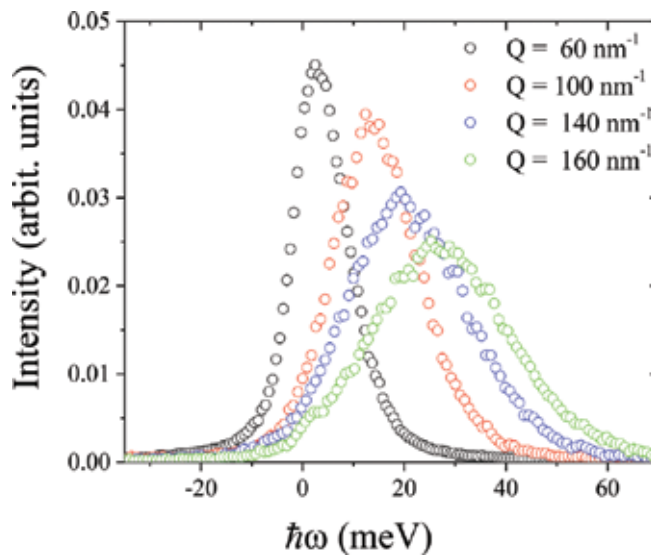
Figure 8. The gradual Q-evolution of the IXS spectrum of Ne [33] toward the Gaussian shape characteristic of the single particle regime.

It is important to stress that the IA regime is only joined asymptotically at extremely high Qs. Before this limit is fully reached, the struck atom cannot be considered as a freely recoiling object and first neighbor interactions need to be taken into account explicitly. It is usually assumed that the latter influence only the final (after scattering) state of the struck particle, while its initial state being still essentially "free." Among various recipes to handle theoretically these "final state effects," the so-called additive approach [34], is the one used in the very few extremely high Q IXS measurements available [33, 35, 36]. This approach stems from an expansion of the intermediate scattering function in time cumulants, in which only the first few lower order term are retained. As a results of this perturbative treatment, deviations from a perfect Gaussian shape can be easily linked to the lowest order (n) spectral moments and contain valuable information on meaningful physical parameters as, e.g., the mean force acting on the atom and the mean square Laplacian, both providing a meaningful and unique characterization of quantum effects (see, e.g., [33]).

5.1. The case of molecular systems

After the work of Monaco et al. on a monoatomic fluid [33], a successive DIXS work [35] aimed at investigating the next simplest case of a diatomic homonuclear system as liquid iodine. In this work, no signature of quantum effects was reported due to both the larger molecular mass and the higher temperature of the sample.

Even in the absence of quantum deviations, the interpretation of the IXS spectrum of a molecular fluid is overly complex, owing to the coupling of the spectroscopic probe with all molecular degrees of freedom [37] as well as their mutual entanglement. In the simplest assumption that all degrees of freedom are decoupled and belong to very disparate energy

windows, the observed response strongly depends on how the exchanged energy, E compares not only with centers of mass translational energies, E_t, but also with intramolecular rotational and vibrational quanta, $\hbar\omega_r$ and $\hbar\omega_v$, respectively.

Specifically, three complementary *IA* regimes can be identified:

- When $E_t << E << \hbar\omega_r, \hbar\omega_v$ the struck molecule is "seen" by the probe as an object with spherical symmetry experiencing a merely translational recoil induced by the collision with the probe. The energy of such a recoil energy is $\hbar^2 Q^2/2M$, with M being the molecular mass. Here the scattered intensity carries direct insight into the merely translational momentum distribution of the molecular centers of mass.

  In an intermediate window ($E_t, \hbar\omega_r << E << \hbar\omega_v$), usually referred to as the *Sachs−Teller(ST)* regime [38], the molecule behaves as a freely recoiling rigid roto-translator. In this Sachs-Teller regime, the rotational component of the recoil can be written as $\hbar^2 Q^2/2M_{ST}$, in which the effective, or Sachs-Teller mass, M_{ST}, is determined by the eigenvalues of the molecular tensors of inertia. In this regime, the spectral density becomes proportional to the distribution of roto-translational momenta of the molecules. The DIXS work in Ref. [35] demonstrated that the Sachs-Teller theory provides a consistent interpretation of the spectral shape of iodine at the largest Q values covered by state-of-art IXS spectrometers.

- Eventually, when the $E >> \hbar\omega_{r,v}$ condition is matched, the exchanged energy becomes overwhelmingly stronger than any intramolecular and intermolecular interaction, therefore, the nucleus inside the molecule is for short-time freed from its bound state experiencing a recoil as a free particle. Under these conditions, the scattering intensity becomes proportional to the single proton initial momentum distribution.

  In principle, at higher exchanged energies and momenta higher-level IA regimes can be probed. This happens when energies transferred in the scattering event are much larger than intranuclear interaction and, correspondingly, subnuclear particle start experiencing free particle recoils. These phenomena belong to a domain of physics complementary to condensed matter Physics and rather fitting in the fields of high energy and particle physics.

6. Summarizing the state of the art of IXS technique

In conclusion, the relevant phenomenology of the spectral evolution from the hydrodynamic to the single particle regime discussed in this chapter is summarized in **Figure 9**. There, the whole crossover of the spectral shape from the hydrodynamic Brillouin triplet to the single particle Gaussian is reported as determined in separate inelastic measurements. The corresponding Q window are indicated in reference to the various regions of the diffraction profile *S(Q)*, reported in the center of the figure. It can be readily noticed that, while "climbing" the wings of the first diffraction peak, the sharp Brillouin triplet (Panel A) gradually transforms into a more complex shape in which the side peaks appear as broad features (Panels B). When Q values become comparable or higher than the position of the dominant S(Q) peak (Panel C),

these shoulder can no longer be resolved due to their intrinsic overdamping. The best-fit components of the spectrum, also reported for the spectra in Panel C, can help to better identify the presence of these "generalized hydrodynamic" modes. Upon further increasing Q, "coherent" oscillations of $S(Q)$ gradually damp out and correspondingly the shape of the spectrum transforms into a Gaussian centered at the recoil energy (Panel D). This gradual evolution can be readily captured by comparing the measured shape with the Gaussian profile in Eq. (6).

Great expectations are raised by the advent of new generation IXS spectrometers further reducing the dynamic gap separating IXS from Brillouin light scattering [39]. This will possibly revitalize the dream of entire generations of condensed matter physicists: a single inelastic spectrometer covering the relevant portion of the crossover from the hydrodynamic to the single particle regimes. Parallel advances in the theory of the spectrum of fluids and the empowering of simulation methods are deemed to improve our understanding of this crossover and all dynamical phenomena happening in a fluid from macroscopic to microscopic scales.
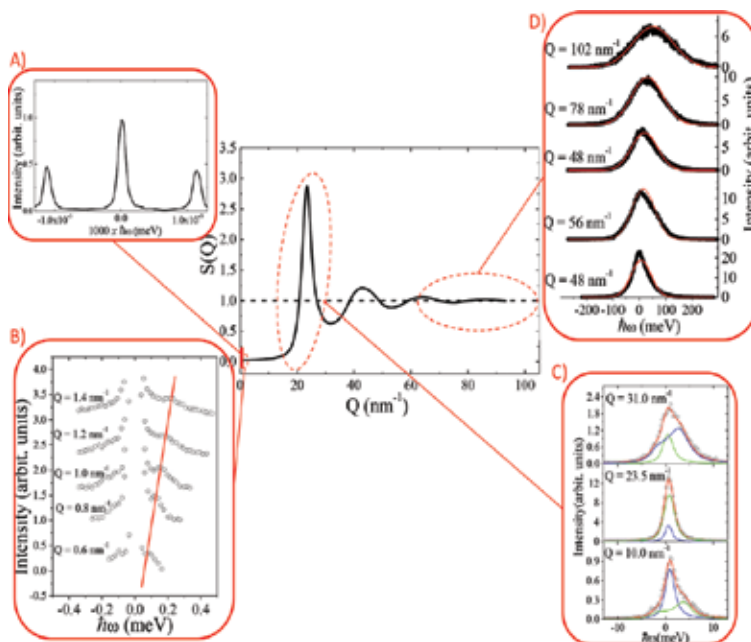
Figure 9. Overview of experimental spectra measured in several Q windows across the transition from the hydrodynamic to the single particle regime in monatomic fluids. Panel A reports Brillouin light scattering spectra of liquid Ar [40]. Panel B displays INS measurements on supercritical Ne [18] with the red line roughly indicating the linear dispersion of side peaks. Panel C shows IXS spectra on liquid Ne [24]) with corresponding best-fitting line shapes and individual spectral components. Finally, Panel D displays IXS spectra of liquid Li from [41] along with the single particle Gaussian shape (red line) predicted by Eq. (9).

Acknowledgements

Author details

Alessandro Cunsolo

Address all correspondence to: acunsolo@bnl.gov

National Synchrotron Light Source II, Brookhaven National Laboratory, Upton, NY, USA

References

[1]   Brockhouse BN, Stewart AT. Scattering of neutrons by phonons in an aluminum single crystal. Physical Review. 1955; 100: 756–757. DOI: http://dx.doi.org/10.1103/PhysRev.100.756

[2]   Burkel E. Phonon spectroscopy by inelastic X-ray scattering. Reports on Progress in Physics, 2000; 63: 171–232. DOI: http://dx.doi.org/10.1088/0034-4885/63/2/203

[3]   Krisch M, Sette F. in Neutron and X-Ray Spectroscopy. Berlin: Springer-Verlag; 2007. pp. 317–370.

[4]   Berne BJ, Pecora R. Dynamic Light Scattering. Mineola: Dover; 1976. 384 p.

[5]   Lovesey SW. Theory of Neutron Scattering from Condensed Matter. Vol. 1. Oxford: Clarendon Press; 1984. 329 p.

[6]   Sinha SK. Theory of inelastic X-ray scattering from condensed matter. Journal of Physics-Condensed Matter, 2001; 13: 7511–7523.

[7]   Cunsolo A. Using X-ray as a probe of the terahertz dynamics of disordered systems—complementarity with inelastic neutron scattering and future perspectives. in Neutron Scattering, WA Monteiro, Editors. Rjeka: InTech; 2016.

[8]   Jackson JD. Classical Electrodynamics. Vol. 3. New York: Wiley; 1962.

[9]   Brillouin L. Diffusion of light and X-rays by a transparent homogeneous body. Annales de Physyque (Paris), 1922; 17: 88.

[10] Mason EA, Marrero TR. The diffusion of atoms and molecules, in Advances in Atomic and Molecular Physics, Bates DR, Immanuel E, Editors. Orlando: Academic Press; 1970. pp. 155–232.

[11] Hansen, JP, IMcDonald IR. Hydrodynamics and transport coefficients, in Theory of Simple Liquids (Third edition), Chapter 8. Burlington: Academic Press; 2006. pp. 219–254.

[12] Bafile U, Guarini E, Barocchi F. Collective acoustic modes as renormalized damped oscillators: unified description of neutron and X-ray scattering data from classical fluids. Physical Review E. 2006; 73: 061203 DOI: http://dx.doi.org/10.1103/PhysRevE. 73.061203.

[13] Chen SH, et al. Co-operative modes of motion in simple liquids. Physics Letters. 1965; 19: 269–271. DOI: 10.1016/0031-9163(65)90980-7

[14] Kroô N, et al. International Atomic Energy Agency. Inelastic scattering of cold neutrons by condensed argon. in Symposium on Inelastic Scattering of Neutrons. Bombay: IAEA; 1964.

[15] Skold K, Larsson KE. Atomic motion in liquid argon. Physical Review. 1967; 161: 102–116.

[16] Randolph PD, Singwi KS. Slow-neutron scattering and collective motions in liquid lead. Physical Review. 1966; 152: 99–112.

[17] Rahman A. Propagation of density fluctuations in liquid rubidium: a molecular-dynamics study. Physical Review Letters. 1974; 32: 52–54.

[18] Bell HG, Kollmar A, Alefeld B, Springer T. Investigation of collective excitations in liquid neon by means of neutron-scattering at small scattering vectors. Physics Letters A. 1973; 45: 479–480. DOI: 10.1016/0375-9601(73)90717-2

[19] Bafile U, Verkerk P, Barocchi F, de Graaf LA, Suck JB, Mutka H. Onset of departure from linearized hydrodynamic behavior in argon gas studied with neutron Brillouin scattering. Physical Review Letters. 1990; 65: 2394–2397. DOI: http://dx.doi.org/10.1103/PhysRevLett.65.2394

[20] Allen MP, Tildesley DJ. Computer Simulation of Liquids. Oxford: Oxford University Press; 1989.

[21] Cunsolo A, Pratesi G, Ruocco G, Sampoli M, Sette F, Verbeni R, Barocchi F, Krisch M, Masciovecchio C, Nardone M. Dynamics of dense supercritical neon at the transition from hydrodynamical to single-particle regimes. Physical Review Letters. 1998; 80: 3515–3518. DOI: http://dx.doi.org/10.1103/PhysRevLett.80.3515

[22] Cunsolo A. Relaxation Phenomena in the THZ Dynamics of Simple Fluids Probed by Inelastic X Ray Scattering. Grenoble: Universite' J. Fourier; 1999.

[23] Egami T, Billinge SJ. Underneath the Bragg Peaks: Structural Analysis of Complex Materials. Vol. 16. Oxford: Elsevier; 2003.

[24] Cunsolo A, Pratesi G, Verbeni R, Colognesi D, Masciovecchio C, Monaco G, Ruocco G, Sette F. Microscopic relaxation in supercritical and liquid neon. Journal of Chemical Physics, 2001; 114: 2259–2267. DOI: http://dx.doi.org/10.1063/1.1334613

[25] Cunsolo A, Pratesi G, Rosica F, Ruocco G, Sampoli M, Sette F, Verbeni R, Barocchi F, Krisch M, Masciovecchio C, Nardone M. Is there any evidence of a positive sound dispersion in the high frequency dynamics of noble gases? Journal of Physics and Chemistry of Solids. 2000; 61: 477–483. DOI: http://dx.doi.org/10.1016/S0022-3697(99)00340-6

[26] De Gennes PG. Liquid dynamics and inelastic scattering of neutrons. Physica. 1959; 25: 825–839. DOI: 10.1016/0031-8914(59)90006-0

[27] Skold K. Small energy transfer scattering of cold neutrons from liquid argon. Physical Review Letters. 1967; 19: 1023–1025. DOI: http://dx.doi.org/10.1103/PhysRevLett.19.1023

[28] NIST. Thermodynamic data are from the database *http://webbook.nist.gov/chemistry/form-ser.html*.

[29] Castillo R, Castaneda S. The bulk viscosity in dense fluids. International Journal of Thermophysics. 1988; 9: 383–390. DOI: 10.1007/BF00513078

[30] Senesi R, Andreani C, Colognesi D, Cunsolo A, Nardone M. Deep-inelastic neutron scattering determination of the single-particle kinetic energy in solid and liquid 3He. Physical Review Letters. 2001; 86: 4584–4587. DOI: http://dx.doi.org/10.1103/PhysRevLett.86.4584

[31] Stringari, S, Pitaevskii L, Stamper-Kurn DM, Zambelli F. Momentum distribution of a bose condensed trapped gas, in Bose-Einstein Condensates and Atom Lasers, S Martellucci, et al., Editors. Boston: Springer; 2002. pp. 77–95.

[32] Silver RN, Sokol PE, Editors. Momentum Distributions. New York: Springer; 2013.

[33] Monaco G, et al. Deep inelastic atomic scattering of X rays in liquid neon. Physical Review Letters. 2002; 88: 227401. DOI: http://dx.doi.org/10.1103/PhysRevLett.88.227401

[34] Glyde HR. Momentum distributions and final-state effects in neutron scattering. Physical Review B. 1994; 50: 6726–6742. DOI: http://dx.doi.org/10.1103/PhysRevB.50.6726

[35] Izzo, MG, Bencivenga F, Cunsolo A, Di Fonzo S, Verbeni R, Gimenez De Lorenzo R. The single particle dynamics of iodine in the Sachs-Teller regime: an inelastic X ray scattering study. Journal of Chemical Physics. 2010; 133: 124514. DOI: 10.1063/1.3483689

[36] Cunsolo A, Monaco G, Nardone M, Pratesi G, Verbeni R. Transition from the collective to the single-particle regimes in a quantum fluid. Physical Review B. 2003; 67: 024507. DOI: http://dx.doi.org/10.1103/PhysRevB.67.024507 38

[37] Krieger TJ, Nelkin MS. Slow neutron scattering by molecules. Physical Review. 1957; 106: 290–295. DOI: http://dx.doi.org/10.1103/PhysRev.106.290

[38] Sachs RG, Teller E. The scattering of slow neutrons by molecular gases. Physical Review. 1941; 60: 18–27. DOI: http://dx.doi.org/10.1103/PhysRev.60.18

[39] Cai YQ, Coburn1 DS, Cunsolo A, Keister JW, Honnicke MG, Huang XR, Kodituwakku CN, Y Stetsko1, Suvorov A, Hiraoka N. The ultrahigh resolution IXS beamline of nsls-ii: recent advances and scientific opportunities. 11th International Conference on Synchrotron Radiation Instrumentation (Sri 2012), 2013; 425: 202001. DOI: http://dx.doi.org/10.1088/1742-6596/425/20/202001

[40] Fleury PA, Boon JP. Brillouin Scattering in Simple Liquids – Argon and Neon. Physical Review. 1969; 186:244–254. DOI: https://doi.org/10.1103/PhysRev.186.244

[41] Scopigno T, Balucani U, Cunsolo A, Masciovecchio C, Ruocco G, Sette F, Verbeni R. Phonon-like and single-particle dynamics in liquid lithium. Europhysics Letters. 2000; 50:189–195. DOI: 10.1209/epl/i2000-00253-5

Grazing-Incidence Small-Angle X-ray Scattering

Grazing Incidence Small Angle X-Ray Scattering as a Tool for In-Situ Time-Resolved Studies

Gonzalo Santoro and Shun Yu

Additional information is available at the end of the chapter

Abstract

With the advent of third-generation synchrotron sources and the development of fast two-dimensional X-ray detectors, X-ray scattering has become an invaluable tool for in-situ time-resolved experiments. In the case of thin films, grazing incidence small angle X-ray scattering (GISAXS) constitutes a powerful technique to extract morphological information not only of the thin film surface but also of buried structures with statistical relevance. Thus, recently in-situ GISAXS experiments with subsecond time resolution have enabled investigating the self-assembly processes during vacuum deposition of metallic and organic thin films as well as the structural changes of polymer and colloidal thin films in the course of wet deposition. Moreover, processing of thin films has also been investigated in-situ employing GISAXS. In this chapter, we review the current trends of time-resolved GISAXS studies. After an introduction to the GISAXS technique, we present exemplary results of metallic and organic thin film preparation, wet deposition of polymer thin films and self-assembly of colloidal thin films, as well as examples of thin film modification in, e.g., microfluidic channels and within working devices. Finally, an overview of the future perspectives in the field is provided.

Keywords: GISAXS, thin films, time-resolved experiments, kinetics, processing

1. Introduction

Nanostructures have become commonly used in our daily lives because of the novel properties arising at the nanoscale. These are mainly associated to the object size offering a higher surface-to-volume ratio than macroscopic entities and, thus, surface processes become more

and more crucial as the material size is reduced. Furthermore, during the last half century several ways of manipulating the materials at the nanometer scale have been developed to control the nanostructure morphology on demand via either building up the nanostructures by atomic manipulation or exploiting self-assembly concepts. The latter presents clear advantages over atomic manipulation such as less demanding fabrication steps and easier scale-up for industrial production. Nevertheless, much is yet to be understood concerning self-assembly. In this sense, apart from the manipulation of materials at the nanoscale, an appropriate and accurate characterization of nanostructures is crucial, especially for studying the kinetics both during fabrication and processing of the nanostructures.

To properly characterize nanostructures, two questions need to bear in mind: what is the size/shape of the nanostructure and how do they separate from each other. The former is critical since nanostructure geometry strongly influences, e.g., the geometric confinement of the electronic structure [1], the catalytic activity [2, 3] or the optical properties [4, 5]. The latter is important since different physical properties may arise from particular nanostructure arrangement or in the space confined between the nanostructures, e.g., highly ordered arrays of plasmonic nanostructures present a collective plasmonic behavior [6], an efficient arrangement of the nano-objects may expose higher surface area on a macroscopic level for catalysis applications [7] or polymers within nanostructured media may show different glass transition temperatures and chain mobility due to confinement [8].

Within a non ideal material system, the size of the nanostructures and the spatial arrangement present a distribution over micro/macroscopic regions. Thus, the collective effects of nanostructured objects call for sound statistic evaluation. In this respect, grazing incidence small angle X-ray scattering (GISAXS) is nowadays one of the most interesting techniques for studying the morphology of nanostructured thin films. As its counterpart, transmission SAXS [9], it is sensitive to the size and shape of the nanoparticles and to the correlation distances between them, being capable of resolving objects and distances ranging from few nanometers to several hundreds of nanometers, in real space. In contrast to SAXS, GISAXS inherently presents high surface sensitivity as a consequence of the measurement geometry employed. In GISAXS, the incident X-ray beam impinges the sample at shallow angles, thus total external reflection on the surface may take place. In addition, this implies that the beam footprint on the sample probes macroscopic areas which, together with the nature of reciprocal space techniques, ensure that high sampling statistics is achieved.

GISAXS was first demonstrated by Levine et al. using a lab source [10]. However, the full potential of GISAXS is realized when a synchrotron is used as X-ray source. This is due to several reasons. First, a high photon flux is required to probe the surface structures, which may be only present in small amount in comparison to the bulk substrate, thus presenting a weak scattering signal; second, highly collimated beams are demanded to improve the reciprocal space resolution, thus the low emittance, small divergence, and partially coherent beams provided by synchrotron radiation sources are in great favor; third, synchrotron sources provide tunable X-ray wavelength, which may be used to probe the chemical composition in parallel to exploring the morphology.

The high X-ray photon flux of synchrotron sources extremely diminishes the acquisition time of a GISAXS pattern. This fact, along with a high flexibility in sample environments—e.g., vacuum chambers, liquid cells, heating stages, vapor exposure chambers, etc.—makes GISAXS a very powerful tool for acquiring morphological information on kinetic processes, which is extremely relevant to elucidate self-assembly processes. Additionally, the combination of parallel characterization techniques—e.g., optical spectroscopy and microscopy, electrical and magnetic characterization—allows correlating the structural information to the properties of the thin films, of utmost importance for tailoring the thin film functionality.

However, to carry out in-situ GISAXS, the high quality X-ray beam offered by synchrotron sources is not sufficient. The development of the 2D pixel detector, especially single photon counter, has played an important role. The high quantum efficiency and fast read-out time of 2D photon-counting pixel detectors can be translated to lower acquisition times—in comparison with CCD detectors; however, at present, CCD cameras offer small pixel size, implying higher resolution in reciprocal space. The low acquisition time renders a faster capture of the morphological features and the fast detector read-out time and efficiency enable high acquisition rates, thus it is possible to promptly track morphological development and/or modifications.

In this chapter, we will present the current trends of in-situ time-resolved GISAXS investigations during thin film preparation and processing. The chapter is structured as follows. Section 2 briefly introduces the GISAXS theory and analysis of GISAXS patterns. In Section 3, selected examples of in-situ GISAXS studies during the vacuum deposition of metals and organic thin films, as well as in-situ GISAXS investigations of wet deposition processes, are presented. Some exemplary studies of thin film processing and in-operando devices in which the use of in-situ GISAXS has resulted essential are compiled in Section 4. Finally, the conclusions and future perspectives of the field, according to the authors' opinion, are summarized in Section 5.

2. Grazing incidence small angle X-ray scattering

In this section, the basics of GISAXS will be shortly described. For more detailed information on the GISAXS theory, the readers are referred to [11–13].

2.1. Geometry, index of refraction and penetration depth

The main particularity of GISAXS lies on the geometry employed. Whereas in SAXS a transmission geometry is used, in GISAXS the X-ray beam impinges on the sample surface under a shallow incident angle, α_i, typically of tenths of a degree. The intensity scattered by the sample is then collected with a two-dimensional (2D) detector as a function of the exit, α_f, and out-of-plane, ψ, angles being the scattering plane that defined by the incident and specularly reflected X-rays. Typical sample-to-detector distances are in the range of 2–5 m and typical values of the scattering vector modulus q are 1–0.01 nm^{-1}, i.e., structures in the range of one to several hundred nanometer size in real space are probed by GISAXS.

The coordinate system usually selected in GISAXS presents the *x*-axis in the direction of the X-ray beam, the *y*-axis parallel to the sample surface and the *z*-axis along the surface normal.[1] The scattering geometry is depicted in **Figure 1**.
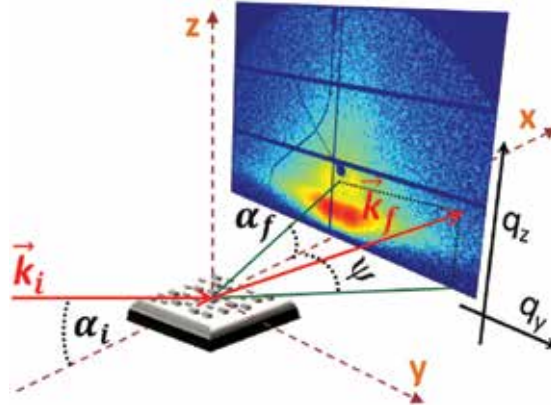

Figure 1. Sketch of the GISAXS scattering geometry. The sample is inclined by a small angle α_i with respect to the incoming X-ray beam and the diffuse scattering is recorded using a 2D detector as a function of the exit angles α_f and ψ. Typical sample-to-detector distances range from 2 to 5 m. Experimentally, the specular and the direct X-ray beams are commonly blocked by beamstops (the specular beamstop is the dark blue circle in the GISAXS pattern shown whereas the direct beamstop is not shown) to prevent the detector from oversaturation due to its strong intensity.

Within this coordinate system, the scattering vector, $\vec{q}$, i.e., the wave vector transfer due to the scattering event, in the case of monochromatic X-rays with an incident wave vector $\vec{k}_i$ and wave number $k_0 = 2\pi/\lambda$ scattered along the $\vec{k}_f$ direction is given by

$$\vec{q} = \vec{k}_f - \vec{k}_i = \begin{pmatrix} q_x \\ q_y \\ q_z \end{pmatrix} = \frac{2\pi}{\lambda} \begin{pmatrix} \cos(\alpha_f)\cos(\psi) - \cos(\alpha_i) \\ \cos(\alpha_f)\sin(\psi) \\ \sin(\alpha_i) + \sin(\alpha_f) \end{pmatrix} \tag{1}$$

Due to the small incident and exit angles involved in the GISAXS geometry a description of the sample based on a mean refractive index is sufficient and basically scattering arises from the variations in refractive index[2]

---

[1] For reasons out of our knowledge, the axes of the coordinate system commonly employed, and more often found in the literature, form an inverse trihedral angle—i.e., the axes are defined by the vector product $\hat{x} \times \hat{y} = -\hat{z}$, where, $\hat{x}$, $\hat{y}$ and $\hat{z}$ represent the axis unit vectors—instead of the usual direct trihedral angle. Anyway, since all the angles involved in GISAXS geometry are small, q_x is negligible (Eq. (1)) and this axis selection is not particularly relevant.

[2] Strictly, the responsible for the scattering events is the variation in electron density, which in a simplified manner is taken into account using a mean refractive index.

$$n(\lambda) = 1 - \delta(\lambda) + i\beta(\lambda) \tag{2}$$

where $\delta(\lambda)$ and $\beta(\lambda)$ represent the dispersion and absorption parts of X-rays, respectively, and are given by the following expressions:

$$\delta(\lambda) = \frac{r_e \lambda^2}{2\pi} \rho \frac{\Sigma_k [f_k^0(\lambda) + f'_k(\lambda)]}{\Sigma_k M_k} \tag{3}$$

$$\beta(\lambda) = \frac{r_e \lambda^2}{2\pi} \rho \frac{\Sigma_k f''_k(\lambda)}{\Sigma_k M_k} \tag{4}$$

in which $r_e = e^2/4\pi\varepsilon_0 m_e c^2$ is the classical electron radius, λ the wavelength, ρ the material mass density and M_k the atomic mass. f_k^0 is the nonresonant term of the atomic scattering factor and can be approximated by the number of electrons Z_k whereas f'_k and f''_k are the dispersion corrections. The summations are performed over all k atoms within the unit cell, molecule or, in the case of polymers, repeating unit.

Since diffuse scattering can be ascribed to changes in the refractive index any type of surface roughness or electronic contrast variation gives rise to diffuse scattering which contains the morphological information of the probed film.

On the other hand, in the case of X-rays the refractive index is less than unity, implying that total external reflection takes place for angles below the critical angle $\alpha_c(\lambda)$ of the material, which is given by

$$\alpha_c = \sqrt{2\delta} \tag{5}$$

The diffuse scattering at $\alpha_{i,f} = \alpha_c$ presents a maximum that is referred to as the Yoneda peak [14] and its position is dependent on the material[3], as is evident from Eqs. (3) and (5). The X-ray penetration depth varies from several nanometers, for incident angles below α_c, to several microns, for incident angles above α_c. In the ideal case of a perfectly flat film the penetration depth, Λ, defined as the depth at which the X-ray intensity is attenuated by $1/e$, for α_i, $\alpha_c \ll 1$ and $\alpha_i = \alpha_f$ adopts the following expression[4] [16, 17]:

---

[3] Experimentally, the Yoneda peak is found at $\alpha_Y = \alpha_i + \alpha_c$ with respect to the direct beam on the detector, since it is the sample which is tilted whereas the incoming X-ray beam remains normal to the detector plane. At an angle α_i from the direct beam position the so-called sample horizon is found and the scattering below the sample horizon is mainly due to scattering through the sample, i.e., in transmission geometry, especially for angles well above the critical angle of the probed film. See [15].

[4] Actually, the depth probed in GISAXS depends on both the incident and exit angles since it is defined as the inverse of the imaginary part of q_z that presents a dependence on both angles. The probed depth is a combination of the penetration depth—incoming beam—and the depth from which scattering escapes the sample—exit beam. See [16, 17].

where β is the imaginary part of the refractive index. Thus, by varying the incident angle different film depths can be probed (**Figure 2**).
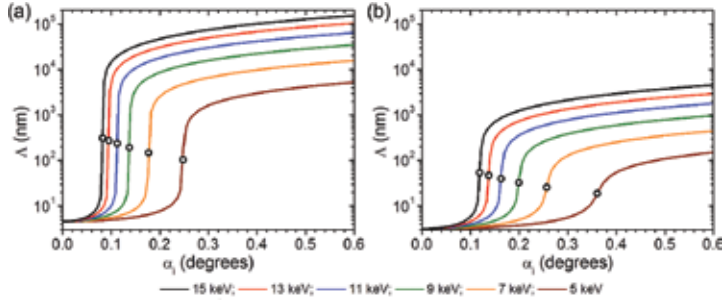

Figure 2. Penetration depth for α_i, $\alpha_c \ll 1$ and α_i, α_i as a function of the incident angle at different X-ray energies for (a) polystyrene (PS) and (b) Si. In (a), a mass density of 1.04 g/cm³ has been assumed. The dots represent the penetration depth at α_c for each energy.

$$\Lambda = \frac{\lambda}{4\pi} \sqrt{\frac{2}{\sqrt{(\alpha_i^2 - \alpha_c^2)^2 + 4\beta^2} - (\alpha_i^2 - \alpha_c^2)}} \tag{6}$$

From the scattering geometry alone, two major advantages of GISAXS over standard microscopic techniques are easily inferred. First, due to the small incident angle used, scattering comes from all the illuminated area within the X-ray footprint—in the order of several mm even for microfocus GISAXS (μGISAXS), i.e., GISAXS performed with X-ray beam sizes of few tenths of microns or lower in both the horizontal and vertical directions—thus providing information of statistical relevance. Second, information not only from the surface but also from buried structures is accessible simply by tuning the incident angle of the X-ray beam with respect to the sample surface normal.

2.2. Scattering intensity: form factor and structure factor

The fact that GISAXS is performed at incident angles close to the critical angle implies that reflection on the surface can occur and thus multiple scattering effects take place. As a consequence the Born approximation (BA) is no longer valid and the diffuse scattering is typically analyzed within the framework of the distorted-wave Born approximation (DWBA) to account for reflection/refraction effects. Nevertheless, the basic concepts from the analysis of transmission scattering still apply, namely the use of a form factor and a structure factor. At present, several software packages are available for modeling of GISAXS data employing the DWBA [18–21].

In the simple BA, the form factor is the Fourier transform of the shape function of the scattering object

$$F(\vec{q}) = \int \exp(i\vec{q} \cdot \vec{r}) d^3r \tag{7}$$

In the DWBA, for the case of a simple object located on a solid substrate, this form factor is replaced by the coherent sum of four terms to take into account different scattering events that involve the reflection of the incident or scattered X-ray beam on the substrate.[5] Thus, the form factor adopts the following expression

$$
\begin{aligned}
F_{DWBA}\left(\vec{q}_{\parallel}, q_z\right) = & F\left(\vec{q}_{\parallel}, k_{z,f} - k_{z,i}\right) + R\left(\alpha_i\right) F\left(\vec{q}_{\parallel}, k_{z,f} + k_{z,i}\right) + R\left(\alpha_f\right) F\left(\vec{q}_{\parallel}, -k_{z,f} - k_{z,i}\right) \\
& + R\left(\alpha_i\right) R\left(\alpha_f\right) F\left(\vec{q}_{\parallel}, -k_{z,f} + k_{z,i}\right)
\end{aligned}
\tag{8}
$$

being $R(\alpha_i)$ and $R(\alpha_f)$ the Fresnel reflection coefficients of the substrate. These four terms are schematically represented in **Figure 3**.
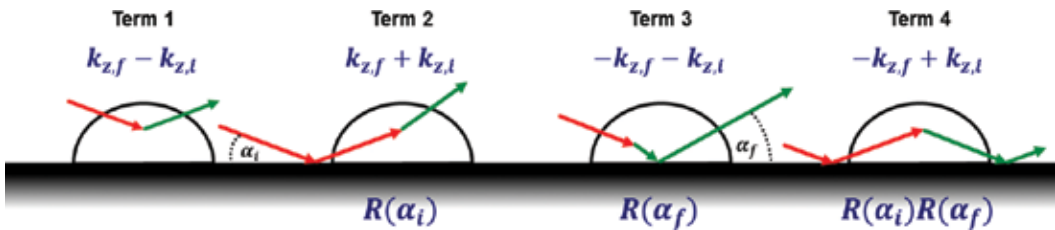

Figure 3. Schematic representation of the four terms involved in the scattering of a supported object on a solid substrate. The scattering event is represented by the color change of the arrows.

The first term is the simple BA and for $\alpha_{i,f} \gg \alpha_c$ Eq. (8) resembles the BA since $R(\alpha_i) = R(\alpha_f) = 0$. In this case—where the BA is valid and reflection/refraction effects can be neglected—the so-called effective layer approximation can be used and the differential cross-section for diffuse scattering can be written as [24, 25]:

$$
\frac{d\sigma}{d\Omega}\bigg|_{diff} = \frac{C\pi^2}{\lambda 4}(1 - n^2) \, |T_i|^2 |T_f|^2 \, P(\vec{q}) \propto P(\vec{q})
\tag{9}
$$

where C is the illuminated surface area, λ the wavelength, $T_{i,f}$ the Fresnel transmission functions and $P(\vec{q})$ is the diffuse scattering factor. Within this simplification, the diffuse scattering factor can be expressed in terms of the product of a form factor $F(\vec{q})$ of individual scattering objects and a structure factor $S(\vec{q}_{\parallel})$ that accounts for the spatial arrangement of the scattering objects on the substrate surface and the interference between individual scattering events.[6] The structure factor is the Fourier transform of the so-called pair correlation

---

[5] In the more general case, transmission has to be taken into account and the Fresnel transmission coefficients appear also in the expression of the form factor. See, e.g., [22, 23].

[6] For this reason, the structure factor, $S(\vec{q}_{\parallel})$, is also often called interference function.

function $g(r)$ that describes the spatial arrangement of scattering entities in real space and several ad hoc pair correlation functions can be used to analyze the GISAXS data.[7] The diffuse scattered intensity $I(\vec{q})$ for a lateral electron density fluctuation on the surface can be then expressed as

$$I(\vec{q}) \propto \langle |\, F_{DWBA}(\vec{q})\,|^2 \rangle S(\vec{q}_\parallel) \tag{10}$$

In highly diluted systems $S(\vec{q}_{\shortparallel})$ tends to 1 since there is no interference between the scattered photons. In these cases, the scattering pattern—being only proportional to $F(\vec{q})$ reflects the shape of the scattering objects. Opposite, in the case of concentrated systems $F(\vec{q})$ and $S(\vec{q}_{\shortparallel})$ are strongly correlated.

2.3. Coupling of form and structure factors: approximations

Although sometimes useful for the analysis of horizontal line cuts—i.e., the intensity distribution as a function of q_y at constant q_z extracted from the 2D scattering pattern—the expression derived for the diffuse scattering intensity in the previous section (Eq. (10)) is a crude simplification since small angle scattering is comprised of a coherent term, which is the product of the form factor and structure factor, and an incoherent one that appears as a consequence of polydispersity in the size distribution of the scattering objects. The incoherent term weaves the form and structure factors and is very difficult to evaluate analytically, thus several approximations have been developed to consider the correlation between the scattering objects and their spatial positions.

The simplest one is the so called decoupling approximation (DA) that assumes that there is no correlation between the kind of scattering object and its position. This approximation is usually applied when the size polydispersity is small or the surface density of scattering entities is low (**Figure 4(a)**).

Opposite to DA, when the polydispersity is high, a full correlation of the size of the scattering object and its position is assumed in the local monodisperse approximation (LMA). LMA considers that within the coherence length of the X-ray beam neighboring objects present the same size and shape, i.e., the polydisperse scattering objects are clustered in monodisperse domains whose scattering intensities are incoherently summed up (**Figure 4(b)**).

In between these extreme cases, the size-spacing correlation approximation (SSCA) [26] was developed to account for more realistic correlations between the size and separation of the scattering entities. Its formalism is derived from the paracrystal theory and introduces a partial correlation of sizes and positions in a probabilistic way. Shortly, within the SSCA, given a scattering object of distinct size and position and a description of the size polydispersity by a

---

[7] Some of the more commonly applied are the Debye hard core interference function, the Gaussian pair correlation function, the gate-pair correlation function, the Lennard-Jones pair correlation function, etc. See [12] and references therein.

statistical function, the probability of finding neighboring objects of particular size and positions with respect to the first scattering object is obtained, considering a particular probability distribution. Thus, both size-dispersion and position disorder are propagated statistically along the arrangement of scattering entities and long-range order is gradually destroyed in a probabilistic way (**Figure 4(c)**).
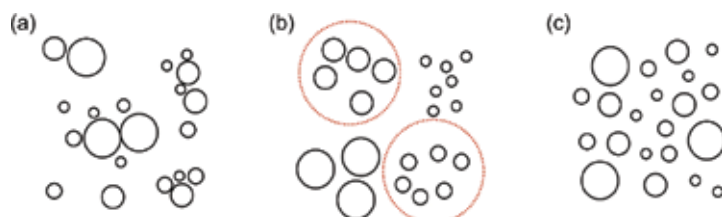

Figure 4. Schematic representation of the size-space correlation of scattering entities within (a) the decoupling approximation (DA), (b) the local monodisperse approximation (LMA), and (c) the size-spacing correlation approximation (SSCA). In (b), the red dotted circles represent the coherent X-ray domains.

3. In-situ GISAXS during deposition processes

During the last decade or so, GISAXS has been established as a very powerful technique to reveal the kinetics of deposition processes for thin film preparation employing different approaches. In particular, GISAXS is strongly contributing to reveal the mechanism of thin film growth and self-assembly both for vacuum and wet deposition processes that are relevant not only from a fundamental point of view but also for technological development. GISAXS presents two decisive advantages over standard microscopic techniques for the investigation of the growth kinetics and self-assembly: first, it provides averaged information over a large sample area—the beam footprint on the sample—thus the information acquired is of statistical significance; second, time resolutions down to several milliseconds are accessible due to the high X-ray intensities offered by third-generation synchrotron sources and the development of fast 2D X-ray detectors, thus fast kinetic processes can be studied.

In this section, exemplary results will be presented illustrating the strong capabilities of in-situ time-resolved GISAXS for the investigation of the stages governing the kinetics of thin film growth and self-assembly, both phenomena of high importance to gain control over the processes so as to tune the thin film properties to the required functionality.

3.1. Vacuum deposition of nanostructured metallic thin films

Vacuum deposition of nanostructured metallic films constitutes a very important technological and research field with applications ranging from coatings for antibacterial activity and catalysis to plasmonics, optoelectronics and sensors. In most cases, the morphology is closely related to the functionality of the film. Therefore, it is extremely important to achieve a deep

understanding of the growth mechanism and morphological development of the nanostructures so as to allow for tailoring the nanostructured metallic thin film to the desired application.

In order to investigate in-situ vacuum deposition processes using GISAXS, deposition chambers have been specifically designed to be installed at synchrotron beamlines [27–29]. In addition, a growing amount of systems have been investigated during the last years—some examples can be found in [30–33] —from which, in the following, only some selected results will be discussed.

In-situ μGISAXS has been applied to study the sputter deposition process of both Au and Ag on SiO$_x$ with time resolutions of 15 and 100 ms, respectively [34, 35]. The growth kinetics of these two systems has been probed to proceed in a similar way and in-situ μGISAXS has contributed to elucidate the growth regimes and the associated kinetic thresholds of the systems. The analysis of the temporal evolution of the main scattering features – namely the position and full-width-at-half-maximum (FWHM) of the out-of-plane scattering peak (line cuts of the 2D scattering pattern along q_y at constant q_z) together with the evolution of the scattering profile of the so-called detector cuts and off-detector cuts (line cuts of the 2D scattering pattern along q_z at $q_y = 0$ and at constant $q_y \neq 0$, respectively) —led to identify four different growth stages dominating the morphological development of Au and Ag thin films, from the nucleation phase to the formation of a complete layer (**Figure 5**).
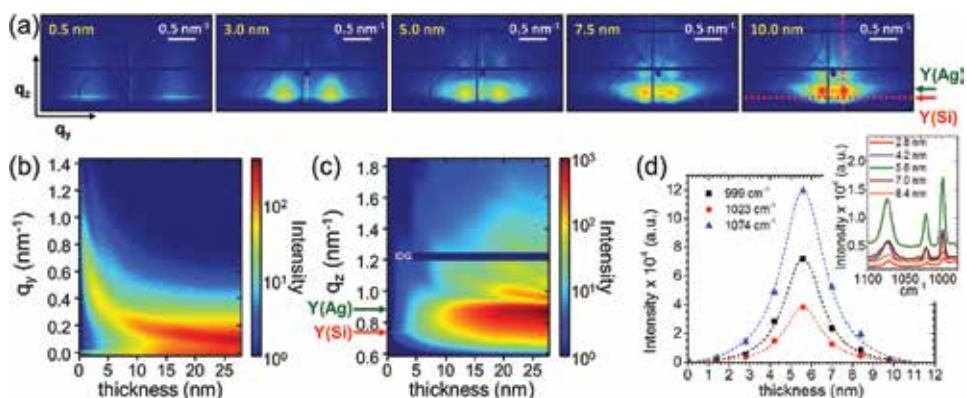

Figure 5. (a) Selected 2D μGISAXS patterns during sputter deposition of Ag on SiO$_x$. The deposition process was continuously monitored with a time resolution of 100 ms. The effective film thickness is indicated in each GISAXS pattern. The dotted lines on the right pattern mark the positions where line cuts were performed to evaluate the data. (b) Out-of-plane (along q_y) line cuts versus sputtered thickness at the Si Yoneda peak ($q_{z,c}$(Si; 13 keV) = 0.733 nm^{-1}). The evolution of the out-of-plane scattering peak from large q_y toward lower values is related to an increase in the mean distance between Ag nanoclusters as a consequence of the increase in clusters size. When the percolation threshold is reached, the peak gets arrested at a nearly constant value. A quantitative analysis of the mean distance D between nanoclusters can be performed from the peak maximum applying $q_y \approx 2\pi/D$. (c) Off-detector (along q_z) line cuts versus sputtered thickness at $q_y = 0.112$ nm^{-1}. As the deposition proceeds, the maximum intensity changes from the Si Yoneda peak to the Ag Yoneda peak and vertical modulations related to the formation of Ag layers appear. (d) Intensity of the characteristic SERS bands of thiophenol shown in the inset for different Ag thickness. The dashed lines are Voigt fittings to the data. IDG: intermodule detector gap. Y(Si): Si Yoneda peak. Y(Ag): Ag Yoneda peak. Adapted with permission from Santoro et al. [35] with the permission of AIP Publishing.

The growth kinetics of Au during sputter deposition, apart from being of industrial and technological relevance, is of significant importance from a basic point of view. To simulate the complete 2D μGISAXS patterns along the deposition process, a geometrical model based on the 2D hexagonal paracrystalline arrangement of hemispherical clusters was developed [34] allowing for extracting important parameters such as the surface coverage, film porosity or cluster density, thus enabling to predict morphology-dependent properties of the thin film such as the optoelectronic response.

Since the growth of Ag on SiO_x proceeds in a similar manner, the geometrical model proposed by Schwartzkopf et al. [34] has been also successfully applied to the deposition of nanostructured Ag thin films on SiO_x for surface enhanced Raman spectroscopy (SERS) (**Figure 5**(d)) [35]. A key point in SERS, whose underlying main mechanism is the enormous enhancement of the local electromagnetic field in the vicinity of nanostructured noble metal surfaces due to localized surface plasmons, is the gap between nanostructures. At the nanostructure gaps—the so-called "hot-spots"—the electromagnetic enhancement is maximum. In this case, in-situ μGISAXS during sputter deposition of Ag allowed not only identifying the main growth regimes and thresholds but also to correlate the developed morphology to the SERS activity. By modeling the full 2D μGISAXS patterns within the DWBA and the SSCA, a maximum SERS enhancement was found for a mean gap of 1 nm between Ag nanoclusters, corresponding to an effective film thickness of 5.6 nm.

On the other hand, the deposition kinetics of Au on a quasi-regular hexagonal array of self-assembled cadmium selenide (CdSe) quantum dots has also been investigated by in-situ μGISAXS [36]. Opposite to the growth of Au and Ag on SiO_x, in the early deposition stage the out-of-plane peak did not change in position but remained fairly constant. The deposition of Au only led to an increase in electronic contrast, thus, of the diffuse scattering intensity produced by the underlying array of CdSe quantum dots. This implies that the quantum dots act as nucleation sites for Au growth. Subsequently, lateral growth and coalescence of Au/CdSe-dot clusters were observed forming a compact Au/CdSe-dot layer. Finally, Au growth proceeded in the surface normal direction developing a capping layer on the CdSe quantum dots array.

In-situ GISAXS has also contributed to shed light on an intriguing issue during the growth of metallic thin films, namely the influence of the chemical affinity between the metal and the substrate on the deposition kinetics and thin film morphology. This is highly important in the case of, e.g., the deposition of metallic electrodes on organic solar cells or light emitting diodes where, in some cases, the electrodes represent the limiting factor in device performance. The great capabilities of in-situ GISAXS studies for this purpose has been demonstrated during the sputter deposition of Al and Ag on tris(8-hydroxyquinolinato)aluminum (Alq3), a key material in organic light emitting diodes. Alq3 presents a strong chemical interaction with Al whereas it interacts weakly with Ag, which translates into different growth mechanisms. In the case of Al deposition, three different stages of growth were identified and modeling of the 2D patterns revealed the formation of Al nanopillars after diffusion of Al in Alq3 and subsequent metal complex agglomeration [37]. On the other hand, without diffusing into the Alq3 thin film, Ag presents a morphological transition from truncated sphere clusters to cylindrical nanostruc-

tures upon surpassing the Ag percolation threshold at an effective film thickness of 5.0 nm (**Figure 6**), which was attributed to the different Ag-Ag and Ag-Alq3 interactions [38].
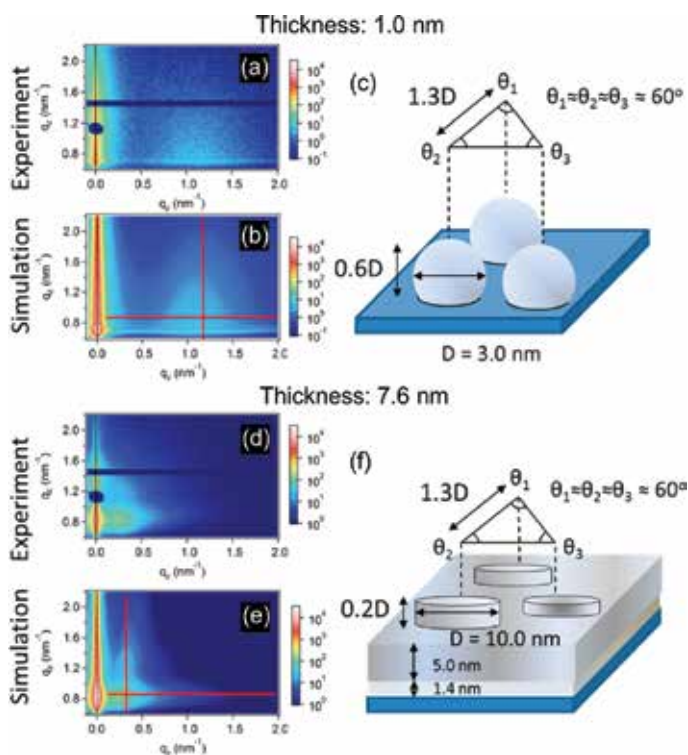

Figure 6. Morphological transition in cluster shape upon surpassing the percolation threshold (effective film thickness of 5.0 nm) during sputter deposition of Ag on a 36.0 nm thick Alq3 film. (a–c) Experimental 2D μGISAXS pattern, simulated 2D μGISAXS pattern and geometrical model used to simulate the data, respectively, at an effective Ag film thickness of 1.0 nm. (d-f) Experimental 2D μGISAXS pattern, simulated 2D μGISAXS pattern and geometrical model used to simulate the data, respectively, at an effective Ag film thickness of 7.6 nm. In both cases, the DWBA and the LMA were employed to simulate the scattering patterns. Adapted and reprinted with permission from Yu et al. [38]. Copyright 2015 American Chemical Society.

The differences in metal interaction and nanocluster diffusion coefficient on different materials can be exploited to tailor the thin film morphology. In this sense, an interesting approach consists in employing polymer thin films as templates in the nanoscale, given the known ability of block copolymers to spontaneously form nanostructures due to phase segregation. In general, when employing vacuum deposition of metals on organic thin films, in a first deposition stage, the metal diffuse into the film which influences the subsequent growth kinetics and, in the case of block copolymers, a selective wetting of the metal on one of the domains is commonly observed, which is ascribed not only to the different metal-polymer interaction but also to the differences in metal diffusion in each of the blocks. From in-situ μGISAXS measurements, the surface diffusion coefficient of Au on polystyrene (PS) has been extracted and a correlation of the developed Au morphology with the optical properties of the

film could be achieved by combining μGISAXS with real-time UV-Vis spectroscopic measurements during the growth [39].

On the other hand, Metwalli et al. [40] have taken advantage of the selective wetting of Co on spontaneously nanostructured polystyrene-block-poly(ethylene oxide) (PS-b-PEO) to prepare ordered Co nanoclusters along highly oriented PS domains. The morphology of the polymer thin film consisted of alternating highly oriented crystalline PEO and PS domains with a periodicity of around 30 nm and the in-situ GISAXS experiments demonstrated that selective wetting occurred below the Co thin film percolation threshold. They also elucidated the growth kinetics of Co on the block co-polymer nanostructured template.

A thorough study on the nanostructure development of transition metals on a PS-b-PEO template has also been recently reported [41]. It has been clearly revealed that the growth of Au, as a fairly inert element, was not influenced by the template, whereas Ag demonstrated slightly improved wetting on the PS domain, forming clusters. In the case of reactive metals, e.g., Fe, Ni, and Pt, well-defined and uniform nanocluster patterns were grown selectively on the PS domains. Additionally, by performing in-situ GISAXS experiments, it has been found that the substrate temperature plays an important role in shaping the metal clusters, showing that above the glass transition temperature, T_g, of PS, Ag clusters become more irregular. In addition, for Fe, flat nanodots with a low surface-to-volume ratio morphology were grown at substrate temperatures above T_g whereas a higher surface-to-volume ratio morphology is obtained for a substrate at room temperature during deposition. This is ascribed to the changes in diffusion coefficient with temperature, so that above T_g a higher diffusion coefficient of metal atoms and clusters during the deposition led to a lower surface-to-volume ratio cluster morphology.

The complicated growth kinetics of hierarchical anisotropic gold nanostructures on polystyrene-block-poly(methyl methacrylate) (PS-b-PMMA) thin films has been also studied with in-situ GISAXS [42]. An anisotropic shape of the deposited metal clusters was achieved by employing a glancing angle deposition (GLAD) geometry. In GLAD, the deposition plume is positioned at an oblique angle regarding the sample surface, which produced nonsymmetric Au clusters and its anisotropic shape manifested as nonsymmetric 2D scattering patterns with respect to the scattering plane ($q_y = 0$). In addition, a hierarchical ordering of the anisotropic Au was achieved benefiting from the selective wetting of Au on the PS domains. The anisotropy of this hierarchical nanostructure was also reflected in the anisotropic optical response of the system.

3.2. Vacuum deposition of organic thin films

Organic thin films are especially important since they are increasingly used in devices. In particular, organic semiconductors are employed in organic light emitting diodes (OLEDs), organic field-effect transistors (OFETs), and organic solar cells (OSCs). However, the basic processes of molecular thin film growth are still far from being understood and connecting molecular and nanoscopic/microscopic processes such as molecular diffusion and island size evolution, remains a major challenge. To this purpose in-situ GISAXS, being a non-invasive technique, is increasingly contributing.

As in the case of vacuum deposition of metals, several organic deposition chambers have been designed and built so as to perform in-situ X-ray scattering and/or diffraction measurements at synchrotron beamlines [43, 44].

To study these particular systems, in-situ grazing incidence X-ray diffraction (GIXD) and in-situ X-ray reflectivity (XRR) are most commonly applied [45–48], though the information provided by in-situ GISAXS is also very valuable since the dimensions probed are different. Whereas GIXD provides access to the crystal structure and molecular arrangement, GISAXS gives complementary information on the island shape and island-island distances as well as on the island electron density. Therefore, the combination of both techniques provides the necessary information to make a link between the molecular and micrometer size crystallite regimes.

These systems are usually investigated in the so called anti-Bragg geometry, i.e., at incident angles so that the specular peak corresponds to the anti-Bragg point of a given ($h\,k\,l$) permitted Bragg reflection of the molecular crystalline structure. The anti-Bragg points correspond to $\left| \vec{q}_{\text{anti–Bragg}} \right| = \frac{1}{2} \left| \vec{q}_{\text{Bragg}} \right|$ and are especially surface sensitive[8] [17]. From a practical point of view, for a selected ($h\,k\,l$) Bragg reflection, α_i is chosen so that at $\alpha_i = \alpha_t$ and $\psi = 0$ − i.e., the specular peak position—the following relationship is satisfied

$$q_z = \frac{2\pi}{\lambda}(\sin(\alpha_i) + \sin(\alpha_f)) = \frac{4\pi}{\lambda}\sin(\alpha_i) = \frac{1}{2}\left| \vec{q}_{Bragg} \right| \qquad (11)$$

Note that in Eq. (11) only q_z is involved since for specular reflection $q_x = q_y = 0$ (Eq. (1)).

At this particular geometry, the specular intensity presents an oscillatory behavior during the growth—the so-called growth oscillations—which arises from destructive interference between neighboring odd and even monolayers (MLs) —lattice planes—so that the scattering from the first, third, fifth ML is cancelled by the growth of the second, fourth, sixth ML, etc. [49]. In the common case of (initial) layer-by-layer growth in organic heteroepitaxy, the periodicity of the oscillations consists in 2 MLs although interference between reflections at the growing surface, the substrate and the interfaces between different film layers can lead to more complex oscillatory behavior.[9] Through correct modeling of the growth oscillations, more complicated epitaxy growth models can be derived making assumptions about the intralayer and interlayer diffusion [50]. Therefore, additional information for the refinement of these models is very useful and can be obtained by performing GISAXS at the anti-Bragg geometry, which allows concurrently following the changes in the specular intensity—the growth oscillations—and the diffuse scattering [51–54].

---

[8] An introduction to surface X-ray diffraction, including the evanescent wave method that corresponds to GIXD, can be found in [17].

[9] For instance, considering an out-of-phase reflection on the substrate, the oscillations maxima appear at even instead of at odd numbers since an additional reflection occurs or, e.g., the oscillations period can change to 1 ML in the case of homoepitaxy. See [49].

The abovementioned geometry has been applied to investigate, e.g., the growth of multilayers of fullerene C_{60} molecules on mica in real time [55]. From the growth oscillations, a layer-by-layer growth was deduced whereas from the in-situ µGISAXS data the mean island distance was extracted and converted into surface island density assuming a hexagonal island arrangement. Interestingly, the GISAXS out-of-plane peaks present intensity oscillations with a period of 1 ML, in contrast to the 2 ML period of the specular intensity at the anti-Bragg point (**Figure 7**). This is due to the fact that diffuse scattering occurs only for uncomplete layers since this is the situation where a lateral variation in electron density—or, in other words, in refractive index—is present, whereas the growth oscillations are due to interference from the reflections at layer interfaces—plus at the substrate and at the growing layer—i.e., diffuse scattering is probing lateral contrast whereas the specular peak probes the structures in the surface normal direction. Through kinetic Monte Carlo simulations and a comparison to the experiments, values of the energy barriers were obtained—namely, the diffusion barrier and lateral binging energy for intralayer events and an Ehrlich-Schwoebel barrier for interlayer diffusion—and, more importantly, this set of parameters was demonstrated to be sufficient to describe the growth of a C_{60} layer on underlying C_{60} layers, of crucial importance so as to predict the growth dependence on the deposition rate and substrate temperature.
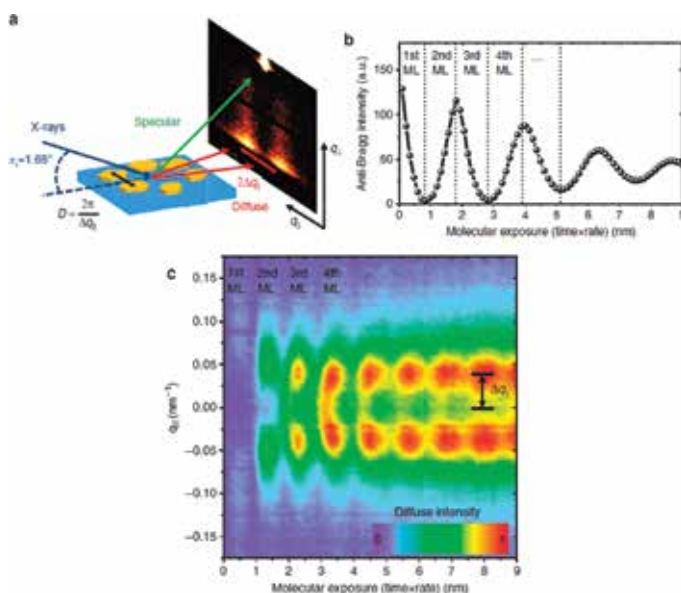
Figure 7. (a) Scattering geometry employed showing the simultaneous acquisition of specular and diffuse scattering. The incident angle is chosen so that the specular peak corresponds to the anti-Bragg position of the C_{60} (1 1 1) reflection. (b) Intensity at the anti-Bragg point $q_z = 0.38$ Å^{-1} as a function of the molecular exposure during the film growth. A damping of the growth oscillations from the third monolayer on is due to surface roughening since an imperfect layer-by-layer growth for high number of MLs occurs, providing a measurement of the roughening onset. (c) Oscillations of the out-of-plane GISAXS intensity as a function of the molecular exposure. From the out-of-plane peak position, the mean island distance can be extracted by $q_y \approx 2\pi/D$. © 2014 S. Bommel, N. Kleppmann, C. Weber, H. Spranger, P. Schäfer, J. Novak, S.V. Roth, F. Schreiber, S.H.L. Klapp and S. Kowarik. Adapted with permission from Bommel et al. [55]; originally published under Creative Commons Attribution 4.0 License. Available from: 10.1038/ncomms6388.

The simultaneous acquisition of the specular intensity and GISAXS signal has also been applied to in-situ investigate the molecular diffusion and island evolution during the growth of diindenoperylene (DIP, $C_{32}H_{16}$) on SiO_x [56]. Opposite to the C_{60} molecule, DIP presents shape anisotropy imposing additional degrees of freedom—tilting and bending—which increases the complexity of the growth process. In this case, above a surface coverage of 3 MLs the GISAXS out-of-plane peak oscillations vanished and the peak position remained constant, meaning a constant island center-to-center distance. This is a clear signature of a transition between a layer-by-layer to a three dimensional (3D) growth, i.e., formation of molecular islands with a fixed surface island density. Additionally, effective activation energies for island nucleation of DIP on SiO_x and of DIP on DIP could be extracted from the mean island diameter —derived from the diffuse scattering peak position—at 0.5 ML and 1.5 ML surface coverage, respectively, by varying the deposition substrate temperature.

Another organic semiconductor with rod-like morphology whose growth has been in-situ investigated performing GISAXS using the anti-Bragg geometry is *N,N'*-dioctyl-3,4,9,10-perylene tetracarboxylic diimide (PTCDI-C_8, $C_{40}H_{42}N_2O_4$) [57]. It has been shown that PTCDI-C_8, as is the case for DIP, underwent a transition from a layer-by-layer growth to a 3D growth but in a smoother fashion. This manifested both as a slow increase in the mean roughness of the completed MLs—derived from the growth oscillations—as well as in a smooth leveling off of the island density—derived from the out-of-plane GISAXS peak position by assuming a hexagonal arrangement of islands. Moreover, the island density extracted from the diffuse scattering at different substrate temperatures, allowed demonstrating higher molecular mobility of PTCDI-C_8 on PTCDI-C_8 than that of PTCDI-C_8 on SiO_x, which is responsible for the decreased island density observed in upper MLs.

3.3. Wet deposition of polymer and colloidal thin films

Wet deposition encompasses a collection of different methods for the fabrication of thin solid films from a liquid solution and/or suspension as precursor. All of them exploit self-assembly concepts to prepare thin films such as colloidal crystals, thin polymer films and nanocomposites with applications ranging from photonic crystals to polymer solar cells and superhydrophobic or superhydrophilic coatings. During wet deposition, the interaction between the suspended particles—or the dissolved compounds—together with the liquid flow—responsible of internal mass transport—govern the drying kinetics and self-assembly. Hence, tuning these parameters makes it possible to control the self-assembly, thus adjusting the morphology of the dried thin film (ideally) on demand.

Grazing incidence X-ray scattering (GIXS) techniques has been applied to study wet deposition processes such as solution casting [58, 59], spin-coating [60], dip-coating [61, 62], and blade coating [63]. Nevertheless, although these deposition methods are very useful for device fabrication at research scale, they are not easily scaled-up and/or they are restricted to specific substrate geometries. In this sense, it is important to explore other wet deposition methods of potential industrial relevance.

In recent years, spray coating is gaining interest due to its easy scale-up and integration into production lines as well as to its lack of substrate geometry/size constrains. Moreover, it has

already been successfully applied to fabricate operating devices such as polymer solar cells [64–66]. Nevertheless, although there are evident similarities to, e.g., solution casting, the drying kinetics present some particularities still not well understood. To this respect, GISAXS has been used to study the self-assemble of colloidal particles during spray coating [65, 67, 68]. In particular, Herzog et al. [67] were able to identify three different stages during the spray deposition of polystyrene (PS) nanoparticles and subsequent drying corresponding to the formation of a structureless thin liquid film, which subsequently breaks up into small droplets allowing for possible transient nanoparticle ordering and a final freezing of a self-assembled colloidal nanostructure once the solvent is fully evaporated, respectively. These three stages were revealed in the in-situ μGISAXS patterns as first, a decrease in the overall scattered intensity due to the homogeneous liquid film right after a 100 ms spray shot; second, an increase and broadening of the Yoneda peak ascribed to the homogeneity loss of the liquid film that breaks into small droplets as the solvent evaporation proceeds and last, the emergence of well-defined out-of-plane symmetric peaks regarding the scattering plane (**Figure 8**). In addition, controlling the evaporation rate by adjusting the substrate temperature the assembly process of the nanocolloids can be managed to achieve different film morphologies, what has been investigated in-situ by μGISAXS as well [68].
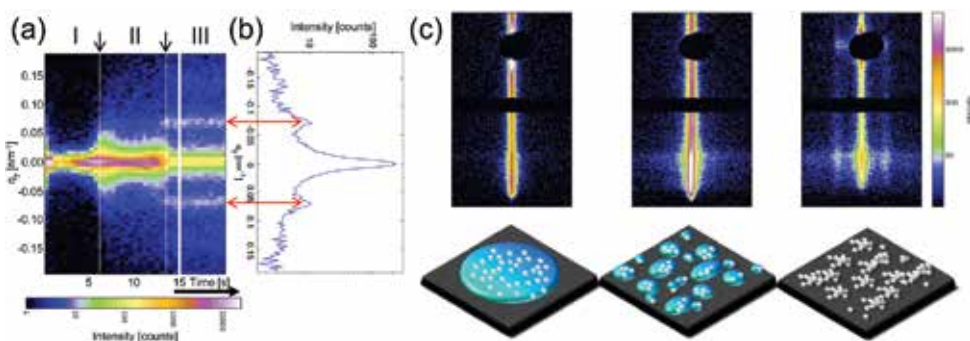

Figure 8. (a) Out-of-plane cuts (along q_y) at the Si Yoneda peak ($q_{z,c}$(Si; 13 keV) = 0.733 nm^{-1}) as a function of time during spray deposition of PS nanoparticles with a nominal diameter of 100 nm. The vertical dotted lines indicate the transitions between drying stages. (b) Individual out-of-plane cut of the dried sample at 15 s after spray deposition displaying side maxima corresponding to the most prominent lateral length scale of ≈ 90 nm. (c) Representative 2D GISAXS patterns of each of the three identified drying stages. Below each pattern a sketch of the corresponding drying stage in real-space is depicted. Reprinted (adapted) with permission from Herzog et al. [67]. Copyright 2013 American Chemical Society.

Apart from spray coating, another interesting approach for large scale low-cost production of organic photovoltaic (OPV) devices is inkjet printing, a method that has drawn considerable attention from an industrial point of view as the field of organic flexible electronics is maturing. As in the case of spray coating, GIXS has been applied to in-situ investigate the structure development during inkjet printing of, e.g., conductive polymer thin films widely used as electrodes in OPV devices [69] as well as of the active layer in bulk-heterojunction (BHJ) polymer solar cells [70]. The film morphology in OPV devices has a direct relationship with its performance and the combination of in-situ wide- and small angle scattering (GIWAXS/

GISAXS) allowed developing qualitative models of the structural evolution of the semicrystalline polymer thin films morphology.

Finally, although it does not present the current large-scale production promises of spray coating and inkjet printing, an interesting approach for wet deposition consist in employing microfluidics, which may be critical for lab-on-chip applications. Here, the peculiarity lies in the nondrying nature of the deposition, i.e., the self-assembly process on the substrate does not take place during solvent evaporation but at the liquid-solid interface during liquid flow. In order to in-situ follow deposition processes using microfluidics by GISAXS—among others; see Section 4—special flow cells have been designed [71]. In this kind of experiments, it is extremely important to adjust the X-ray beam footprint on the substrate to the size of the fluidic channel so as to prevent an overillumination of the sample not in contact with the fluid, thus minimizing undesired signal that could obscure the accessible information. Therefore, the use of μGISAXS becomes essential [72]. This specific setup has been used to investigate the attachment of Au nanoparticles to a polymer thin film (**Figure 9**) and different stages could be identified, namely the dried polymer film before the liquid inlet was opened (denoted as 1 in **Figure 9**), a wetted film by the liquid vapor once the liquid inlet was opened (denoted as 2 in **Figure 9**) and the attachment of Au nanoparticles once the liquid flow reached the probed thin film position (denoted as 3 in **Figure 9**). Moreover, the increase in intensity of the out-of-plane peak as the experiment proceeded indicated a cumulative deposition of the Au nanoparticles from which it is possible to analyze the deposition kinetics.
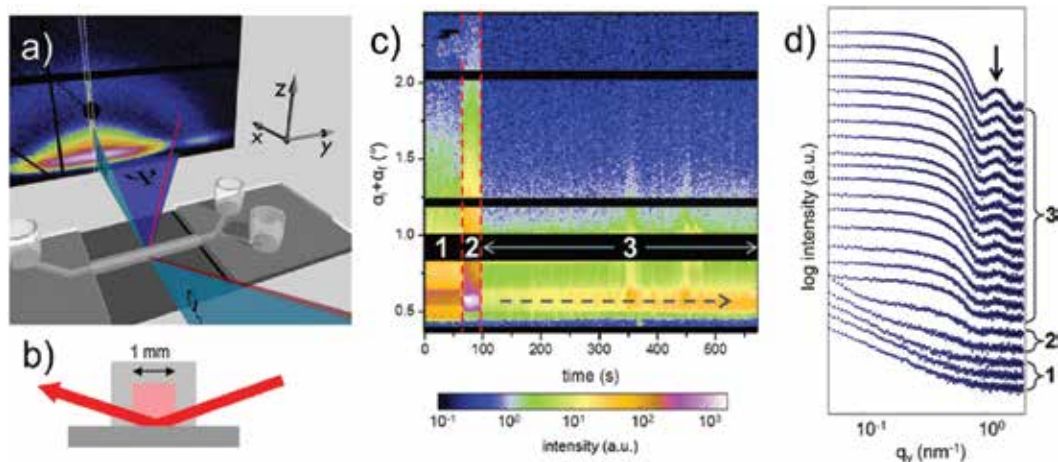
Figure 9. (a) Sketch of the μGISAXS setup with microfluidic cell. (b) Illustration of the X-ray beam transmitting the channel walls and the footprint on the sample surface. For clarity the incident angle and X-ray beam size are not in scale. (c) Detector cuts (along q_z at $q_y = 0$) as a function of time while 10 nm diameter Au nanoparticles attach to a poly(ethyleneimine) (PEI) thin film on a SiO$_x$ substrate. Black regions correspond to the specular beamstop and the intermodule detector gaps. (d) Out-of-plane cuts (along q_y) at the Si Yoneda peak ($q_{z,c}$(Si; 13 keV) = 0.733 nm^{-1}) as sum of 10 consecutive measurements. The curves are vertically shifted for clarity. The numbers denote the deposition stages. Reprinted from Santoro et al. [72], with the permission of AIP Publishing.

4. In-situ GISAXS during thin film processing

In addition to the aforementioned deposition processes, a different kind of studies in which in-situ GIXS is increasingly contributing consist in thin film processing. GIXS has been performed during thin film nanostructuring in order to gain insight into the morphology transformation processes, e.g., metal nanocluster formation through high temperature annealing induced dewetting [73, 74], dewetting of organic multilayer films [75], or refinement of block co-polymer thin film morphology during solvent vapor annealing [76]. Furthermore, working devices have also been investigated by in-situ GIXS so as to identify the structural changes that the active thin film undergo during operation with the aim of improving the device design and final performance, e.g., catalysis on nanoparticles [77], roughening of surfaces during electrodeposition [78], electrochemistry in ionomer matrices of interest in fuel-cell devices [79], or BHJ polymer solar cells [80, 81]. As in the previous section, the development of specific environmental cells to be installed at synchrotron beamlines commonly constitutes a prerequisite to conduct this kind of experiments. In the following, we will shortly describe some recent exemplary results of in-operando and in-situ GISAXS during thin film processing.

As mentioned in the previous paragraph, a well-known way of producing – or modifying the morphology of—metal nanoclusters on a surface consists in the thermal induced dewetting of metallic thin films. This process has been in-situ investigated by GISAXS for the case of Au on Si (1 1 1) up to the bulk eutectic point T_e of the Au/Si system [82]. After the deposition of Au thin nanostructured films by thermal evaporation, a linear increase of the mean distance between Au nanoclusters was observed—associated to an increase in cluster size—together with an increase in the mean cluster height as the temperature approached T_e, which jointly translated to an increase in the contact angle of the nanoclusters. More interestingly, from the Au nanoclusters contact angle at T_e, the liquid-solid interface tension of nanometer-sized Au clusters was calculated and it was found to be larger than that of macroscopic Au droplets on Si (1 1 1). Additionally, the work of adhesion of an Au nanodroplet at the system eutectic point was derived.

In the case of semiconductor materials, ion beam bombardment is a very useful process to induce surface nanostructuring. During the erosion of a surface by accelerated ions, the produced instabilities can lead to the formation of self-assembled patterns of nanostructures and different surface topographies can be obtained as a function of the ion mass, ion energy and bombardment geometry. In-situ GISAXS with partially coherent X-ray beams (Co-GISAXS) has been employed to study the nanodot formation on a gallium antimonide (GaSb) (0 0 1) surface by normal incidence bombardment of 500 eV Ar ions [83]. The use of partially coherent beams allows not only accessing the kinetic phenomena but also the dynamics. Under a coherent illumination, the scattered intensity consists of a speckle pattern (**Figure 10**) and the speckle distribution and speckle intensity fluctuations reflect the underlying dynamics of the surface morphology [84]. From a kinetic point of view—GISAXS analysis—the mean size and distance of the nanodots as a function of time was extracted and the kinetic regimes and onsets derived. More interestingly, though the characteristic GISAXS signal remained stable after saturation of the nanostructuring process, the dynamics showed that ageing—slow down

of the dynamics—was occurring, mainly ascribed to hindered mass redistribution phenomena. The dynamics was extracted from the speckle analysis through the so-called two-time correlation function that accounts for the fast variation of intensity redistribution within the scattering peak with respect to the averaged intensity distribution over time. Finally, a dynamical transition to a regime dominated by the build-up of stress at the surface was identified.
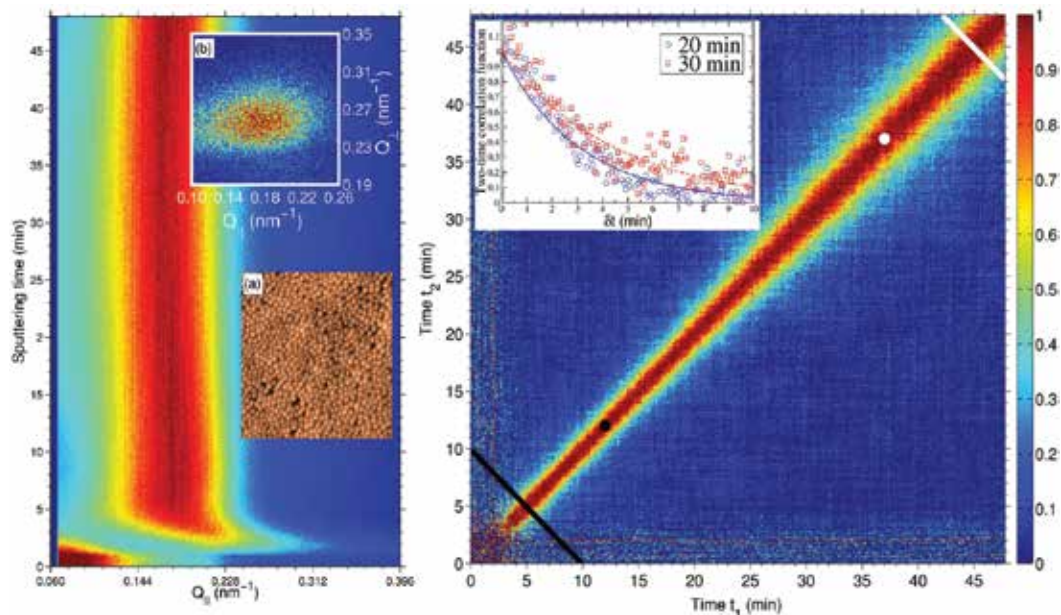

Figure 10. Left: Evolution of the GISAXS out-of-plane peak as a function of ion bombardment time. The onset of surface nanostructuring is evidenced by the emergence of the side peak 1 min after erosion started. After around 5 min the out-of-plane peak remained at constant position revealing the saturation of the nanostructuring process. The upper inset show the speckle distribution within the out-of-plane peak at t = 47 min whereas the lower inset shows the real-space morphology as revealed by atomic force microscopy. Right: Normalized two-time correlation function calculated around the out-of-plane GISAXS peak. The black and white lines mark the start and end of aging, respectively, whereas the black and white dots correspond to the average times where a change in the correlation time occurred (change in dynamical regimes). The inset shows cuts of the two-time correlation function as function of $\delta t = t_2 - t_1$ (hollow blue dots and hollow red squares). A good fitting was achieved using exponential decay functions. © 2013 O. Bikondoa, D. Carbone, V. Chamard and T.H. Metzger. Adapted from Bikondoa et al. [83]; originally published under Creative Commons Attribution 3.0 Unported License. Available from: 10.1038/srep01850.

On the other hand, nanostructuring of polymer thin films is an intense field of research and different strategies are being employed, e.g., nanoimprint lithography, porous anodic aluminum oxide (AAO) templating or, as mentioned in Section 3.1, the design of block co-polymer morphologies. An interesting approach consists in the formation of nanostructured surfaces by the so-called laser-induced periodic surface structure (LIPSS) formation, a technique that has been used for years to nanostructure metals and semiconductors but has only recently been applied to polymers [85, 86]. In LIPSS, a pulsed laser of a definite polarization is shined

on the material at fluences (optical energy per surface area) well below the ablation threshold and the material surface gets nanostructured by interference of the incoming and scattered electromagnetic wave through a feeding mechanism not yet well understood. In the common case of linearly polarized incident light the process induces ripple formation on the surface with a periodicity resembling the wavelength of the laser employed. By performing in-situ GISAXS measurements while irradiating a poly(trimethylene therephthalate) (PTT) thin film the onset of ripple formation at different laser repetition rates and fluences has been revealed [87]. Moreover, the results support a feeding mechanism based on a local heating of the polymer thin film so that LIPSS formation becomes more efficient the shorter is the laser pulse separation, whereas for long enough laser pulse separation heat dissipation takes place between pulses hindering the ripple formation.

A different way in which polymer thin films are processed does not consist in the promotion of structuring to tailor the material properties but in the processes that polymeric materials undergo during operation. For instance, in several applications the polymeric material is in contact with fluids, e.g., in the case of polymeric materials used in human implants. Here, the combination of μGISAXS and microfluidics offers unique capabilities for investigating the morphological changes of polymer thin films in contact with a fluid flow.

A model system comprising of a thin film of sodium alginate with embedded dispersed PS nanoparticles have been investigated by in-situ μGISAXS during water flow in a microfluidic device [88]. This system served as a model to investigate the detachment of thin films and nanoparticle aggregates therein by a fluid flow, both with and without additional sodium alginate cross-linking. More interestingly, the combination of in-situ μGISAXS and a micro-fluidic cell have resulted in the accurate description of the swelling behavior of the thermo-responsive poly(N-isopropylacrylamide) (PNIPAM) polymer, a well-known hydrogel when cross-linked [89]. An important feature observed in the GISAXS pattern of soft thin films deposited on rough surfaces is the correlated roughness of the film, i.e., the soft matter thin film present a roughness that replicates that of the substrate. Thus, the film shows X-ray wave-guiding effects producing scattering with partial coherence and resonant diffuse scattering is observed [13]. In this case, the diffuse scattering with partial phase coherence coming from the different interfaces concentrates into narrow sheets parallel to the q_x direction and appear in the 2D GISAXS pattern as intensity modulations in the scattering plane (along q_z at $q_y = 0$). These modulations enable a direct determination of the distance between the correlated surfaces by $q_z = 2\pi/d_{corr}$ (**Figure 11(a)** and **(b)**). It is important to calculate d_{corr} for large q_z values so that the Yoneda peak intensity does not introduce an additional signal that could distort an accurate determination of d_{corr}. From the in-situ μGISAXS measurements, neither the thickness nor the topography of the PNIPAM thin film was observed to change during exposure to highly undersaturated water vapor. However, as early as the film is brought in contact with liquid water it starts swelling mostly in a 1D manner, i.e., mainly an increase of film thickness occurs, being the restructuration of the surface topography (surface flattening) slightly retarded but obviously correlated to the swelling process (**Figure 11(c)**).
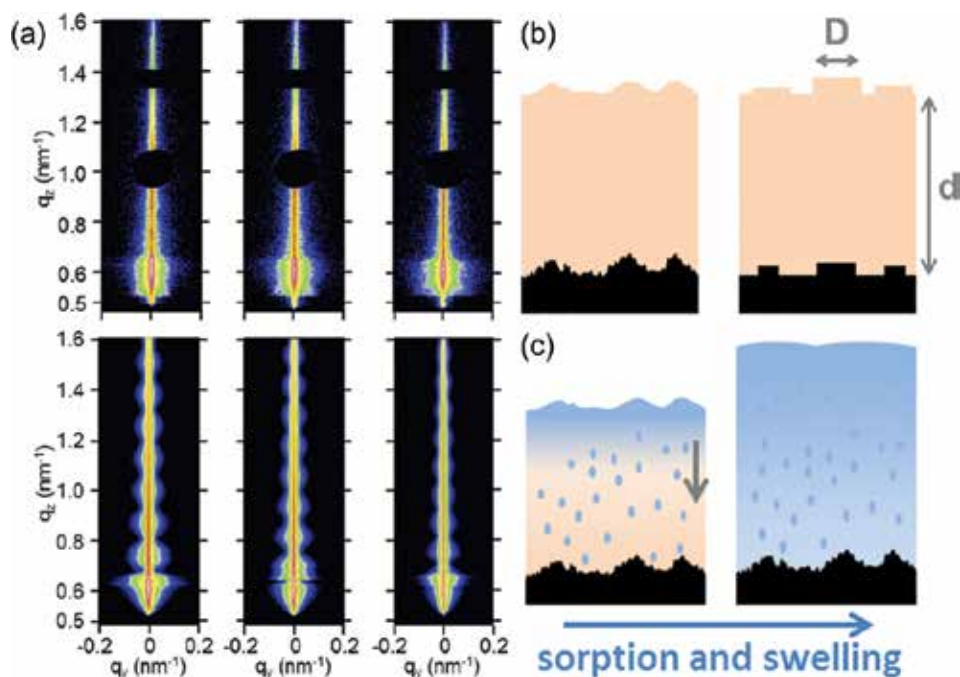
Figure 11. (a) Experimental (upper row) and simulated (lower row) 2D μGISAXS patterns during swelling of a PNI-PAM thin film under water flow in a microfluidic cell. The scattering patterns correspond to exposure to water vapor (left), after 30 s of water flow (middle) and after 48 s of water flow (right). The GISAXS patterns were continuously acquired before and during water flow with a time resolution of 1 s. The DWBA and the LMA were employed to simulate the scattering patterns. (b) Schematic drawings of the glass-supported, as-spun PNIPAM film, possessing partially correlated interfaces (left) and the corresponding morphological model used in the simulations (right). The parameters that were varied to simulate the water uptake process are the thickness of the PNIPAM layer, d, and the diameter of the PNIPAM discs, D. (c) Illustration of the surface restructuration in the course of the swelling of the thin, glass-supported PNIPAM film. Left: sorption of liquid water, filling the accessible free PNIPAM volumes and inducing the devitrification of its near-surface layer. Right: mainly 1D swelling occurs as the gel-glass phase boundary propagates into the depth of the film; the surface flattens as the mobility of the macromolecules is sufficient. Reprinted (adapted) with permission from Philipp et al. [89]. Copyright 2015 American Chemical Society.

Other polymeric thin films that have been investigated by in-situ GISAXS during operation are the active layers of BHJ polymer solar cells (**Figure 12**). In general, although polymer solar cells hold the promise of future low-cost flexible solar cells, a major problem of these OPV devices is the performance loss during operation. In this sense, in-operando μGISAXS studies have revealed that the active layer suffer from morphological changes during operation [90]. These morphological changes are directly related to the decrease in short-circuit current density (SCCD) that was derived from the simultaneous measurement of current-voltage curves while the device was illuminated by a solar simulator. In order to demonstrate this unequivocal relationship between performance loss and morphological transformation, Monte Carlo (MC) simulations of the SCCD were performed using the structural parameters extracted from modeling of the μGISAXS patterns. The agreement between the MC simulations and the measured SCCD was excellent (**Figure 12(c)**) concluding that an increase in P3HT

domain size and separation during illumination is responsible for the decrease of effective light harvesting area, thus decreasing the exciton splitting events, whereas the PCBM domain size and distance remained fairly constant. Moreover, a temperature effect was ruled out since the solar cell did not exceed 45°C during the experiments due to Peltier cooling.
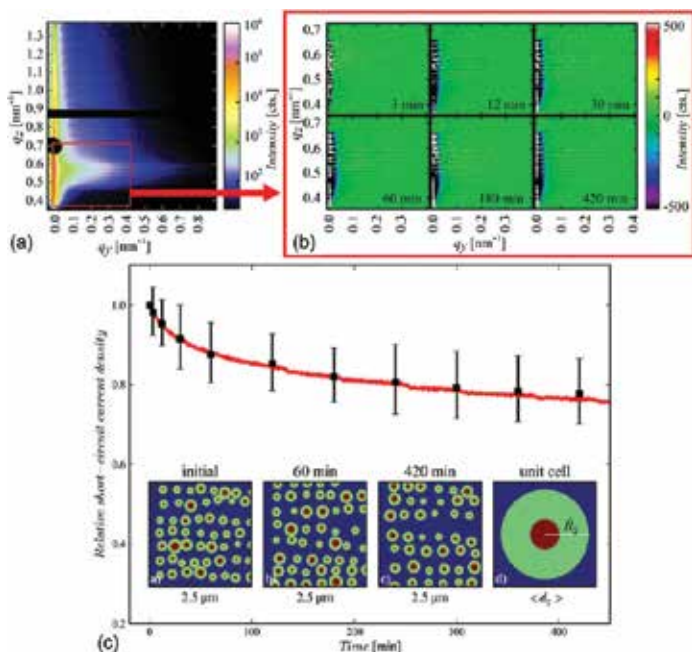

Figure 12. (a) 2D µGISAXS pattern of the polymer solar cell before illumination. (b) Difference scattering patterns, i.e., 2D µGISAXS measurements obtained at different operation times after subtraction of the initial scattering pattern within the marked window (red box) in (a). Negative values mean a loss of signal with respect to the initial measurement. (c) Simulated (black dots) and measured short-circuit current density (red line). The simulated short-circuit current density was derived from the morphological parameters extracted by µGISAXS. The insets show the inner film morphology at different times as generated by the Monte Carlo simulations. The inset on the right presents the domain morphology model used in the simulations and extracted from the µGISAXS experiments: red correspond to the core of P3HT domains, green to the effective light harvesting area and blue to the non-active effective area of the solar cell. Reproduced with permission from Schaffer et al. [90]. Copyright 2013, John Wiley and Sons.

5. Conclusions

In this chapter, we have reviewed the current trends in the application of time-resolved GISAXS for in-situ and in-operando studies during thin film formation and processing. It has been shown that GISAXS presents unique capabilities as a noninvasive technique with intrinsic statistical relevance and time resolutions down to the millisecond regime. Moreover, GISAXS constitutes a very versatile technique that can be applied to a large variety of materials with a vast range of applications, and the relative easiness of combining it with other characterization

techniques for simultaneous measurements offers the possibility of correlating the film structure to its properties, of utmost importance in most of the applications of thin films.

In the near future, the present developments for the next generation of 2D X-ray photon counting pixel detectors will allow investigating even faster processes since frame rates higher than 10 kHz with large detector dynamic ranges are foreseen. Additionally, the application of present technique improvements to in-situ studies will further contribute to gain deeper knowledge of thin film fabrication and processing. In this sense, the present advances in grazing incidence resonant soft X-ray scattering (GI-RSoXS), with its inherent material contrast through tuning the incident beam energy to one of the absorption edges of the materials under investigation, will certainly help in understanding, e.g., alloying, blending or phase segregation phenomena in-situ with adequate time resolution. Furthermore, the decrease in beam emittance at synchrotrons is currently enabling longer sample to detector distances—up to several tens of meters—which translates in access to lower q ranges (of the order of 0.001 nm^{-1} or even lower, i.e., real space sizes in the micron range) by performing grazing incidence ultra-small angle X-ray scattering (GIUSAXS) experiments. Thus, through the combination of in-situ GIWAXS ($q \approx 1$–50 nm^{-1}), GISAXS ($q \approx 0.01$–1 nm^{-1}) and GIUSAXS ($q \approx 0.01$–0.0001 nm^{-1}) real space structures from 1 Å to 10 μm will be accessible, which will provide a complete morphological description of the processes from the atomic structure to the microscopic regime allowing to establish an extremely important link between atomic, nanoscopic and macroscopic ordering, which is not yet fully developed.

Finally, the development of new magnet arrays in storage rings is currently taking place and diffraction-limited sources are not far from becoming available. This will provide an enhanced coherence of the X-ray beams and therefore, it is not difficult to anticipate a growth in the application of time-resolved coherent GISAXS (Co-GISAXS). So far, most of the GISAXS experiments are noncoherent, thus the scattered photon phase is lost making modeling indispensable during data analysis. On the contrary, in Co-GISAXS the phase information can be directly retrieved via mathematical algorithms so that, to some extent, the morphology of the scattering entity can be directly reconstructed from the experimental data. Furthermore, as already known from other X-ray coherent techniques such as X-ray photon correlation spectroscopy (XPCS), not only kinetics but also dynamics of the nano-objects may be probed. However, a good resolution of the speckles is necessary to guarantee an accurate determination of the dynamical processes. This requires a high q resolution that corresponds to small detector pixel size and for fast dynamic processes 2D X-ray photon counting pixel detectors with pixel sizes comparable to those of CCD detectors will be indispensable.

Acknowledgements

Author details

Gonzalo Santoro[1*] and Shun Yu[2]

*Address all correspondence to: gonzalo.santoro@icmm.es

1 Materials Science Institute of Madrid (ICMM-CSIC), Madrid, Spain

2 KTH Royal Institute of Technology, Stockholm, Sweden

References

[1]   Zhao XY, Wei CM, Yang L, et al. Quantum confinement and electronic properties of silicon nanowires. Phys. Rev. Lett. 2004; 92. DOI: 10.1103/PhysRevLett.92.236805.

[2]   Sun YG, Mayers B, Xia YN. Metal nanostructures with hollow interiors. Adv. Mater. 2003; 15:641–646. DOI: 10.1002/adma.200301639.

[3]   Narayanan R,El-Sayed MA. Shape-dependent catalytic activity of platinum nanoparticles in colloidal solution. Nano Lett. 2004; 4:1343–1348. DOI: 10.1021/nl0495256.

[4]   Kelly KL, Coronado E, Zhao LL, et al. The optical properties of metal nanoparticles: the influence of size, shape, and dielectric environment. J. Phys. Chem. B. 2003; 107:668–677. DOI: 10.1021/jp026731y.

[5]   Daniel MC,Astruc D. Gold nanoparticles: assembly, supramolecular chemistry, quantum-size-related properties, and applications toward biology, catalysis, and nanotechnology. Chem. Rev. 2004; 104:293–346. DOI: 10.1021/cr030698+.

[6]   Hentschel M, Saliba M, Vogelgesang R, et al. Transition from isolated to collective modes in plasmonic oligomers. Nano Lett. 2010; 10:2721–2726. DOI: 10.1021/nl101938p.

[7]   Jiao F, Frei H. Nanostructured cobalt oxide clusters in mesoporous silica as efficient oxygen-evolving catalysts. Angew. Chem. Int. Ed. 2009; 48:1841–1844. DOI: 10.1002/anie.200805534.

[8]   Ellison CJ,Torkelson JM. The distribution of glass-transition temperatures in nanoscopically confined glass formers. Nat. Mater. 2003; 2:695–700. DOI: 10.1038/nmat980.

[9]   Glatter O, Kratky O, editors. Small Angle X-ray Scattering. London: Academic Press Inc.; 1982. 515 p. ISBN: 0-12-286280-5.

[10]   Levine JR, Cohen LB, Chung YW, et al. Grazing-incidence small-angle X-ray-scattering—new tool for studying thin-film growth. J. Appl. Crystallogr. 1989; 22:528–532. DOI: 10.1107/s002188988900717x.

[11] Müller-Buschbaum P. Grazing incidence small-angle X-ray scattering: an advanced scattering technique for the investigation of nanostructured polymer films. Anal. Bioanal. Chem. 2003; 376:3–10. DOI: 10.1007/s00216-003-1869-2.

[12] Renaud G, Lazzari R, Leroy F. Probing surface and interface morphology with grazing incidence small angle X-ray scattering. Surf. Sci. Rep. 2009; 64:255–380. DOI: 10.1016/j.surfrep.2009.07.002.

[13] Müller-Buschbaum P. A basic introduction to grazing incidence small-angle X-ray scattering. In: Ezquerra TA, Nogales A, García-Gutiérrez MC, et al., editors. Applications of Synchrotron Light to Scattering and Diffraction in Materials and Life Sciences. Berlin, Heidelberg: Springer; 2009. p. 61–89. DOI: 10.1007/978-3-540-95968-7_3.

[14] Yoneda Y. Anomalous surface reflection of X rays. Phys. Rev. 1963; 131:2010–2013. DOI: 10.1103/PhysRev.131.2010.

[15] Lu XH, Yager KG, Johnston D, et al. Grazing-incidence transmission X-ray scattering: surface scattering in the Born approximation. J. Appl. Crystallogr. 2013; 46:165–172. DOI: 10.1107/s0021889812047887.

[16] Dosch H. Evanescent X-ray scattering. In: Dosch H, editor. Critical Phenomena at Surfaces and Interfaces: Evanescent X-Ray and Neutron Scattering. Berlin, Heidelberg: Springer; 1992. p. 6–31. DOI: 10.1007/BFb0045211.

[17] Robinson IK, Tweet DJ. Surface X-ray diffraction. Rep. Prog. Phys. 1992; 55:599–651. DOI: 10.1088/0034-4885/55/5/002.

[18] Lazzari R. IsGISAXS: a program for grazing-incidence small-angle X-ray scattering analysis of supported islands. J. Appl. Crystallogr. 2002; 35:406–421. DOI: 10.1107/s0021889802006088.

[19] Babonneau D. FitGISAXS: software package for modelling and analysis of GISAXS data using IGOR Pro. J. Appl. Crystallogr. 2010; 43:929–936. DOI: 10.1107/s0021889810020352.

[20] Chourou ST, Sarje A, Li XS, et al. HipGISAXS: a high-performance computing code for simulating grazing-incidence X-ray scattering data. J. Appl. Crystallogr. 2013; 46:1781–1795. DOI: 10.1107/s0021889813025843.

[21] Durniak C, Ganeva M, Pospelov G, et al. BornAgain—software for simulating and fitting X-ray and neutron small-angle scattering at grazing incidence [Internet]. 2015. Available from: http://www.bornagainproject.org [Accessed: 2016-05-23].

[22] Lee B, Yoon J, Oh W, et al. In-situ grazing incidence small-angle X-ray scattering studies on nanopore evolution in low-*k* organosilicate dielectric thin films. Macromolecules. 2005; 38:3395–3405. DOI: 10.1021/ma048214e.

[23] Busch P, Rauscher M, Smilgies DM, et al. Grazing-incidence small-angle X-ray scattering from thin polymer films with lamellar structures—the scattering cross section in

the distorted-wave Born approximation. J. Appl. Crystallogr. 2006; 39:433–442. DOI: 10.1107/s0021889806012337.

[24] Salditt T, Metzger TH, Peisl J, et al. Determination of the height-height correlation function of rough surfaces from diffuse X-ray scattering. Europhys. Lett. 1995; 32:331. DOI: 10.1209/0295-5075/32/4/008.

[25] Hexemer A, Mueller-Buschbaum P. Advanced grazing-incidence techniques for modern soft-matter materials analysis. IUCrJ. 2015; 2:106–125. DOI: 10.1107/s2052252514024178.

[26] Lazzari R, Leroy F, Renaud G. Grazing-incidence small-angle X-ray scattering from dense packing of islands on surfaces: development of distorted wave Born approximation and correlation between particle sizes and spacing. Phys. Rev. B. 2007; 76. DOI: 10.1103/PhysRevB.76.125411.

[27] Döhrmann R, Botta S, Buffet A, et al. A new highly automated sputter equipment for in situ investigation of deposition processes with synchrotron radiation. Rev. Sci. Instrum. 2013; 84. DOI: 10.1063/1.4798544.

[28] Cantelli V, Geaymond O, Ulrich O, et al. The In situ growth of nanostructures on surfaces (INS) endstation of the ESRF BM32 beamline: a combined UHV-CVD and MBE reactor for in situ X-ray scattering investigations of growing nanoparticles and semiconductor nanowires. J. Synchrotron Radiat. 2015; 22:688–700. DOI: 10.1107/s1600577515001605.

[29] Ibrahimkutty S, Seiler A, Prussmann T, et al. A portable ultrahigh-vacuum system for advanced synchrotron radiation studies of thin films and nanostructures: EuSi2 nano-islands. J. Synchrotron Radiat. 2015; 22:91–98. DOI: 10.1107/s1600577514019705.

[30] Renaud G, Lazzari R, Revenant C, et al. Real-time monitoring of growing nanoparticles. Science. 2003; 300:1416–1419. DOI: 10.1126/science.1082146.

[31] Lazzari R, Renaud G, Revenant C, et al. Adhesion of growing nanoparticles at a glance: surface differential reflectivity spectroscopy and grazing incidence small angle X-ray scattering. Phys. Rev. B. 2009; 79:125428. DOI: 10.1103/PhysRevB.79.125428.

[32] Revenant C, Renaud G, Lazzari R, et al. Defect-pinned nucleation, growth, and dynamic coalescence of Ag islands on MgO(001): an in situ grazing-incidence small-angle X-ray scattering study. Phys. Rev. B. 2009; 79:235424. DOI: 10.1103/PhysRevB.79.235424.

[33] Kaune G, Metwalli E, Meier R, et al. Growth and morphology of sputtered aluminum thin films on P3HT surfaces. ACS Appl. Mater. Interfaces. 2011; 3:1055–1062. DOI: 10.1021/am101195m.

[34] Schwartzkopf M, Buffet A, Korstgens V, et al. From atoms to layers: in situ gold cluster growth kinetics during sputter deposition. Nanoscale. 2013; 5:5053–5062. DOI: 10.1039/c3nr34216f.

[35] Santoro G, Yu S, Schwartzkopf M, et al. Silver substrates for surface enhanced Raman scattering: correlation between nanostructure and Raman scattering enhancement. Appl. Phys. Lett. 2014; 104:243107. DOI: 10.1063/1.4884423.

[36] Paul N, Metwalli E, Yao Y, et al. Templating growth of gold nanostructures with a CdSe quantum dot array. Nanoscale. 2015; 7:9703–9714. DOI: 10.1039/c5nr01121c.

[37] Yu S, Santoro G, Sarkar K, et al. Formation of Al nanostructures on Alq3: an in situ grazing incidence small angle X-ray scattering study during radio frequency sputter deposition. J. Phys. Chem. Lett. 2013; 4:3170–3175. DOI: 10.1021/jz401585d.

[38] Yu S, Santoro G, Yao Y, et al. Following the island growth in real time: Ag nanocluster layer on Alq3 thin film. J. Phys. Chem. C. 2015; 119:4406–4413. DOI: 10.1021/jp512675w.

[39] Schwartzkopf M, Santoro G, Brett CJ, et al. Real-time monitoring of morphology and optical properties during sputter deposition for tailoring metal-polymer interfaces. ACS Appl. Mater. Interfaces. 2015; 7:13547–13556. DOI: 10.1021/acsami.5b02901.

[40] Metwalli E, Körstgens V, Schlage K, et al. Cobalt nanoparticles growth on a block copolymer thin film: a time-resolved GISAXS study. Langmuir. 2013; 29:6331–6340. DOI: 10.1021/la400741b.

[41] Erb DJ, Schlage K, Röhlsberger R. Uniform metal nanostructures with long-range order via three-step hierarchical self-assembly. Sci. Adv. 2015; 1:e1500751. DOI: 10.1126/sciadv.1500751.

[42] Roth SV, Santoro G, Risch JFH, et al. Patterned diblock co-polymer thin films as templates for advanced anisotropic metal nanostructures. ACS Appl. Mater. Interfaces. 2015; 7:12470–12477. DOI: 10.1021/am507727f.

[43] Ritley KA, Krause B, Schreiber F, et al. A portable ultrahigh vacuum organic molecular beam deposition system for in situ X-ray diffraction measurements. Rev. Sci. Instrum. 2001; 72:1453–1457. DOI: 10.1063/1.1336822.

[44] Ferrer P, Rubio-Zuazo J, Heyman C, et al. A multipurpose ultra-high vacuum-compatible chamber for in situ X-ray surface scattering studies over a wide range of temperature and pressure environment conditions. J. Phys.: Conf. Series. 2013; 425:132002. DOI: 10.1088/1742-6596/425/13/132002.

[45] Schreiber F, Eberhardt A, Leung TYB, et al. Adsorption mechanisms, structures, and growth regimes of an archetypal self-assembling system: Decanethiol on Au(111). Phys. Rev. B. 1998; 57:12476–12481. DOI: 10.1103/PhysRevB.57.12476.

[46] Kowarik S, Gerlach A, Sellner S, et al. Real-time observation of structural and orientational transitions during growth of organic thin films. Phys. Rev. Lett. 2006; 96:125504. DOI: 10.1103/PhysRevLett.96.125504.

[47] Mayer AC, Kazimirov A, Malliaras GG. Dynamics of bimodal growth in pentacene thin films. Phys. Rev. Lett. 2006; 97. DOI: 10.1103/PhysRevLett.97.105503.

[48] Kowarik S, Gerlach A, Schreiber F. Organic molecular beam deposition: fundamentals, growth dynamics, and in situ studies. J. Phys.: Condens. Matter. 2008; 20. DOI: 10.1088/0953-8984/20/18/184005.

[49] Kowarik S, Gerlach A, Skoda MWA, et al. Real-time studies of thin film growth: measurement and analysis of X-ray growth oscillations beyond the anti-Bragg point. Eur. Phys. J.: Special Topics. 2009; 167:11–18. DOI: 10.1140/epjst/e2009-00930-y.

[50] Woll AR, Desai TV, Engstrom JR. Quantitative modeling of in situ X-ray reflectivity during organic molecule thin film growth. Phys. Rev. B. 2011; 84. DOI: 10.1103/PhysRevB.84.075479.

[51] Alvarez J, Lundgren E, Torrelles X, et al. Effect of a surfactant in homoepitaxial growth of Ag (001): dendritic versus faceted island morphologies. Surf. Sci. 2000; 464:165–175. DOI: 10.1016/s0039-6028(00)00648-8.

[52] Fleet A, Dale D, Woll AR, et al. Multiple time scales in diffraction measurements of diffusive surface relaxation. Phys. Rev. Lett. 2006; 96. DOI: 10.1103/PhysRevLett.96.055508.

[53] Ferguson JD, Arikan G, Dale DS, et al. Measurements of surface diffusivity and coarsening during pulsed laser deposition. Phys. Rev. Lett. 2009; 103. DOI: 10.1103/PhysRevLett.103.256103.

[54] Frank C, Banerjee R, Oettel M, et al. Analysis of island shape evolution from diffuse X-ray scattering of organic thin films and implications for growth. Phys. Rev. B. 2014; 90. DOI: 10.1103/PhysRevB.90.205401.

[55] Bommel S, Kleppmann N, Weber C, et al. Unravelling the multilayer growth of the fullerene C60 in real time. Nat. Commun. 2014; 5:5388. DOI: 10.1038/ncomms6388.

[56] Frank C, Novak J, Banerjee R, et al. Island size evolution and molecular diffusion during growth of organic thin films followed by time-resolved specular and off-specular scattering. Phys. Rev. B. 2014; 90:045410. DOI: 10.1103/PhysRevB.90.045410.

[57] Zykov A, Bommel S, Wolf C, et al. Diffusion and nucleation in multilayer growth of PTCDI-C8 studied with in situ X-ray growth oscillations and real-time small angle X-ray scattering. J. Chem. Phys. Accepted manuscript.

[58] Vegso K, Siffalovic P, Jergel M, et al. A non-equilibrium transient phase revealed by in situ GISAXS tracking of the solvent-assisted nanoparticle self-assembly. J. Nanopart. Res. 2014; 16:1–11. DOI: 10.1007/s11051-014-2536-6.

[59] Corricelli M, Altamura D, Curri ML, et al. GISAXS and GIWAXS study on self-assembling processes of nanoparticle based superlattices. Cryst. Eng. Commun. 2014; 16:9482–9492. DOI: 10.1039/C4CE01291G.

[60] Chou KW, Yan B, Li R, et al. Spin-cast bulk heterojunction solar cells: a dynamical investigation. Adv. Mater. 2013; 25:1923–1929. DOI: 10.1002/adma.201203440.

[61] Perlich J, Schwartzkopf M, Körstgens V, et al. Pattern formation of colloidal suspensions by dip-coating: an in situ grazing incidence X-ray scattering study. Phys. Stat. Sol. Rapid Res. Lett. 2012; 6:253–255. DOI: 10.1002/pssr.201206114.

[62] Nagpure S, Das S, Garlapalli RK, et al. In situ GISAXS investigation of low-temperature aging in oriented surfactant-mesostructured titania thin films. J. Phys. Chem. C. 2015; 119:22970–22984. DOI: 10.1021/acs.jpcc.5b06945.

[63] Smilgies D-M, Li R, Giri G, et al. Look fast: crystallization of conjugated molecules during solution shearing probed in-situ and in real time by X-ray scattering. Phys. Stat. Sol. Rapid Res. Lett. 2013; 7:177–179. DOI: 10.1002/pssr.201206507.

[64] Abdellah A, Virdi KS, Meier R, et al. Successive spray deposition of P3HT/PCBM organic photoactive layers: material composition and device characteristics. Adv. Funct. Mater. 2012; 22:4078–4086. DOI: 10.1002/adfm.201200548.

[65] Sarkar K, Braden EV, Pogorzalek S, et al. Monitoring structural dynamics of in situ spray-deposited zinc oxide films for application in dye-sensitized solar cells. ChemSusChem. 2014; 7:2140–2145. DOI: 10.1002/cssc.201402049.

[66] Song L, Wang W, Körstgens V, et al. Spray Deposition of titania films with incorporated crystalline nanoparticles for all-solid-state dye-sensitized solar cells using P3HT. Adv. Funct. Mater. 2016; 26:1498–1506. DOI: 10.1002/adfm.201504498.

[67] Herzog G, Benecke G, Buffet A, et al. In situ grazing incidence small-angle X-ray scattering investigation of polystyrene nanoparticle spray deposition onto silicon. Langmuir. 2013; 29:11260–11266. DOI: 10.1021/la402254q.

[68] Zhang P, Santoro G, Yu S, et al. Manipulating the assembly of spray-deposited nanocolloids: in situ study and monolayer film preparation. Langmuir. 2016; 32:4251–4258. DOI: 10.1021/acs.langmuir.6b00892.

[69] Palumbiny CM, Liu F, Russell TP, et al. The crystallization of PEDOT:PSS polymeric electrodes probed in situ during printing. Adv. Mater. 2015; 27:3391–3397. DOI: 10.1002/adma.201500315.

[70] Pröller S, Liu F, Zhu C, et al. Following the morphology formation in situ in printed active layers for organic solar cells. Adv. Energy Mater. 2016; 6:1501580. DOI: 10.1002/aenm.201501580.

[71] Moulin JF, Roth SV, Müller-Buschbaum P. Flow at interfaces: a new device for X-ray surface scattering investigations. Rev. Sci. Instrum. 2008; 79:015109. DOI: 10.1063/1.2816220.

[72] Santoro G, Buffet A, Döhrmann R, et al. Use of intermediate focus for grazing incidence small and wide angle X-ray scattering experiments at the beamline P03 of PETRA III, DESY. Rev. Sci. Instrum. 2014; 85:043901. DOI: 10.1063/1.4869784.

[73]   Felici R, Jeutter NM, Mussi V, et al. In situ study of the dewetting behavior of Ni-films on oxidized Si(001) by GISAXS. Surf. Sci. 2007; 601:4526–4530. DOI: 10.1016/j.susc. 2007.04.210.

[74]   Daudin R, Nogaret T, Schuelli TU, et al. Epitaxial orientation changes in a dewetting gold film on Si(111). Phys. Rev. B. 2012; 86. DOI: 10.1103/PhysRevB.86.094103.

[75]   Bommel S, Spranger H, Weber C, et al. Thermally-activated post-growth dewetting of fullerene C60 on mica. Phys. Status Sol. Rapid Res. Lett. 2015; 9:646–651. DOI: 10.1002/pssr.201510258.

[76]   Zhang J, Posselt D, Smilgies D-M, et al. Lamellar diblock copolymer thin films during solvent vapor annealing studied by GISAXS: different behavior of parallel and perpendicular lamellae. Macromolecules. 2014; 47:5711–5718. DOI: 10.1021/ma500633b.

[77]   Hejral U, Muller P, Balmes O, et al. Tracking the shape-dependent sintering of platinum-rhodium model catalysts under operando conditions. Nat. Commun. 2016; 7:10964. DOI: 10.1038/ncomms10964.

[78]   Ruge M, Golks F, Zegenhagen J, et al. In operando GISAXS studies of mound coarsening in electrochemical homoepitaxy. Phys. Rev. Lett. 2014; 112:055503. DOI: 10.1103/PhysRevLett.112.055503.

[79]   Modestino MA, Kusoglu A, Hexemer A, et al. Controlling nafion structure and properties via wetting interactions. Macromolecules. 2012; 45:4681–4688. DOI: 10.1021/ma300212f.

[80]   Wang W, Schaffer CJ, Song L, et al. In operando morphology investigation of inverted bulk heterojunction organic solar cells by GISAXS. J. Mater. Chem. A. 2015; 3:8324–8331. DOI: 10.1039/C5TA01109D.

[81]   Schaffer CJ, Palumbiny CM, Niedermeier MA, et al. Morphological degradation in low bandgap polymer solar cells—an in-operando study. Adv. Energy Mater. 2016; 1600712. DOI: 10.1002/aenm.201600712.

[82]   Daudin R, Revenant C, Davi G, et al. Growth and dewetting of gold on Si(1 1 1) investigated in situ by grazing incidence small angle X-ray scattering. Physica E: Low Dimens. Syst. Nanostruct. 2012; 44:1905–1909. DOI: 10.1016/j.physe.2012.05.021.

[83]   Bikondoa O, Carbone D, Chamard V, et al. Ageing dynamics of ion bombardment induced self-organization processes. Sci. Rep. 2013; 3:1850. DOI: 10.1038/srep01850.

[84]   Nugent KA. Coherent methods in the X-ray sciences. Adv. Phys. 2010; 59:1–99. DOI: 10.1080/00018730903270926.

[85]   Rebollar E, Vazquez de Aldana JR, Martin-Fabiani I, et al. Assessment of femtosecond laser induced periodic surface structures on polymer films. Phys. Chem. Chem. Phys. 2013; 15:11287–11298. DOI: 10.1039/c3cp51523k.

[86] Martínez-Tong DE, Rodríguez-Rodríguez A, Nogales A, et al. Laser fabrication of polymer ferroelectric nanostructures for nonvolatile organic memory devices. ACS Appl. Mater. Interfaces. 2015; 7:19611–19618. DOI: 10.1021/acsami.5b05213.

[87] Rebollar E, Rueda DR, Martín-Fabiani I, et al. In situ monitoring of laser-induced periodic surface sStructures formation on polymer films by grazing incidence small-angle X-ray scattering. Langmuir. 2015; 31:3973–3981. DOI: 10.1021/acs.langmuir. 5b00285.

[88] Körstgens V, Philipp M, Magerl D, et al. Following initial changes in nanoparticle films under laminar flow conditions with in situ GISAXS microfluidics. RSC Adv. 2014; 4:1476–1479. DOI: 10.1039/c3ra44554b.

[89] Philipp M, Körstgens V, Magerl D, et al. Sorption of water and initial stages of swelling of thin PNIPAM films using in situ GISAXS microfluidics. Langmuir. 2015; 31:9619–9627. DOI: 10.1021/acs.langmuir.5b01978.

[90] Schaffer CJ, Palumbiny CM, Niedermeier MA, et al. A direct evidence of morphological degradation on a nanometer scale in polymer solar cells. Adv. Mater. 2013; 25:6760–6764. DOI: 10.1002/adma.201302854.

Grazing-Incidence Small Angle X-Ray Scattering in Polymer Thin Films Utilizing Low-Energy X-Rays

Katsuhiro Yamamoto

Additional information is available at the end of the chapter

Abstract

The intricate nanoscopic morphology of soft materials such as block copolymer and polymer blend system successfully analyzed by small angle X-ray scatterings (SAXS). In thin films, those soft material systems have attracted great attention because of a potential for practical use of functional materials. The morphology has been revealed by grazing-incidence (GI) methods. Recently, advanced grazing-incidence technique for analysis for surface-, volume-, and material-sensitive method (high time, spatial, and/or material resolution) has been reported. Using low X-ray photon energy, tender X-ray (1–4 eV) and soft X-ray near K-edge carbon, allows probing a complex nanomorphology with those sensitivity. In this chapter, recent GI-SAXS with tender X-ray and resonant soft X-ray (GI-RSoX) will be picked up to open for discussion on new possibility of structural analyses.

Keywords: grazing-incidence X-ray scattering, organic thin film, block copolymer, tender X-rays, depth profiling

1. Introduction

Block copolymer (BCP) composed of two (more) immiscible polymers form variety structures with the periodicity of several tens nanometer both in bulk and thin films. BCP thin film has attracted great attention as an applicable material to various fields, e.g., solar cell [1–3], nanolithography [4–6], and size-selective separation [7, 8]. In bulk state, microphase-separated structure is predicted by the Flory-Huggins interaction parameter, the degree of polymerization, and the volume fraction of blocks [9], whereas in thin film, film thickness [10, 11] and substrate-polymer interaction and/or also polymer-air interaction[12] must be taken into

consideration. Controlling morphology, orientation and size of the structures are necessary for practical use although phase-separation behavior of BCP in thin film becomes more complicated. This has motivated numerous orientation control methodology studies that have examined the influence of film thickness [10, 11, 13, 14], surface/or interfacial free energy [14–17], surface topology [15, 18, 19], external applied fields (shear-induced [4, 20], electric field [21], magnetic field [22], and light-driven [23, 24]), solvent vapor or thermal annealing[25–30], and directional solidification [31–33]. Since functionality and physical property are also strongly related to the structure and the mobility in the vicinity of interface, revealing structure in detail is required. Suitable characterization techniques are required to monitor the structures of BCP both laterally and in-depth. Several approaches have been used to find BCP structures. Atomic force microscopy (AFM), electron microscopy, dynamic secondary ion mass spectrometry (DSIMS), X-ray photoelectron spectroscopy (XPS), grazing incidence small angle X-ray or neutron scattering (GISAXS, GISANS), X-ray or neutron reflectivity (XRR, NR), etc. have been used to study the structure of BCP thin films. AFM can enable an access of the information only near the surface although the surface structure can be directly observed and easily understandable. Electron microscopy is a powerful tool for visually examining a cross-sectional view of polymeric thin films in two-and three-dimensional real space [34]. DSIMS can elucidate the BCP morphology and the self-diffusion of polymer chains in thin films along a depth direction [35]. Time-of-flight (ToF) SIMS using ion cluster beam was reported to be a particularly well-suited technique that enables the in-depth profiling of polymers [36, 37]. X-ray photoelectron spectroscopy depth profiling with C60$^+$ sputtering revealed the ion distribution in lithium salt-doped BCP thin films [38, 39].Electron microscopy, DSIMS, and XPS techniques are essentially accompanied by the destruction of specimen because of processing such as sectioning or etching for analysis. In particular, it is important to take into account the deformation and losing of a precise original spatial coordinate induced by sectioning and chemical reactions induced by etching in the analysis of results obtained by these techniques. In contrast, neutron reflectivity (NRR) measurements enable a practically nondestructive analysis of depth profiles and ordering of microphase-separated structure in BCP thin films [40, 41]. However, the NRR provides structural information (density profile) only in the vertical direction to the sample surface and lateral information of the structure is inaccessible. In addition, accuracy of the density profile (depth-resolved information) perpendicular to the surface becomes worse when the film thickness is large for analyzing periodicity of microphase-separated structure. Generally, NRR depth profiling is suited for very thin film (less than 100 nm) as in the above case. GISAXS is another very powerful tool for understanding the nanostructure in both vertical and lateral directions of organic thin film (BCP thin film). And GISAXS is essentially nondestructive method under the condition of the no radiation damage of X-rays [42–47]. Commonly, SAXS and GISAXS methods have been conducted using hard X-rays with energy range of 6–14 keV. However, under these conditions, the penetration depth of X-rays rapidly reaches the thickness scale of the organic materials in the vicinity of the critical angle α_C of total reflection at the polymeric surface, which is making depth-resolved GISAXS measurements with hard X-rays totally impractical. A depth-sensitive GISAXS method using tender X-ray (1.77 keV) was first reported for the BCP thin film by Okuda et al. [48] and Wernecke et al. [49]. They investigated the structural relaxation near the

surface and the dynamic heterogeneity of polymer chains in thin films. At even lower X-ray photon energies, near the adsorption K edges of the polymeric materials (the oxygen, nitrogen, and carbon K edges), the fine structure of the adsorption edge can be utilized in GISAXS as reported by Ruderer et al. [50]. The grazing-incidence resonant soft X-ray (GI-RSoXS) has been applied for polymer blend thin films with low contrast in the real part of the refractive index for the hard X-rays but with significant differences in the soft X-ray regime. Furthermore, the X-ray penetration depth is drastically affected by the changes in the X-ray photon energy across the K-edge. The surface-and volume-sensitive structure of polymer blend films had been analyzed using this technique [50]. Similar to the GISAXS, GISANS has been developed by Müller-Buschbaum and co-workers. GISANS is a perfectly nondestructive approach for structure analysis and has essentially the same capability for surface-sensitive [51], interface-sensitive (structural information near the polymer-substrate interface enabled by the ability of the neutrons to go through the substrate) [52, 53], and depth-sensitive analysis [54]. Moreover, in time-of-flight mode GISANS (ToF-GISANS) [52, 55] a broad wavelength band is used instead of a single neutron wavelength, i.e., a range of different scattering vectors is directly probed by the measurement under a fixed angle of incidence. At an appropriate incident angle, it is possible to simultaneously conduct surface- and bulk-sensitive measurements. While GISANS possesses advantages as compared with the GISAXS, GISANS experiments still remain very rare because GISANS requires very high-flux sources to measure the much weaker signals in grazing-incidence geometry and the need for deuterium labeling (in some cases, of course, this is beneficial for structure analysis by tuning the contrast). These GISANS techniques have been well summarized in the reviews [56].

In this chapter, recent advanced GISAXS experiment utilizing low-energy X-rays will be introduced. GISAXS probes the complex nano- and microphase-separated structure in polymer thin films. Especially, tuning the energy of GISAXS in the tender and soft X-ray regime allows to the tailoring of X-ray penetration depth and contrast and thereby the probing of more complex morphologies in polymer thin films. GI-RSoXS has been applied for polymer blend thin films with low contrast in the real part of the refractive index for the hard X-rays but with significant differences in the soft X-ray regime. Furthermore, the X-ray penetration depth is drastically affected by the changes in the X-ray photon energy across the K-edge. The surface- and volume-sensitive structure of polymer blend films had been analyzed using this technique.

2. Grazing-incidence small angle X-ray scattering

Incident X-ray beam goes into the sample surface at a very shallow angle α_i (normally less than 1°). Scattering is measured with a two-dimensional detector as a function of the exit angle α_f (out-of-plane angle) and the in-plane angle 2θ. The magnitude of the scattering vector is given by $q = 4\pi\sin\theta/\lambda$ (λ: wavelength of X-ray, 2θ: scattering angle). The scattering vector q_z means the component vertical to the film surface. The q_x and q_y are the components of scattering vectors in the sample surface, perpendicular to and directed to the X-ray beam, respectively. For each data set I(y, z), pixels of the detector were converted into exit angle α_f normal to the

sample surface and a scattering angle 2θ parallel to the surface by simple geometrical consideration. The amplitude of scattering vector q is composed of q_x, q_y, and q_z related to the experimental angles by

$$q = \begin{pmatrix} q_x \\ q_y \\ q_z \end{pmatrix} = \frac{2\pi}{\lambda} \begin{pmatrix} \cos 2\Theta \cos \alpha_f - \cos \alpha_i \\ \sin 2\Theta \cos \alpha_f \\ \sin \alpha_i + \sin \alpha_f \end{pmatrix},$$ (1)

As shown in **Figure 1**, typical sample-to-detector distances (SSD) for GISAXS are of the order of 1–2 m. In the case of small angle scattering, the two-dimensional detector probes mainly the q_y and q_z information because q_x is very small and the curvature of the Ewald sphere is negligible. The calculation of the out-of-plane scattering vector is considerably complex. Above critical angle α_C of polymeric materials, the theoretical penetration depth is much larger than the film thickness (order of micro-meter) (when hard X-ray is normally used) as shown in **Figure 2**. The transmitted wave can therefore be reflected at the polymer-substrate interface in combination with diffraction from the structures in the thin film. Under the assumption that each X-ray scatters no more than once from the objects and there is no transmission through the substrate, there are four possible scattering events to happen, additionally refraction at the sample surface (air-polymer interface) (**Figure 3**).
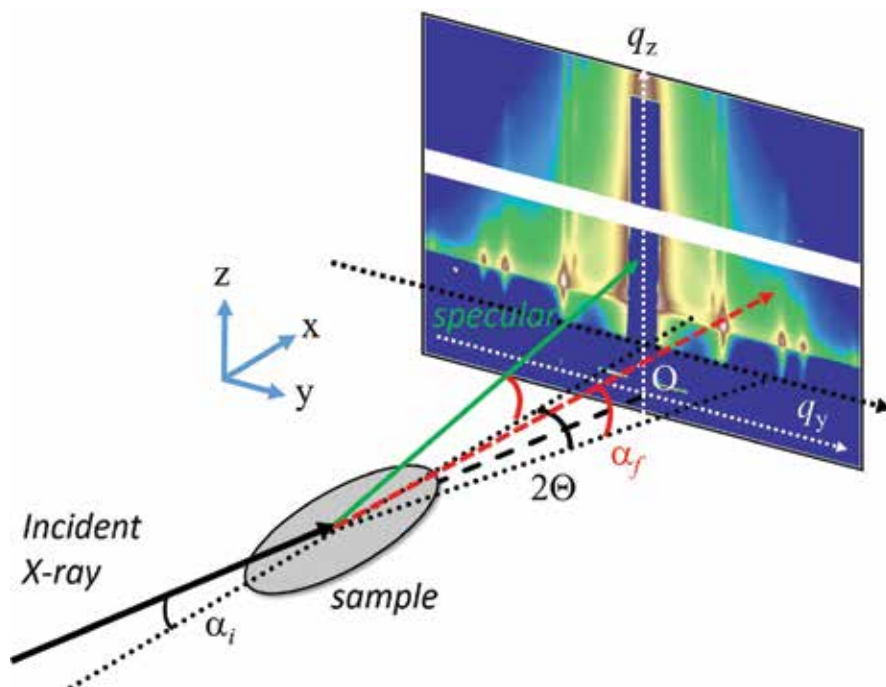

Figure 1. Schematic illustration of the scattering geometry used in GISAXS. The sample surface is inclined by incident angle with respect to the horizon. The exit and in-plane angles are denoted α_i and 2θ, reepectively.
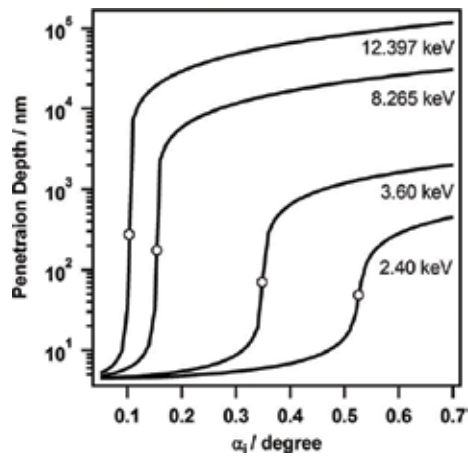
Figure 2. Penetration depth calculated for a block copolymer (S2VP) film for different X-ray energies, 12.397, 8.265, 3.60, and 2.40 keV.
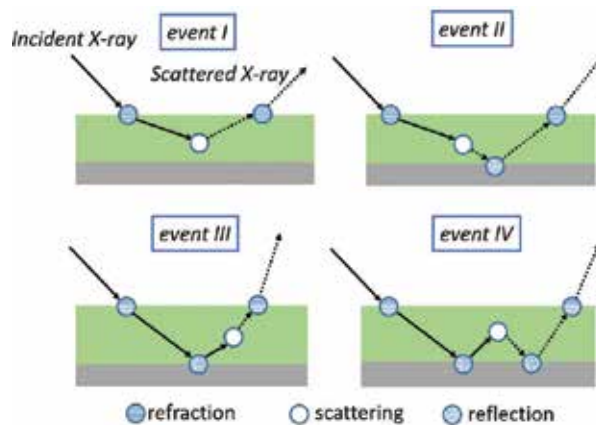

Figure 3. Four scattering events, demonstrating different combinations of reflection from the substrate with diffraction from the objects.

3. Depth-resolved structure analysis of microphase-separated structures in block copolymer thin film by grazing-incidence small angle X-ray scattering utilizing tender X-ray

3.1. Cylindrical microdomain in block copolymer thin film [57]

In this section, GISAXS measurement with low energy (tender) X-ray (2.40 keV) is introduced in order to precisely elucidate the depth profile of a microphase-separated structure (hexago-

nally packed cylinders) of a polystyrene-b-poly (2-vinylpyridine (S2VP) thin film on a silicon wafer with the cylindrical microdomains (poly (2-vinylpyridine): P2VP) oriented parallel to the substrate after the appropriate thermal annealing in vacuum. The cylindrical domains in the S2VP thin film were preferentially oriented parallel to the surface of the substrate induced by the surface free energies and/or an interfacial interaction between S2VP and the substrate. In GISAXS, the structural parameters of the cylindrical domains in both the lateral and vertical directions are accessible because the diffraction spots appear with the offset in the q_y direction.

S2VP thin film (number average molecular weight M_n = 26,400, molecular weight polydispersity index = 1.24, and φ_{PS} = 76.3 vol%) was prepared by spin casting from toluene solution (10 wt%) of S2VP onto a silicon wafer substrate at 3000 rpm for 30 s. Subsequently, the S2VP thin film was thermally annealed under vacuum at 170 °C for 48 h. The sample surface was composed of PS component (X-ray photoelectron spectroscopy and water contact angle [58], predicted by surface free energies of components [59]) was a very flat and smooth examined by atomic force microscopy and optical white-light interferometer microscopy measurements.

Tender X-ray GISAXS measurement (room temperature) was performed at BL15A2 [60] at the Photon Factory, KEK, Tsukuba in Japan. The BL15A2 is an undulator beamline where X-rays in a wide energy range from 2.1 to 15 keV (energy resolution is 2×10^{-4}) is available. In this study, the energy of X-ray was set at 2.40 keV (the wavelength of 5.16 Å) and the sample-to-detector distance (SDD) was 830 ± 5 mm. The accuracy of the camera lengths arises from the scattering vector calibration on a detector with a standard specimen and a footprint of the incident beam on the sample surface (sample size of c.a.1 cm). The X-ray incident angle was varied between 0.290° and 0.620° and PILATUS 2M designed for usage in vacuum was used as a detector for the 2D scattering pattern. X-ray exposure time of 300 s was sufficient to obtain a clear scattering pattern. Hard X-ray (wavelength 1.0 Å) GISAXS measurements were performed at BL10C in Photon Factory and BL03XU57 in SPring-8, Harima, Japan using PILATUS 2M and CCD (Hamamatsu Photonics) detectors with SDD of 2.3 m. All detectors were calibrated using lead stearate prepared in-house (d = 5.01 nm, calibrated).

The X-ray penetration depth Λ is defined as the depth at which the X-ray intensity is attenuated by 1/e. The value of Λ depends on X-ray energy (wavelength λ), the critical angle, α_C, of total reflection, and the incident angle α_i. Surface roughness influences practically the penetration depth of X-rays because various α_i are provided. The roughness of the surface used here is regarded as sufficiently small to estimate the penetration depth as evidenced by the clear observation of the critical angle in XRR. Under experimental conditions with the ideally flat surface, Λ is given by

$$\Lambda = \frac{\lambda}{4\pi} \sqrt{\frac{2}{\sqrt{(\alpha_i^2 - \alpha_c^2)^2 + 4\beta^2} - (\alpha_i^2 - \alpha_c^2)}}, \tag{2}$$

where β is the imaginary part of the complex refractive index. The critical angle α_C is specified as $\alpha_C \sim \sqrt{2\delta}$ where δ is deviation from the real part of the refractive index, δ and β are given by

$$\delta = \left(r_e \lambda^2 N_A / 2\pi\right)\rho_M \sum_Z w_Z \left(f_{0Z} + f'_Z(E)\right)/ \sum_Z w_i A_Z, \tag{3}$$

$$\beta = \left(r_e \lambda^2 N_A / 2\pi\right)\rho_M \sum_Z w_Z f''_Z(E) / \sum_Z w_Z A_Z, \tag{4}$$

where r_e is the classical electron radius (2.82×10^{-5} Å), N_A is Avogadro's number, ρ_M is the mass density, w_Z is the fraction of element Z, A_Z is the relative atomic mass, f_{0Z} is the nonresonant term of the atomic scattering factor corresponding to the atomic number, and $f'_Z(E)$ and $f''_Z(E)$ are the real and imaginary parts of the anomalous dispersion for the incident X-ray energy E, respectively. For example, here we used 4.1468×10^{-5} for δ and 7.0239×10^{-7} for β of PS at 2.40 keV. The α_c value of S2VP thin film using GISAXS and XRR measurements was obtained. The calculated S2VP penetration depth is shown in **Figure 2**. It is hard to precisely control the penetration depth Λ at the nanometer scale for GISAXS experiment conducted using hard X-rays (8–12.4 keV) because the value of Λ rises steeply at α_C. On the other hand, as the X-ray energy decreases, Λ changes more gradually near the critical angle and shows decreased depth values at angles even greater than α_C. Hence, better control of Λ is expected for depth-resolved GISAXS measurements using tender X-ray (2.40 keV) because of the critical angle and attenuation coefficient values that are much greater than those for the hard X-rays.

GISAXS measurements of the S2VP thin film (thickness of 420 nm) using tender X-ray were performed at various incident angles and many Bragg spots were measured as shown for large α_i in **Figure 4**. All spots were assigned to parallel oriented hexagonally packed cylinders. GISAXS patterns at approximately q_y of 0.26 nm^{-1} are presented in **Figure 4(c)** and **(d)** and show a remarkable elongation of the Bragg spots in the q_z direction for smaller α_i. One-dimensional scattering profiles vertically cut at q_y = 0.26 nm^{-1} with various incident angles are shown in **Figure 5**. Bragg peaks were assigned to the scattering from transmitted (denoted by T) and reflected (denoted by R) beams by the substrate. These two scattering events are typically noticeable in GISAXS measurements [45, 46]. The second-order peaks derived from (11) reflection at q_z approximately 0.6 and 0.7 nm^{-1} were used for structure analysis because the primary peak from the (10) plans was partially invisible due to the detector gap. The magnitudes of the Bragg spot full widths at half maximum (FWHM) varied in the vicinity of the α_C, with larger FWHM values observed at smaller incident angles.
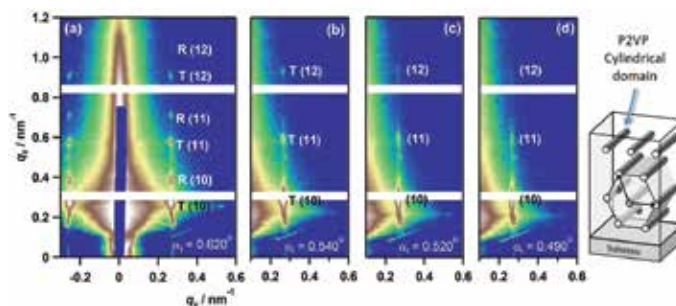
Figure 4. 2D-GISAXS (with λ of 5.166Å) patterns of S2VP-25k thin film annealed for 48 h at 170°C. (a) α_i was set at 0.62° ($\alpha_i > \alpha_C$), (b) 0.54°($\alpha_i > \alpha_C$), (c) 0.52°($\alpha_i < \alpha_C$), and (d) 0.49° ($\alpha_i > \alpha_C$). Schematic illustration represents the cross section of cylindrical microdomains in the thin film forming HEX aligned parallel to the substrate.
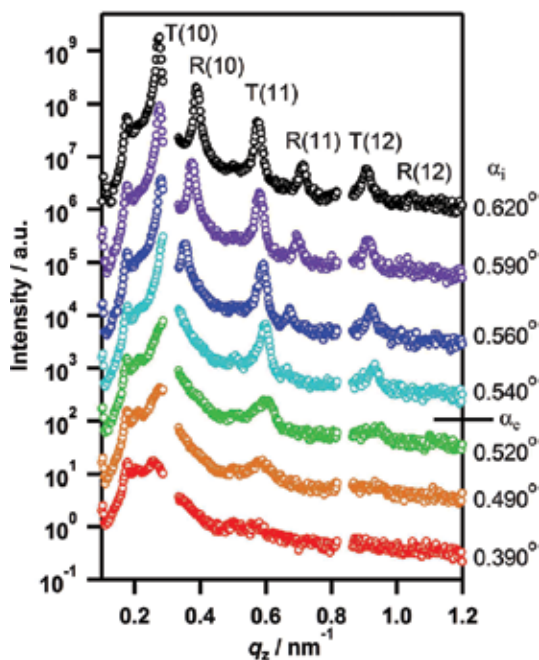

Figure 5. One-dimensional GISAXS profiles along q_z direction obtained by vertical cut at q_y = 0.26 mn^{-1}. Reprinted with permission from Saito et al. [57]. Copyright 2015 American Chemical Society.

The observed peak broadening can be interpreted by the change in the penetration depth. While generally such broadening can be understood by either the grain size effect and/or disordering of the crystal lattice, the FWHM in the q_y indicated no change irrespective of the incident angles as shown in **Figure 6**, eliminating the influence of the lattice disordering because the broadening was mainly seen in the q_z direction and the size effect was dominantly considered. Rather, the broadening in this case is because of the reduction in the size of the

observed region. The FWHM of a scattering peak depends on the grain size of a crystal, as expressed by the Laue function, $L(q)$
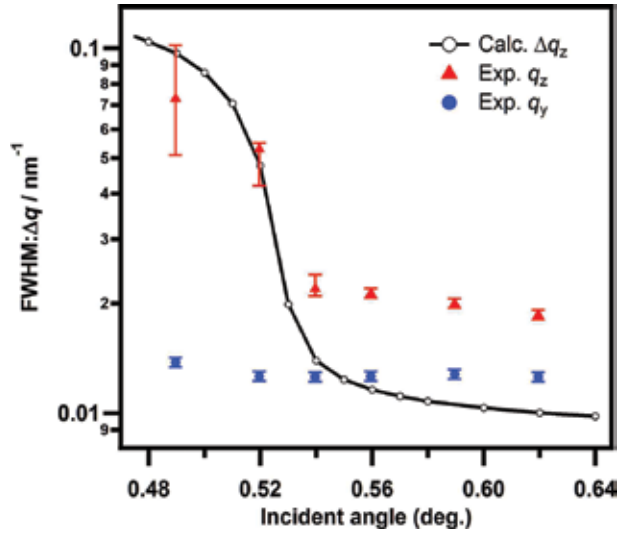

Figure 6. FWHM values of (11) Bragg spots obtained experimentally and calculated using Eq. (6). Reprinted with permission from Saito et al. [57]. Copyright 2015 American Chemical Society.

$$L\left(q_z\right) = \sum_N \exp\left(iNq_Z \cdot b\right) = \frac{\sin\left[\left(N+1\right)q_z \cdot b / 2\right]}{\sin\left[q_z \cdot b / 2\right]}, \tag{5}$$

where N is the number of the reflection plane and b is the unit lattice vector related to z-direction normal to the surface. Here, the X-ray wave decays exponentially, and considering attenuation decay, the Laue function can be re-expressed as

$$L(q_z) = \sum_N \frac{\sin[(N+1)q_z \cdot D_{01}/2]}{\sin[q_z \cdot D_{01}/2]} \exp\left[-\frac{\left(\frac{1}{2} + \frac{2}{3}N\right)D_{01}}{2\Lambda}\right], \tag{6}$$

where D_{01} is the periodicity of the (01) plane. Since the scattering intensity is proportional to the square of the Laue function, the FWHM can be calculated simply. The FWHM of the Bragg spots of the T (11) plane in q_z direction experimentally obtained is shown in **Figure 6**. The calculated values for FWHM in the q_z direction for the penetration depth Λ given by Eq. (2)

are also plotted in **Figure 6**. The change in the calculated width shows the same trend as the experimental results, indicating that the broadening of the Bragg spots can be explained by the size effect determined by the depth Λ. Thus, the observed region of GISAXS measurement can be controlled with the incident angle, enabling depth-resolved GISAXS.

When $\alpha_i < \alpha_C$, X-rays travel on the surface of the film and cannot propagate in the film. Only the evanescent wave can penetrate from the sample surface into the film. In this situation, the scattering peak α_z along the q_z direction is observed at the position given by the sum of the incident angle and the true scattering angle α_S derived from the period of the observed structure. Thus, α_s can be given as follows:

$$\alpha_S = \alpha_Z - \alpha_i \tag{7}$$

Using above relation, the true q_z value of the (11) spot can be estimated from the experimental peaks. On the other hand, in the case of $\alpha_i < \alpha_C$, an X-ray wave can travel into the film. The X-ray first refracts at the sample surface, goes through the film, is reflected by the interface between the sample and substrate, and finally exits out of the film surface with refraction as shown in **Figure 3**. Normally, some scattering events in GISAXS experiments occur because of the refracted X-rays at the polymer surface and reflected X-ray on the substrate surface, resulted in appearance of a number of scattering peaks. The scattering cross-section for GISAXS of the block copolymer thin film has been calculated within the framework of the distorted wave Born approximation (DWBA) [61]. Lee et al. [44], Yoon et al. [44, 45], and Busch et al. [46, 47] introduced the DWBA (or a combination of Bragg's and Snell's laws, refraction and reflection) to estimate the scattering peak positions. Scattering intensity due to the incident X-ray (transmission) and reflected X-ray (reflection) were pronounced. Debye-Scherrer rings of the block copolymer films with powder-like orientation of lamellar domains. The scattering peaks arising from transmitted and reflected X-rays at the substrate can be calculated following [53]

$$q_z = \frac{2\pi}{\lambda}\left[\sin\alpha_i + \left\{\sin^2\alpha_c + \left[\left\{\left(\frac{m\lambda}{D}\right)^2 - \left(\frac{q_y\lambda}{2\pi}\right)^2\right\}^{\frac{1}{2}} \mp (\sin^2\alpha_i - \sin^2\alpha_c)^{\frac{1}{2}}\right]^2\right\}^{\frac{1}{2}}\right], \tag{8}$$

where m represents the peak order, which is $3^{1/2}$ for the (11) plane in hexagonally packed cylindrical microdomains. The upper (−) and lower (+) branches in the equation indicate the Bragg diffraction of the transmitted and reflected X-rays, respectively. D is the characteristic length of the given plane. As for the (11) plane, Eq. (9) can be derived from Eq. (8) as follows:

$$q_z = \frac{2\pi}{\lambda}\left[\sin\alpha_i + \left\{\sin^2\alpha_c + \left[\frac{3\lambda}{2D} \mp (\sin^2\alpha_i - \sin^2\alpha_c)^{\frac{1}{2}}\right]^2\right\}^{\frac{1}{2}}\right], \tag{9}$$

where D corresponds to the D_{01} in this case. When the D_{01} was set to 18.8 nm, the DWBA calculation Eqs. (8) and (9) gave the best representation for all Bragg spots as shown by crosses in **Figure 7**.
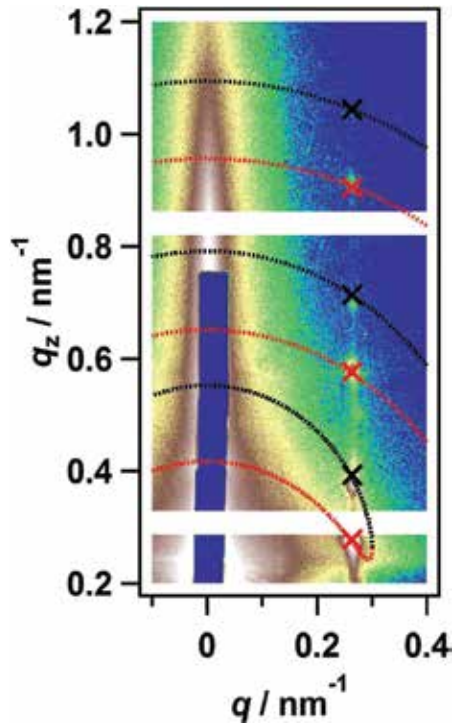

Figure 7. GISAXS patterns measured with tender X-ray (2.40 keV) at the angle of incidence 0.620. The dotted lines of the calculated Debye-Scherrer like rings from transmitted (red) and reflected (black) beams obtained using Eq. (8) as assuming the characteristic length $D_{\perp}$ (perpendicular to the surface) is smaller than the $D_{\parallel}$ (virtual parallel component). The $D_{\perp}$ corresponds to D_{01}. The crosses were obtained using Eqs. (8) and (9).

For GISAXS experiment in the soft X-ray region, the large curvature of the Ewald sphere may give rise to an apparent distortion of the GISAXS pattern when the measurements are conducted with a fixed angle of incidence and using the area 2D plane detector. Yamamoto et al. [62] discussed the effect of the Ewald sphere curvature and performed model calculations using DWBA [61]. At the lower energy of 1.77 keV, while the interparticle interference peaks extended and bent inward at large q_z, (approximately 2.0 nm⁻¹), no bending of the extended peaks was observed using hard X-rays. In the presence of the Ewald sphere curvature, the unmodified equation is no longer valid. In this study, Eq. (9) that had been developed for the hard X-ray regime to explain the experimental GISAXS pattern is confirmed to be valid for this observed q-range with tender X-ray regime 2.40 keV [57].

The lattice constant **b** associated with the direction perpendicular to the surface was slightly smaller than the lateral lattice constant **a**. The hexagonal lattice was slightly deformed, in

particular, the nanocylinders were packed into distorted hexagonal lattice that was laterally elongated and/or vertically collapsed. The distorted hexagonal lattice in polymeric films has been often observed during the drying of solvents [63]. The lattice constant remained almost constant with respect to the depth. In contrast, the constant b and the angle ϕ between the lattice vectors increased with decreasing depth, i.e., approaching the surface, the lattice deformation was relaxed to a normal hexagonal lattice (**Figure 8**).
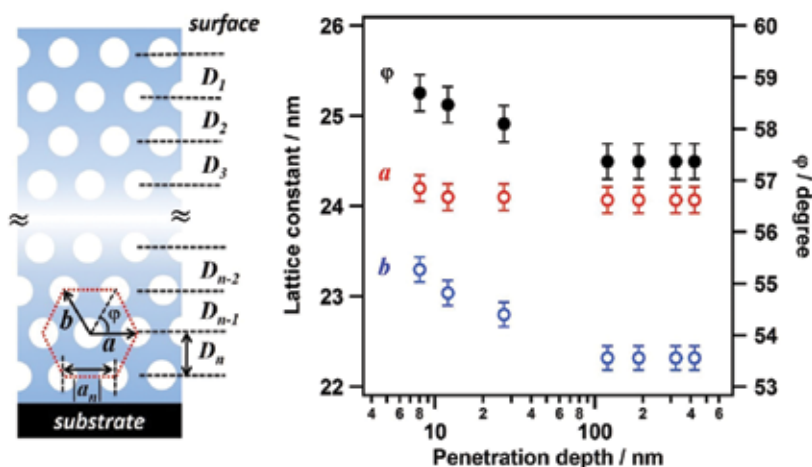

Figure 8. Lattice parameters plotted against the penetration depth (left). Right illustration indicates parallel-aligned cylindrical domains in thin film and the unit cell. The spacing D_n corresponds to the vertical distance neighboring planes (1). $|a_n|$ and $|b_n|$ represents the distance between neighboring cylindrical domains. The following relations were obtained by analysis; $D_1 > D_2 > D_3 > \cdots > D_c = \cdots = D_n$. $|a_0| = |a_1| = \cdots = |a_n|$. $|a_n| > |b_n|$. Here, D_c means D_n reached constant value. Reprinted with permission from Saito et al. [57]. Copyright 2015 American Chemical Society.

3.2. Orientation and relaxation behaviors of lamellar microdomains of poly(methyl methacrylate)-b-poly(n-butyl acrylate) thin film [64]

In this section, we investigated the phase-separation behavior of poly (methyl methacrylate-b-n-butyl acrylate) (PMMA-PnBA) forming a lamellar structure aligned parallel to the substrate after appropriate thermal annealing with GISAXS measurement. The structure development through such as degree of the lamellar orientation and relaxation of the lamellar domain spacing was inquired. Also, the GISAXS with tender X-ray for depth-sensitive analysis was conducted to reveal that the difference of the lamellar domain spacing near the surface from the bulk.

To obtain a thin film of the block copolymer PMMA-b-PnBA (M_n = 32,000, M_w/M_n = 1.17, f_{PMMA} = 0.44), PMMA-b-PnBA in toluene (5 wt% polymer solution) was prepared. The thin film was obtained by spin cast on silicon wafer at 3000 rpm for 30 s. The thin films (thickness was 280±30 nm) were dried at room temperature, subsequently thermal annealing was performed at 160° for given time. GISAXS measurement utilizing hard X-ray and tender (soft) X-ray was performed. Hard X-ray GISAXS measurement was conducted at beamlines BL6A and BL10C

in Photon Factory of KEK, Tsukuba in Japan and BL03XU in SPring-8, Hyogo in Japan [65, 66] with wavelength of 0.15 (BL6A), 0.1488 (BL10C), and 0.1 nm (BL03XU), respectively. Tender X-ray GISAXS measurement was performed at BL15A2 in Photon Factory.

2D GISAXS (hard X-ray) patterns with various annealing times were shown in **Figure 9**. The pattern of as-spun sample (**Figure 9a**) was shaped like an ellipse, which might arise from kinetically frozen or poorly ordered structure. Partially intense scattering was observed at q_z of 0.25–0.28 nm^{-1} where was emphasized due to the so-called Yoneda peak, i.e., it did not indicate specific orientation, suggesting that no orientation of phase-separated structure of PMMA-b-PnBA appeared without thermal annealing. After the sample was thermally annealed for even 1 min, the scattering intensity around $q_y = 0$ (near the beam stop) grew. In addition, two clear ring-shaped scattering patterns like Debye-Scherrer rings were observed. Each scattering ring was arising from transmitted (denoted by T) and reflected (denoted by R) beams as described in previous section. The scattering intensity near beam stop became strong with annealing time. This change in GISAXS pattern indicates the growth of the parallel orientation of the lamellar microdomain. The development of the normalized scattering intensity [64] from parallel lamellar structure is shown in **Figure 10**. Orientation is nearly complete after annealing for 60 min. The GISAXS measurement gave structure information about domain spacing of the lamellar morphology. The domain spacing (D) of the lamellar structures aligned parallel to the surface was estimated. To determine the accurate domain spacing, the distorted wave Born approximation (DWBA) was applied for analysis of the GISAXS patterns. The experimentally estimated D values are also plotted as a function of the annealing time in **Figure 10**. The value of the D approached to the D_0 of the bulk sample (independently obtained to be 21.6 nm) with an increase in annealing time. The D of the parallel orientated structure was slightly smaller than D_0 even after 4 h thermal annealing, i.e., the spacing collapsed vertically. Consequently, the lamellar structure was deformed along the depth direction (similar phenomena as the previous section). Thermal annealing induced the relaxation of the domain spacing and it seems taking approximately more than 2 h to complete the relaxation of D (equals to the value of the bulk)
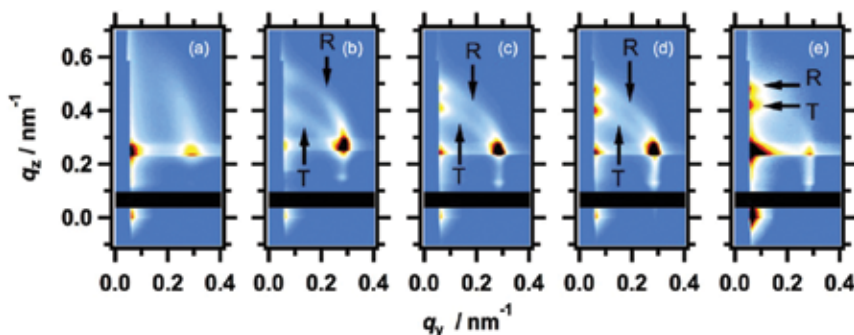

Figure 9. GISAXS patterns (hard X-ray, 1.488 Å) of PMMA-b-PnBA thin film (a) as cast and (b–e) as annealed at 160°C with given annealing time; (b) 1, (c) 3, (d) 5, and (e) 10 min. R and T denoted the scatterings from reflected and transmitted X-rays, respectively. Reprinted from Saito et al. [64]. Copyright Nature Publishing Group.
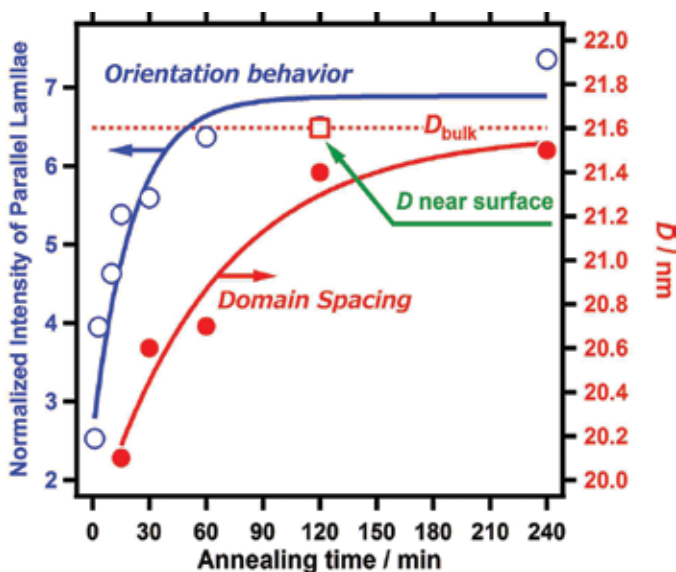
Figure 10. Time evolution of the orientation of the lamellar domain (open circles) and the relaxation of the lamellar *D* (filled circles). The solid lines were drawn as a guide to eyes. Dotted line shows the D_0 value of the bulk. Open square indicates the *D* value near the surface. Reprinted from Saito et al. [64]. Copyright Nature Publishing Group.

As is well known, preferential wetting of surface and substrate interfaces plays an important role of orientation in thin film [12, 17]. In this case, surface energies of PMMA, PnBA, and Si substrate are 41.1, 33.7, and 77.4 ± 0.5 mJ/m², respectively [16]. According to the surface free energies, it will be predicted that PMMA segregates to the surface of the silicon substrate, whereas PnBA segregates to air surface. As a result of preferential wetting, the parallel orientation of lamellar structure is induced at the surface and/or the polymer/substrate interfaces and the oriented lamellae propagate into the entire film [67]. In fact, XPS measurement proved that surface molar fractions of PnBA (within a few nanometers) were 80 mol% (repeat unit) in as-cast film and the PnBA component perfectly covered on the surface after thermal annealing with only 60 s. The segregation of each component, orientation of the lamellae, and relaxation of the domain spacing occurred in different time scale. It can be concluded that the PnBA first segregated at air surface within a minute after annealing (PMMA may segregated at the interface), second the microphase-separated structure aligned parallel to the surface, followed by relaxation of the domain spacing.

The polymer thin films have reported to have different mobility dependent on the local region, i.e., near the surface, inside, or near the polymer/substrate interface. It is quite intriguing to investigate that the depth dependence of structure difference exists, in other words, whether there are difference between the structure (orientation, morphology, d-spacing, etc.) in the vicinity of the surface and inside of the film, or not. The GISAXS measurements of PMMA-b-PnBA thin film thermally annealed for 2 h with tender X-ray was performed with various incident angles. As shown in **Figure 11(a)** and **(b)**, in the case of $\alpha_i < \alpha_c$, the scattering (marked arrows) of the lamellar structure oriented parallel to the substrate was considerably diffuse

and broaden, while in the case of $\alpha_i > \alpha_c$, the scattering became clear and sharp. The FWHM values of scattering peak (parallel lamellar domains) in the one-dimensional GISAXS profile obtained vertically cut at various incident angles can be simulated as the same manner of the size effect of measured region as discussed in the previous section (modified the Laue function). Thus, the penetration depth was controlled by changing the incident angle. At near the critical angle, the surface-sensitive measurement is possible as predicted from Eq. (2). The true q_z value of the oriented lamellar structure parallel to the substrate is estimated using the experimentally observed peaks, i.e. D near the surface can be estimated. At α_i of 0.525° (penetration depth Λ of 32.4 nm), D was obtained to be 21.6 nm which is equal to the D_0 value (21.6 nm) of the bulk sample. The value of D near the surface is slightly larger than the value 21.4 nm obtained from DWBA calculation (inside the whole film). This means that relaxation of the domain spacing near the film surface preceded that of the inside. According to previous reports, polymer chain near the surface indicates higher mobility (lower glass transition temperature or viscosity) [68–70]. Moreover, the lamellar structure started to orient from both the air/polymer and polymer/substrate interfaces, which was induced by segregation of one component in the BCP. Therefore, that the faster relaxation of the D of the lamellar structure near the surface was caused by the faster orientation and higher mobility in the vicinity of the surface.
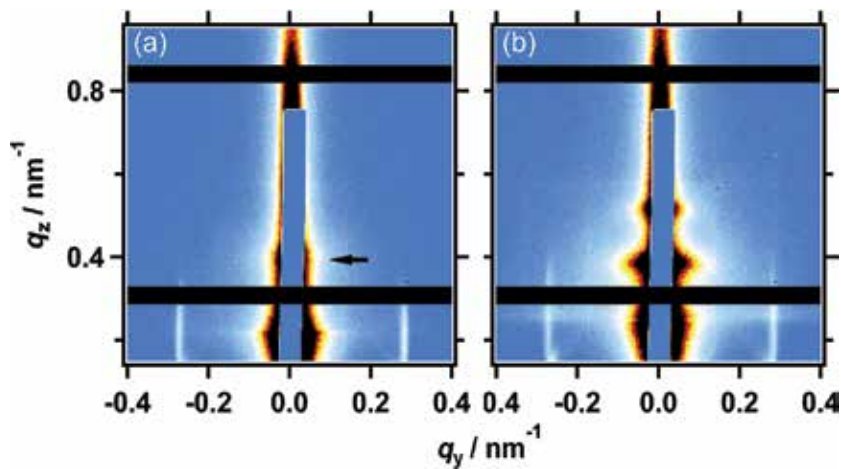

Figure 11. Tender X-ray (2.40 keV) GISAXS patterns of PMMA-b-PnBA thin films annealed at 160 °C for 2 hours at incident angles (a) 0.525° and (b) 0.625°. Reprinted from Saito et al. [64]. Copyright Nature Publishing Group.

3.3. Evaluation of mesogen orientation in thin films of polyacrylate with cyanobiphenyl side chain [71]

Understanding the orientation behavior of polymer chain in the vicinity of interfaces (both substrate and free surfaces) is of practical importance in organic thin film technologies such as coating and photoresisting processes. Thus, a large amount of fundamental knowledge has been ever accumulated. It has been broadly recognized that diverse physical properties of

polymeric materials in ultrathin film state are very different from those in the bulk state. Compared with the vast amount of studies for amorphous and crystalline (LC) polymers, studies on the anomaly in structure and orientation of side chain liquid crystalline polymers in ultrathin film states are rather unexplored. A large number of data related to mesogen orientation have been reported [72–78]. Accordingly, the side chain LC polymers are mostly aligned homeotropically [23, 79–81] The significant effect of the sample surface is apparent from the fact that the mesogen orientation changes to a planer orientation as the sample surface is covered by another layer or material [23, 82–84]. A cyanobiphenyl(CB)-containing polymethacrylate (PCBMA) exceptionally indicated the planar orientation regardless of the fact that the homologous polyacrylate (PCBA) oriented homeotropically [33]. This unexpected orientation behavior is responsible for the difference in the main chain rigidity (but still no rational explanation). In these contexts, the investigation to reveal in detail the orientation of PCBA is proceeded by the GISAXS measurements by systematically changing the film thickness. Additionally, GISAXS with hard (8.05 keV) and tender (2.30 keV) X-rays were carried out.

The side chain LC polymer PCBA (chemical structure shown in **Figure 12**, M_n = 12,000, M_w/M_n = 1.83, glassy state – 13°C (T_g: glass-transition temperature)–smectic A - 95°C (T_i: isotropization temperature)) films on quartz plates were prepared by spin-casting from 0.12–3.0 wt % chloroform solutions to make different thickness samples. The spin-cast film samples were annealed at 135 °C, cooled to a target temperature, kept for 10 min, and then subjected to the measurements. The layer spacing of the smectic A of LC polymers in the bulk was estimated to be 4.6 nm (SAXS). GI-SAXS experiments with hard X-rays (Cu Kα radiation (λ = 0.154 nm)) were conducted with a FR-E X-ray diffractometer equipped with two-dimensional imaging plate R-AXIS IV detector (Rigaku). GI-SAXS experiments using low-energy X-rays were performed at BL-15A2 [60] at the Photon Factory, KEK, Tsukuba, Japan. Experimental details of the GI-SAXS measurements were described in previous sections.
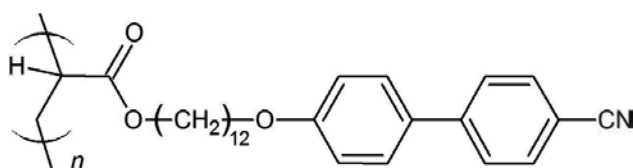

Figure 12. Chemical structure of the side chain LC polymer.

Figure 13 indicates GI-SAXS data measured with hard X-rays (λ = 0.154 nm) for 30 nm thick at 80 °C. For 140 nm thick film, the scattering peaks corresponding to d (smectic layer) = 4.6 nm (100) and 2.3 nm (200) were clearly seen in both out-of-plane and in-plane directions. The intensity of the peaks in the out-of-plane direction was significantly small in 30 nm thick film (as peaks was weakly shown in 1D profile), and no peaks were essentially recognized for 15 nm thick film, although those in the in-plane direction were clearly seen. These results evidently indicate the coexistent of planarly and homeotropically oriented CB in the films with film thickness greater than 30 nm, and that the CB mesogens were oriented only planarly at 15 nm thickness.
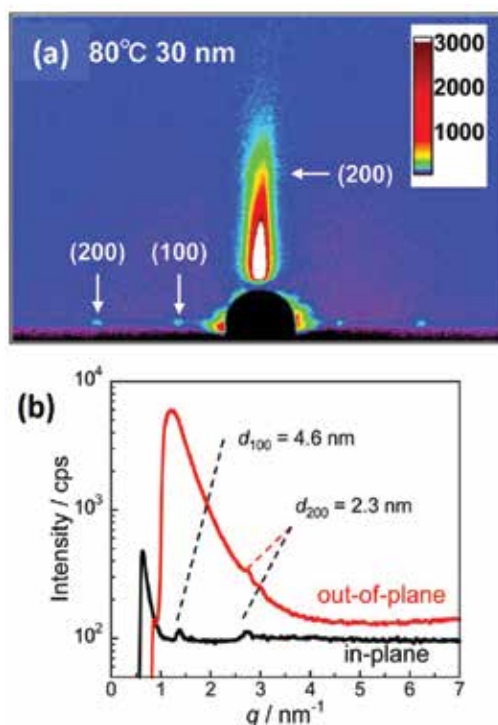
Figure 13. 2D GI-SAXS (Cu Kα) patterns (a) of PCBA films with a thickness of 30 nm at 80 °C. Lower figure (b) indicates 1D intensity profiles (black: in-plane; red: out-of-plane directions). Reprinted with permission from Tanaka et al. [71]. Copyright 2016 American Chemical Society.

GI-SAXS measurements with synchrotron tender X-rays ($\lambda = 0.539$ nm, 2.30 keV) were achieved at various α_i. **Figure 14** shows the 2D GI-SAXS images for 30 nm thick film at room temperature. The CB mesogens at this thickness as mentioned before are oriented both in the homeotropic and planar directions (coexistence). The α_c in this sample was estimated at about 0.54° for this X-ray energy. Under conditions of $\alpha_i < \alpha_c$ (α_c is about 0.54° for 2.30 keV), the scattering signals in the thin film was observed only the out-of-plane direction as shown in **Figure 14a** and **b**, where Λ is estimated as in the range less than 10–20 nm in these experimental conditions. It is apparently indicated that the CB mesogens adopt homeotropic orientation in the free surface region. When $\alpha_i > \alpha_c$, the out-of-plane scatterings were split into double peaks in the q_z direction as shown in **Figure 14c–e**. The split double peaks originate from the transmitted X-ray through the film and then reflected on the substrate [44]. Hence, the high q_z peak of the double peaks can be assigned to the scattering from the reflection path on the film surface. The split spots means that the X-ray beam actually travelled through the overall film thickness and reached the sample/substrate interface. When $\alpha_i > \alpha_c$ ($\Lambda > 100$ nm), the peaks appeared in-plane direction due to the planar orientation were clearly observed as shown in **Figure 14d–f** with arrows. These signals undoubtedly originate from the mesogens near the polymer/substrate interface.
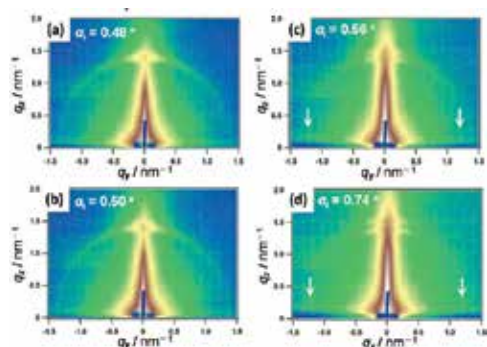
Figure 14. Two-dimensional GI-SAXS patterns for PCBA thin film with 30 nm thickness using tender X-rays (0.539 nm). Measurements were conducted at α_i = 0.48 (Λ = 11 nm) (a), 0.50 (Λ = 16 nm) (b), 0.56 (Λ = 167 nm) (c), 0.74 (Λ = 453 nm), and (d). Note that α_c (0.54°) is positioned between (b) and (c). Reprinted with permission from Tanaka et al. [71]. Copyright 2016 American Chemical Society.

From the overall data of UV-vis absorption spectroscopic [71] and the GISAXS measurements utilizing hard and tender X-rays, the orientation structural models of CB mesogens in PCBA thin films are schematically illustrated in **Figure 15**. In thick films with 140 nm, the CB mesogens are almost aligned homeotropically. However, a considerable number of the CB mesogens planarly anchored exist near the substrate (polymer/substrate interface) as revealed by GI-SAXS measurements with hard X-rays (**Figure 13**). At a thickness of 30 nm, the amounts of homeotropically and planarly oriented CB mesogens is comparable, where depth-resolved information is obtained by GI-SAXS with tender X-ray experiments (**Figure 14**). In the film thickness of 10–15 nm, the CB mesogens adopt almost planar alignment. When the film becomes further thinner from the critical level of 7 nm, the planar alignment near the surface disappears where the liquid crystal structuring (antiparallel packing of the CB mesogens) is lost.

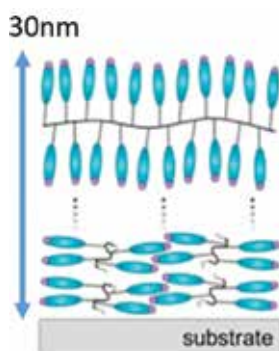**Figure 15.** Schematic illustration of orientation of the CB mesogens in films with film thickness 30 nm. Purple circles indicate the cyano group at the terminal of mesogen. Note that the antiparallel interactions (LC structuring) are kept among the CB mesogens at thickness above 10–15 nm. Such LC structuring is lost at thickness of 7 nm. Reprinted with permission from Tanaka et al. [71]. Copyright 2016 American Chemical Society.

4. Grazing-incidence resonant soft X-ray scattering [50]

The GI-RSoXS is a novel technique, which is in particular suited for more complex system such as multicomponent block copolymer and polymer blend films. Resonant soft X-ray scattering has already been successful for probing morphology and spatial structure in organic photo-voltaic (OPV) systems [85, 86] and triblock copolymer system [87]. GI-RSoXS allows for detecting near surface and inner structure separately at fixed incident angle by tuning X-ray photon energy because the penetration depth of the X-ray beam is drastically affected by the change in X-ray photon energy across the adsorption edge. Adsorption K edge for organic materials composed of mainly carbon, nitrogen, and oxygen are 284, 409, and 543 eV. The fine structure of the adsorption edge can be utilized in GISAXS measurements. Near edge X-ray adsorption fine structure (NEXAFS) spectrum needs to be probed for the polymeric materials in order to estimate the complex refractive index of X-ray that becomes important for depth-sensitive and component sensitive analyses. Typically, the NEXAFS spectra of polymers, which have low contrast in the real part of the refractive index in the hard photon energy regime, indicate considerable differences in the soft X-ray regime. In this section, investigation of nanostructure in the polymer blend thin film, poly(3-hexylthiophene) (P3HT) and poly[5-(2-ethylhexyloxy)-2-methoxycyanoterephtalylidene] (MEH-CN-PPV), is introduced as an example of GI-RSoXS experiment carried out by Ruderer et al. [50].

GI-RSoXS measurements with soft X-ray were conducted at the synchrotron beamline 11.0.1.2 of the advanced light source (ALS) at the LBNL in Berkeley (USA) [88, 89]. Due to the high adsorption of soft X-ray in air, full setup (sample and X-ray detector) was kept in high vacuum. The energy of X-ray was used in the range of 280–320 eV (λ: 4.4–3.9 nm). Sample-to-detector was 18.5 cm that was sufficient for detecting length scale in the range from 21 nm to a few micron meters. An incident angle $\alpha_i = 2°$, which is near the critical angle α_C of 2.3° for 280eV and 1.5° for 283 eV. The both polymers (P3HT and MEH-CN-PPV) were dissolved in chloro-form. The thin film of polymer blend was prepared by spin coating from the solution; the thickness was controlled to be about 70 nm. The films were annealed at 200 °C for 10 min in air without degradation. The NEXAFS spectroscopy measurement was conducted for taking the wavelength dependent refractive index ($n = 1 − \delta + i\beta$) of polymers used here for electro-magnetic radiation near the adsorption edge. NEAXFS spectra were also obtained at the same beam line of the ALS. The sample environment is identical to the GI-RSoXS setup. The polymer thin films were prepared on silicon nitride membranes and measured in transmission geom-etry. The adsorption part β of the refractive index was obtained through Beer's law. The real part δ of the refractive index was calculated from the β using Kramers-Krongis relation.

Figure 16a shows the X-ray energy dependence of the dispersion δ and the adsorption β of P3HT and MEH-CN-PPV homopolymer. The spectra of respective homo polymers are different. NEXAFS spectra of the blend system with different blend ratio can be obtained by a linear superposition of the spectra of P3HT and MEH-CN-PPV homopolymer weighted with the corresponding blend ratio. The dispersion δ spectra of P3HT and MEH-CN-PPV reveal positive and negative values and differ strongly depending X-ray energy. Therefore, the scattering contrast depends on the X-ray energy. Using the adsorption β spectra, the

penetration depth Λ of the soft X-rays into the blend film is calculated as shown in **Figure 16b**. **Figure 17** indicates the GI-RSoXS patterns of as spun P3HT/MEH-CN-PPV bulk heterojunction films with a P3HT content of 70 wt% for different energies from 280 to 289 eV (wavelength of X-rays from 4.43 to 4.29 nm). Although the wavelength is varied by only 3%, the scattering patterns significantly change. For energy below 284 eV, an intensity oscillation in vertical direction is observed, which comes from the correlated roughness originating from the interference of scattered X-rays from different interfaces. The correlated roughness vanishes with increasing energies of the X-rays. It indicates no scattering signal from the substrate interface is detected and X-ray penetrates near the surface as shown in **Figure 17**. The low scattering intensity of GI-RSoXS at 284 eV (**Figure 17c**) is due to the very low incident intensity at this energy. The reduction of the intensity at 286 eV (**Figure 17e**) can be ascribed to the significant low contrast between P3HT and MEH-CN-PPV at this energy. Thus, the surface structure is accessible at 286 eV. The change in the total scattered intensity was attributed to the changed contrast conditions from the contrast variation.

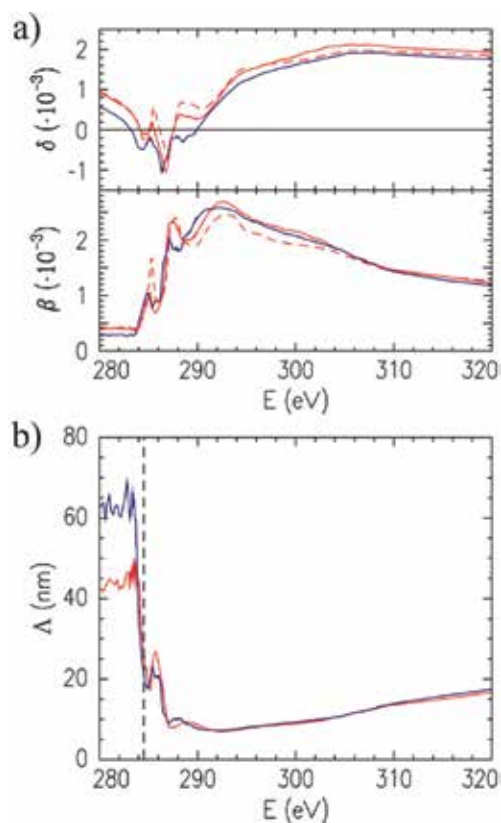**Figure 16.** (a)Dispersion δ and the absorption β of P3HT (red solid lines) and MEH-CN-PPV (blue solid lines) as a function of the X-ray energy. For comparison, the calibrated P3HT spectra (dashed lines) from the database [90] are drawn. (b) Penetration depth of X-ray of P3HT (red) and MEH-CN-PPV (blue) as a function of X-ray energy. Reprinted with permission from Ruderer et al. [50]. Copyright 2016 American Chemical Society.
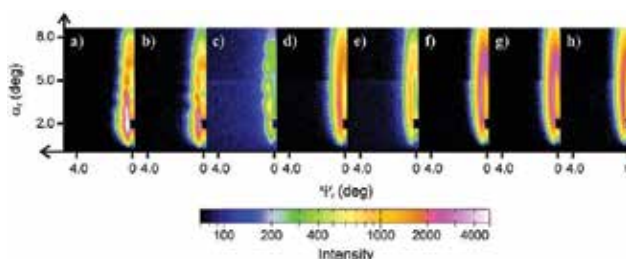
Figure 17. Two-dimensional GI-RSoXS patterns of as-spun P3HT: MEH-CN-PPV film with a P3HT content of 70 wt% with different X-ray energies. The X-ray energy: (a) 282, (b) 283, (c) 284, (d) 285, (e) 286, (f) 287, (g) 288, and (h) 289 eV. Copyright American Chemical Society, Ruderer et al. [50].

Author details

Katsuhiro Yamamoto

Address all correspondence to: yamamoto.katsuhiro@nitech.ac.jp

Department of Life Science and Applied Chemistry, Frontier Research Institute for Materials Science, Field of Soft Materials, Graduate School of Engineering, Nagoya Institute of Technology, Nagoya, Japan

References

[1] Zhang, Q.; Cirpan, A.; Russell, T. P.; Emrick, T. Donor-acceptor poly (thiophene-block-perylene diimide) copolymers: synthesis and solar cell fabrication. Macromolecules. 2009;42:1079–1082.

[2] Sun, S. S.; Zhang, C.; Ledbetter, A.; Choi, S.; Seo, K.; Bonner, C. E. Jr; Dress, M; Sariciftchi, N. S. Photovoltaic enhancement of organic solar cells by a bridged donor-acceptor block copolymer approach. Appl. Phys. Lett. 2007;90:043117.

[3] Crossland, E. J. W.; Kamperman, M.; Nedelcu, M.; Ducati, C.; Wiesner, U.; Smilges, D.-M.; Toombes, G. E. S.; Hilmyer, M. A.; Ludwigs, S.; Steiner, U.; Naith, H. J. A bicontinuous double gyroid hybrid solar cell. Nano Lett. 2008;9:2807–2812.

[4] Singh, G.; Yager, K.; Berry, B.; Kim, H.-C.; Karim, A. Dynamic thermal field-induced. ACS Nano. 2012;6:10335–10342.

[5] Luo, Y.; Montarnal, D.; Kim, S.; Shi, W.; Barteau, K. P.; Pester, C. W.; Hustad, P. D.; Christianson, M. D.; Fredrickson, G. H.; Kramer, E. J.; Hawker, C. J. Poly(dimethylsi-

loxane-b-methyl methacrylate): a promising candidate for sub-10 nm patterning. Macromolecules. 2015;48:3422–3430.

[6] Gu, W.; Zhao, H.; Wei, Q.; Coughlin, E. B.; Theato, P.; Russell, T. P. Line patterns from cylinder-forming photocleavable block copolymers. Adv. Mater. 2013;25:4690–4695.

[7] Wan, L.-S.; Li, J.-W.; Ke, B.-B.; Xu, Z.-K. Ordered microporous membranes template by breath figures for size-selective separation. J. Am. Chem. Soc. 2012;134:95098.

[8] Jeong, U.; Ryu, D. Y.; Kim, J. K.; Kim, D. H.; Wu, X.; Russell, T. P. Precise control of nanopore size in thin film using mixtures of asymmetric block copolymer and homo-polymer. Macromoelcules. 2003;36:10126–10129.

[9] Matsen, M. W.; Schick, M. Stable and unstable phases of a diblock copolymer melt. Phys. Rev. Lett. 1994;72:2660–2663.

[10] Stein, G. E.; Kramer, E. J.; Li, X.; Wang, J. Layering transitions in thin films of spheri-cal-domain block copolymers. Macromolecules. 2007;40:2453–2460.

[11] Suh, H. S.; Kang, H.; Nealey, P. F.; Char, K. Thickness dependence of neutral parame-ter windows for perpendicularly oriented block copolymer thin films. Macromole-cules. 2010;43:4744–4751.

[12] Albert, J.; Epps, T. H. Self-assembly of block copolymer thin films. Mater. Today. 2010;13:24–44.

[13] Jung, J.; Park, H. W.; Lee, S.; Lee, H.; Chang, T.; Matsunaga, T.; Jinnai, H. Effect of film thickness on the phase behaviors of diblock copolymer thin film. ACS Nano. 2010;4:3109–3116.

[14] Luo, M.; Seppala, J. E.; Albert, J. N. L.; Lewis, R.; Mahadevapuram, N.; Stein, G. E.; Epps, T. H. Manipulating nanoscale morphologies in cylinder-forming poly (styrene-b-isoprene-b-styrene) thin films using film thickness and substrate surface chemistry gradient. Macromolecules. 2013;45:1803–1811.

[15] Kim, S. O.; Solak, H. H.; Stoykovich, M. P.; Ferrier, N. J.; Pablo, J. J.; Nealey, P. F. Epi-taxial self-assembly of block copolymers on lithographically defined nanopatterned substrates. Nature. 2003;424:411–414.

[16] Shelton, C. K.; Epps, T. H. Decoupling substrate surface interactions in block polymer thin film self-assembly. Macromolecules. 2015;48:4572–4580.

[17] Mansky, P.; Liu, Y.; Huang, E.; Russell, T. P.; Hawker, C. Controlling polymer-surface interactions with random copolymer brushes. Science. 1997;275:1458–1460.

[18] Park, S.; Lee, D. H.; Xu, J.; Kim, B.; Hong, S. W.; Jeong, U.; Xu, T.; Russell, T. P.. Macro-scopic 10-terabit–per–square-inch arrays from block copolymers with lateral order. Science. 2009;323:1030–1033.

[19] Sivaniah, E.; Hayashi, Y.; Iino, M.; Hashimoto, T.; Fukunaga, K. Observation of per-pendicular orientation in symmetric diblock copolymer thin films on rough substrates. Macromolecules. 2003;36:5894–5896.

[20] Qiang, Z.; Zhang, L.; Stein, G. E.; Cavicchi, K. A.; Vogt, B. D. Macromolecules. Unidir-ectional Alignment of Block Copolymer Films Induced by Expansion of a Permeable Elastomer during Solvent Vapor Annealing. 2014;47:1109–1116.

[21] Xu, T.; Zvelindovsky, A. V.; Sevink, G. J. A.; Lyakhova, K. S.; Jinnai, H.; Russell, T. P. Electric field alignment of asymmetric diblock copolymer thin films. Macromolecules. 2005;38:10788–10798.

[22] Gopinadhan, M.; Majewski, P. W.; Osuji, C. O. Macromolecules. 2010;43:3286–3293.

[23] Fukuhara, K.; Nagano, S.; Hara, M.; Seki, T. Free-surface molecular command. Nat. Commun. 2014;5:3320.

[24] Sano, M.; Nakamura, S.; Hara, M.; Nagano, S.; Shinohara, Y.; Amemiya, Y.; Seki, T. Pathways toward photoinduced alignment switching in liquid crystalline block copolymer films. Macromolecules. 2014;47:7178–7186.

[25] Cui, G.; Ohya, S.; Matsutani, T.; Nagano, S.; Dohi, T.; Nakamura, S.; Sakurai, S.; Miyazaki, T.; Yamamoto, K. Perpendicular orientation of sub-10 nm channels in polystyrene-b-poly(4-hydroxyl styrene)/PEG oligomer blend thin films. Nanoscale. 2013;5:6713–6719.

[26] Gu, W.; Xu, J.; Kim, J.-K.; Hong, S. W.; Wei, X.; Yang, X.; Lee, K. Y.; Kuo, D. S.; Xiao, S.; Russell, T. P. Solvent-assisted directed self-assembly of spherical microdomain block copolymers to high areal density arrays. Adv. Mater. 2013;25:3677–3682.

[27] Kim, S. H.; Misner, M. J.; Yang, L.; Gang, O.; Ocko, B. M.; Russell, T. P. Salt complexation in block copolymer thin films. Macromolecules. 2013;39:8473–8479.

[28] Jeong, J. W.; Park, W. I.; Kim, M.-J.; Ross, C. A.; Jung, Y. S. Highly tunable self-assembled nanostructures from a poly(2-vinylpyridine-b-dimethylsiloxane) block copolymer. Nano Lett. 2011;11:4095–4101.

[29] Park, S.; Wang, J.-Y.; Kim, B.; Xu, J.; Russell, T. P. A simple route to highly oriented and ordered nanoporous block copolymer templates. ACS Nano. 2008;2:766–772.

[30] She, M.-S.; Lo, T.-Y.; Ho, R.-M. Long-range ordering of block copolymer cylinders driven by combining thermal annealing and substrate functionalization. ACS Nano. 2013;7:2000–2011.

[31] Tang, C.; Wu, W.; Smilgies, D. M.; Matyjaszewski, K.; Kowalewski, T. J. Am. Chem. Soc. Robust Control of Microdomain Orientation in Thin Films of Block Copolymers by Zone Casting. 2011;133:11802–11809.

[32] De Rosa, C.; Park, C.; Thomas, E. L.; Lotz, B. Nature. Microdomain patterns from directional eutectic solidification and epitaxy. 2000;405:433–437.

[33] Reiter, G.; Castelein, G.; Hoerner, P.; Riess, G.; Blumen, A.; Sommer, J. U. Phys. Rev. Lett. Nanometer-Scale Surface Patterns with Long-Range Order Created by Crystallization of Diblock Copolymers. 1999;83:3844–3847.

[34] Niihara, K.; Matsuwaki, U.; Torikai, N.; Atarashi, H.; Tanaka, K.; Jinnai, H. Macromolecules. A Novel Structural Analysis for a Cylinder-Forming Block Copolymer Thin Film Using Neutron Reflectivity Aided by Transmission Electron Microtomography. 2007;40:6940–6946.

[35] Yokoyama, H.; Kramer, E. J.; Rafailovich, M. H.; Sokolov, J.; Schwarz, S. A. Macromolecules. Structure and Diffusion of Asymmetric Diblock Copolymers in Thin Films: A Dynamic Secondary Ion Mass Spectrometry Study. 1998;31:8826–8830.

[36] Ninomiya, S.; Ichiki, K.; Yamada, H.; Nakata, Y.; Seki, T.; Aoki, T.; Matsuo, J. Rapid Commun. Mass Spectrom. 2009;23:1601.

[37] Terlier, T.; Tiron, R.; Gharbi, A.; Chevalier, X.; Veillerot, M.; Martinez, E.; Barnes, J. P. Surf. Interface Anal. 2014;46:83–91.

[38] Gilbert, J. B.; Rubner, M. F.; Cohen, R. E. Proc. Natl. Acad. Sci. U. S. A. 2013;110:6651–6656.

[39] Gilbert, J. B.; Luo, M.; Shelton, C. K.; Rubner, M. F.; Cohen, R. E.; Epps, T. H. III . ACS Nano. 2015;9:512–520.

[40] Mayes, A. M.; Russell, T. P.; Bassereau, P.; Baker, S. M.; Smith G. S. Macromolecules. 1994;27:749–755.

[41] Koneripalli, N.; Singh, N.; Levicky, R.; Bates, F. S.; Gallagher, P. D.; Satija, K. Macromolecules. 1995;28:2897–2904.

[42] Müller-Buschbaum, P. Anal. Bioanal. Chem. 2003;376:3–10.

[43] Roth, S. V.; Burghammer, M.; Riekel, C.; Bushbaum, P. M. Appl. Phys. Lett. 2003;82:1935–1937.

[44] Lee, B.; Park, I.; Yoon, J.; Park, S.; Kim, J.; Kim, K. W.; Chang, T.; Ree, M.. Macromolecules. 2005;38:4311–4323.

[45] Yoon, J.; Yang, S. Y.; Lee, B.; Joo, W.; Heo, K.; Kim, J. K.; Ree, M. J. Appl. Crystallogr. 2007;40:305–312.

[46] Busch, P.; Smilgies, D. M.; Rauscher, M.; Posselt, D.; Papadakis, C. M. J. Appl. Crystallogr. 2006;39:433–442.

[47] Busch, P.; Posselt, D.; Smilgies, D. M.; Rauscher, M.; Papadakis, C. M. Macromolecules. 2007;40:630–640.

[48] Okuda, H.; Takeshita, K.; Ochiai, S.; Sakurai, S.; Kitajima, Y. J. Appl. Crystallogr. 2011;44:380–384.

[49] Wernecke, J.; Okuda, H.; Ogawa, H.; Siewert, F.; Krumrey, M. Macromolecules. 2014;47:5719–5727.

[50] Ruderer, M. A.; Wang, C.; Schaible, E.; Hexemer, A.; Xu, T.; Müller-Buschbaum, P. Macromolecules. 2013;46:4491–4501.

[51] Müler-Buschbaum, P.; Maurer, E.; Bauer, E.; Cubitt, R. Langmuir. 2006;22:9295–9303.

[52] Müller-Buschbaum, P.; Schulz, L.; Metwalli, E.; Moulin, J.-F.; Cubitt, R. Langmuir. 2009;25:4235–4242.

[53] Busch, P.; Rauscher, M.; Moulin, J.-F.; Müller-Buschbaum, P. J. Appl. Crystallogr. 2011;44:370–379.

[54] Müller-Buschbaum, P.; Schulz, L.; Metwalli, E.; Moulin, J.-F.; Cubitt, R. Langmuir. 2008;24:7638–7644.

[55] Müller-Buschbaum, P.; Kaune, G.; Haese-Seiller, M.; Moulin, J.-F. J. Appl. Crystallogr. 2014;47:1228–1237.

[56] Müller-Buschbaum P. Grazing incidence small-angle neutron scattering: challenges and possibilities. Polymer J. 2013;45:34–42. DOI: 0.1038/pj.2012.190

[57] Saito, I.; Miyazaki, T.; Yamamoto, K. Depth-resolved structure analysis of cylindrical microdomain in block copolymer thin film by grazing-incidence small-angle X-ray scattering utilizing low-energy X-rays. Macromolecules. 2015;48:8190–8196. DOI: 10.1021/acs.macromol.5b01883

[58] Yin, J.; Yao, X.; Liou, J.-Y.; Sun, W.; Sun, Y.-S.; Wang, Y. ACS Nano. 2013;7:9961–9974.

[59] Kim, J.; Lew, B.; Kim, W. S. Nanoscale Res. Lett. 2011;6:616.

[60] Photon-Factory KEK. BL-15A2: High-brilliance Small-Angle X-ray Scattering beamline [Internet]. Available from: http://pfwww.kek.jp/saxs/beamline/bl15a2.html

[61] Sinha, S. K.; Sirota, E. B.; Garoff, S. Phys. Rev. B: Condens. Matter. Mater. Phys. X-ray and neutron scattering from rough surfaces. 1988;38:2297–2311.

[62] Yamamoto, T.; Okuda, H.; Takeshita, K.; Usami, N.; Kitajima, Y.; Ogawa, H. J. Synchrotron Radiat. Grazing-incidence small-angle X-ray scattering from Ge nanodots self-organized on Si(001) examined with soft X-rays. 2014;21:161–164.

[63] Tokarev, I.; Krenek, R.; Burkov, Y.; Schmeisser, D.; Sidorenko, A.; Minko, S.; Stamm, M. Macromolecules. Microphase Separation in Thin Films of Poly(styrene-block-4-vinylpyridine) Copolymer−2-(4′-Hydroxybenzeneazo)benzoic Acid Assembly. 2005;38:507−516.

[64] Saito, I.; Shimada, D.; Aikawa, M.; Miyazaki, T.; Shimokita, K.; Takagi, H.; Yamamoto, K. Orientation and relaxation behaviors of lamellar microdomains of poly(methyl methacrylate)-b-poly(n-butyl acrylate) thin films as revealed by grazing-incidence small-angle X-ray scattering. Polymer J. 2016;48:399–406. DOI: 10.1038/pj.2016.2

[65] Ogawa, H.; Masunaga, H.; Sasaki, S.; Goto, S.; Tanaka, T.; Seike, T.; Takahashi, S.; Takeshita, K.; Nariyama, N.; Ohashi, H.; Ohata, T.; Furukawa, Y.; Matsushita, T.; Ishizawa, Y.; Yagi, N.; Takata, M.; Kitamura, H.; Takahara, A.; Sakurai, K.; Tashiro, K.; Kanaya, T.; Amemiya, Y.; Horie, K.; Takenaka, M.; Jinnai, H.; Okuda, H.; Akiba, I.; Takahashi, I.; Yamamoto, K.; Hikosaka, M.; Sakurai, S.; Shinohara, Y.; Sugihara, Y.; Okada, A. Experimental station for multiscale surface structural analyses of oft-material films at SPring-8 via a GISWAX/GIXD/XR-integrated system. Polymer J. 2012;45:109–116.

[66] Masunaga, H.; Ogawa, H.; Takano, T.; Sasaki, S.; Goto, S.; Tanaka, T.; Seike, T.; Takahashi, S.; Takeshita, K.; Nariyama, N.; Ohashi, H.; Ohata, T.; Furukawa, Y.; Matsushita, T.; Ishizawa, Y.; Yagi, N.; Takata, M.; Kitamura, H.; Sakurai, K.; Tashiro, K.; Takahara, A.; Amamiya, Y.; Horie, K.; Takenaka, M.; Kanaya, T.; Jinnai, H.; Okuda, H.; Akiba, I.; Takahashi, I.; Yamamoto, K.; Hikosaka, M.; Sakurai, S.; Shinohara, Y.; Okada, A.; Sugihara, Y. Multipurpose soft-material SAXS/WAXS/GISAXS beamline at SPring-8. Polymer J. 2011;43:471–477.

[67] Russell, T. P.; Coulon, G.; Deline, V. R.; Miller, D. C. Characteristics of the surface-induced orientation for symmetric diblock PS/PMMA copolymers. Macromolecules. 1989;22:4600–4604.

[68] Kawaguchi, D.; Tanaka, K.; Kajiyama, T.; Takahara, A.; Tasaki, S. Mobility gradient in surface region of monodisperse polystyrene films. Macromolecules. 2003;36:1235–1240.

[69] Kajiyama, T.; Tanaka, K.; Takahara, A. Depth dependence of the surface glass transition temperature of a poly (styrene-block-methyl methacrylate) diblock copolymer film on the basis of temperature-dependent x-ray photoelectron spectroscopy. Macromolecules. 1995;28:3482–3484.

[70] Inoue, R.; Kawashima, K.; Matsui, K.; Nakamura, M. Interfacial properties of polystyrene thin films as revealed by neutron reflectivity. Phys. Rev. E. 2011;84:031802.

[71] Tanaka, D.; Mizuno, T.; Hara, M.; Nagano, S.; Saito, I.; Yamamoto, K.; Seki, T. Evaluations of mesogen orientation in thin films of polyacrylate with cyanobiphenyl side chain. Langmuir. 2016;32:3737–3745. DOI: 10.1021/acs.langmuir.6b00538

[72] Henn, G.; Stamm, M.; Poths, H.; Rücker, M.; Rabe, J. P. Influence of order in thin smectic polymer films on the structure at the surface. Phys. B. 1966;221:174–184.

[73] Mensinger, H.; Stamm, M.; Boeffel, C. Order in thin films of a liquid crystalline polymer. J. Chem. Phys. 1992;96:3183–3190.

[74] Elben, H.; Strobl, G.. Smectic surface structures in the isotropic phase of liquid-crystalline polymers studied by x-ray reflectivity. Macromolecules. 1993;26:1013–1018.

[75] van der Wielen, M. W. J.; Cohen Stuart, M. A.; Fleer, G. J.; de Boer, D. K. G.; Leenaers, A. J. G.; Nieuwhof, R. P.; Marcelis, A. T. M.; Sudhölter, E. J. R. Order in thin films of side-chain liquid-crystalline polymers. Langmuir. 1997;13:4762–4766.

[76] van der Wielen, M. W. J.; Cohen Stuart, M. A.; Fleer, G. J. Autophobicity and layering behavior of thin liquid-crystalline polymer films. Langmuir. 1998;14:7065–7071.

[77] Wu, J.-S.; Fasolka, M. J.; Hammond, P. T. Mixed surface morphologies of well-defined smectic diblock copolymer ultrathin films. Macromolecules. 2000;33. DOI: 1108-1110

[78] Morikawa, Y.; Nagano, S.; Watanabe, K.; Kamata, K.; Iyoda, T.; Seki, T. Optical alignment and patterning of nanoscale microdomains in a block copolymer thin film. Adv. Mater. 2006;18:883–886.

[79] Uekusa, T.; Nagano, S.; Seki, T. Highly ordered in-plane photoalignment attained by the brush architecture of liquid crystalline azobenzene polymer. Macromolecules. 2009;42:312–318.

[80] Haque, H. A.; Kakehi, S.; Hara, M.; Nagano, S.; Seki, T. High density liquid-crystal-line azobenzene polymer brush attained by surface-initiated ring-opening metathesis polymerization. Langmuir. 2013;29:7571–7575.

[81] Asaoka, S.; Uekusa, T.; Tokimori, H.; Komura, M.; Iyoda, T.; Yamada, T.; Yoshida, H. Normally oriented cylindrical nanostructures in amphiphilic PEO–LC diblock co-polymers films. Macromolecules. 2011;44:7645–7658.

[82] Fukuhara, K.; Fujii, Y.; Nagashima, Y.; Hara, M.; Nagano, S.; Seki, T. Liquid-crystal-line polymer and block copolymer domain alignment controlled by free-surface seg-regation. Angew. Chem. Int. Ed. 2013;52:5988–5991.

[83] Komura, M.; Yoshitake, A.; Komiyama, H.; Iyoda, T. Control of air-interface-induced perpendicular nanocylinder orientation in liquid crystal block copolymer films by a surface-covering method. Macromolecules. 2015;48:672–678.

[84] Tanaka, D.; Nagashima, Y.; Hara, M.; Nagano, S.; Seki, T. Alternation of side-chain mesogen orientation caused by the backbone structure in liquid-crystalline polymer thin films. Langmuir. 2015;31:11379–11383.

[85] Swaraj, S.; Wang, C.; Yan, H.; Watts, B.; Lüning, J.; McNeill, C. R.; Ade, H. Nano Lett. Nanomorphology of Bulk Heterojunction Photovoltaic Thin Films Probed with Reso-nant Soft X-ray Scattering. 2010;10:2863–2869.

[86] Chen, W.; Xu, T.; He, F.; Wang, W.; Wang, C.; Strzalka, J.; Liu, Y.; Wen, J.; Miller, D. J.; Chen, J.; Hong, K.; Yu, L.; Darling, S. B. Nano Lett. Hierarchical Nanomorphologies Promote Exciton Dissociation in Polymer/Fullerene Bulk Heterojunction Solar Cells. 2011;11:3707–3713.

[87] Wang, C.; Lee, D. H.; Hexamer, A.; Kim, M. I.; Zhao, W.; Hasegawa, H.; Ade, H.; Russell, T. P. Nano Lett. Defining the Nanostructured Morphology of Triblock Copolymers Using Resonant Soft X-ray Scattering. 2011;11:3906–3911.

[88] Wang, C.; Hexemer, A.; Nasiatka, J.; Chan, E. R.; Young, A. T.; Padmore, H. A.; Schlotter, W. F.; Lüning, J.; Swaraj, S.; Watts, B.; Gann, E.; Yan, H.; Ade, H. IOP Conf. Ser.: Mater. Sci. Eng. Resonant Soft X-ray Scattering of Polymers with a 2D Detector: Initial Results and System Developments at the Advanced Light Source. 2010;14:012016.

[89] Gann, E.; Young, A. T.; Collins, B. A.; Yan, H.; Nasiatka, J.; Padmore, H. A.; Ade, H.; Hexemer, A.; Wang, C. Rev. Sci. Instrum. Soft x-ray scattering facility at the Advanced Light Source with real-time data processing and analysis. 2012;83:045110.

[90] Watts, B.; Swaraj, S.; Nordlund, D.; Lüning, J.; Ade, H. J. Chem. Phys. Calibrated NEXAFS spectra of common conjugated polymers. 2011;134:024702.

Microfluidics for Small-Angle X-ray Scattering

Serena A.J. Watkin, Timothy M. Ryan,

Antonia G. Miller, Volker M. Nock,

F. Grant Pearce and Renwick C.J. Dobson

Additional information is available at the end of the chapter

Abstract

Small-angle X-ray scattering is a well-established biophysical technique, whilst microfluidics is proving to be a convenient technology for creating miniaturised multifunctional devices. Both fields are highly versatile and find use in multiple scientific disciplines. Together, they offer the potential to obtain structural information on biomacromolecules, nanoparticles and condensed matter, in a high-throughput manner and with enhanced time-resolution capabilities. This chapter provides practical design considerations for X-ray-based microfluidic systems and examines some of the existing microfluidic platforms used in conjunction with small-angle X-ray scattering. As the exclusive advantages of microfluidics become recognised and accessible, the prevalence of microfluidic sample environments in X-ray scattering measurements will hopefully increase.

Keywords: microfluidics, high throughput, time-resolved SAXS, continuous flow, laminar flow, hydrodynamic focusing, turbulent mixing, structural biology

1. Introduction

1.1. Principles and potential of microfluidics

The interdisciplinary field of microfluidics encompasses the science and technology underlying the development of devices that process and manipulate small volumes of fluids within micron-scale channels. A microfluidic 'chip', so-called because its fabrication method was adapted from that used to manufacture computer microchips [1], can be designed with interconnected networks of channels and chambers. These designs can integrate a range of

functions on a single, microsized 'lab-on-a-chip' device, also known as a 'micro total analysis system' (µTAS). Along with the ready possibility of automation and potential for high-throughput screening that microfluidics presents, other general benefits of scaling down include lower sample consumption and consequently lower cost. In addition, microfluidic devices offer precise control over fluid flow and mixing, shorter processing times and hence more rapid results. Accordingly, the technology of microfluidics is influencing many areas of science, from materials to microbiology.

1.1.1. Physics of fluid flow on the microscale

In contrast to fluids moving in large channels, which mix turbulently, a key property of fluid flow in microchannels is that it is laminar. Laminar flow occurs in smooth parallel streams with no significant mixing between streams other than by diffusion [2]. This is a result of the ratio of inertial to viscous forces, described by the Reynolds number (*Re*), which for small channel dimensions is low, meaning that viscous forces dominate. The Reynolds number is defined by

$$Re = \frac{\rho v w}{\mu} \qquad (1)$$

where ρ is the fluid density, v is the flow velocity, w is the characteristic dimension of the flow geometry and μ is the fluid viscosity [3]. A *Re* of <1–100 corresponds to pure laminar flow, whilst a Re of >1000–2000 is approaching turbulent flow. The low Reynolds number flow property of microchannels can be exploited, but is not ideally suited to all applications.

1.2. The combination of microfluidics and small-angle X-ray scattering

Small-angle X-ray scattering (SAXS) is a valuable and versatile technique. SAXS is utilised by biochemists and material physicists alike, providing both quantitative and qualitative structural information about biomacromolecules, nanoparticles and condensed matter [4–13]. In structural biology, although SAXS is unable to afford atomic resolution, it serves as a complementary technique to X-ray crystallography and nuclear magnetic resonance (NMR) and compensates for limitations of these techniques, by enabling structural parameters to be determined in biologically relevant solutions, without the size restriction typically imposed by NMR and with no requirement for extrinsic biomolecule labelling or crystals. Further, SAXS allows the characterisation of conformational changes, dynamics and interactions of biomolecules in response to different experimental conditions, which makes it ideally suited to monitoring important biochemical events, such as protein folding, ligand binding and association/dissociation reactions.

1.2.1. Why incorporate microfluidics into SAXS?

SAXS already involves the manipulation of relatively small volumes of fluid; however, the typical solution sample environment for SAXS is based on thin-walled quartz capillaries. These offer a convenient method to acquire SAXS data on solutions, but they do have a number of

restrictions. Microfluidic devices offer the opportunity to develop customised systems with the flexibility to enable advanced sample handling, such as concentrating, diluting, mixing and filtering, in line with the SAXS measurement. Unsurprisingly, given its broadly applicable advantages, microfluidics has been incorporated into several other techniques in assorted scientific fields and within structural biology, including for screening of protein crystallisation conditions, for a closely related technique, X-ray crystallography [14], and with few perceivable disadvantages, the question really becomes, why not SAXS? Indeed, several groups have already recognised the potential benefits and taken advantage of microfluidics, successfully demonstrating its use with SAXS for studying a diverse variety of specialised systems [12], including the assembly of biomacromolecules such as intermediate filaments [15] and silk fibres [16]; the growth of gold nanoparticles [17]; the rheology of complex fluids, such as liquid crystals [18, 19] and wormlike micelles [20]; as well as numerous studies on protein [21–29] and RNA folding [30, 31]. Perhaps the most obvious, more general advantage that microfluidics can offer SAXS, as it has offered many other techniques, is the potential to provide automated, high-throughput platforms which minimise sample consumption and shorten measurement times whilst maintaining a high level of accuracy and reproducibility, and researchers have begun to lay the groundwork for devices of this type [32–34].

1.2.2. What makes microfluidics particularly well-suited to SAXS?

Several fundamental aspects of these technologies are exceptionally compatible. First, the size of the X-ray beam relative to the size of the channels within a microfluidic chip is quite comparable. Thus beam is not being used to measure extraneous material, and conversely, all of the sample molecules are in the beam interaction volume. Therefore the sample is providing the optimal amount of signal, without being wasted. Second, the continuous flow typical within these systems mitigates radiation damage to samples, improving the reliability and data quality obtainable from SAXS measurements. Moreover, the high-throughput potential mentioned above is especially important for synchrotron-based techniques such as SAXS, where the experiment time is often limited, as a microfluidic sample-handling platform could help to ensure maximum use of the allocated beam time [33, 35]. This is what prompted Lafleur et al. and, very recently, Schwemmer et al., to develop their respective microfluidic high-throughput sample-handling environments [33, 34], which will be discussed. Microfluidics also offers the opportunity to extend the time-resolution capability of SAXS. Various groups have demonstrated the possibility to study reaction kinetics of protein and RNA folding events or complex fluids, using alternative microfluidic approaches to prevail over commercially available stopped-flow devices which fall short of the requisite microsecond time range, and this will be covered in the latter part of this chapter.

2. Incorporating microfluidics into SAXS

In the first part of this section, some general design considerations for microfluidic systems in the context of SAXS will be discussed. In subsequent sections, existing examples of microfluidic chips and how they have been applied using SAXS in order to increase either the throughput

or the time resolution will be examined. As well as providing some background and giving an overview of the current status of the field, it is hoped that this chapter will contain practical information for those looking to realise the benefits of incorporating microfluidic technology into SAXS.

2.1. Design considerations for SAXS microfluidic systems

Whilst the specifications of the system will differ depending on the particular application, some generally applicable guidelines are given here, supplemented with specific examples. As for any analytical microfluidic setup, there are three main aspects of the system which need to be considered: (i) the design and fabrication of the microfluidic chip itself, (ii) the sample delivery system and method of fluid control and (iii) integration with the experimental apparatus, in this case, the SAXS beamline (although the possibility of an on-chip X-ray source has been envisaged [36]). Each aspect will be discussed separately here whilst bearing in mind that these aspects are all interrelated and will have certain SAXS-specific requirements that differ from other light-based detection methods.

2.1.1. Chip design and fabrication

The first key consideration regarding the microfluidic chip is the choice of material, the properties of which, in this case, must be compatible with X-rays. The possibilities will be further narrowed down by practical considerations specific to the particular application, e.g. if high flow rates are required for mixing or time-resolution purposes, the chip material and bonding must be robust enough to withstand the subsequent high pressure generated, without deformation of the microchannels [20, 27]. Cost, both in terms of fabrication time and resources, will also likely factor into material choice, and the type of material will dictate the method of fabrication, which may be limited by available facilities. Microfabrication does require some special equipment and sometimes a clean room, commonplace in a nanofabrication facility, but not found in the average biochemistry lab. If access to the necessary facilities is not available, there are several microfluidic manufacturing companies offering custom microfabrication services.

Microfluidic chips were originally manufactured from silicon using standard photolithography and often bonded to glass, which is not an ideal window material for SAXS [36]. The first microfluidic device used in conjunction with SAXS comprised a silicon chip and silicon nitride windows [21], but in more recent times, silicon has been exchanged for synthetic polymer materials, such as thermoplastics, e.g. polymethyl methacrylate (PMMA), or the silicone elastomer, polydimethylsiloxane (PDMS). The latter is cast from a replication master mould, which can be fabricated using similar lithographic techniques, whilst the former can be fabricated by a range of micromachining methods (milling, electric discharge, laser ablation) and templating techniques (thermoforming, transfer moulding). Both options are cheaper than silicon chips and highly flexible in terms of the possible channel geometries.

Unfortunately, there are two major limitations of PDMS for microfluidic SAXS devices: its low X-ray transparency [36] and its low X-ray endurance—continuous X-ray exposure rapidly

deteriorates this material [20]. Nevertheless, PDMS can be utilised for channel structures, as long as appropriate X-ray compatible material is chosen for sample observation windows, as Dootz et al. demonstrated [19]. As another example, Stehle et al. used a PDMS chip for a microfluidic droplet-forming module, separate from the thin-walled glass capillary used for SAXS detection [12]. The large dead volumes that are introduced *via* the connecting tubing in this system are the disadvantage of this approach. PDMS also finds use in other constituents of a microfluidic system, as its elasticity and adhesive properties render it useful for valves and seals [33].

Kapton (polyimide) has commonly been used for X-ray-related applications due to its high X-ray resistance and low X-ray absorption [19]. However, in a qualitative assessment of the suitability of various polymer materials for SAXS microfluidic chips by Toft et al., the SAXS profile obtained from a 100 μm thick Kapton foil revealed a diffuse diffraction peak that occurs at in the middle of biologically relevant q-ranges [32]. Given that biological scattering is relatively weak, this feature was suggested to perhaps cause issues with background subtraction [32]. In spite of this, Barrett et al. have fabricated a microfluidic device out of two 150 μm thick Kapton films bonded together, using laser ablation techniques to produce the channels, whilst Graceffa et al. used Kapton windows for their stainless steel turbulent-flow mixing chip [27], as did Dootz et al. for their PDMS chip [19].

Greaves and Manz deemed polycarbonate (PC) to be the best chip-building material in terms of X-ray transmission, with PMMA a close second [36]; however, PC and PMMA were rated poorly by Toft et al., in terms of X-ray endurance and cleaning, and PC was also judged as poor for bonding and machinability, although both materials display low small-angle X-ray scattering [32]. Ultimately, polystyrene (PS) was the polymer of choice for Toft et al., meeting all the criteria for their 'BioXTAS' chip [32, 33], whilst Lafleur et al. selected PMMA for a mixing attachment containing rotary valves by virtue of its superior machinability [33]. Combinations of different plastics have also been demonstrated successfully by Møller et al., who used a PMMA substrate with PS windows, developing a strong PS to PMMA bonding procedure for this design [37].

A second, crucial consideration relating to SAXS chip design concerns the size of the sample detection compartments versus the size of the X-ray beam. For maximum signal, the depth of the sample compartment should be as close to the optimal pathlength as practically possible. The scattering volume and the beam energy both factor into determining the optimum pathlength. Conversely, using smaller compartments results in lower sample consumption. A finite constraint is that the dimensions of the beam must be smaller than the dimensions of the channel or chamber to minimise background intensity resulting from X-ray interaction with the substrate wall, and the X-ray focusing or slitting down ability and resultant flux of individual beamlines will set a lower limit on these dimensions. It is important to note that the beam dimension under consideration is the total beam width, as opposed to the commonly defined full width at half maximum, as the weak outer beam background will still cause parasitic scattering from the chip which will affect data quality. Thus the design must be optimised to the expected beam dimensions and balance signal requirements against sample consumption.

2.1.2. Sample input and fluidic control

For continuous flow systems, fluid delivery *via* pumps would ideally be controlled remotely by software, so as to facilitate fast sample turnover time and minimise the need to access the beamline hutch, thereby increasing the efficiency of the experimental procedure. This is essential for time-resolved measurements, where data acquisition must be initiated immediately after sample mixing. Toft et al. developed software to couple control of commercial syringe pumps delivering samples and buffer to the chip with the beamline shutter system, thereby coordinating sample preparation and data collection [32], whilst Lafleur et al. developed both the software and hardware, including the individually controlled syringe pumps used in conjunction with integrated rotary valves, for their next-generation setup [33]. For stopped-flow systems, sample introduction to the chip and any on-chip processes such as mixing, diluting could be done prior to chip introduction to the beamline, provided that time-resolved data are not required. Alternatively, Schwemmer et al. eliminate the need for pumps and tubing altogether (along with any associated plumbing problems) by depositing samples directly into reservoirs on their 'LabDisk' using regular pipettes. This keeps all fluids confined entirely to the chip and relies on centrifugal forces to transport fluids through the mixing channels, though this does require a custom-built processing device to spin the disk at preset rotational frequencies [34].

2.1.3. Interfacing to a SAXS beamline

Once the chip is fabricated and fluidic control is established, the final considerations to complete the microfluidic SAXS experimental setup and ensure optimal ease of use involve appropriate interfacing to the beamline. This may require some adjustments to the conventional beamline setup to accommodate the microfluidic system. At a minimum, a chip holder, which allows for any necessary inlet and outlet tubing connecting to the fluid delivery system, is needed for stable attachment to an adjustable stage (ideally motor-controlled) to facilitate precise alignment with the X-ray beam. More advanced chip holder designs have included a borescope or camera for sample visualisation and to assist with chip positioning [34, 37]. For the best-quality data, the beamline setup should ensure a vacuum along the complete X-ray flight path, from synchrotron to microfluidic sample chip to detector to avoid air scatter, and contain a minimum of extra window components to reduce background intensity [34]. Temperature control is another important consideration, particularly for unstable biological samples, and has been achieved *via* a channel in the chip holder through which a cooled solution can be passed [37].

2.2. Microfluidics for high-throughput SAXS sample handling

Prior to the development of sample-changing robots at synchrotron SAXS beamlines, loading samples by hand was a tedious and time-consuming process, especially with the necessary sample cell cleaning and drying steps between each sample [35]. This motivated Toft et al. to develop a microfluidic front end, the BioXTAS chip, along with software for external control of the syringe pumps regulating fluid flow through the chip [32]. At the time, this was a considerable improvement upon manual sample handling, with the added benefit of elimi-

nating the inherent human error associated with sample preparation, such as that of a dilution series, which is generally still a manual task, at present. The first-generation BioXTAS chip (**Figure 1A**) contained four fluidic inlets, providing the option to utilise up to three different solutions that are premixed prior to merging with the sample solution, an extended serpentine mixing channel in which homogenous mixing of sample and buffer solutions occurs *via* diffusion, with the mixing ratio determined by the flow rate, and a 200 nl sample chamber, where the sample is exposed to the X-ray beam and scattering data is collected whilst flow is stopped [32]. In this setup, samples are stored in syringes connected to the chip by a 30 cm length of tubing which requires 150 µl of solution to fill, and following a 15 min pressure-equilibration period, 6 min is required to fill the sample chamber, at a flow rate of 6 µl/min [32]. Consequently, whilst only 36 µl of sample is consumed per measurement, and reasonable quality data has been shown from a mere 200 nl sample volume (of 1–10 mg/ml protein), unfortunately this sample economy is compromised by the dead volume contained in the syringe and tubing, as well as by the pressure-equilibration time. Although the stopped flow during data collection strategy contributes to low sample consumption, it does increase the susceptibility of the sample to radiation damage, particularly with long exposure times. Nevertheless, this BioXTAS chip represents a respectable first proof of concept of a microfluidic alternative for SAXS sample handling and has subsequently been utilised for a study on the oligomeric state of cancer-related protein, as further demonstration of its practicality and promise [37].
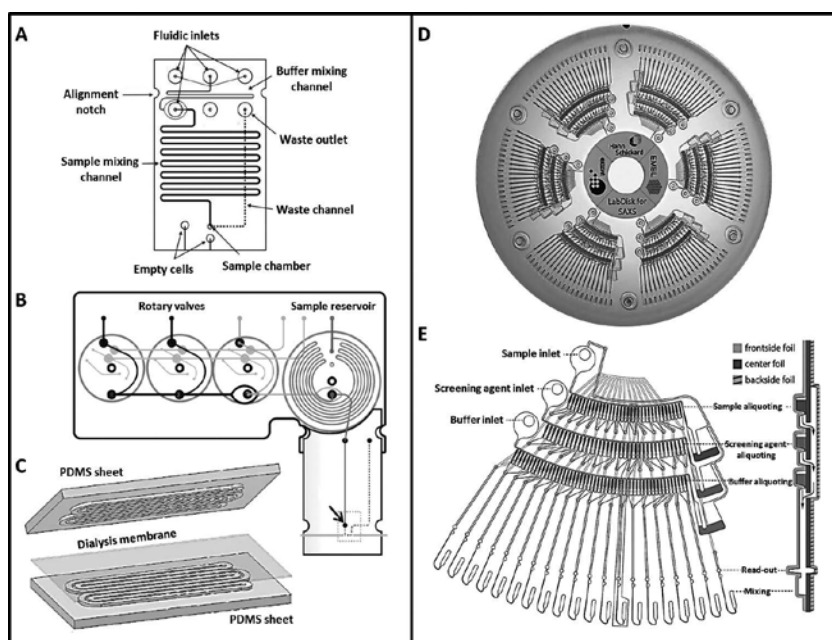

Figure 1. Microfluidic answers to the demand for automated, high-throughput, low consumption sample-handling systems for SAXS. (A–C) The BioXTAS chip by Toft et al. [32] and additions by Lafleur et al. [33] and Skou et al. (2014) [38]. (D and E) The LabDisk for SAXS by Schwemmer et al. [34]. See text for details.

The first-generation BioXTAS chip was subsequently developed to incorporate an additional mixing module (**Figure 1B**), which contains an on-chip sample reservoir and motor-controlled rotary valves to enable more precise fluidic control, in addition to integrated UV absorbance detection capabilities by means of optical fibres built into the separate sample detection chip, enabling UV absorbance measurements to be acquired concurrently with scattering data [33]. The option for data acquisition in continuous flow mode, which would reduce radiation damage, albeit at the expense of sample consumption, is made available in the custom-developed control software [33]. With much shorter exposure times on a more powerful X-ray source and a faster flow rate, the complete experimental cycle time (including cleaning) was considerably reduced from 28 to 3 min whilst consuming slightly less sample than for the first-generation chip [32, 33]. The on-chip sample reservoir does enable a reduction in the dead volume of the system, although external syringe pumps and associated tubing are still required to supply the buffers and pressure on the protein sample, so in order to take full advantage of the on-chip reservoir to minimise the sample volume, the suggestion is made to use an immiscible fluid to supply the necessary volume in the tubing syringe for injecting the sample [33].

Related to this idea of introducing a second fluid phase is the droplet-based microfluidic approach, in which discrete droplets of one liquid are generated, dispersed in and carried by a second, immiscible fluid within a microchannel [12]. These microdroplets can be used to compartmentalise samples, which can then be manipulated as individual vessels: for sorting, splitting, merging and even for performing chemical or biological assays [12]. The usefulness of this approach in association with SAXS was demonstrated by Stehle et al., who used it to analyse gold nanoparticles encapsulated by water droplets dispersed in oil, with each SAXS measurement comprising data averaged from ~ 9000 droplets, over a 15 min period [12]. In view of the available sample-changing robots, which have similar sample requirements and low dead volumes and perform all of the necessary cleaning in a fully automated fashion, distinct advantages of microfluidic devices for SAXS may have thus far been unclear, whereas discrete droplet formation is an example of an exclusive capability of microfluidic approaches which highlights the versatile possibilities created by this technology and which the standard SAXS setups lack. Another example is provided by Skou et al., who adjusted the second-generation BioXTAS design to incorporate a sample dialysis chip, comprising two PDMS sheets: one which contains channels for a polyethylene glycol (PEG) solution and the other which contains channels for the protein sample solution and a dialysis membrane sandwiched in-between (**Figure 1C**) [38]. When utilised with SAXS, this additional microfluidic module offers the unique ability to gradually concentrate protein samples as structural information is continually acquired, to reveal changes in protein oligomeric state and detect concentration-induced protein aggregation early in the experiment. Alternatively, if a different buffer is used instead of a PEG solution, the device can be used to monitor the effect of different experimental conditions, such as a change in ionic strength or pH, during buffer exchange [38]. Further advanced sample-handling features envisaged for microfluidic SAXS include on-chip size exclusion chromatography [32].

Although the BioXTAS chip readily facilitates mixing of multiple solutions with small volumes of a single sample and prepares dilutions with ease (simply by varying the flow rate), in order to properly meet the high-throughput objective, the BioXTAS system would require further development to increase its sample capacity or the means to enable easy and rapid sample changing, to bring it up to par with current autosampler robots. Schwemmer et al. presented an innovative centrifugal microfluidic platform, 'LabDisk for SAXS', which overcomes some of the shortcomings of the BioXTAS system by having six sample modules on a single chip (**Figure 1D**), each containing on-chip reservoirs for sample, buffer and screening agents and requiring only 2.5–3.5 μl of solution, with dead volumes of just over 1 μl, which is the allowance for pipetting errors and guaranteeing complete filling of channels and chambers [34]. The sophisticated fluidic geometry (**Figure 1E**) enables aliquoting and mixing of fixed combina-tions of protein, buffer and screening agents, simultaneously generating 15 different sample conditions and the five corresponding buffer solutions for background subtraction, with a high degree of accuracy and precision, in under 5 min [34]. Short (20 × 50 ms) exposures make for fast readouts, with the experimental time currently limited by manual positioning of the measurement chambers in the X-ray beam, although this is expected to be automated in due course [34]. Higher noise in the data collected on the LabDisk than the conventional sample changer is attributed to factors relating to the air gap in which the LabDisk is operated, which results in higher background, as well as the shorter pathlength of the measurement chamber and smaller X-ray beam, which result in lower signal [34]. Owing to the relatively low signal of biomolecules, composed of light, weakly scattering atoms, the background subtraction, which accounts for both the solvent and the instrumentation, needs to be carried out as precisely as practically possible. As such, the use of the same sample compartment for both sample and background measurements is considered important, to avoid introducing anoma-lies due to subtle differences in sample cell [35]. However, the LabDisk has separate readout chambers for samples and buffers, which has potential to cause issues with background subtraction.

2.3. Microfluidics for time-resolved SAXS

The suitability of microfluidic devices for time-resolved studies was recognised early on in the rise of microfluidics, and it has played a key role in increasing the time resolution attainable by SAXS. Whilst stopped-flow techniques have been extensively used for time-resolved SAXS studies, predominantly of protein folding [39–45], since Moody et al. reported the first device used in conjunction with SAXS in 1980 [46] and stopped-flow apparatus specifically for SAXS are commercially available [13], these have only been able to achieve dead times of 0.5 ms at best. Microfluidics offers the potential to extend the accessible time resolution of SAXS to the microsecond time range; however, rapid mixing, which is a crucial requirement, is the challenge, due to the low Reynolds number flow in microchannels.

The two main microfluidic approaches are both continuous flow-based techniques but differ in their mixing strategy; the turbulent-flow approach aims to generate high Reynolds number flow in microchannels, whilst the laminar-flow approach utilises the inherent low Reynolds number flow. The common underlying principle is that data collected at different distance

points along an observation channel after mixing correspond to different time points over the course of the reaction, with the flow velocity determining the temporal resolution. This approach has been coupled with various techniques, such as circular dichroism and fluorescence spectroscopy [29], but with SAXS, the radius of gyration represents an easily determined parameter which can be monitored, whilst the data also provide low-resolution structural information, making it useful for monitoring structural changes such as folding, oligomerization and ligand-induced rearrangements. As previously mentioned, continuous flow offers the SAXS-specific advantage of lower radiation damage but disadvantage of higher sample consumption, particularly at the high flow rates required for the turbulent mixing approach.

Rapid turbulent mixing in a multicapillary device was pioneered by Regenfuss et al. [47], who credits Moskowitz and Bowman [48], and this idea has since been developed by several groups, with various devices emerging [49, 50], including microfabricated versions of the original capillary-based mixer [51, 52]. The 'T-mixer' produced by Takahashi et al. [51] (**Figure 2A**) was subsequently utilised with SAXS to study the folding dynamics of various proteins [23–26, 31], achieving dead times as low as 160 µs [23]. The T-shaped geometry of this microfluidic device forces two solutions flowing at high velocities to meet at a junction and change direction, resulting in rapid mixing, before being transported through to the observation channel, where measurements are obtained [51]. Bilsel et al. advanced this design by altering the angle of the input channels such that they form an arrow-shaped junction (**Figure 2A** inset), which forces the two fluids to undergo a greater change in momentum, theoretically giving rise to more efficient mixing [52]. Using a device of this type, with channel widths of 75 µm, at a flow rate of 10 ml/min, the Reynolds number is calculated to be 2000, and the mixing time was demonstrated to be ~50 µs [52]. For time-resolved SAXS studies of protein folding, the dimensions of the observation channel were increased to 100 µm wide by 400 µm deep to increase the signal to noise, whilst the width of the input channels and mixing region was 30 µm, resulting in a dead time of ~100 µs at flow rates of 10–20 ml/min [27] (**Figure 2B**). Whilst these microfluidic setups are impressive in terms of the time resolution they can achieve, their major drawback is the large sample quantities necessitated by the high flow rates.

The laminar-flow-based rapid-mixing approach, introduced by Knight et al. in 1998, is referred to as 'hydrodynamic focusing' [53]. This approach relies solely on diffusive mixing, without introducing turbulence, taking advantage of the natural mixing process in microfluidic chips that function at low Reynolds numbers. For the hydrodynamic focusing geometry, two input fluids approach a central input fluid from either side, squeezing the central fluid into a thin, focused stream, across which diffusion occurs on a relatively short timescale [21, 53]. SAXS investigations of protein and RNA folding have subsequently been carried out using this type of device [21, 22, 30], achieving a minimum dead time of 240 µs [22]. This is a significant improvement on stopped-flow devices, but has not been improved further to match turbulent-flow mixers, at least, not in combination with SAXS. The hydrodynamic focusing approach for time-resolved SAXS is substantially limited by the size of the X-ray beam, as in order to access shorter timescales, the focused stream must be made even narrower; however, without the matching ability to adequately focus the X-ray beam, the system will suffer from low signal to noise. To complicate matters further, even if the beamline optics allow adequate microfocus-

sing, radiation damage to the slowly flowing sample becomes a particularly severe issue. Hydrodynamic focusing has been used with alternative detection methods [54], which have been able to accomplish mixing times as short as 10 μs [55], demonstrating the potential of this microfluidic approach for time-resolved measurements and providing incentive to work towards optimising optical designs of future SAXS beamline setups to overcome current technical barriers and take full advantage of it.
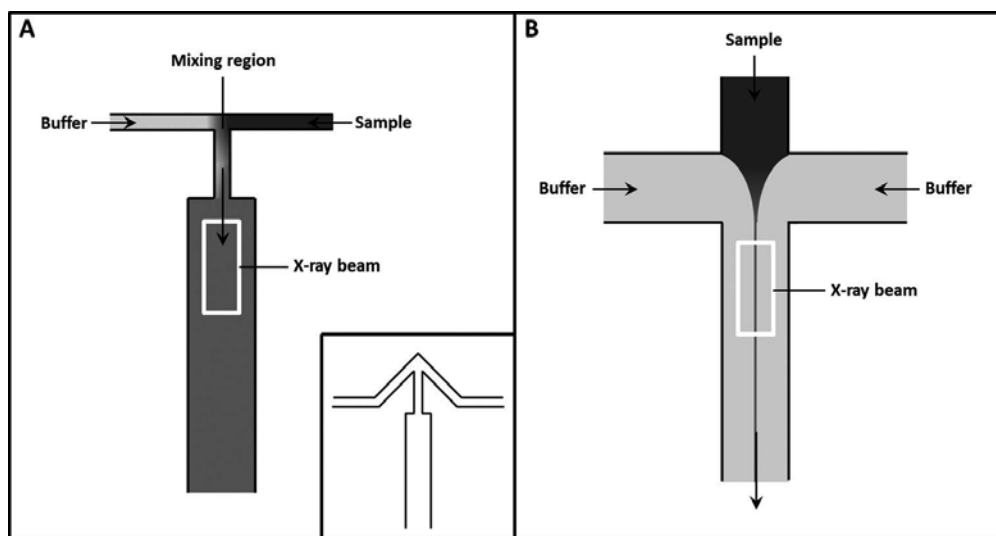

Figure 2. Two alternative rapid-mixing approaches in microfluidic channels for time-resolved SAXS. (A) Turbulent-flow mixing using the T-mixer [23] and arrow-shaped geometry [27] (inset). (B) Laminar-flow hydrodynamic focusing [21].

3. Conclusions and outlook

Over the last two to three decades, since microfluidics arose, various groups have recognised the advantage offered by this miniaturised technology and have successfully demonstrated its incorporation with SAXS. In particular, its high-throughput sample-handling potential and time-resolution–enhancing abilities have begun to be exploited. However this is still an emerging field, and microfluidic technology continues to push the boundaries and open up new possibilities, some likely yet to be conceived. With the current technology, 100 μs time resolution for SAXS studies on protein folding has been achieved. Although the turbulent- and laminar-flow mixers discussed above have been the most popular microfluidic approaches thus far, others have been looking to develop new mixing strategies, which could reduce dead times further, whilst the development of smaller, more highly focussed X-ray beams will be key to accessing faster timescales.

Author details

Serena A.J. Watkin[1,3], Timothy M. Ryan[2], Antonia G. Miller[4], Volker M. Nock[1,5], F. Grant Pearce[1,3] and Renwick C.J. Dobson[1,3*]

*Address all correspondence to: renwick.dobson@canterbury.ac.nz

1 Biomolecular Interaction Centre, University of Canterbury, Christchurch, New Zealand

2 Australian Synchrotron, Melbourne, Victoria, Australia

3 School of Biological Sciences, University of Canterbury, Christchurch, New Zealand

4 Protein Science & Engineering Team, Callaghan Innovation, Christchurch, New Zealand

5 Department of Electrical & Computer Engineering, University of Canterbury, Christchurch, New Zealand

References

[1]   Bhatia, S.N. and D.E. Ingber, Microfluidic organs-on-chips. Nature Biotechnology, 2014. 32(8): p. 760–772.

[2]   Whitesides, G.M., The origins and the future of microfluidics. Nature, 2006. 442(7101): p. 368–373.

[3]   Hansen, C., Microfluidics in structural biology: smaller, faster… better. Current Opinion in Structural Biology, 2003. 13(5): p. 538–544.

[4]   Pearce, F.G., et al., Characterization of monomeric dihydrodipicolinate synthase variant reveals the importance of substrate binding in optimizing oligomerization. Biochimica et Biophysica Acta, 2011. 1814(12): p. 1900–1909.

[5]   Keown, J.R., et al., Small oligomers of ribulose-bisphosphate carboxylase/oxygenase (rubisco) activase are required for biological activity. Journal of Biological Chemistry, 2013. 288(28): p. 20607–20615.

[6]   Cross, P.J., et al., Tyrosine latching of a regulatory gate affords allosteric control of aromatic amino acid biosynthesis. The Journal of Biological Chemistry, 2011. 286(12): p. 10216–10224.

[7]   Mills, R.D., et al., Domain organization of the monomeric form of the tom70 mitochondrial import receptor. Journal of Molecular Biology, 2009. 388(5): p. 1043–1058.

[8]   Griffin, M.D., et al., Characterisation of the first enzymes committed to lysine biosynthesis in Arabidopsis thaliana. PLoS One, 2012. 7(7): p. e40318.

[9] Crowther, J.M., et al., Ultra-high resolution crystal structure of recombinant caprine beta-lactoglobulin. FEBS Letters, 2014. 588(21): p. 3816–3822.

[10] Poen, S., et al., Exploring the structure of glutamate racemase from Mycobacterium tuberculosis as a template for anti-mycobacterial drug discovery. Biochemical Journal, 2016. 473(9): p. 1267–1280.

[11] Chen, K., et al., Genome-wide binding and mechanistic analyses of smchd1-mediated epigenetic regulation. Proceedings of the National Academy of Sciences of the United States of America, 2015. 112(27): p. E3535–E3544.

[12] Stehle, R., et al., Small-angle X-ray scattering in droplet-based microfluidics. Lab on a Chip, 2013. 13(8): p. 1529–1537.

[13] Panine, P., et al., Probing fast kinetics in complex fluids by combined rapid mixing and small-angle X-ray scattering. Advances in Colloid and Interface Science 2006. 127(1): p. 9–18.

[14] Hansen, C.L., et al., A robust and scalable microfluidic metering method that allows protein crystal growth by free interface diffusion. Proceedings of the National Academy of Sciences of the United States of America, 2002. 99(26): p. 16531–16536.

[15] Brennich, M.E., et al., Dynamics of intermediate filament assembly followed in micro-flow by small angle X-ray scattering. Lab on a Chip, 2011. 11(4): p. 708–716.

[16] Martel, A., et al., Silk fiber assembly studied by synchrotron radiation SAXS/WAXS and Raman spectroscopy. Journal of the American Chemical Society, 2008. 130(50): p. 17070–17074.

[17] Polte, J., et al., Nucleation and growth of gold nanoparticles studied via in situ small angle X-ray scattering at millisecond time resolution. ACS Nano, 2010. 4(2): p. 1076–1082.

[18] Otten, A., et al., Microfluidics of soft matter investigated by small-angle X-ray scattering. Journal of Synchrotron Radiation, 2005. 12(Pt 6): p. 745–750.

[19] Dootz, R., et al., Rapid prototyping of X-ray microdiffraction compatible continuous microflow foils. Small, 2007. 3(1): p. 96–100.

[20] Barrett, R., et al., X-ray microfocussing combined with microfluidics for on-chip X-ray scattering measurements. Lab on a Chip, 2006. 6(4): p. 494–499.

[21] Pollack, L., et al., Compactness of the denatured state of a fast-folding protein measured by submillisecond small-angle x-ray scattering. Proceedings of the National Academy of Sciences of the United States of America, 1999. 96(18): p. 10115–10117.

[22] Pollack, L., et al., Time resolved collapse of a folding protein observed with small angle x-ray scattering. Physical Review Letters, 2001. 86(21): p. 4962–4965.

[23] Akiyama, S., et al., Conformational landscape of cytochrome c folding studied by microsecond-resolved small-angle x-ray scattering. Proceedings of the National Academy of Sciences of the United States of America, 2002. 99(3): p. 1329–1334.

[24] Uzawa, T., et al., Collapse and search dynamics of apomyoglobin folding revealed by submillisecond observations of alpha-helical content and compactness. Proceedings of the National Academy of Sciences of the United States of America, 2004. 101(5): p. 1171–1176.

[25] Uzawa, T., et al., Time-resolved small-angle X-ray scattering investigation of the folding dynamics of heme oxygenase: implication of the scaling relationship for the submillisecond intermediates of protein folding. Journal of Molecular Biology, 2006. 357(3): p. 997–1008.

[26] Kimura, T., et al., Specific collapse followed by slow hydrogen-bond formation of beta-sheet in the folding of single-chain monellin. Proceedings of the National Academy of Sciences of the United States of America, 2005. 102(8): p. 2748–2753.

[27] Graceffa, R., et al., Sub-millisecond time-resolved SAXS using a continuous-flow mixer and X-ray microbeam. Journal of Synchrotron Radiation, 2013. 20(Pt 6): p. 820–825.

[28] Arai, M., et al., Microsecond hydrophobic collapse in the folding of Escherichia coli dihydrofolate reductase, an alpha/beta-type protein. Journal of Molecular Biology, 2007. 368(1): p. 219–229.

[29] Wu, Y., et al., Microsecond acquisition of heterogeneous structure in the folding of a TIM barrel protein. Proceedings of the National Academy of Sciences of the United States of America, 2008. 105(36): p. 13367–13372.

[30] Russell, R., et al., Rapid compaction during RNA folding. Proceedings of the National Academy of Sciences of the United States of America, 2002. 99(7): p. 4266–4271.

[31] Kimura, T., et al., Specifically collapsed intermediate in the early stage of the folding of ribonuclease A. Journal of Molecular Biology, 2005. 350(2): p. 349–-362.

[32] Toft, K.N., et al., High-throughput small angle X-ray scattering from proteins in solution using a microfluidic front-end. Analytical Chemistry, 2008. 80(10): p. 3648–3654.

[33] Lafleur, J.P., et al., Automated microfluidic sample-preparation platform for high-throughput structural investigation of proteins by small-angle X-ray scattering. Journal of Applied Crystallography, 2011. 44(5): p. 1090–1099.

[34] Schwemmer, F., et al., LabDisk for SAXS: a centrifugal microfluidic sample preparation platform for small-angle X-ray scattering. Lab on a Chip, 2016. 16(7): p. 1161–1170.

[35] Round, A.R., et al., Automated sample-changing robot for solution scattering experiments at the EMBL hamburg SAXS station X33. Journal of Applied Crystallography, 2008. 41(Pt 5): p. 913–917.

[36] Greaves, E.D. and A. Manz, Toward on-chip X-ray analysis. Lab on a Chip, 2005. 5(4): p. 382–391.

[37] Moller, M., et al., Small angle X-ray scattering studies of mitochondrial glutaminase C reveal extended flexible regions, and link oligomeric state with enzyme activity. PLoS One, 2013. 8(9): p. e74783.

[38] Skou, M., et al., In situ microfluidic dialysis for biological small-angle X-ray scattering. Journal of Applied Crystallography, 2014. 47(4): p. 1355–1366.

[39] Kihara, H., Stopped-flow apparatus for X-ray scattering and XAFS. Journal of Synchrotron Radiation, 1994. 1(Pt 1): p. 74–77.

[40] Eliezer, D., et al., The radius of gyration of an apomyoglobin folding intermediate. Science, 1995. 270(5235): p. 487–488.

[41] Arai, M., et al., Kinetic refolding of β-lactoglobulin. Studies by synchrotron X-ray scattering, and circular dichroism, absorption and fluorescence spectroscopy1. Journal of Molecular Biology, 1998. 275(1): p. 149–162.

[42] Plaxco, K.W., et al., Chain collapse can occur concomitantly with the rate-limiting step in protein folding. Nature Structural Biology, 1999. 6(6): p. 554–556.

[43] Jacob, J., et al., Early collapse is not an obligate step in protein folding. Journal of Molecular Biology, 2004. 338(2): p. 369–382.

[44] Tsuruta, H., et al., Influence of nucleotide effectors on the kinetics of the quaternary structure transition of allosteric aspartate transcarbamylase. Journal of Molecular Biology, 2005. 348(1): p. 195–204.

[45] Roh, J.H., et al., Multistage collapse of a bacterial ribozyme observed by time-resolved small-angle X-ray scattering. Journal of the American Chemical Society, 2010. 132(29): p. 10148–10154.

[46] Moody, M.F., et al., Stopped-flow x-ray scattering: the dissociation of aspartate transcarbamylase. Proceedings of the National Academy of Sciences of the United States of America, 1980. 77(7): p. 4040–4043.

[47] Regenfuss, P., et al., Mixing liquids in microseconds. Review of Scientific Instruments, 1985. 56(2): p. 283.

[48] Moskowitz, G.W. and R.L. Bowman, Multicapillary mixer of solutions. Science, 1966. 153(3734): p. 428–429.

[49] Chan, C.K., et al., Submillisecond protein folding kinetics studied by ultrarapid mixing. Proceedings of the National Academy of Sciences of the United States of America, 1997. 94(5): p. 1779–1784.

[50] Segel, D.J., et al., Characterization of transient intermediates in lysozyme folding with time-resolved small-angle X-ray scattering. Journal of Molecular Biology, 1999. 288(3): p. 489–499.

[51] Takahashi, S., et al., Folding of cytochrome c initiated by submillisecond mixing. Nature Structural Biology, 1997. 4(1): p. 44–50.

[52] Bilsel, O., et al., A microchannel solution mixer for studying microsecond protein folding reactions. Review of Scientific Instruments, 2005. 76(1): p. 014302.

[53] Knight, J.B., et al., Hydrodynamic focusing on a silicon chip: mixing nanoliters in microseconds. Physical Review Letters, 1998. 80(17): p. 3863–3866.

[54] Park, H.Y., et al., Conformational changes of calmodulin upon Ca^{2+} binding studied with a microfluidic mixer. Proceedings of the National Academy of Sciences of the United States of America, 2008. 105(2): p. 542–547.

[55] Hertzog, D.E., et al., Femtomole mixer for microsecond kinetic studies of protein folding. Analytical Chemistry, 2004. 76(24): p. 7169–7178.

Small-Angle X-ray Scattering

SAXS Evaluation of Size Distribution for Nanoparticles

Shinichi Sakurai

Additional information is available at the end of the chapter

Abstract

Size distribution is an important structural aspect in order to rationalize relationship between structure and property of materials utilizing polydisperse nanoparticles. One may come to mind the use of dynamic light scattering (DLS) for the characterization of the size distribution of particles. However, only solution samples can be analyzed and even for those, the solution should be transparent or translucent because of using visible light. It is needless to say that solid samples are out of range. Furthermore, the size distribution only in the range of several tens of nanometers can be characterized, so DLS is useless for particles in the range of several nanometers. Therefore, the small-angle X-ray scattering (SAXS) technique is much superior when considering the determination of the size distribution in several nanometers length scale for opaque solutions and for solid specimens. Furthermore, the SAXS technique is applicable not only for the spherical particle but also for platelet (lamellar) and rod-like (cylindrical) particles. In this chapter, we focus on the form factor of a variety of nanostructures (spheres, prolates, core-shell spheres, core-shell cylinders and lamellae). Also getting started with a monodisperse distribution of the size of the nanostructure, to unimodal distribution with a narrow standard deviation or wide-spreading distribution and finally to the discrete distribution can be evaluated by the computational parameter fitting to the experimentally obtained SAXS profile. In particular, for systems forming complicated aggregations, this methodology is useful. Not only the size distribution of 'a bunch of grapes' but also the size distribution of all 'grains of grapes in the bunch' can be evaluated according to this methodology. This is very much contrasted to the case of the DLS technique by which only 'a bunch of grapes' is analyzed but 'grains of grapes in the bunch' cannot be. It is because the DLS technique in principle evaluates diffusion constants of particles and all of the grains in the same bunch of grapes diffuse as a whole. Thus, the methodology is important to highlight versatility and diversity in real materials, especially in soft matter, both in the liquid and in the solid states.

Keywords: SAXS, form factor, sphere, cylinder, lamella, prolate, core-shell sphere, core-shell cylinder, discrete distribution function

1. Introduction

In recent years, controlling of nanostructures has been more significantly considered in the field of materials science, especially relating to the soft matter [1]. Versatile properties or functions can be obtained through designing nanostructures in solid-state materials, as well as nanomaterials dispersed in liquid-state substance. Even for contradictory properties such as hard and soft, they may be coexistent in one material when fabricating so-called inclined nanostructures (for instance, nanoparticle size is gradually changing as a function of the position in material). This in turn indicates that size distribution of the nanostructures should be rigorously evaluated for better understanding effects of nanostructure on properties and functions. For biological systems or supramolecular organizations, situation is very much contrast to the other ubiquitous materials as described above because they form spontaneously a regular aggregation. Therefore, the size distribution is narrow and follows a simple mathematical function with a comparatively small standard deviation. By contrast, discrete distribution of the size is required to determine for the ubiquitous materials. However, even for regular nanostructures, the determination of the discrete distribution of the nanostructure size is needed to reveal a transient state upon transition from the state 1 to the state 2, being triggered by sudden change in temperature, pH, or other external parameters.

It is well known that the size distribution of particles can be evaluated by the use of dynamic light scattering (DLS). However, only solution samples can be analyzed and even for those, the solution should be transparent or translucent because of using visible light. It is needless to say that solid samples are out of range. Furthermore, the size distribution only in the range of several tens of nanometers can be characterized, so DLS is useless for particles in the range of several nanometers. Therefore, the small-angle X-ray scattering (SAXS) technique is much superior when considering the determination of the size distribution in several nanometers length scale for opaque solutions and for solid specimens [2]. Furthermore, the SAXS technique is applicable, not only for the spherical particle but also for platelet (lamellar) and rod-like (cylindrical) particles and it enables us to determine the thickness distribution of lamellae or the cross-sectional radius distribution of cylinders. Namely, the SAXS technique does not matter types of particle shape even for hallow cylinders or hollow spheres [3].

The principle is simple. Scattering comprises not only contribution from regularity of space-filling ordering (the lattice factor) of particles but also from a single particle (the form factor). The particle scattering can be mathematically formulated depending on the type of particle shape (lamella, cylinder or sphere). In the block copolymer microdomain systems, the Gauss distribution of the particle size has been assumed. Only recently, direct determination of the discrete size distribution has been available by conducting fitting theoretical scattering function to the experimentally obtained SAXS profile (the plot of the scattering intensity as a function of the magnitude of the scattering vector, q [$= (4\pi/\lambda)$ sin $(\Theta/2)$ with Θ and λ being the scattering angle and the wavelength of X-ray, respectively] where the abundance of the particle having a given size was treated as a floating parameter with a step of 1 nm (the step can be more precise). In this chapter, getting started

with nanoparticles with a narrow size distribution, we will see characteristic shape of the form factors for protein self-assembly, block copolymer microdomains and peptide amphiphile nanofibers. Then, we shift our target to the evaluation of discrete distribution of size of nanostructures by SAXS. The examples shown are thickness distribution of the crystalline lamellae of polyethylene glycol in polymer blends and thickness distribution of the hard segment domains for supramolecular elastomers (starblocks of soft polyisobutylene and hard oligo(β^-alanine) segments). Other notable examples are sterically stabilized polypyrrole-palladium (PPy-Pd) nanocomposite particles, hybrid amphiphilic poly(N-isopropylacrylamide)/metal cyanide complexes and the cobalt(II) terpyridine complexes with diblock copolypeptide amphiphiles. For this example, this methodology is useful. Not only the size distribution of 'a bunch of grapes' but also the size distribution of all 'grains of grapes in the bunch' can be evaluated according to this methodology. This is very much contrasted to the case of the DLS technique by which only 'a bunch of grapes' is analyzed but 'grains of grapes in the bunch' cannot be. It is because the DLS technique in principle evaluates diffusion constants of particles and all of the grains in the same bunch of grapes diffuse as a whole. Thus, the methodology is important to highlight versatility and diversity in real materials, especially in soft matter, both in the liquid and in the solid states.

2. Nanoparticles with a narrow size distribution

First of all, some typical examples of the experimentally observed form factor are demonstrated. The samples are self-assembly of proteins, block copolymer microdomains and peptide amphiphiles. Apoferritin is a protein having ability to store iron atoms and it is referred to as ferritin when iron atoms are bound. Apoferritin forms a spherical shell as a self-assembled nanostructure with a very uniform size. As indicated in **Figure 1** (pH-dependence of SAXS profiles), its SAXS profiles (apoferritin, 24-mer) exhibit characteristic features with many peaks due to its uniform shape for pH ≥3.40 [4]. Dramatic change in the SAXS profile is detected between pH = 1.90 and 3.40. This means that apoferritin is disassembled for acidic condition. Time-resolved SAXS measurements have been utilized to study disassembling and reassembling process upon the change in pH [4, 5]. In **Figure 1**, the curve shows the result of the SAXS modeling by the scattering program GNOM [6]. Since protein molecules produce the typical form factor, it is frequently used to obtain commissioning data for newly launched SAXS beamline or apparatus [7–9].

It is known that block copolymer spontaneously forms a regular nanostructure with a narrow size distribution. **Figure 2** shows examples of the SAXS profiles for sphere-forming block copolymer (SEBS; polystyrene-block-poly(ethylene-co-butylene)-block-polystyrene triblock copolymer) having Mn = 6.7 × 10^4, Mw/Mn = 1.04, PS volume fraction = 0.084) [10], where Mn and Mw denote number-average and weight-average molecular weights, respectively. In **Figure 2**, the solid curve is the results of the model calculation for the spherical particle, but not only the form factor, but also the lattice factor of BCC (body-centered cubic) is taken into account. The full equation is as follows [11–14]:
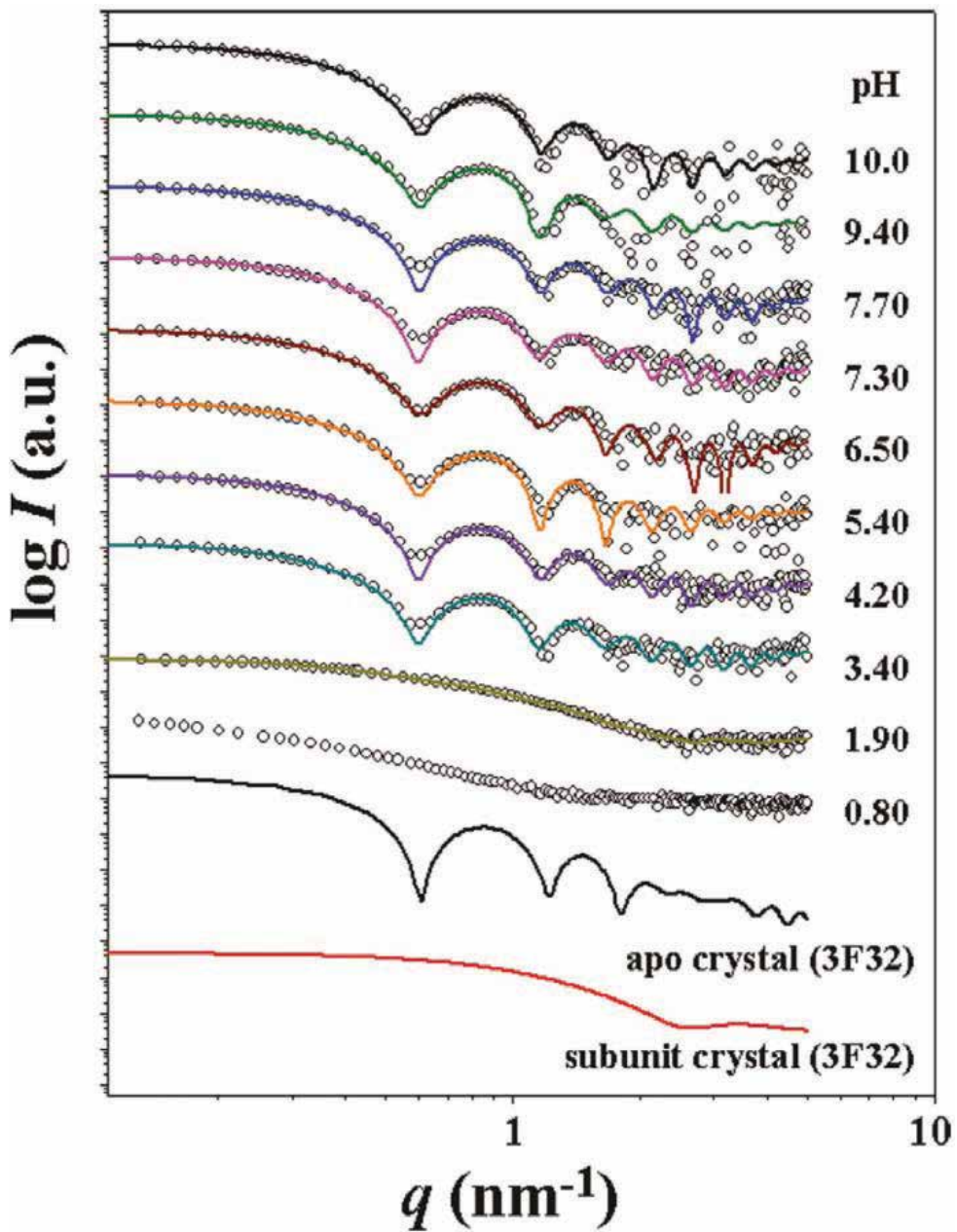
Figure 1. pH-dependence of SAXS profiles for an apoferritin aqueous solution. The symbols indicate the experimental data, and the solid lines indicate the fits obtained using the GNOM program. The solid lines without symbols are the theoretical SAXS curves calculated from the crystal structure of apoferritin and its subunit crystal (PDB code 3F32). For clarity, each plot is shifted along the log I axis [4].
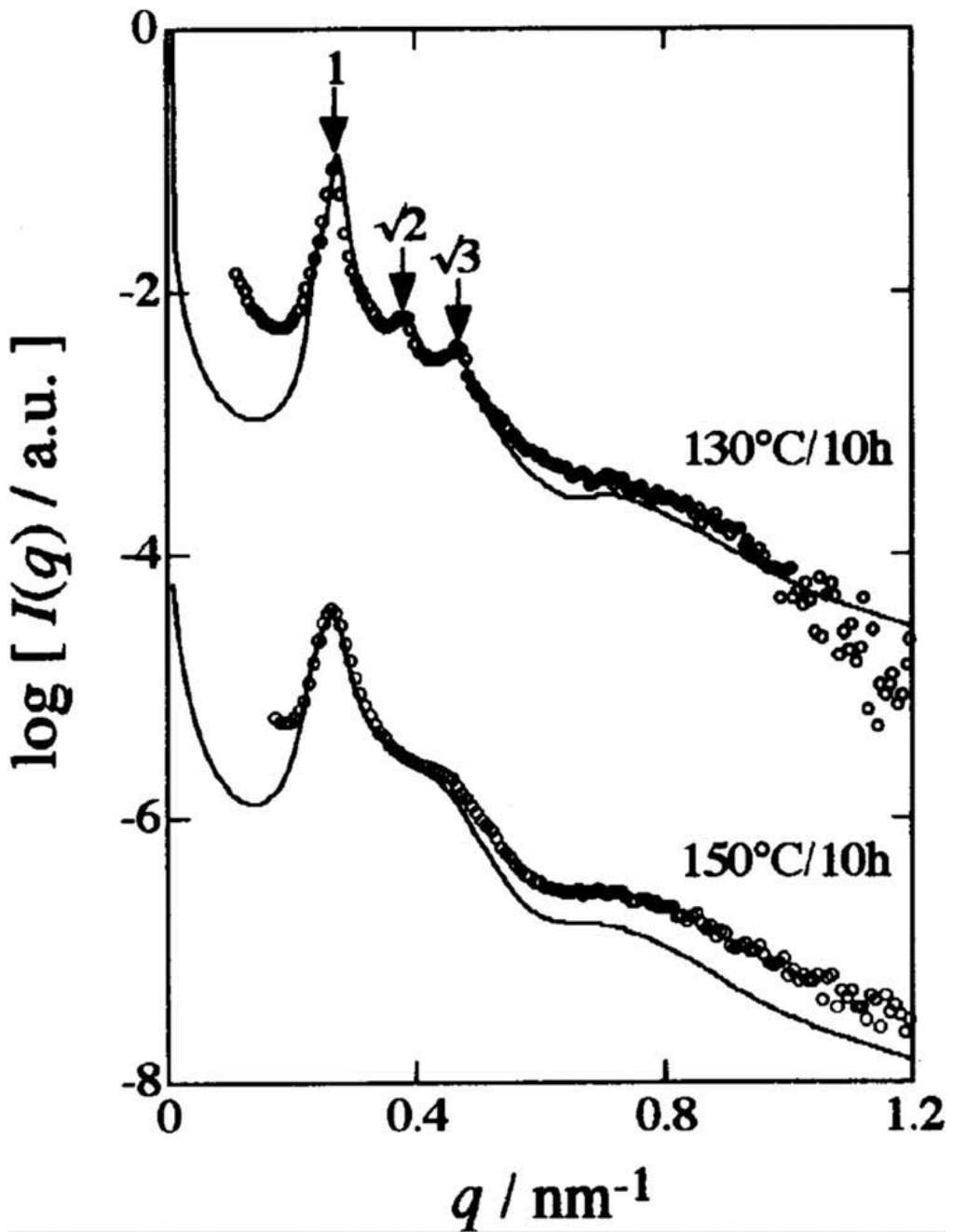
Figure 2. SAXS profiles for SEBS-8 specimens (sphere-forming triblock copolymer) annealed at 130 and 150°C for 10 h [10].

$$I(q) - \langle |f^2(q)| \rangle - |\langle f(q) \rangle|^2 + |\langle f(q) \rangle|^2 Z(q) \tag{1}$$

where $\langle x \rangle$ is the average of the quantity of x. $f(q)$ and $Z(q)$ are particle and lattice factor, respectively, designating the scattering amplitude due to the intraparticle interference and the scattering intensity due to the interparticle interference, respectively. The form factor $f(q)$ for a spherical particle with its radius, R, can be given as

$$f(q) = A_e \Delta \rho \, V \frac{3[\sin(qR) - qR\cos(qR)]}{(qR)^3} \tag{2}$$

where A_e is the scattering amplitude of the Thomson scattering, $\Delta\rho$ is the difference in the electron density between sphere and matrix, V is the volume of the spheres. Here, the Gauss distribution is used for R with σ_R being the standard deviation. On the other hand, the lattice factor $Z(q)$ is given by Eq. (3) with Eulerian angles, θ and ϕ, which define orientation of the unit cell of a given grain with respect to the experimental Cartesian coordinates:

$$
\begin{aligned}
Z(q,\theta,\phi) = {} & \frac{1 - F_k^2}{\left[1 - 2F_k \cos\left(\frac{\sqrt{6}}{4} q d\alpha\right) + F_k^2\right]} \\[2mm]
& \times \frac{1 - F_k^2}{\left[1 - 2F_k \cos\left(\frac{\sqrt{6}}{4} q d\beta\right) + F_k^2\right]} \times \frac{1 - F_k^2}{\left[1 - 2F_k \cos\left(\frac{\sqrt{6}}{4} q d\gamma\right) + F_k^2\right]}
\end{aligned}
\tag{3}
$$

with

$$F_k = \exp\left[-\frac{3}{16} g^2 d^2 q^2 (\alpha^2 + \beta^2 + \gamma^2)\right] \tag{4}$$

and $g = \Delta d / \langle d \rangle$ which is the degree of the lattice distortion (Δd denotes the standard deviation in d due to the paracrystalline distortion). In Eq. (4),

$$\alpha = \sin\theta\cos\phi + \sin\theta\sin\phi + \cos\theta \tag{5}$$

$$\beta = -\sin\theta\cos\phi - \sin\theta\sin\phi + \cos\theta \tag{6}$$

$$\gamma = -\sin\theta\cos\phi + \sin\theta\sin\phi - \cos\theta \tag{7}$$

for the bcc lattice and

$$\alpha = \sin\theta\sin\phi + \cos\theta \tag{8}$$

$$\beta = -\sin\theta\cos\phi + \cos\theta \tag{9}$$

$$\gamma = -\sin\theta\cos\phi + \sin\theta\sin\phi \tag{10}$$

for the fcc lattice. In Eqs. (3) and (4), d denotes the Bragg spacing. The spacing for {110} and {111} planes for the bcc and fcc lattices, respectively, gives rise to the first-order peaks. For

randomly oriented polygrains in actual samples, the scattering is isotropic. Therefore, $Z(q,\theta,\phi)$ is averaged with respect to θ and ϕ to obtain isotropic $Z(q)$:

$$Z(q) = \frac{1}{4\pi} \int_0^{2\pi} \int_0^{\pi} Z(q,\theta,\phi) \sin\theta d\theta d\phi \tag{11}$$

As clearly observed in **Figure 2**, the broad peak around $q = 0.71$ nm^{-1} is due to the form factor. The model curve is the result of calculation with $<R> = 7.90$ nm for 130°C annealed specimen and $<R> = 8.10$ nm for 150°C annealed specimen and the standard deviation of the size distribution (σ_R) being 1.09 and 1.10 nm, respectively. Thus, evaluated value of $<R>$ is consistent with the result of transmission electron microscopic observation (as shown in **Figure 3**). Note also here that the order-disorder transition temperature locates between 130 and 150°C, so that bcc ordering is quite regular for the specimen annealed at 130°C, while it is poor for 150°C annealed specimen. The SAXS profile for the 130°C annealed specimen displays clear lattice peaks at the relative q values of 1:√2:√3, indicating high regularity of the bcc ordering. The sphere-forming block copolymers exhibit mostly the bcc ordering due to the entropic profit [14] and the fcc ordering has been found for some particular case. Comparison between the results shown in **Figures 1** and **2** clearly indicates that many peaks for monodisperse particle are easy to collapse to become more featureless when the size distribution is incorporated even if it is small. Nevertheless, it is characteristic for the block copolymer microdomains that one peak can be discernible for the form factor.
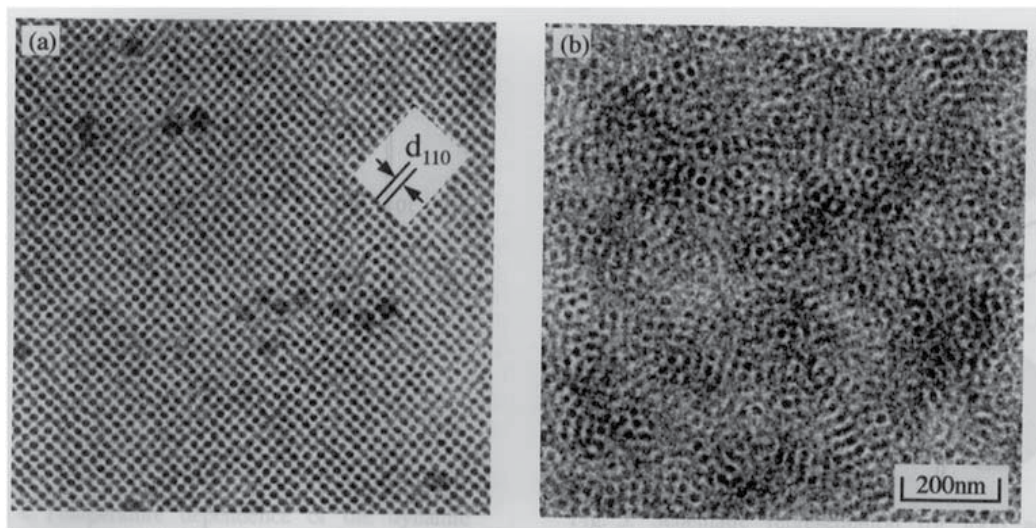

Figure 3. TEM micrographs for SEBS-8 specimens annealed at (a) 130 and (b) 150°C for 10 h. The polystyrene microdomains were stained with ruthenium tetroxide [10].

Very recently, it has been found that PS spherical microdomains were deformed upon the uniaxial stretching of the SEBS-8 film specimens [15]. Since SEBS triblock copolymer with the glassy PS spherical microdomains can be used as a thermoplastic elastomer (TPE), the film

specimen can be stretched. In **Figure 4**, 2D-SAXS patterns are displayed to recognize the deformation of the round shape form factor upon the uniaxial stretching. **Figure 4a** shows the 2D-SAXS pattern for the SEBS-8 film specimen. Here, it is clearly observed that the round shape form factor appears at $q = 0.77$ nm^{-1}. The round peak of the form factor is deformed to become an ellipsoid in **Figure 4b** upon uniaxial stretching of the film specimen up to the strain of 3.65 (stretching ratio is 4.65) at room temperature. The peak position in the q^-direction parallel to the stretching direction ($q//$SD) is lower than that in the q^-direction perpendicular to SD ($q\perp$SD). This means that the size of the particle in the $q_{//}$ direction is bigger than that in $q_\perp$ direction, which in turn implies deformation of the spherical particles. Therefore, the model calculation of the form factor, $P(q)$, for prolate was conducted using the mathematical equation as follows:

$$P(q) = \int_0^{2\pi} \int_0^{\pi/2} \int_0^{\infty} \int_1^{\infty} f^2(q, v, R_{\min}, \phi)\, \Omega(v)\, \Xi(R_{\min})\, \Psi_\phi(\phi)\Psi_\mu(\mu)\, \sin\phi\, dv\, dR_{\min}\, d\phi d\mu \quad (12)$$

$$f(q, v, R_{\min}) = V\frac{3(\sin U - U\cos U)}{U^3} \quad (13)$$

$$U(q, v, R_{\min}, \phi) = qR_{\min}\sqrt{\sin^2\phi + v^2\cos^2\phi} \quad for\ q//SD \quad (14)$$

$$U(q, v, R_{\min}, \phi, \mu) = qR_{\min}\sqrt{\sqrt{1 - \sin^2\phi\cos^2\mu} + v^2\sin^2\phi\cos^2\mu} \quad for\ q\perp SD \quad (15)$$

$$v = \frac{R_{\max}}{R_{\min}} > 1 \qquad V = \frac{4\pi}{3}R_{maj}R_{\min}^2 = \frac{4\pi}{3}vR_{\min}^3 \quad and\ (volume\ of\ the\ prolate) \quad (16)$$
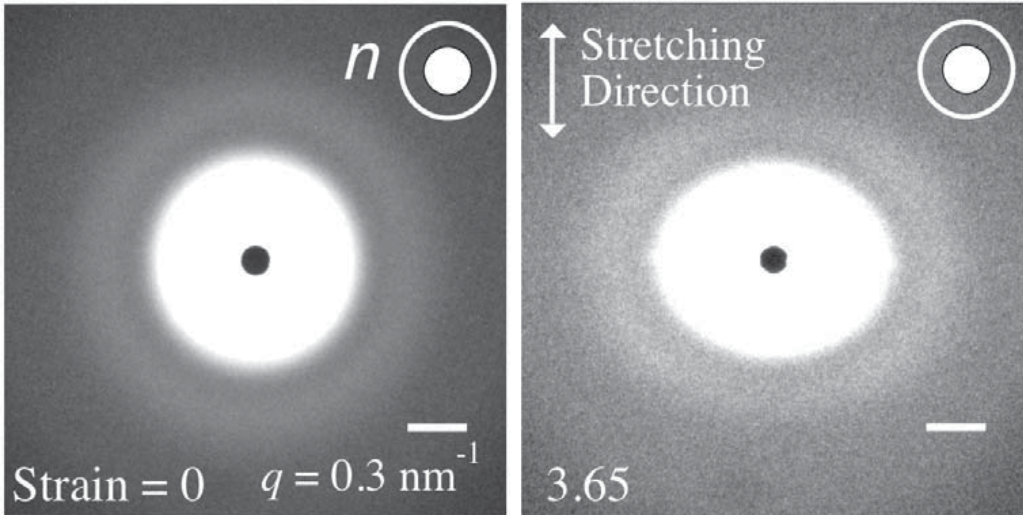

Figure 4. 2D-SAXS patterns for SEBS-8 specimens (a) unstretched state and (b) being stretched at the strain of 3.65 at room temperature [15].

Here, R_{maj} and R_{min} stand for the radius of the longer axis and the radius of the shorter axis of the prolate, respectively (**Figure 5**) and ϕ is the angle between the $\boldsymbol{q}$ direction and the long axis of the prolate. To fit the SAXS profile with the model calculation, the distributions in R_{min}, ν and ϕ are required. Note here that the distributions in ϕ and μ define the orientational distribution function: $\Psi_\phi(\phi)$ and $\Psi_\mu(\mu)$, respectively. However, for this particular case, ϕ can be considered to be zero with no distribution, namely perfect orientation of the prolates with their log axes parallel to SD because the uniaxial stretching prolongs spherical microdomains to result in prolates with their long axes parallel to SD, which in turn enables us to set $\Psi_\mu(\mu) = 1$ regardless of μ. Therefore, due to decreased numbers of the parameters, the situation became easier to evaluate the average values of R_{min} and ν with their distributions (ΞR_{min} and $\Omega(\nu)$).

The results for the 1D-SAXS profiles in $q_{//}$ and in $q_\perp$ directions are shown in **Figure 6a** and **b**, respectively. In the both cases, the 1D-SAXS profile for the unstretched film specimen (before the stretching) is shown together. It is clearly observed that the peak of the form factor moved toward lower and higher q range upon the stretching in $q_{//}$ and in $q_\perp$ directions, respectively. Furthermore, both of the SAXS profiles can be fit by the prolate model, using Eqs. (1), (12)–(16) with the bcc lattice factor. Here, the $<R_{min}>$ = 6.44 nm and $<\nu>$ = 1.20 were used for the model calculation. Note that $<R_{min}>$ = 6.85 nm for the unstretched specimen. Moreover, the distributions in R_{min} and ν (ΞR_{min} and $\Omega(\nu)$) used for the calculation are plotted in **Figure 7a** and **b**, respectively. Such a mathematical function for the size distribution is enough to explain the experimentally observed SAXS profile under the stretched state. However, it should be noted that both of the distributions were required and otherwise, the model SAXS curve did not fit well the experimental results for both the $q_{//}$ and $q_\perp$ directions. **Figure 6a** and **b** also includes the SAXS profiles measured after complete removal of the stretching force. At a first glance, the peak positions of the form factor in **Figure 6a** and **b** seem to recover its original position for the unstretched specimens. However, this does not imply the recovery of the original spherical shape upon the removal of the load because the deformation of the glassy PS microdomains is permanent. Then, why did the form factor recover its original peak position? It may be ascribed to randomization of the prolates orientation upon the removal of the load. To check this speculation, we conducted the SAXS modeling of the prolate form factor by setting $\Psi(\phi) = 1$ irrespective of ϕ but with keeping the size distribution R_{min} and ν (ΞR_{min} and $\Omega(\nu)$) unchanged. The results of the modeling are shown with the red curves in **Figure 6a** and **b**, indicating clearly good agreements with the experimentally obtained SAXS profiles. This in turn confirms the speculation of randomization of the prolates orientation upon the removal of the load.

Core-shell sphere and cylinder models are significantly important for the amphiphilic self-assembly. For the core-shell sphere [16, 17], the form factor is formulated as:

$$P(q) = \left\{ (\rho_C - \rho_S)V_C \frac{3[\sin(qR_C) - qR_C\cos(qR_C)]}{(qR_C)^3} + (\rho_S - \rho_0)V_S \frac{3[\sin(qR_S) - qR_S\cos(qR_S)]}{(qR_S)^3} \right\}^2 \quad (17)$$
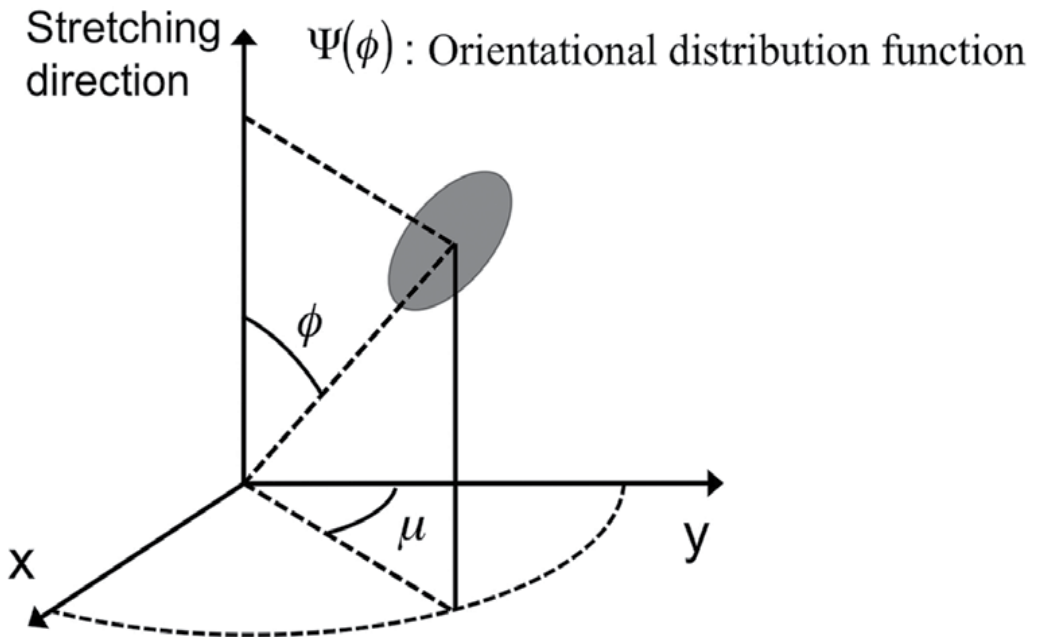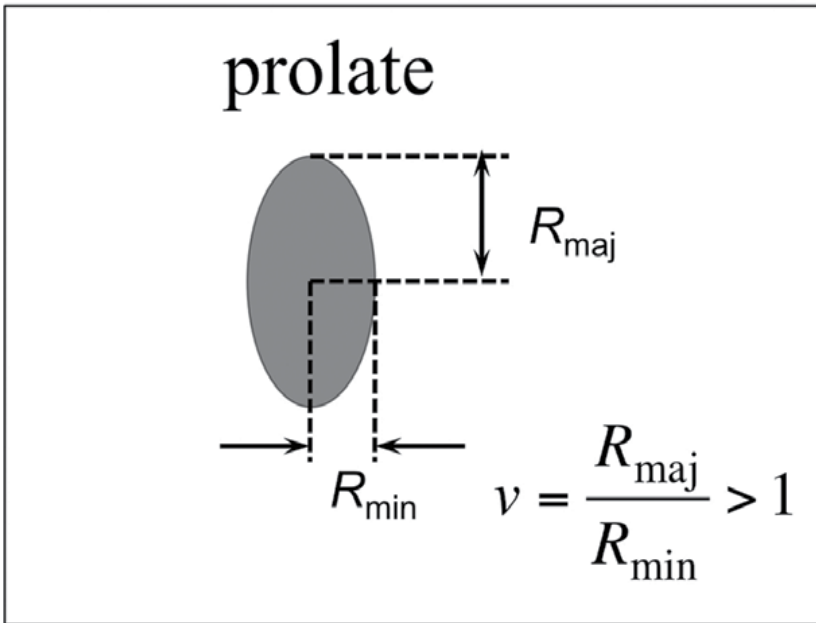
$$v = \frac{R_{maj}}{R_{min}} > 1$$

Figure 5. Prolate model used for the SAXS modeling. Here, R_{maj} and R_{min} stand for the radius of the longer axis and the radius of the shorter axes of the prolate, respectively. Eulerian angles, μ and ϕ, define orientation of the prolate with respect to the experimental Cartesian coordinates [15].
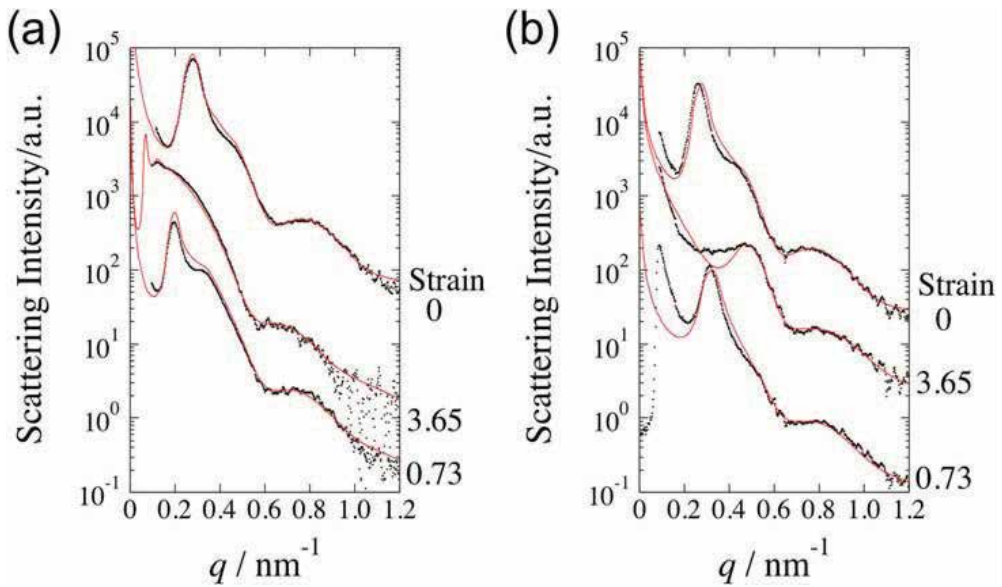
Figure 6. 1D-SAXS profiles extracted from the SAXS patterns as shown in **Figure 5** in (a) $q_{//}$ and in (b) $q_{\perp}$ directions. Black dots are for the experimentally obtained SAXS profiles, and red curves are calculated SAXS profiles [15].
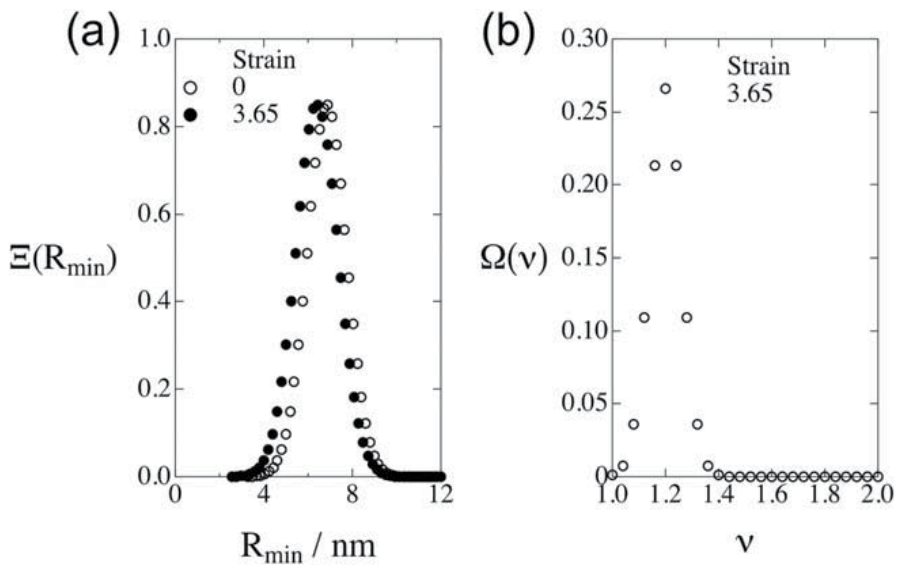
Figure 7. Evaluated $\Xi(R_{min})$ and $\Omega(\nu)$ of the prolate for SEBS-8 specimens stretched at the strain of 3.65. For comparison, the size distribution function for the radius of sphere is shown together for the unstretched specimen [15].

if the homogeneous densities in the core and in the shell can be assumed with ρ_c and ρ_s, respectively. Here, V_c and V_s designate the volume of the core and the shell, respectively. Moreover, R_c and R_s denote the radii of the core and the shell, respectively. ρ_0 is the electron density of the matrix. On the other hand, when the shell density changes as a function of r (the core density is homogeneous) as defined with $\rho_s(r)$, then the form factor is formulated as [18, 19]:

$$P(q) = \left\{ (\rho_C - \rho_S) V_C \frac{3[\sin(qR_C) - qR_C \cos(qR_C)]}{(qR_C)^3} + 4\pi \int_{R_C}^{R_S} \left(\rho_S(r) - \rho_0 \right) r^2 \frac{\sin(qr)}{qr} dr \right\}^2 \qquad (18)$$

As for core-shell cylinders, the form factor is:

$$P(q) = \int_0^{\pi/2} \left\{ (\rho_S - \rho_{solv}) V_S \frac{\left[\sin\left(\frac{qH_S \cos\theta}{2}\right) \right]}{\frac{qH_S \cos\theta}{2}} \frac{2J_1(qR_S \sin\theta)}{qR_S \sin\theta} + \right.$$

$$\left. (\rho_C - \rho_S) V_C \frac{\left[\sin\left(\frac{qH_C \cos\theta}{2}\right) \right]}{\frac{qH_C \cos\theta}{2}} \frac{2J_1(qR_C \sin\theta)}{qR_C \sin\theta} \right\}^2 \sin\theta d\theta \qquad (19)$$

where $J_1(x)$ is the first-order Bessel function. θ is defined as the angle between the cylinder axis and q. R_C and R_S are the core and shell radii, respectively. H_C and H_S are the core and shell lengths, respectively. V_C and V_S are the core and shell volumes, respectively ($V_x = \pi R_x^2 H_x$; $x = C$, S, or $solv$; C: core, S: shell, $solv$: solvent). ρ_x is the electron density of the core, shell, or solvent.

Matson et al. [20] have reported the SAXS modeling of the form factor of the core-shell cylinder for self-assembling peptide amphiphiles (PAs) as shown in **Figure 8A** and **B**. The molecules self-assembled into the core-shell cylinder are illustrated in **Figure 8C**. Such cylinders can be detected with cryogenic TEM as shown in **Figure 9**. The SAXS profile is shown in **Figure 10** with the model curve, where the size distribution in the core radius is modeled using a log-normal distribution with the polydispersity being around 27–30% (see **Table 1** for the structural parameter determined by the SAXS modeling), while the radial shell thickness is assumed to be monodisperse. Although the modeling results explain very well the experimentally obtained SAXS profiles, the fact that the radial shell thickness is assumed to be monodisperse means it is difficult to determine individually two distributions in inner and outer radius. For more detailed structure analyses, more experimental variations are required to gather information from different kinds of aspects, like the example shown in **Figure 6a** and **b** (parallel and perpendicular to SD).
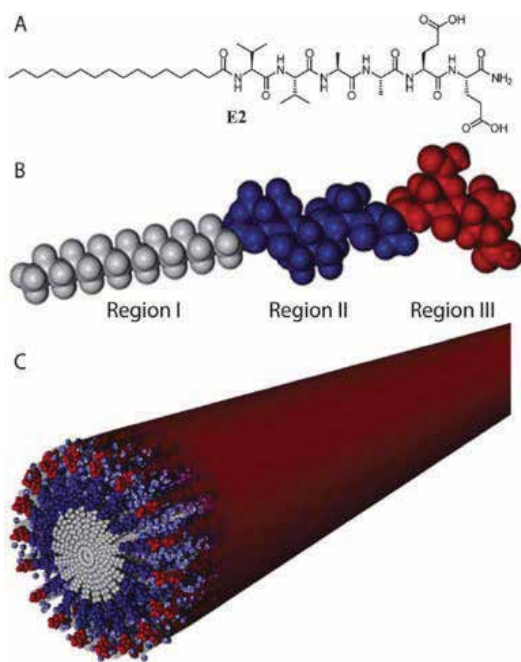
Figure 8. (A) Chemical structure of self-assembling peptide amphiphiles (PA: E2 C16V2A2E2). (B) The different regions of the PA are highlighted in a space-filling model. (C) Schematic illustration of a self-assembled PA nanofiber [20].
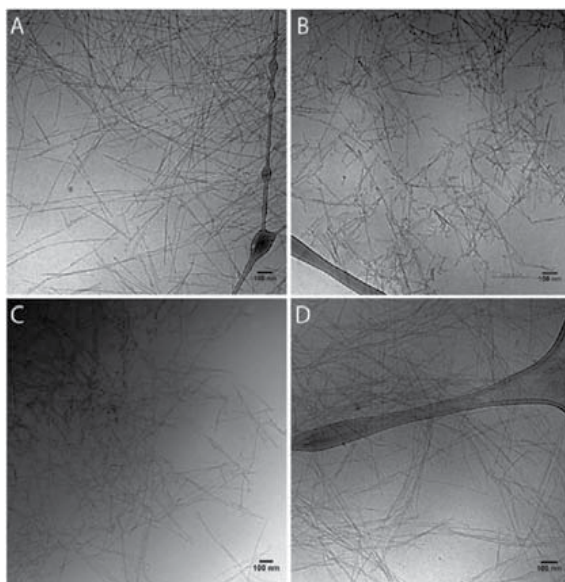

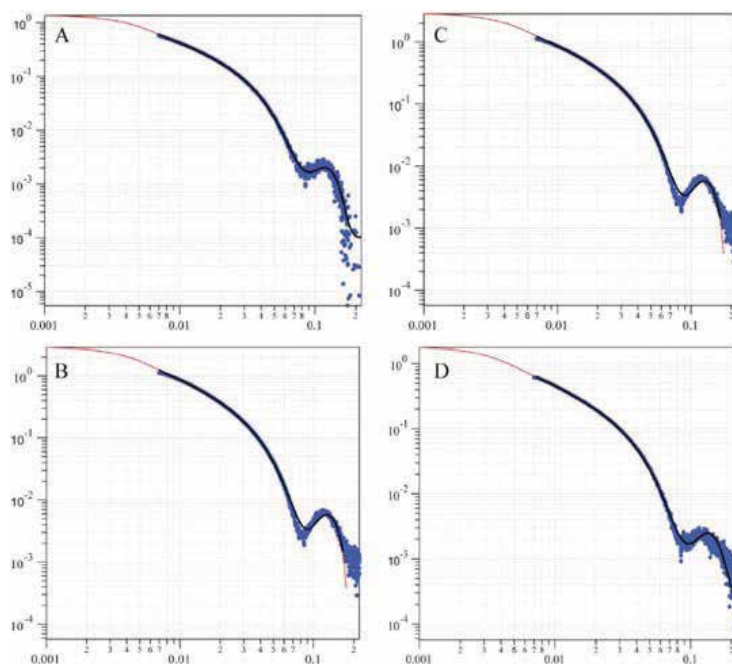**Figure 9.** Cryogenic TEM of (A) PA 5, (B) PA 6, (C) PA 7, and (D) PA 8 as 1: 3 w/w mixtures with E2 PA [20].

Figure 10. I SAXS profiles of PAs 5-8 (A-D) fitted to a polydisperse core-shell cylinder model. The solid red line represents the best fit to a core-shell cylinder form factor, where the core was allowed to be polydisperse according to a log-normal distribution. The solid black line represents the portion of the curves where fits were performed [20].

PA	5	6	7	8
Mean core radius (A)	12	12	12	12
Radial shell thickness (A)	29	27	25	25
Total diameter (nm)	8.2	7.8	7.4	7.4
Radial polydispersity (σ)	0.3	2.7	0.3	0.28

NaOH without $CaCl_2$ (from Ref. [20]).

Table 1. Selected SAXS data from PAs 5–8 at 0.25% in 4 mM.

3. Concept of evaluation of discrete distribution by SAXS

In this section, the concept of evaluation of the discrete distribution of the size of the nanostructure is explained. As an example, the lamellar model calculations are displayed in **Figure 11**, for which the mathematical equation is [21]:

$$P(q) = q^{-2}L^2[\{\sin(qL/2)\}/(qL/2)]^2 \tag{20}$$

where L is the lamellar thickness and the prefactor (q^{-2}) is the so-called Lorentz factor which is required to randomize the orientation of the lamellar particle. Here, it was assumed that the lamellar particle has infinitely large extent in the direction parallel to the lamellar surface.

Figure 11a and **b** shows the calculated profiles when L was set to 10 and 20 nm, respectively. It can be seen that the characteristics in the shapes of lamellar form factor are similar to the case of spherical form factor. As a matter of fact, many peaks appear. Summing up these two profiles gives the one, which is also shown in **Figure 11c**. This in turn means that the form factor is as shown in **Figure 11c** when the lamellar thickness distribution is as shown in the inset of **Figure 11**. It is noteworthy that the characteristic shape of the one shown in **Figure 11c** (L = 10 nm + L = 20 nm) is similar to the case of **Figure 11a** (L = 10 nm). When the distribution is somewhat modified as indicated in **Figure 12b**, the form factor is dramatically altered to the one as shown in **Figure 12a**. This seems to be no more characteristic form factor. Thus, the experimentally observed form factor can be a fingerprint and the size distribution may be evaluated as far as the shape of the nanostructure can be uniquely assumed.
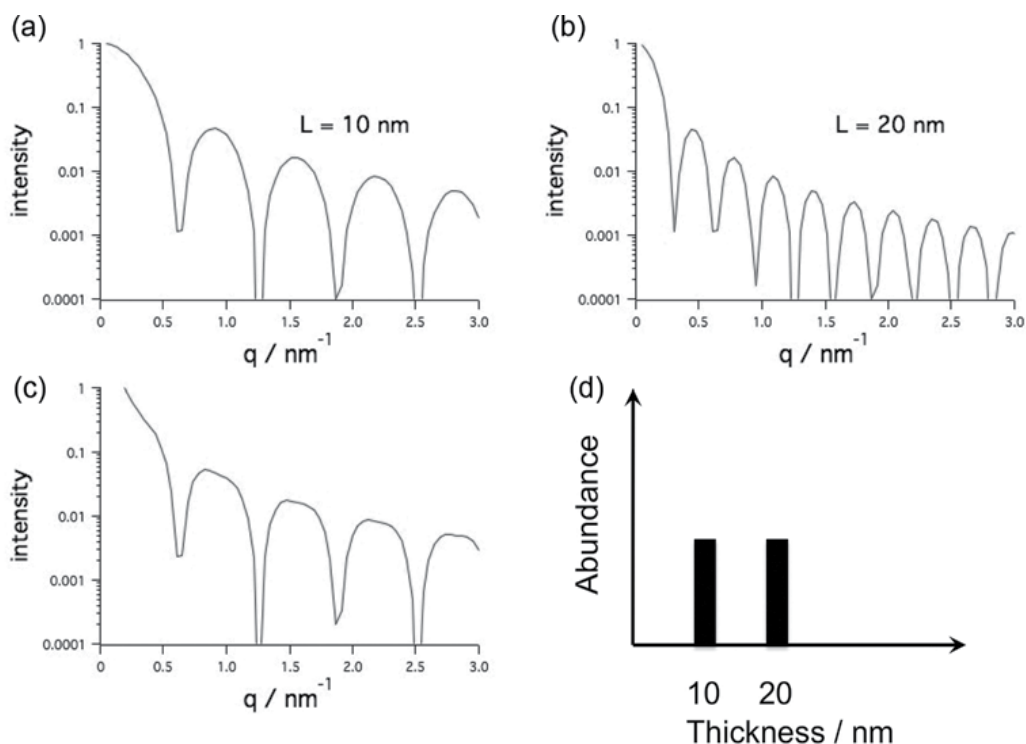

Figure 11. Calculated SAXS profiles for lamellar particle with (a) L = 10 nm, (b) L = 20 nm, and (c) L = 10 nm + L = 20 nm. The inset shows a hypothetical distribution function used for the calculation of the profile shown in **Figure 11c**.

Figure 12c shows one of the typical results of the SAXS profiles for poly(oxyethylene) (PEG), which forms lamellar crystallites. The exact sample used for the result of **Figure 12c** was a polymer blend of PEG with poly (D, L-lactide) (PDLLA), which is a racemic copolymer and therefore amorphous. The compositions of PEG/PDLLA were 80/20 (DL20) by weight. **Figure 12c** shows the result of the SAXS measurement at 64.0°C in the heating process [22].

At the temperature of 64.0°C slightly below the melting temperature of PEG (64.5°C), the typical form factor of lamellar particle was observed first time for the crystalline polymer. It was expected that the thinner lamellar which has a lower melting temperature melted away in the heating process. The thickest lamellae can only survive at the highest temperature and therefore, the thickness distribution became sharp. This may be the reason of the observation of the typical form factor of lamellar particle. As a matter of fact, a very sharp distribution was evaluated as shown in **Figure 12d** by the method described below.
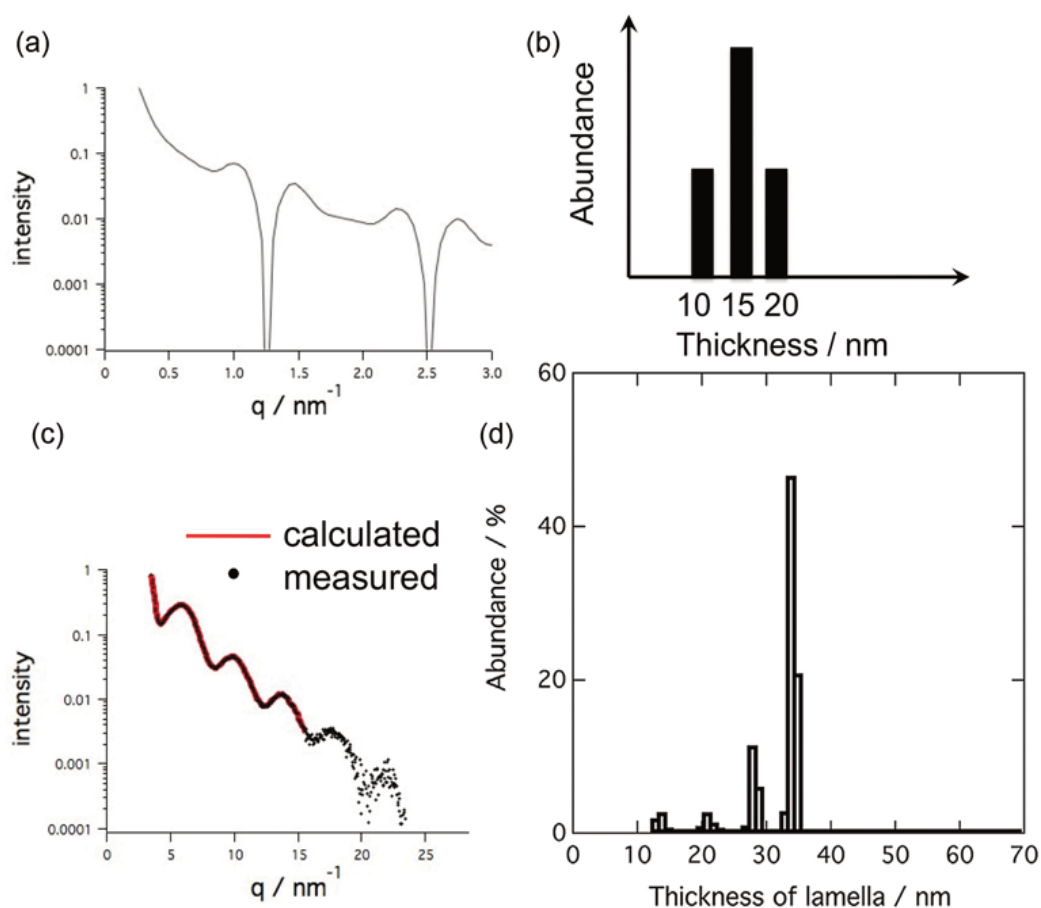

Figure 12. (a) Calculated SAXS profile for lamellar particle with assuming a hypothetical distribution function as shown in part (b). (c) One of the typical results of the SAXS profiles for PEG/PDLLA 80/20 blend at 64.0°C in the heating process. Black dots are for the experimentally obtained SAXS profile, and red curves are the calculated SAXS profile. (d) Evaluated thickness distribution from the result shown in part (c).

Hereafter, the data analysis method for the direct determination of the thickness distribution of lamellar particle is described. The model particle scattering intensity, $I(q)$, with a distribution of thicknesses can be given as:

$$I(q) = k\Sigma[n(L)P(q)]\qquad(21)$$

with $P(q)$ defined by Eq. (20). In Eq. (21), k is a numerical constant and $n(L)$ is the number fraction of lamella with a thickness of L, providing the thickness distribution of lamellae. A protocol was employed to directly determine $n(L)$ by fitting the calculated $I(q)$ from Eq. (21) to the experimentally observed 1D-SAXS profile where the following parameters were being floated as the fitting parameters: the numerical constant k and $n(L = 1\ nm)$, $n(L = 2\ nm)$, $n(L = 3\ nm)$,…, $n(L = 40\ nm)$ which are the abundance number of particles having thickness L in a step of 1 nm. By this protocol, the best fit was successfully performed, which is shown by the solid curve on the 1D-SAXS profile in **Figure 12c**. Although most of the features seem to be well described by the particle scattering, the first-order peak is not. For some SAXS profiles, the full calculation including the lattice factor $Z(q)$ and the particle scattering can describe the SAXS profile well. The mathematical formulation of $Z(q)$ is [23]:

$$Z(q) = \frac{1-|F|^2}{1-2|F|\cos(qD) + |F|^2} \tag{22}$$

$$|F| = \exp\left(-\frac{g^2 D^2 q^2}{2}\right) \tag{23}$$

Thus, the thickness distribution as shown in **Figure 12d** was also evaluated. Although such a sharp distribution around $L = 33.5\ nm$ accounts for the particle scattering dominant SAXS profile, the presence of thinner lamellae is clearly suggested.

4. Widely spread discrete distribution evaluated by SAXS

4.1. Lamellar case

Tien et al. have reported results of comprehensive studies of the higher-order crystalline structure of PEG in blends with PDLLA [22, 24, 25]. For several blend compositions, they have discussed the effects of blending PDLLA on the structural formation of PEG. It is remarkable that they found more regular higher-order structure for PEG 20 wt % composition (DL20) as compared to the PEG 100% sample in the as-cast blend sample (cast from a dichloromethane solution). More interestingly, they reported that the 1D-SAXS profile markedly changed from lattice peak dominant type to particle scattering dominant type when heating the as-cast sample, as shown in **Figure 13**. The compositions of PEG/PDLLA were 100/0, 95/5 (DL5), 90/10 (DL10) and 80/20 (DL20) by weight. **Figure 13** shows the results of the SAXS measurements in the heating process. Based on the results, we have conducted the evaluation of the lamellar thickness distribution in the heating process from the as-cast state up to 64°C and succeeded in showing that the distribution became sharper with the average thickness becoming larger, as shown in **Figure 14**. That study is the first showing quantitative evidence of the well-known concept of 'lamellar thickening' when a crystalline polymer is thermally annealed just below its melting temperature. Tien et al. have also conducted the same evaluation under higher pressure (5 and 50 MPa) [26].
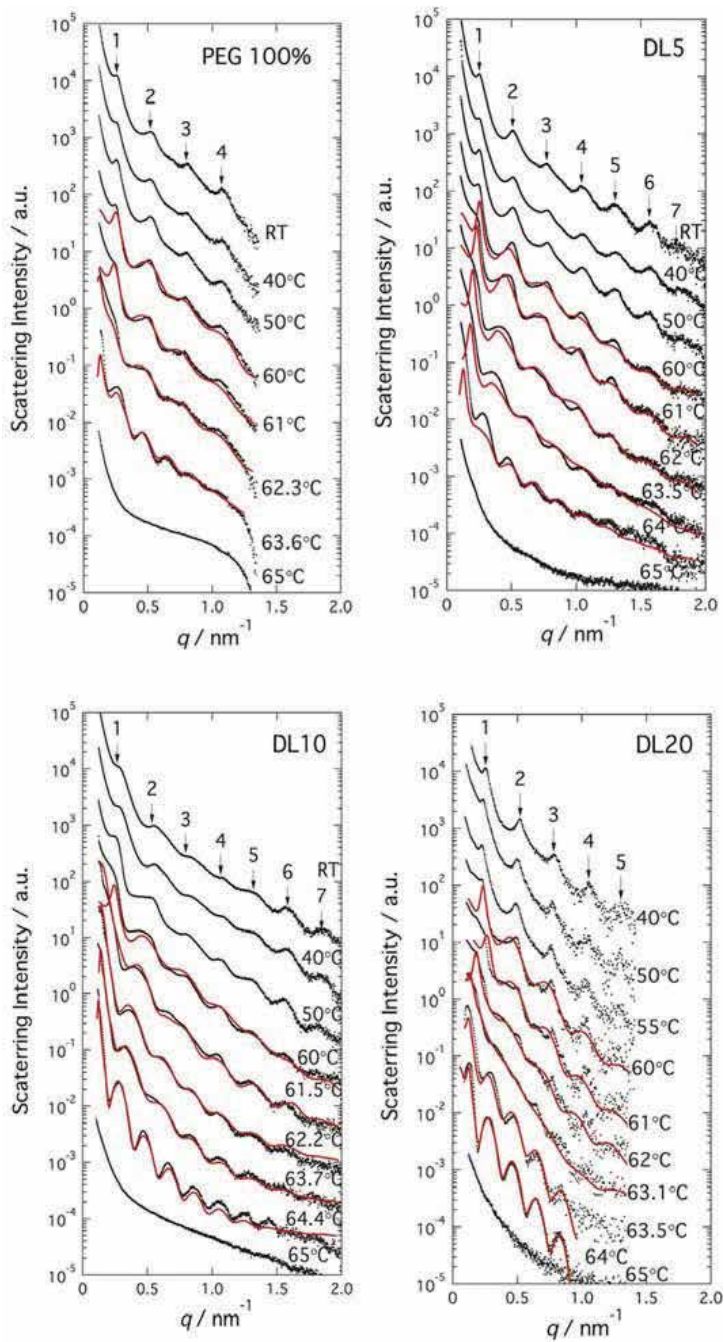
Figure 13. SAXS profiles for PEG/PDLLA blends with 100/0, 95/5 (DL5), 90/10 (DL10), and 80/20 (DL20) by weight. The SAXS measurements were conducted in the heating process. Black dots are for the experimentally obtained SAXS profiles, and red curves are the calculated SAXS profiles [22].
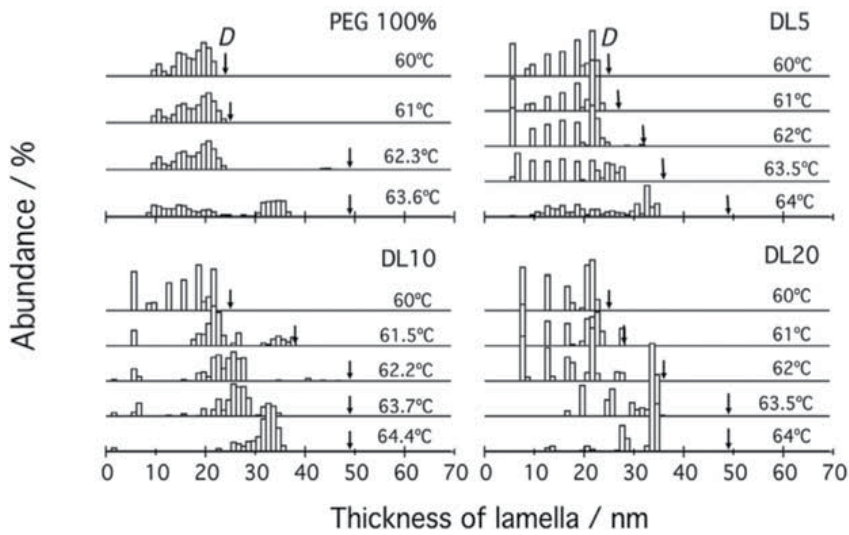
Figure 14. Evaluated thickness distribution from the result shown in **Figure 13** [22].

Jia et al. [27] have recently evaluated thickness distribution of the hard segment domains for supramolecular elastomers (starblocks of soft polyisobutylene and hard oligo(β^-alanine) segments). The molecule is a novel type of supramolecule as schematically shown in **Figure 15** where the green chains are soft polyisobutylene. Due to the formation of the lamellar crystallites of oligo (β^-alanine) segments, the specimen has rubber-like elasticity, that is, supramolecular self-assembly leads the specimen to TPE. Since such lamellar crystallites can be hardly observed by TEM, the SAXS measurement was conducted. The result is shown in **Figure 16** with the evaluated thickness distribution which is shown in the inset. Almost monodispersed distribution was evaluated with the peak at L = 2.0 nm (inset of **Figure 16**), which is in good agreement with the size of the oligo (β^-alanine) contour length. This case clearly demonstrates the significance of the SAXS technique.
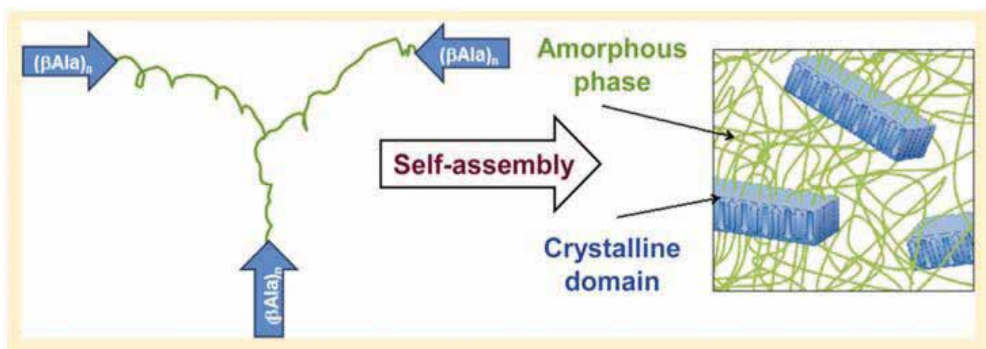

Figure 15. Schematic illustrations for supramolecular elastomers (starblocks of soft polyisobutylene and hard oligo(β-alanine) segments) where the green chains are soft polyisobutylene [27].
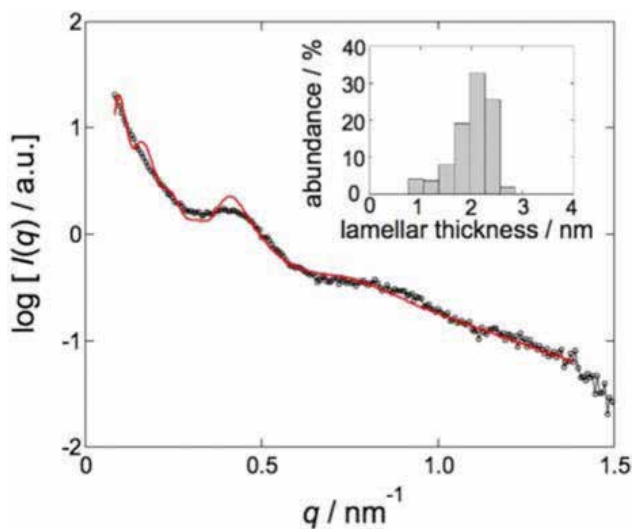
Figure 16. SAXS profile for the supramolecular elastomer schematically shown in **Figure 15**. Black dots are for the experimentally obtained SAXS profile, and red curve is the calculated SAXS profile. The inset shows the evaluated thickness distribution [27].

4.2. Spherical case

In this subsection, the size distribution of nanoparticles is described. Fujii et al. [28, 29] have synthesized novel for sterically stabilized polypyrrole-palladium (PPy-Pd) nanocomposite particles. Such a characteristic particle containing heavy element has recently been attracting intensively general interests of researchers in many fields under the name of element-blocks [30]. **Figure 17** shows a TEM image of these particles with a schematic of the structure. The ordinary 1D-SAXS profiles of 1, 2 and 3% aqueous dispersions of the nanocomposite particles are shown together in **Figure 18a** as a plot of $\log[I(q)]$ versus $\log q$. This plot clearly shows that the shapes of the profiles are similar. When the curves are vertically shifted, all of the data collapse onto a single curve (**Figure 18b**), suggesting that the nanocomposite particles are dispersed in the aqueous medium without ordering into a lattice, at least up to a particle concentration of 3%. Thus, the 1D-SAXS profile can be attributed directly to the particle scattering (the form factor). Although the TEM results revealed that the nanocomposite particles are not spherical, a mathematical equation describing particle scattering is not available for such an unusual shape of particles. Therefore, a spherical shape is assumed for simplicity. The model particle scattering intensity, $I(q)$, with a distribution of thicknesses can be given as:

$$I(q) = k\Sigma[n(R)P(q)] \tag{24}$$

The form factor, $P(q)$, for spherical particles is given as:

$$P(q) = (4\pi R^3/3)^2[\Phi(q)]^2 \tag{25}$$

and

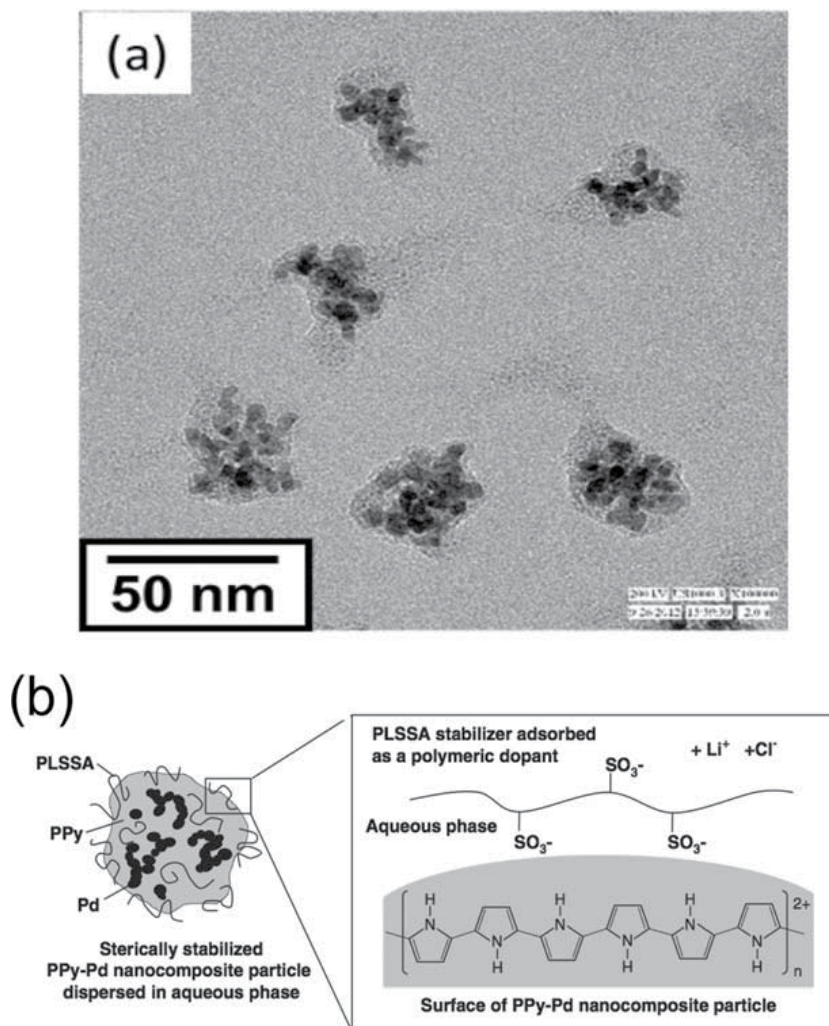$$\Phi(q) = 3/(qR)^3[\sin(qR) - qR\cos(qR)] \tag{26}$$

Figure 17. (a) TEM image of sterically stabilized polypyrrole-palladium (PPy-Pd) nanocomposite particles, and (b) a schematic of the structure [28].

In Eq. (24), k is a numerical constant and $n(R)$ is the number fraction of spheres with a radius of R, providing the size distribution of spheres. Attempts to fit a theoretical function given by Eq. (24) to the measured 1D-SAXS profile assuming a Gauss or Schulz-Zimm-type distribution for $n(R)$ were unsuccessful. We then employed a protocol in which $n(R)$ was directly determined by fitting the calculated $I(q)$ from Eq. (24) to the experimentally observed 1D-SAXS profile by the same method as described above for the lamellar case. The best fit is shown in **Figure 18a** with the dotted black curve for the 1D-SAXS profile (3% aqueous solution). The reason of using this profile is because of being most intense and therefore the most reliable. Thus, the obtained particle size distribution is shown in **Figure 19**, where the abundance is shown in the units of vol%, which was calculated by the following equation from the number fraction $n(R)$:
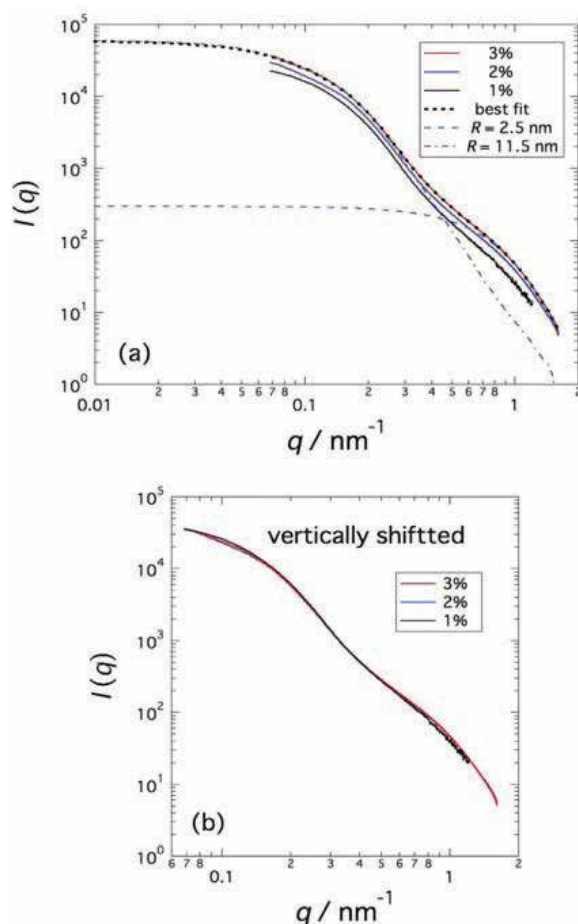
Figure 18. (a) SAXS profiles of 1, 2, and 3% aqueous dispersions of the PPy-Pd nanocomposite particles as a plot of log [$I(q)$] versus log q. The best-fit curve is shown as a dotted black curve on the 1D-SAXS profile for the 3% aqueous solution (most intense and therefore most reliable). (b) Master curve for the SAXS profile obtained by vertically shifting the three 1D-SAXS profiles in (a) (not shifted in q-axis direction) [28].

$$\text{abundance } (vol\%) = n(R)R^3/\Sigma[n(R)R^3] \times 100 \qquad (27)$$

Bimodal size distribution was clearly obtained with two peaks at approximately $R = 2.5$ and 11.5 nm. It is recognized that smaller particles (assuming $n(R)$ with a single peak at approximately $R = 2.5$ nm) could explain the shape of the SAXS profile in the higher q range (see the broken curve in **Figure 18a**), whereas larger ones (assuming $n(R)$ with a single peak at approximately $R = 11.5$ nm) characterized the SAXS profile in the lower q range (see the dotted and broken curve). This result does not indicate the real distribution of the PPy-Pd nanocomposite particles themselves, but the additional abundance of tiny Pd nanoparticles existing in the nanocomposite particles. These speculations are confirmed by TEM observations (**Figure 17**), indicating that the average radius was approximately 16 nm with a unimodal distribution and by close examination of the high-resolution TEM image ($R = 2.7$ nm; **Figure 17**). Thus, it was possible to evaluate not only the size of 'a bunch of grapes' but also the size of all 'grains of grapes in the bunch.'
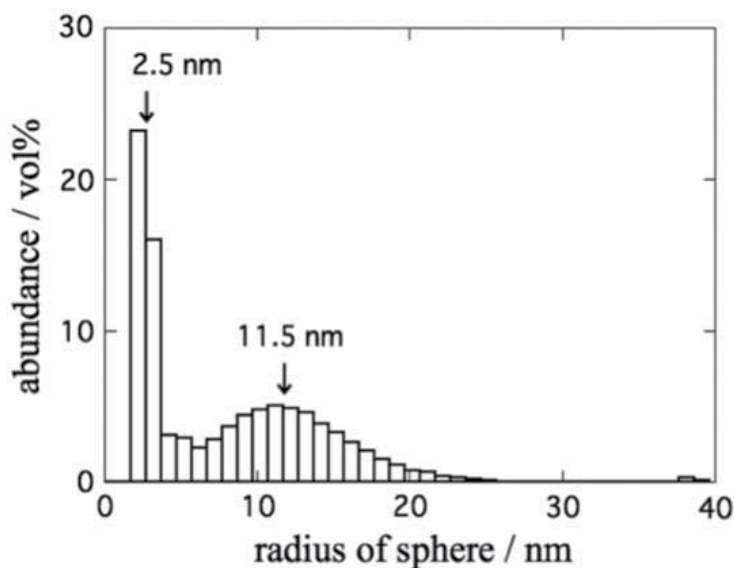
Figure 19. Evaluated particle size distribution based on the result shown in **Figure 18** [28].

Kuroiwa et al. [31, 32] have synthesized novel amphiphilic *N*-isopropylacrylamide (NIPPAm) oligomers with dodecyl groups and carboxyl groups, as shown in **Figure 20a**, by the RAFT polymerization of NIPPAm with *S*-1-dodecyl-*S'*-(α,α'-dimethyl-α''- acetic acid) trithiocarbonate (DTC). It was interestingly found that the DTC-NIPPAm oligomers form network aggregation upon addition of Cu^{2+} ion in an aqueous solution, as revealed by TEM (**Figure 20b** for the dried specimen from an aqueous solution of DTS-NIPPAm35 with Cu^{2+} ions). It seems that the network diameter is somewhat 30 nm or above. There is a possibility to consider that the constitutive unit of the network should be a micelle as schematically illustrated in **Figure 20c**. Since the TEM observation can be only conducted for the dried specimen, the resultant TEM image might be quite different from the real structure in the aqueous media. In order to reveal real structure in the aqueous media, the in situ SAXS measurement was performed at room temperature. Then, the spherical model fitting was applied to the resultant SAXS profile. **Figure 21** shows the SAXS profile with the model form factor. The experimentally obtained SAXS curve (black curve) is available for $q > 0.06$ nm^{-1} and characteristic dent and hump are observed around $q = 0.15$ and 0.50 nm^{-1}, respectively. By assuming the spherical model, the calculated SAXS profile (red curve) can perfectly fit to the experimental one as displayed in **Figure 21**. Thus, evaluated discrete distribution of the radius is shown in **Figure 22**. Here, the main distribution is found around 2–7 nm, implying the cores of the micelles. Because the core contains sulfur atoms, the contrast is considered to be highest and therefore, the core can be the most intense scatterer. This is the reason of observing majority in 2–7 nm in the distribution. This in turn implies that the network aggregation comprises micelles, which can never be detected by TEM. Close examination of the resultant distribution revealed minor abundance around 17 and 21 nm. This agrees well with the least radius of the network aggregation in the TEM observation, as mentioned above. The same distribution is shown in the inset of Figure? with the logarithmic axis for the abundance. Then, it is clear that not only the minor abundance around 17 and 21 nm, but many

minor ones are discernible in the wide range from 17 to 58 nm. As a matter of fact, such big spheres can be occasionally seen in the TEM image (**Figure 20b**). Thus, once again for this kind of complicated aggregation, the method of evaluation of the discrete distribution of size from the SAXS result is approved to be quite effective [33].
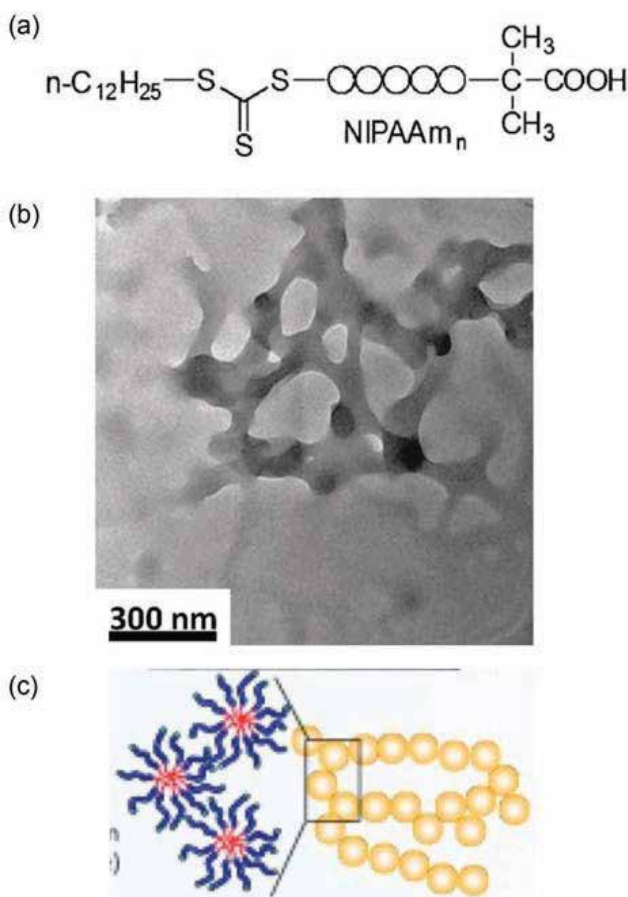

Figure 20. (a) Novel amphiphilic *N*-isopropylacrylamide (NIPPAm) oligomers with dodecyl groups and carboxyl groups. (b) TEM micrograph for the dried specimen from an aqueous solution of DTS-NIPPAm35 with Cu^{2+} ions. (c) Schematic illustration of the micelle network [31, 32].

5. Concluding remarks

In this chapter, we focused on the form factor of a variety of nanostructures (spheres, prolates, core-shell spheres, core-shell cylinders and lamellae). Also getting started with a mono-disperse distribution of the size of the nanostructure, to unimodal distribution with a narrow standard deviation or wide-spreading distribution and finally to the discrete distribution can be evaluated by the computational parameter fitting to the experimentally obtained SAXS profile. In particular, for systems forming complicated aggregations, this methodology is useful. Not only the size
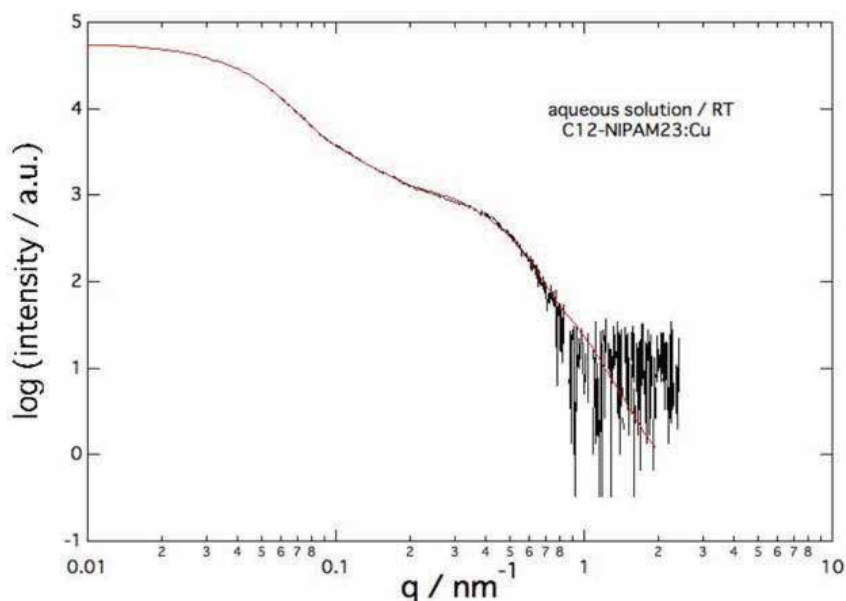
Figure 21. SAXS profile for an aqueous solution of DTS-NIPPAm35 with Cu^{2+} ions with the model form factor. The black curve is the experimentally obtained SAXS profile, and the red curve is the calculated SAXS profile [31, 32].
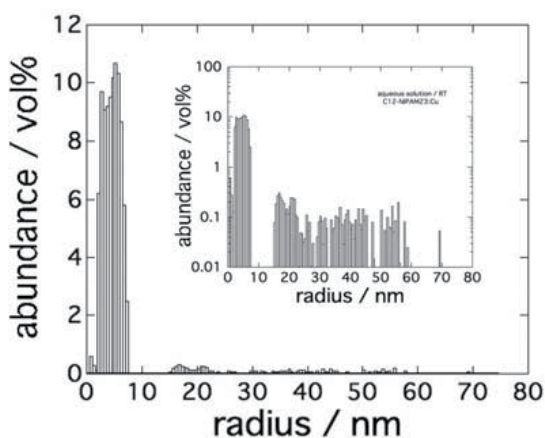

Figure 22. Evaluated size distribution based on the result shown in **Figure 21** [31, 32].

distribution of 'a bunch of grapes' but also the size distribution of all 'grains of grapes in the bunch' can be evaluated according to this methodology. This is very much contrasted to the case of the DLS technique by which only 'a bunch of grapes' is analyzed but 'grains of grapes in the bunch' cannot be. It is because the DLS technique in principle evaluates diffusion constants of particles and all of the grains in the same bunch of grapes diffuse as a whole. Thus, the methodology is important to highlight versatility and diversity in real materials, especially in soft matter,

both in the liquid and in the solid states. At present, however, the shape of the nanostructure is limited in spherical or lamellar. On extending the methodology to the complicated structures such as cylinder, prolate, oblate, or core-shell type, there are tremendous difficulties. For cylinder, prolate, or oblate, difference in the degree of orientation of such particles spoils the methodology such that the size distributions for two principal directions (height and radius for the cylinder case/long axis radius and short axis radius for the prolate and oblate cases) cannot be uniquely evaluated. As for core-shell type particles, the inner and outer radii couple to alter its form factor, so that the size distributions for them cannot be uniquely evaluated either. As a matter of fact, the size distribution is introduced with keeping constant of the ratio of the inner and outer radii for the core-shell spheres [16]. Similarly, for the core-shell cylinders [20], the size distribution in the core radius is incorporated, while the radial shell thickness is assumed to be monodisperse. For more detailed structure analyses, more experimental variations are required to gather information from different kinds of aspects, like the example shown in **Figure 6a** and **b** (parallel and perpendicular to SD). These difficulties should be overcome.

Author details

Shinichi Sakurai

Address all correspondence to: shin@kit.ac.jp

Department of Biobased Materials Science, Kyoto Institute of Technology, Matsugasaki, Sakyo-ku, Kyoto, Japan

References

[1] S. Kobayashi, M. Klaus (Eds.), Encyclopedia of Polymeric Nanomaterials, Springer, New York (2015).

[2] W. H. de Jeu, Basic X-ray Scattering for Soft Matter, Oxford University Press, Oxford, UK (2016).

[3] J. S. Pedersen, Adv. Colloid Interface Sci., 70, 171–210 (1997).

[4] M. Kim, Y. Rho, K. S. Jin, B. Ahn, S. Jung, H. Kim, M. Ree, Biomacromolecules, 12(5), 1629–1640 (2011).

[5] D. Sato, H. Ohtomo, Y. Yamada, T. Hikima, A. Kurobe, K. Fujiwara, M. Ikeguchi, Biochemistry, 55(2), 287–293 (2016).

[6] A. V. Semenyuk, D. I. J. Svergun, Appl. Crystallogr, 24, 537 (1991).

[7] T. Fujisawa, K. Inoue, T. Oka, H. Iwamoto, T. Uruga, T. Kumasaka, Y. Inoko, N. Yagi, M. Yamamoto, T. Ueki, J. Appl. Crystallogr, 33, 797–800 (2000).

[8] U-S. Jeng, C. H. Su, C.-J. Su, K.-F. Liao, W.-T. Chuang, Y.-H. Lai, J.-W. Chang, Y.-J. Chen, Y.-S. Huang, M.-T. Lee, K.-L. Yu, J.-M. Lin, D.-G. Liu, C.-F. Chang, C.-Y. Liu, C.-H. Chang, K. S. Liang, J. Appl. Crystallogr, 43, 110–121 (2010).

[9] T. Sibillano, L. De Caro, D. Altamura, D. Siliqi, M. Ramella, F. Boccafoschi, G. Ciasca, G. Campi, L. Tirinato, E. Di Fabrizio, C. Giannini, Sci. Rep., 4, 6985 (2014). doi:10.1038/srep06985

[10] S. Aida, S. Okamoto, S. Sakurai, J. Masamoto, S. Nomura, Mater. Soc. Res. Int., 7, 234 (2001).

[11] H. Matsuoka, H. Tanaka, T. Hashimoto, N. Ise, Elastic scattering from cubic lattice systems with paracrystalline distortion. Phys. Rev. B, 36, 1754 (1987).

[12] H. Matsuoka, H. Tanaka, T. Hashimoto, N. Ise, Elastic scattering from cubic lattice systems with paracrystalline distortion. II. Phys. Rev. B, 41, 3854 (1990).

[13] T. Kota, K. Imaizumi, S. Sasaki, S. Sakurai, Polymers, 3, 36–50 (2011).

[14] K. Imaizumi, T. Ono, T. Kota, S. Okamoto, S. Sakurai, J. Appl. Crystallogr., 36, 976–981 (2003).

[15] S. Tomita, N. Shimizu, N. Igarashi, H. Takagi, S. Sasaki, S. Sakurai, to be published (2016).

[16] J. Wagner, J. Appl. Crystallogr., 37, 750–756 (2004).

[17] I. Akiba, A. Takechi, M. Sakou, M. Handa, Y. Shinohara, Y. Amemiya et al., Macromolecules, 45, 6150–6157 (2012).

[18] J. S. Pedersen, C. Svaneborg, K. Almdal, I. W. Hamley, R. N. Young, Macromolecules, 36, 416–433 (2003).

[19] Y. Sanada, I. Akiba, K. Sakurai, K. Shiraishi, M. Yokoyama, E. Mylonas et al., J. Am. Chem. Soc., 135, 2574–2582 (2013).

[20] J. B. Matson, C. J. Newcomb, R. Bitton, S. I. Stupp, Soft Matter, 8, 3586–3595 (2012) (and the supporting information).

[21] S. Sakurai, S. Okamoto, T. Kawamura, T. Hashimoto, J. Appl. Crystallogr., 24, 679–684 (1991).

[22] N. D. Tien, T. P. Hoa, M. Mochizuki, K. Saijo, H. Hasegawa, S. Sasaki, S. Sakurai, Polymer, 54, 4653–4659 (2013).

[23] M. Shibayama, T. Hashimoto, Macromolecules, 19(3), 740–749 (1986).

[24] N. D. Tien, T. P. Hoa, G. Kimura, Y. Yamashiro, H. Fujiwara, M. Mochizuki, S. Sasaki, S. Sakurai, J. Phys. Conf. Ser., 272, 012007-1–012007-7 (2011).

[25] N. D. Tien, S. Sasaki, H. Masunaga, N. Shimizu, N. Igarashi, S. Sakurai, Polymer, 55, 2562–2569 (2014).

[26] N.-D. Tien, S. Sasaki, S. Sakurai, Polym. Bull., 73, 399–408 (2016).

[27] J. Scavuzzo, S. Tomita, S. Cheng, H. Liu, M. Gao, J. P. Kennedy, S. Sakurai, S. Z. D. Cheng, L. Jia, Macromolecules, 48, 1077–1086 (2015).

[28] H. Takeoka, N. Fukui, S. Sakurai, Y. Nakamura, S. Fujii, Polymer J., 46, 704–709 (2014).

[29] H. Takeoka, S. Wada, S. Yusa, S. Sakurai, Y. Nakamura, S. Fujii, J. Adhes. Soc. Jpn., 51 (S1) (special issue on WCARP-V), 255–263 (2015).

[30] Y. Chujo, K. Tanaka, Bull. Chem. Soc. Jpn., 88, 633–643 (2015).

[31] K. Kuroiwa, C. Higuma, Y. Shimogawa, H. Hachisako, S. Sakurai, Kobunshi Ronbunshu, 71, 457–466 (2014) (in Japanese).

[32] K. Kuroiwa, Y. Koga, Y. Ishimaru, T. Nakashima, H. Hachisako, S. Sakurai, Polym. J., 48, 729–739 (2016).

[33] K. Kuroiwa, T. Arie, S. Sakurai, S. Hayami, T. J. Deming, J. Mater. Chem. C, 3, 7779–7783 (2015).

X-Ray Scattering Techniques Applied in the Development of Drug Delivery Systems

Margareth Kazuyo Kobayashi Dias Franco,

Daniele Ribeiro de Araújo, Eneida de Paula,

Leide Cavalcanti and Fabiano Yokaichiya

Additional information is available at the end of the chapter

Abstract

The advances in nanotechnology have found application in different fields, such as food, agriculture, materials, chemistry, and medicine. However, one of the most important approaches is the development of nanocarriers and, in order to understand their structural organization, different physicochemical techniques have been used. In particular, small angle X-ray scattering (SAXS) and X-ray diffraction (XRD) have given important contribution to the study of organization phase of nanocarriers such as organic/inorganic nanoparticles, micelles, liposomes, cyclodextrins, polymers, and their interaction with drugs and other bioactive molecules. In this chapter, we will present theoretical aspects, experimental design, and the applications of both techniques for the development of delivery systems for bioactive molecules.

Keywords: drug delivery, diffraction, small angle X-ray scattering

1. Introduction

The term nanocarriers have been used to describe colloidal systems (emulsions, nano-spheres, nanoparticles, nanocapsules, liposomes, and micelles) and other compounds such as natural, synthetic, organic, or inorganic materials (ceramic, bioglasses, organometallic compounds, carbon or peptide nanotubes etc.) with dimensions smaller than 500 nm for use as biomaterials, depots, implants, biosensors, vaccines, and biomarkers, in chromatography separation, diagnosis or imaging, and drug delivery systems (DDS) for bioactive

compounds such as peptides, proteins, oligonucleotides, nucleic acids, etc., as shown in **Figure 1**. Those carrier systems can be formulated into various preparations including suspensions, emulsions, capsules, tablets, gels, creams, and ointments for parenteral, oral, or topical use [1].
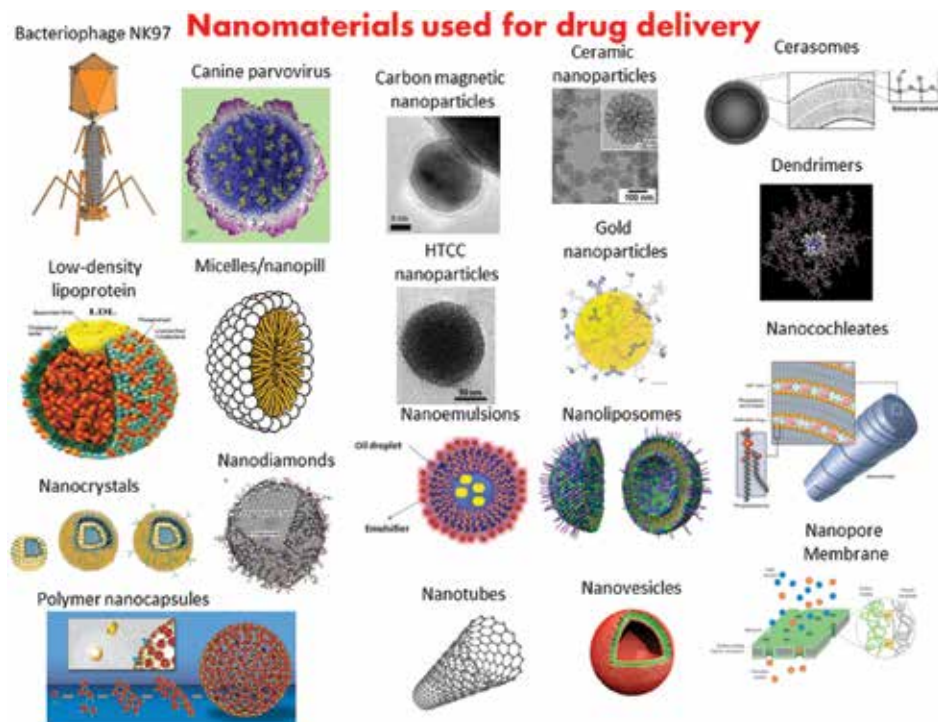

Figure 1. Examples of several drug delivery systems [2–20].

The development of new biomaterials, drug delivery systems (DDS), and modified release pharmaceutical formulations have allowed the modulation of physicochemical and biopharmaceutical properties of the several molecules, enhancing their therapeutic effects and promoting their clinical use. The different drug carriers described in the literature presented results specifically for molecules with limited aqueous or lipid solubility, low bioavailability, low stability, and high local or systemic toxicity [21].

The aim is the encapsulation of the bioactive molecule on a specific carrier destined to deliver it at a controlled rate over a prolonged period. The advantages of some DDS, such as nanoparticles, are their high circulation-residence time and drug bioavailability with enhanced therapeutic efficiency.

Despite several studies that report the physicochemical and biological applications of these nanocarriers, few studies have presented a relationship between their applications and structural aspects. In this chapter, our aim is to describe the basic concepts about X-ray scattering and its application for structural analysis of drug delivery systems.

This chapter explains the basic concepts of X-ray scattering and its applications in drug delivery systems. The basic equations for converting information obtained during the measurements in structural parameters of the object are also presented. We shall restrict ourselves to coherent and elastic small-angle X-ray scattering (SAXS), which is used in structural studies of soft condensed matter and in the X-ray diffraction (XRD) technique.

2. SAXS: small angle scattering technique

2.1. Introduction

Among drug delivery systems (DDS), carriers such as liposomes, micelles, hydrogels, and several kinds of hybrid organic-inorganic nanoparticles [22] can be found. For an effective or stable carrier, the colloidal size, which goes approximately from 1 nm to 1 μm, is an important criterion to select the delivery system that can permeate tissues, circulate with body fluids, or interact with cell membranes. Therefore, the structure is directly correlated with each function and the structural characterization of colloidal systems is in the range of the electron microscopy and X-ray scattering. In this study, we are going to discuss about small angle X-ray scattering (SAXS).

Unlike many other characterization techniques, the success of the SAXS study will highly depend on the prior knowledge available about the system. It means that one has to study thoroughly the sample preparation history, particle morphology, size distribution, aging stability, etc., before proposing SAXS method. The size distribution in the range of some hundreds of nm can be characterized by dynamic light scattering (DLS) [23] and the results can give a hint about agglomeration of the colloidal system that can favor polydispersity, which causes trouble in the resolution of the scattering signal in some cases. Mapping the aging stability is a crucial task in colloidal studies in order to have a fair referential for comparing a series of samples. Aging of colloidal systems can promote agglomeration or crystallization or even degradation and for each case, there will be a different scattering pattern. Morphology, studied using electron microscopy, prior to SAXS measurements, promotes an easier startup on the SAXS modeling and simulation. Fragile organic colloidal systems are better visualized through cryo-TEM (transmission electron microscopy) or cryofracture microscopy [24]. It is also import to know about the surface electric charges of the particles, through Zeta potential measurements [25], prior to SAXS measurements in order to facilitate the understanding of the interaction among all the sample constituents, which helps to build the most likely model structure to simulate the scattering intensity.

The SAXS technique is a nondestructive method and the experiment of scattering is relatively simple and fast. All the hard work will be charged on the treatment and analysis of the acquired data. Measurements taken for few days in a synchrotron lab will be enough for one whole year of analyzing data. Thus, the more you know about the system prior to the measurements, the more precise will be the experiment and the earlier you will be compensated by the information that can be determined through SAXS study.

2.2. Elements of SAXS theory

There are several good references for studying basic SAXS theory; the most popular is the book of Glatter and Kratky [26]. For amphiphilic systems, it is worth to check the article, also from Glatter, published in 1991 [27]; the work from Kratky on biological macromolecules, including some aspects from neutron scattering [28]; and more recent studies from our collaborators Trevisan et al. [29], showing the SAXS analysis for an example of modified liposomes after shearing preparation process, published in 2011; and the article of Oliveira et al. showing an efficient method to model and simulate SAXS intensity from unilamellar and multilamellar liposomes [30].

The SAXS technique comes from the fact that X-rays can interact with the electrons of the materials. When X-rays strike any matter, part of the energy is absorbed or transmitted. However, the part of the energy that is interesting for this technique is the one that scatters elastically (conserving the original frequency) depending on the structure of the material. The word "scattering" is already explaining everything about the method: instead of passing through the material, some photons are deviated (scattered) after the interaction with the electrons. The angle between the original direction of the photons and the deviation is called the scattering angle. The structure dimensions of the colloids are in the very size limits of the SAXS technique. The bigger the scattering objects, the smaller will be the scattering angle; this is the reason for calling this technique "small angle" scattering in contrast with the "wide angle" scattering used to study atomic distances.

The aim of the method is to study the scattering angle, or the scattering vector $\vec{q}$, in order to learn the characteristics of the object that caused the scattering. In this technique, the object is just a bunch of electrons with some structure. SAXS will give knowledge of the electronic density of the material and its spatial organization.

After X-rays strike the sample, the amplitude $A(\vec{q})$ of the scattered wave in the direction of the scattering vector $\vec{q}$ is represented by the expression:

$$A(\vec{q}) = \rho(\vec{r})e^{-i\vec{q}.\vec{r}} \tag{1}$$

where $\rho(\vec{r})$ is the average electronic density of the system and $\vec{r}$ is the position of one atom of the material. The total amplitude scattered by all atoms of the material will be represented by the following expression:

$$F(\vec{q}) = \int \rho(\vec{r})e^{-i\vec{q}.\vec{r}}d\vec{r} \tag{2}$$

which one can recognize as the Fourier transformation of the electronic density. The inverse Fourier transformation would yield the electronic density of the material, which is the very

subject of the study. But the SAXS experiment provides only the intensity of the scattered wave, which is the square modulus of the amplitude of the wave:

$$I(\vec{q}) = |F(\vec{q})|^2 \qquad (3)$$

Extracting the electronic density of the material from the intensity $I(\vec{q})$ is not a straight forward task like the inverse Fourier transformation; it does not give a unique solution because we lost information of the phase of the wave when we squared the modulus; and that is why we need the support of the complementary techniques to find a reasonable model for the electronic density of the material.

On calculating the square modulus of the wave amplitude of Eq. (3), it could be understood that the expression of the intensity will be dependent not only on the electronic density of one point of the structure, but there will be a crossing term indicating that the intensity is the sum over the pair distance distribution function (PDDF) of the system, which expresses a contrast of the electronic density. This aspect is better explained with some examples of colloidal systems that naturally have this contrast of electronic density, for example, the contrast of electrons in proteins and the solution in which they are embedded; or liposomes and the buffer where they are dispersed; or even the contrast between the hydrogels and the pores that they form.

As the interaction with electrons is the origin of the phenomenon, the more electrons the materials have, the higher will be the intensity of the SAXS signal. Organic molecules have low electronic density compared to inorganic materials, so the signal is weak and the experiment need high brilliance sources like synchrotron facilities or lab equipment with enhanced optics for the best performance.

2.3. Experiment

The routine of the experiment is as follows:

Data acquirement: a sample is kept in front of the X-ray source and the scattering intensity at all angles is collected by a detector. Several facilities are prepared with special sample holders, environment conditions, *in situ* parallel techniques, and efficient detectors, as shown in **Figure 2**.

Data treatment: the scattering curve is recovered after data treatment which removes the background scattering caused by possible air gaps, windows, slits, or other parts of the instrumentation. Vacuum chambers are strategically placed to remove air gaps and light materials as beryllium, mica, and polymer films are used as windows to minimize spurious scattering.

Modeling: from the results of complementary techniques the parameters such as particle size, interaction among compounds, crystallization, polydispersity, etc., will help to build a model for the scattering object. For example, one can take a vesicle as a core of water surrounded by lipid bilayers and this model is known as core-shell structure. The size of the core and shell,

as well as the shape of objects interacting with this core-shell phase or the particles that can exist dissolved or crystallized in water, will all be a part of the model. There are several known models to start the approach of the scattering object, for instance, hard or hollow spheres, cylinders or other shapes, and also combined models for polydispersed systems. The scattering of these objects are called form factor scattering in contrast with structure factor, which is related to the periodicity of the shapes that can exist in some systems, for example, in multi-layered liposomes.
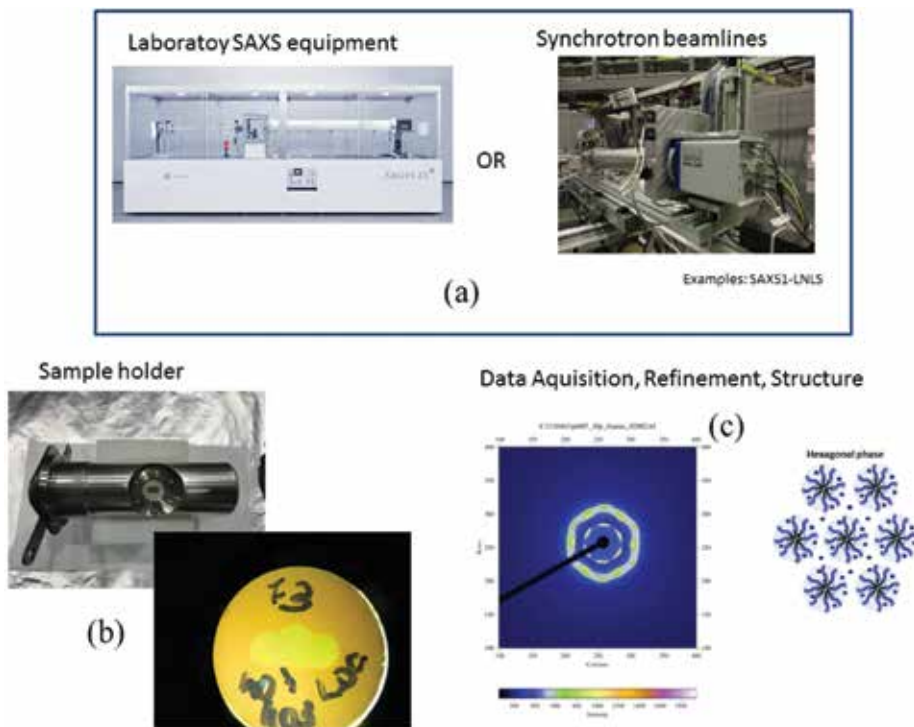

Figure 2. (a) Laboratory SAXS equipment or Synchrotron SAXS beamline can be used to characterize drug delivery systems. (b) Sample holder pictures; (c) some results from poloxamer systems used as drug delivery systems obtained using the SAXS technique [31].

Simulation: after having a model one can calculate the scattering intensity of the model, which is easier if done by computing programs. There are several software tools on the market for SAXS analysis that offer ready-to-use form factors like the ones that we commented before: hard spheres, core-shell, etc. Some software tools even offer possibilities to build your own form factor, considering more complex models.

Fitting: the final step is to compare the simulated scattering intensity with the experimental data. If they fit together, this is the end of the process and one can assume that the chosen model is a reasonable structure supported by all experimental results, not only SAXS, but everything else that helped to build the model. If the simulation does not fit the experimental

data, one can make adjustments on the model, make another simulation and compare again until it fits as good as they want.

In the study of Brzustowicz and Brunger [32], they used a model of hard spheres to fit the dispersion of stearoyloleoyl phosphatidylserine (SOPS) micelles in buffer. This study used a monodisperse micelle sample with the main purpose to propose a different approach for analyzing lipid bilayer SAXS data. The graph of **Figure 3** of that paper shows a perfect fitting between calculated and experimental data. The results were good to determine the size of the inner core of the liposome and the electronic density profile across the membrane.

A successful SAXS analysis was reported in the work of some collaborators Gasperini et al. [33] after Balbino et al. [34]. In both cases, a biopolymer was inserted in liposome dispersions, hyaluronic acid (HA), and DNA, respectively. The results indicate that there are similarities at low concentration of incorporation of polymer inside the liposome dispersion. The negatively charged polymers bonded together neighbor unilamellar cationic liposomes like an electro-static plastic glue. At higher concentrations of polymer, one can observe distinct behavior for these two biopolymers: DNA succeeded to disrupt the lipid membrane promoting the organization of multilamellar liposomes; and HA was able to coat individual unilamellar liposomes stabilizing the dispersion.

The SAXS analysis of these two studies, together with the results of the complementary techniques, was able to reveal all these details. For this, the liposome preparation was carefully controlled to have minimum polydispersity and the systems were studied strictly under the aging stability period. Several methods were used as complementary techniques such as DLS, zeta potential, TEM, cryo-TEM, and chromatography to help build the structure model to calculate the simulated scattering to be compared to the SAXS experimental data. Reasoning aspects were considered to minimize fitting parameters to increase the reliability of the results.

For other nanocarriers, such as thermosensitive poloxamer (or Pluronics® -PL)-based micelles and hydrogels (see **Figure 3**), SAXS technique have presented important contributions for understanding the structural changes after the incorporation of drugs/carriers or the formation of systems composed of PL with different hydrophilic-lipophilic balance (HLB).

SAXS studies have reported the formation of wormlike micelles for PL-P84 [35]; the gelation mechanisms and micelle packing under hexagonal and body-centered cubic phases for PL-P85 and PL-F88, respectively. However, for the PL-F88/PL-P85 mixture, the destabilization of the hexagonal phase after PL-F88 addition [36], a PL with higher HLB (28) compared to PL-P85 (16) was observed [37]. Other authors also reported SAXS analysis for PL-based binary hydrogels (PL concentrations ranging from 20 to 30% m/v) with different HLB values, such as PL-F127/PL-F68 [38] and PL-F127/PL-L81 [39], being observed in the formation of a hexagonal phase at physiological temperature and their purpose as sumatriptan and ropivacaine delivery systems for application by infiltrative routes. However, for fluid systems (with PL concentrations lower than 18% m/v) the binary micelles composed of PL-F127/PL-L81 presented a lamellar phase structural organization, even after the incorporation of the drug chlorproma-zine [40].
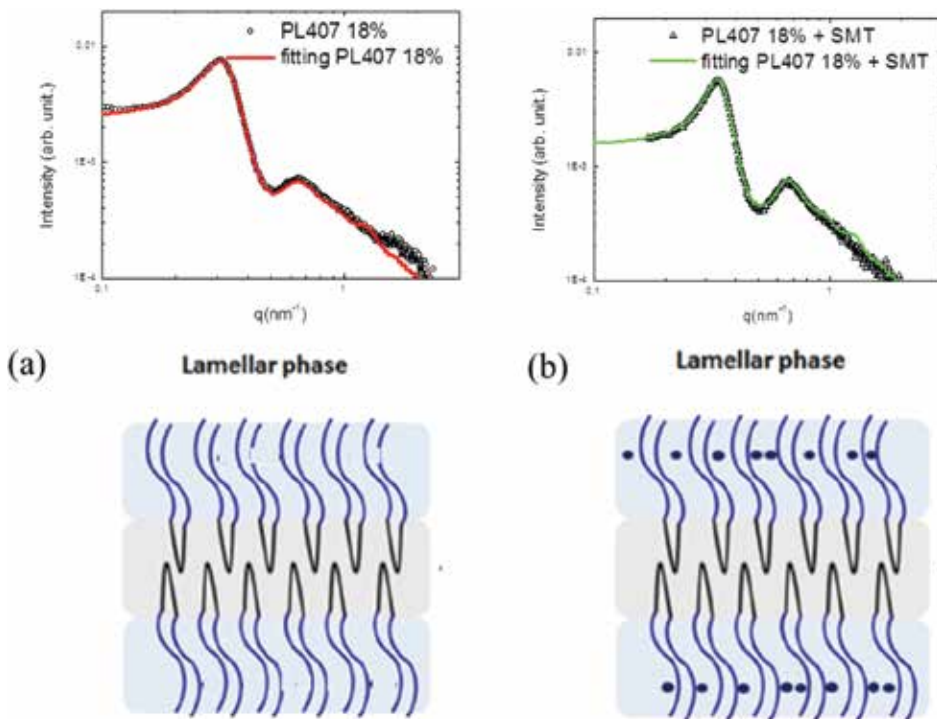
Figure 3. Example of successful SAXS analysis of a drug delivery system based on poloxamers (a) poloxamer without drug; (b) poloxamer with sumatriptane (SMT).

In fact, the drug incorporation of PL-based systems, studied by SAXS, has been highlighted in the literature. In a recent work, Avachat and Parpani [41] described the formulation of liquid crystal nanoparticles for efavirenz oral delivery. The study showed the formation of cubossomes after the incorporation of PL-F127 and phytantriol, a cosmetic ingredient. Chen et al. [42] studied the acetaminophen and bifonazole crystallization mechanism within polyethylene glycol (PEG), polypropylene glycol (PPG), and PL-F127 matrices, observing an improvement of crystallization rate for both drugs.

Another innovative approach relates to the combination of different carrier systems (natural and synthetic, for example) that perform different functions, usually synergistic, in the same pharmaceutical formulation. These new carriers, hybrid systems, can provide (in combination) levels of structural organization and different biopharmaceutical properties of the individual carriers, being used as a strategy to overcome limitations in relation to the physicochemical properties (such as aqueous solubility), pharmacokinetic (control local absorption and/or uptake to the bloodstream), pharmacodynamic (increased drug duration of action) or toxicological properties (improvement in biocompatibility, reduced local and systemic toxicity) [43, 44]. In this sense, the interactions and the structural patterns formed between PL and cyclodextrins, inorganic nanoparticles, and natural or synthetic polymers have been described in the literature.

SAXS studies revealed a face-centered cubic phase for PL-F127 hydrogels (30 wt%) after interaction with PEG 6000 or PEG 35000 and polyvinylpirrolidone [45]. On the other hand, the PL supramolecular structure was destabilized after incorporation of Fe_3O_4 nanoparticles into PL-F108 hydrogels, showing that the thermogelation is due to the clustering of nanoparticles into a fractal network [46]. In a different manner, a cubic symmetry was observed by SAXS characterization of the systems composed of ordered mesoporous silica nanoparticles in PL-F127 hydrogels [47].

For other nanocarriers, such as cyclodextrins (CD), different structural arrangements have been described, being also related to the delivery capability of those systems. Simões et al. [48] reported the development of a syringeable hydrogel composed of PL-F127 and α-CD for the delivery of vancomycin. In others reports, the incorporation of α-CD, studied by SAXS, showed a significant change on gelation behavior of PL-F68 and PL-F127 due to the formation of polypseudorotaxane (interaction of the hydrophobic PL unimers with the hydrophobic cavity of CDs, stabilized by noncovalent bonds, van der Waals forces, and interactions between the hydroxyl groups of adjacent CDs and hydrophilic polyethylene glycol polymer unimers) supramolecular complexes, in a similar manner observed in the interaction between β-CD and PL-F108 [49, 50].

3. X-ray diffraction

3.1. Introduction

One of the biggest challenges of the pharmaceutical science is to understand how the drugs interact with the cells in the body. This study is directly linked to physical and chemical properties of the drugs and the drug delivery systems. Therefore, it is important and necessary to use appropriate techniques for characterization, suitable for the development and improvement of the efficacy of the drugs.

For this reason, X-ray diffraction techniques stands out amongst several characterization techniques to distinguish the solid forms, like salt, polymorphs, solvates and cocrystal, and amorphous forms. X-ray diffraction provides information about the long ordering crystalline samples and also short ordering in vitreous or amorphous materials. This technique helps to relate the X-ray diffraction patterns with the structural ordering or disordering in materials science. It is worth to note that there is a clear difference between the crystalline materials, and amorphous and vitreous materials when observed via X-ray diffractometer. In the X-ray diffraction pattern for crystalline materials, several sharp peaks can be observed. On the other hand, for vitreous or amorphous materials the diffraction pattern display typically three or less halos (large peaks).

In 1999, Wunderlich [51] proposed a classification system based on the structural ordering and molecular packing present in the organic forms using three ordering parameters: translation, orientation, and conformation, as summarized in **Table 1**.

Solid form	Translation	Conformation	Orientation
Crystal	Long order	Long order	Long order
Condis Crystal	Long order	Short order	Long order
Plastic Crystal	Long order	Short order	Short order
Liquid Crystal	Short order	Short order	Long order
Vitreous or amorphous	Short order	Short order	Short order

Table 1. Classification system of solid forms as described by Wunderlich [51].

Solid-form crystals with a long ordering structure can be indexed characterized using X-ray powder diffraction technique (XRPD) due to its unique combination of order parameters. Although the solid forms of amorphous and vitreous materials do not exhibit any long ordering structure, they can be identified and characterized by their local molecular (short) ordering.

Some applications of X-ray diffraction techniques used to analyze the properties of the solid state of the drugs are: (1) characterizing the ordering in the active pharmacological ingredient (API); (2) identifying the existence forms in the API; (3) determining the solid form of API in the final drug product; (4) determining the physical and chemical stabilities; (5) identifying the components existing in the drug product; (6) detecting impurities or contaminants in the drug product; (7) monitoring changes in the sold form of the drug due to the fabrication; and (8) analyzing quantitatively and qualitatively the final drug product.

Based on the sensitivity of the technique to the ordering of structure, with appropriate data obtained from XRPD, it is possible to determine the structure of the solid forms and also the packing of the molecules in the solid. This information contributes significantly in the understanding of the chemical content in the solid state of the drug. Moreover, it is also important from the regulatory perspective.

3.2. Elements of diffraction theory

The X-ray diffraction technique measures the X-ray photons after the collision with the electronic cloud of the sample that changes the photon trajectory, though keeping the same phase and energy of the incoming photon. This is the key concept of the coherent elastic scattering process.

In organic samples, there are some specific facts that must be considered:

1. The application of a mathematical simplification known as first Born approximation is important and useful in the explanation of the X-ray diffraction process.

2. As expected, the interaction of the solid forms in the organic samples with incoming X-ray beam is weak and the amplitude of the multiple radiation scattering is almost negligible when compared to the simple radiation scattering.

3. In the presence of crystal defects, grain boundary or disordering systems, the multiple radiation scattering become even less significant.

Based on these considerations and their limits, we can model the process of diffraction as a Fourier transform of the electronic density inside the sample.

While each atom is considered a specific source of scattering process, the molecules can also be reduced to specific sources of scattering, considering that the distribution of the electronic density of a collective set of atoms is the sum of electronic density distribution attributed to centralized atoms individually.

Although the atoms in a molecule are not necessary the same as the free atoms, they are frequently considered as being free atoms. In this way, the ordering of the specific centers of scattering in the real space produces a group of diffraction events in the reciprocal space that corresponds to the intensity of the peaks.

A d spacing between the punctual centers (molecules) in the real space corresponds to a peak of the $\frac{2\pi}{d}$ spacing in the reciprocal space (also called Q-space).

As the Fourier transform can be applied in any molecular translational ordering that exists inside a solid form, the diffracted peak positions can be expressed in terms of d-space, Q-space or, more common, in 2θ.

In order to cause a constructive interference of the scattered waves, it is necessary that the Bragg's law be obeyed. The Bragg's law relates the X-ray scattering angle θ with the d-spacing parameter, as shown in **Figure 4**.
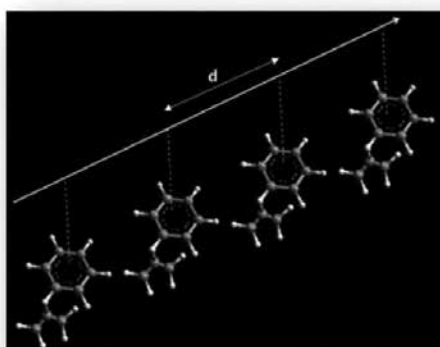

Figure 4. Representation of a simple periodic array of an organic molecule with a single orientation and conformation. The molecules are periodic, separated by a constant spacing d.

$$n\lambda = 2d \sin\theta \tag{4}$$

where λ is wavelength of the incident radiation; n is an integer number; d is interplanar distance to a set of *hkl* planes of the crystalline structure; θ is X-ray incident angle, as shown in **Figure 5**.
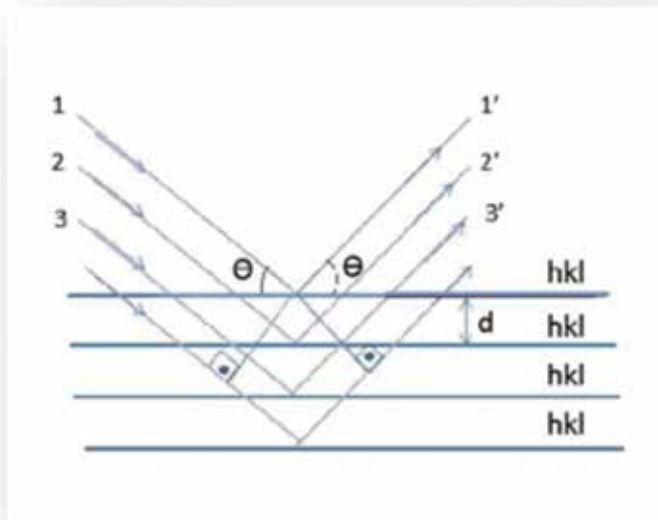

Figure 5. Schematic representaion of the Bragg's law for the X-ray diffraction.

The samples analyzed by the X-ray diffraction technique can be in the powder form or solid with plane surfaces.

Analyzing the diffractogram of a polycrystalline sample, we verify that the peaks related to different set of planes show different intensities. If we build a diffractogram using just geometric aspects (Bragg's law), we will expect that all the peaks display the same intensity since all of them are subjected to constructive interference.

However, there are several physical aspects that influence the intensity of the peaks in a diffractogram, such as:

- Atomic scattering factor (this value indicates how an atom can scatter to a certain angle in a certain wavelength).

- Structure factor (quotient of amplitudes of scattered waves by all the atoms in a unit cell and the amplitude of the scattered wave by on electron).

- Multiplicity factor (there are planes that, for having the same interplanar distance, scatter to the same peak. This is the case, for instance, of 100, 010, and 001 planes in a cubic cell. Adding also the planes, qith −1 instead of 1, we have in total six planes contributing to the same peak, implying in a factor of multiplicity 6).

In order to get the expression for the intensity, we need three more correction factors: (a) Lorentz factor, (b) polarization factor, and (c) temperature factor. The first two are related to the geometric corrections that affect the diffracted intensity. Finally, the last one is related to temperature process that can cause shift in the position of the peaks, decreasing the intensity of the peaks and increasing the background.

A more complete explanation of the expression for the intensity and the factor that affects the intensity can be found in the reference of this chapter [52–57].

3.3. Experiment

The optics and the instrumentation used in the X-ray diffraction technique are directly related to the type of the X-ray source. However, we can define three generic elements: X-ray source, sample (including here the sample holder and sample environment, such as furnaces and cryostat), and detector.

An optimized experiment has as premise the following three conditions:

- Suitable X-ray source with efficient beam conditioning.

- A sample properly prepared, an optimized sample holder with low background and minimum influence in the measurement, and an appropriated sample environment that allows a stabilization of the sample in certain conditions as for example, temperature.

- Optimized detection systems (with or without optics to reduce background and to focus the scattered beam in order to improve the signal to noise ratio).

3.3.1. Experimental procedures of X-ray diffraction

The diffractograms show the diffracted intensities as a function of experimental parameter 2θ (angle between the diffracted and undeviated X-ray waves). The intensity is typically expressed in counts or counts per seconds while the peaks are listed as positions in degrees or in d-spacing (measured in Å or nm).

3.4. Crystalline materials

For materials with long ordering structure (crystalline materials) the diffractograms show sharp peaks, which the shape and the width depend on the instrument geometry where the data were collected. In **Figure 6**, we display an example of a diffractogram of a drug delivery system, β-cyclodextrin. The measurements were performed in a conventional diffractometer with Cu radiation, and, it was possible to perform a Rietveld refinement to obtain the final structure (as shown in the insert of **Figure 6**).

The range of the measurement for crystalline materials depends on the aim of the study. For example, when we study big molecules (for instance, biological samples), it is beneficial to measure at low angles, allowed by the geometry of the instrument (approximately 0.5° can be reached in a typical laboratory configuration in modern instruments or less than 0.5° using synchrotron sources).
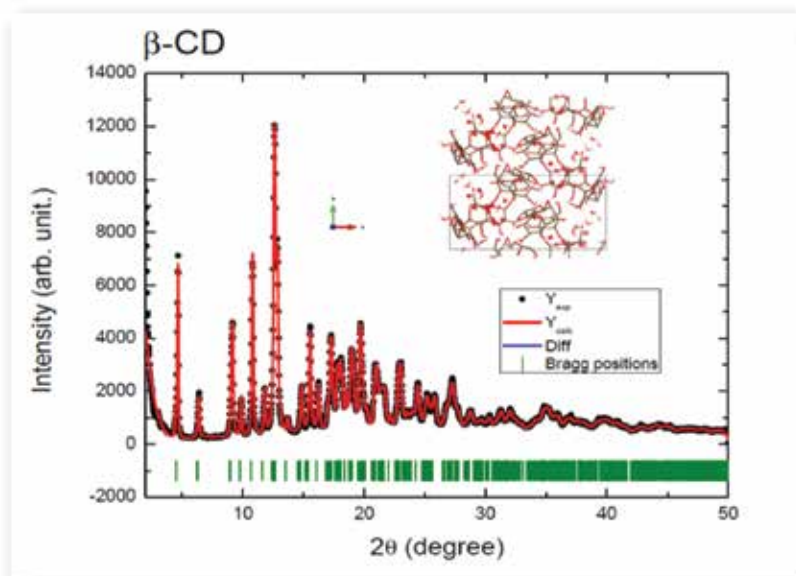
Figure 6. Diffractogram of crystalline β-cyclodextrin measured in a conventional diffractometer using Cu radiation. Also, Rietveld refinement was performed in order to obtain the crystal structure.

The time for collecting the data varies according to the application, for example, to study polymorphism in drugs. Good diffraction patterns of the crystalline material, using conventional X-ray instruments can be obtained in the range of 2–10 min per step. In configurations that use high efficiency X-ray sources (synchrotron) to samples mounted in a planar configuration, the collected time can be less than 1 min. The X-ray diffraction technique that is typically nondestructive (if the flux of X-ray is too high, we can observe the radiation damage effect that can affect the sample), needs 2–20 mg of sample, depending on the configuration geometry of the instrument and the application.

The quality of the sample and its correct preparation in order to perform the XRPD experiment influences significantly in the characterization or identification of the crystalline material. We can cite two factors related to the preparation of the sample that can affect the results:

1.   Orientation of the crystallites: ideal sample has a big number of random oriented crystallites.

2.   Statistics of particles orientation: the reproducibility of an X-ray pattern depends on the statistic of the particles orientation when the preferred orientation limits the degree in which the pattern represents the structure.

For these reasons, one must evaluate the statistics of the particle orientation and the degree of the preferred orientation before starting the identification and analysis.

The effect of the preferred orientation of the crystallites in a sample can be observed as the increase in the intensity on some of the peaks and the decrease in the intensity on others. The

variation of the intensity is proportional to the degree of preferred orientation. In some cases, the sample holder geometries of the diffractometer can also generate different set of relative intensities.

Using samples that show a relatively small number of crystallites results in a diffractogram with poor statistics. If the small population of the big crystallites does not represent all the possible orientations, the relative intensities will not be reproducible.

The effect of the preferred orientation on the particle orientation can be minimized by spinning the sample holder.

3.5. Amorphous materials

Amorphous materials (disorder, vitreous or amorphous materials) have characteristic diffractograms with large halos and do not show sharp peaks in the XRPD patterns. **Figure 7(c)** and **(d)** displays examples of a typical diffractogram of an amorphous material.

However, using suitable computational methods it is possible to extract structural information from this X-ray diffraction patterns. In this case, it is necessary a large angular range, typically from 1 to 100° in 2θ. Besides, the time to collect the data must be longer than the frequently
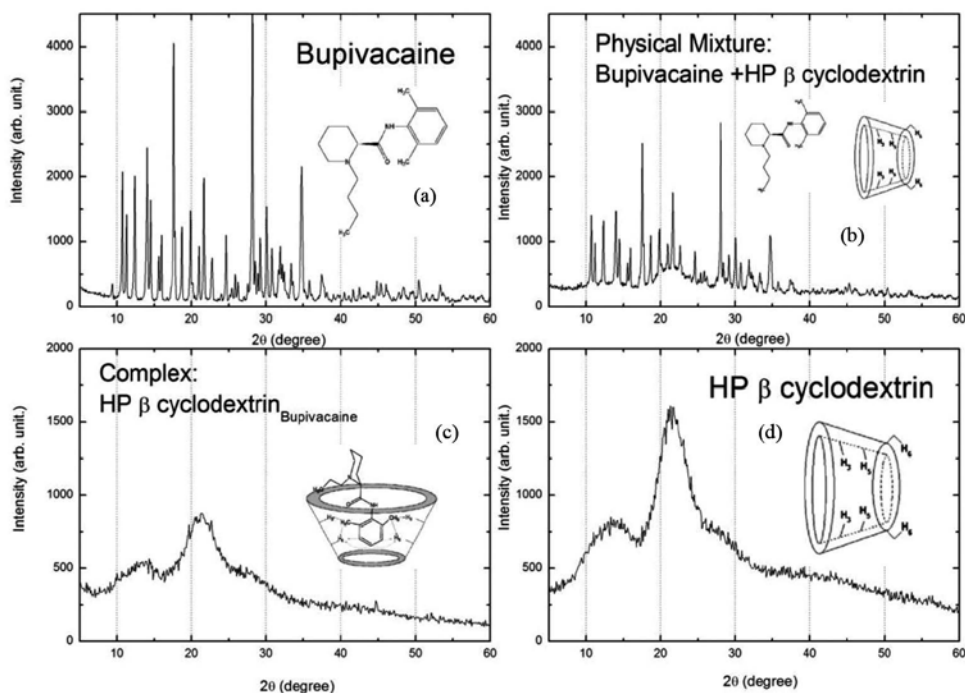

Figure 7. (a) Diffractogram of bupivacaine (BPV); (b) a physical mixture of BPV and HP-β-cyclodextrin; (c) complex of BPV and HP-β-cyclodextrin and (d) diffractogram of HP-β-cyclodextrin. Observe the amorphous diffractogram of the drug delivery systems, HP-β-cyclodextrin and the complex (drug delivery with drug).

used in conventional diffraction, due to the signal-noise ratio in an amorphous X-ray pattern be typically poor.

In order to obtain a good diffractogram through the X-ray diffraction technique for amorphous samples, usually one needs 5–100 mg of the samples, depending on the geometry of the instrument.

XRPD patterns, for crystalline materials or for amorphous materials, contain artifacts from the instrument, for example, background functions from the instrument, fingerprints from the sample holder, incoherent scattering (Compton), polarization and Lorenz effects, and air scattering. A relatively small pattern generated from the samples means that these artifacts represent a portion bigger of the overall diffracted intensity. Therefore, computational methods used to analyze amorphous materials are more sensitive to experimental artifacts.

3.6. Instrumentation

X-ray diffraction instrument used typically in conventional laboratories consists in three parts: (1) X-ray source; (2) sample holder, and (3) detector system.

There are several X-ray sources that it can be possible to use in a conventional laboratory, but the most common is the copper source (Cu). Slits and optics are used to focus the X-ray incident beam in the sample and also, the X-ray diffracted waves scattered from the sample into the X-ray detector. In order to minimize artifacts from the sample (mentioned before), usually, the sample holder is spinning. The X-ray detectors can be punctual, linear or area. The detector area has the advantage of being fast in the data acquisition and also makes it possible to evaluate the statistics of the particle orientation and preferred orientation of the samples, through the analysis of the Debye rings in the detector.

Synchrotron sources can be used to measure special systems in order to collect high quality data.

Diffractometers can be operated typically in reflection (Bragg-Brentano) or transmission (Debye-Scherrer). In the reflection setup, the incident beam is reflected from the surface of the sample and the scattered beam is focused into the detector.

The X-ray penetrates several layers below the surface in organic samples. This means that the average diffracted surface is located below the surface of the sample. This penetration effect can yield to an error of a displacement of the peak positions in the diffraction pattern of the tenth of a degree

Errors caused by the displacement of the peaks happen due to the difficulty in the preparation of the sample in the sample holder (**Figure 8(b)**). The surface of the sample must be leveled with the surface of the flat sample holder (where the instrument is focused). Although computational methods can be used to correct the position of the peaks, the proper preparation of the sample is the only solution to solve this problem.
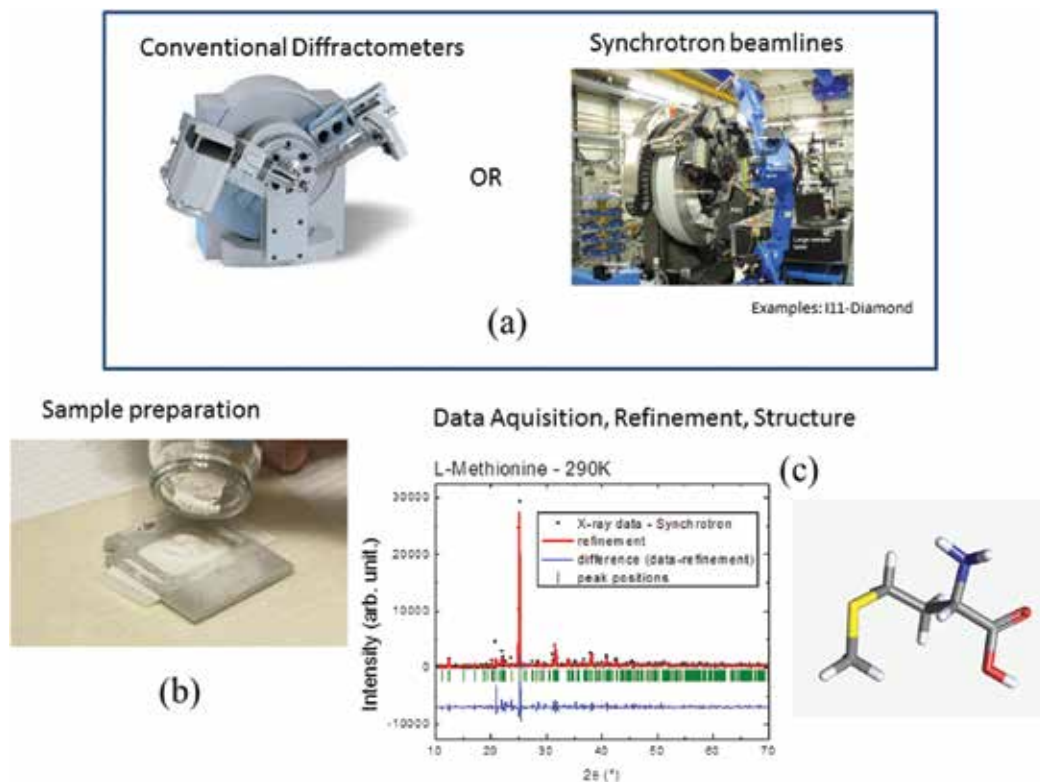
Figure 8. (a) Laboratory XRPD equipment or Synchrotron XRPD beamline can be used to characterize drug delivery systems and drugs; (b) preparation of samples; (c) some results from a biological material, L-methionine, measured at XRPD synchrotron beamline. Also observed the Rietveld refinement and the possible structure of the sample.

Usually measurement at low angles (below 2.5° in 2θ) is not appropriate due to the limitation of the instrument used mainly for big molecules, where it is expected to find reflections in the range from 0 to 2.5°. Measurements using the transmission setup can solve this limitation, when the instrument is properly set. In the transmission setup the X-ray incident beam pass through the sample. This configuration is possible for organic samples due to its relative transparence for X-rays. In this case, the sample does not need to be leveled with the sample holder surface, but the thickness of the sample is important and can cause errors in the displacement of the peaks. Besides, it is essential in this configuration that the sample holder is transparent to X-rays. In the case of amorphous materials, it is necessary an extra effort to operate the instrument in order to improve the quality of the data.

Acknowledgements

Author details

Margareth Kazuyo Kobayashi Dias Franco, Daniele Ribeiro de Araújo, Eneida de Paula, Leide Cavalcanti and Fabiano Yokaichiya

*Address all correspondence to: margareth_franco@yahoo.com.br; mkfranco@ipen.br

1 Brazilian Multipurpose Reactor, Nuclear and Energy Research Institute, IPEN, São Paulo, SP, Brazil

2 Human and Natural Sciences Center, Federal University of ABC, Santo André, SP, Brazil

3 Biochemistry and Tissue Biology Department, Biology Institute, State University of Campinas-Campinas, SP, Brazil

4 Chemical Engineering, State University of Campinas-Campinas, SP, Brazil

5 Department of Quantum Phenomena in Novel Materials, Helmholtz Zentrum Berlin, Berlin, Germany

References

[1]   Neubert. Potentials of new nanocarriers for dermal and transdermal drug delivery. Eur. J. Pharm. Biopharm. 2011;77(1–2).

[2]   Solarex. SX-40 & SX-50 Photovoltaic Modules [Internet]. http://www.trichord-inc.com/pricing/frames/content/solar_power.pdf. 1999

[3]   Mc Grath S, van Sinderen D (editors). (2007). Bacteriophage: Genetics and Molecular Biology (1st ed.). Caister Academic Press. https://en.wikipedia.org/wiki/Bacteriophage(ISBN 978-1-904455-14-1)

[4]   http://www.virology.wisc.edu/virusworld/images/cpv-half-nuc.jpg. 2014.

[5]   Grass RN, Robert N, Athanassiou EK, Stark WJ.Covalently functionalized cobalt nanoparticles as a platform for magnetic separations in organic synthesis". Angew. Chem. Int. Ed. 2007;46(26): 490912. doi:10.1002/anie.200700613.https://en.wikipedia.org/wiki/Magnetic_nanoparticles.

[6]   https://en.wikipedia.org/wiki/Nanoparticle#/media/File:Mesoporous_Silica_Nano-Particle.jpg. 2015.

[7]   http://www.omicsonline.org/articles-images/2161-0398-2-105-g001.gif.

[8]   http://www.foresight.org/Conference/MNT7/Papers/Cagin3/.

[9] http://cmb.gu.se/english/research/organic-and-medicinal-chemistry/Biomedical_Photonics/projects/gold-nanoparticles-.

[10] http://pubs.acs.org/doi/abs/10.1021/bm2010774.

[11] http://image.slidesharecdn.com/lipoproteins-150424045513-conversion-gate02/95/lipoproteins-8-638.jpg?cb=1429869399.

[12] http://www.pharmatutor.org/articles/nanocochleate-novel-bypass-of-conventional-drug-elivery-system.

[13] http://www.ebioscience.com/media/images/resources/knowledge-center/product-line/efluor/efluor-nc/nc-technology/efluor-nanocrystal-compostion.png.

[14] http://www.photonics.com/Article.aspx?AID=57396.

[15] http://blogs.nottingham.ac.uk/malaysiaknowledgetransfer/files/2013/06/Siva001.jpg.

[16] http://www.keystonenano.com/platform/liposomes.

[17] http://www.nature.com/nnano/journal/v3/n2/fig_tab/nnano.2008.13_F1.html.

[18] http://web.mit.edu/lms/www/images/Fig.%205B%20sm.jpg.

[19] http://www.carbonallotropes.com/carbon-nanotubes/39-single-wall-carbon-nanotubes.html.

[20] http://www.nature.com/nnano/journal/v2/n4/fig_tab/nnano.2007.90_F1.html.

[21] Oshiro A, da Silva DC, Santos ACM, Akkari ACS, de Araujo, Daniele R. Development of drug-delivery systems: strategies for new pharmaceutical formulations based on liposomal and micellar systems. Supramolecular Chemistry, Nanotechnology (1st ed.). São Paulo: Atheneu In: Alve WA. (Org.). 2014;vol.1; pp. 249–264.

[22] Holowka E, Bhatia SK. Drug Delivery, Material Design and Clinical Perspective. Springer-Verlag New York. 2014. ISBN 978-1-4939-1998-7, DOI: 10.1007/978-1-4939-1998-7

[23] Egelhaaf SU, Wehrli E, Muller M, Adrian M, Schurtenberger P. Determination of the size distribution of lecithin liposomes: A comparative study using freeze fracture, cryoelectron microscopy and dynamic light scattering. J. Microsc (Oxf). 1996;184:214–228. (ISSN 0022-2720)

[24] Evjen TJ, Hupfeld S, Barnert S, Fossheim S, Schubert R, Brandl M. Physicochemical characterization of liposomes after ultrasound exposure-mechanisms of drug release. J. Pharm. Biomed. Anal. 2013;78–79:118–122. DOI: 10.1016/j.jpba.2013.01.043

[25] Zuidam NJ, de Vrueh R, Crommelin Daan JA. (2003). Characterization of Liposomes In: Liposomes: A Practical Approach. Torchilin, Vladimir P, Weissig, Volkmar (eds). Oxford University Press, London (2nd ed.) pp. 31–78.

[26] Glatter O, Kratky O. Small Angle X-Ray Scattering. Academic Press, London. 1982.

[27] Glatter O. Scattering studies on colloids on biological interest (Amphiphilic Systems). Progr. Colloid. Polym. Sci. 1991;84:46–54.

[28] Kratky O. The world of neglected dimensions, SAS of X-ray and neutrons of biological macromolecules. Nova Acta Leopoldina NF 55; 1983.

[29] Trevisan J, Cavalcanti LP, Oliveira CLP, de la Torre L, Santana MH. Technological aspects and scalable enhanced processes for production of functional cationic liposomes as delivery system in gene therapy. In: Non-viral Gene Therapy. Yuan, X. (ed), Intech, Croatia OPEN ACCESS: http://dx.doi.org/10.5772/17869. (ISBN 978-953-307-538-9)

[30] Oliveira CLP, Gerbelli BB, Silva ERT, Nallet F, Navailles L, Oliveira EA, Pedersen JS. Gaussian deconvolution: A useful method for a form-free modeling of scattering data from mono- and multilayered planar systems. J. Appl. Crystallogr. 2012;45:1278–1286.

[31] http://www.azom.com/equipment-details.aspx?EquipID=3095. 2016.

[32] Brzustowicz MR, et al. X-ray scattering from unilamellar lipid vesicles. J. Appl. Cryst. 2005;15:38:126–131.

[33] Gasperini A, Puentes-Martinez X, Balbino T, Rigoletto T, Corrêa G, Cassago A, Portugal R, de La Torre LG, Cavalcanti LP. Association between cationic liposomes and low molecular weight hyaluronic acid. Langmuir (2015) 31:3308.

[34] Balbino TA, Gasperini AAM, Oliveira CLP, Azzoni A, Cavalcanti LP, de la Torre L. Correlation of the physico-chemical and structural properties of pDNA/cationic liposome complexes with their in vitro transfection. Langmuir. 2012;28:11535.

[35] Castelletto V, Parras P, Hamley IW, Bäverbäck P, Pedersen JS, Panine P. Wormlike micelle formation and flow alignment of a Pluronic block copolymer in aqueous solution. Langmuir. 2007;23(13):6896–6902.

[36] Artzner F, Geiger S, Olivier A, Allais C, Finet S, Agnely F. Interactions between poloxamers in aqueous solutions: Micellization and gelation studied by differential scanning calorimetry, small angle X-ray scattering, and rheology. Langmuir. 2007;23(9): 5085–5092.

[37] Alexandridis P, Hatton T. Poly(ethylene oxide)-poly(propylene oxide)-poly(ethylene oxide) block copolymer surfactants in aqueous solutions and at interfaces: Thermodynamics, structure, dynamics, and modeling. Coll. Surf. A: Physicochem. Eng. Asp. 1995;96:1–46.

[38] Santos Akkari AC, Ramos Campos EV, Keppler AF, Fraceto LF, de Paula E, Tófoli GR, de Araujo DR. Budesonide-hydroxypropyl-β-cyclodextrin inclusion complex in binary poloxamer 407/403 system for ulcerative colitis treatment: A physico-chemical study from micelles to hydrogels. Colloids. Surf. B: Biointerfaces. 2016;38:138–147.

[39] Oshiro A, da Silva DC, de Mello JC, de Moraes VW, Cavalcanti LP, Franco MK, Alkschbirs MI, Fraceto LF, Yokaichiya F, Rodrigues T, de AraujoDR. Pluronics f-127/l-

81 binary hydrogels as drug-delivery systems: Influence of physicochemical aspects on release kinetics and cytotoxicity. Langmuir. 2014;30(45):13689–13698.

[40] Mello JC, Moraes VW, Watashi CM, da Silva DC, Cavalcanti LP, Franco MK, Yokaichiya F, de Araujo DR, Rodrigues T. Enhancement of chlorpromazine antitumor activity by Pluronics F127/L81 nanostructured system against human multidrug resistant leukemia. Pharmacol. Res. 2016;111:102–112.

[41] Avachat AM, Parpani SS. Formulation and development of bicontinuous nanostructured liquid crystalline particles of efavirenz. Colloids. Surf. B: Biointerfaces. 2015;126:87–97.

[42] Chen Z, Liu Z, Qian F. Crystallization of bifonazole and acetaminophen within the matrix of semicrystalline, PEO-PPO-PEO triblock copolymers. Mol. Pharm. 2015;12(2): 590–599.

[43] Kopeček J, Yang J. Smart self-assembled hybrid hydrogel biomaterials. Angew. Chem. Int. Ed. Engl. 2012;51:7396–7417.

[44] Zhang L, Zhang N. How nanotechnology can enhance docetaxel therapy. Int. J. Nanomed. 2013;8:2927–2941.

[45] Ricardo NM, Ricardo NM, Costa Fde M, Bezerra FW, Chaibundit C, Hermida-Merino D, Greenland BW, Burattini S, Hamley IW, Nixon KS, Yeates SG. Effect of water-soluble polymers, polyethylene glycol and poly(vinylpyrrolidone), on the gelation of aqueous micellar solutions of Pluronic copolymer F127. J. Colloid. Interface. Sci. 2012;368(1):336–341.

[46] Nambam JS, Philip J. Thermogelling properties of triblock copolymers in the presence of hydrophilic Fe_3O_4 nanoparticles and surfactants. Langmuir. 2012;28(33):12044–12053.

[47] Kerkhofs S, Willhammar T, Van Den Noortgate H, Kirschhock CE, Breynaert E, Van Tendeloo G, Bals S, Martens JA. Self-assembly of Pluronic F127-silica spherical core-shell nanoparticles in cubic close-packed structures. Chem. Mater. 2015;27(15):5161–5169.

[48] Simões SM, Veiga F, Torres-Labandeira JJ, Ribeiro AC, Sandez-Macho MI, Concheiro A, Alvarez-Lorenzo C. Syringeable Pluronic-α-cyclodextrin supramolecular gels for sustained delivery of vancomycin. Eur. J. Pharm. Biopharm. 2012;80(1):103–112.

[49] Pradal C, Jack KS, Grøndahl L, Cooper-White JJ. Gelation kinetics and viscoelastic properties of Pluronic and α-cyclodextrin-based pseudopolyrotaxane hydrogels. Biomacromolecules. 2013;14(10):3780–3792.

[50] Shih KC, Li CY, Li WH, Lai HM. Fine structures of self-assembled beta-cyclodextrin/ Pluronic in dilute and dense systems: A small angle X-ray scattering study. Soft. Matter. 2014;10(38):7606–7614.

[51] Wunderlich B. A classification of molecules and transitions as recognized by thermal analysis. Thermochim. Acta. 1999;340/41:37–52.

[52] Als-Nielsen J, McMorrow D. Elements of Modern X-ray Physics. Wiley, New York ; Chichester. 2001; xi:318 p.

[53] Cullity BD, Stock SR. Elements of X-ray Diffraction. Addison-Wesley Reading, MA. 1978

[54] Klug HP, Alexander LE. X-ray Diffraction Procedures for Polycrystalline and Amorphous Materials. Wiley, New York; 2nd ed, 1974; xxv:966 p.

[55] Warren BE. X-ray Diffraction. Dover Publications, New York, 1990; vii:381p.

[56] Young RA, The Rietveld Method (International Union of Crystallograhy Oxford University Press, [Chester, England] Oxford; New York, 1993; x: 298 p.

[57] Zachariasen WH, Theory of X-ray Diffraction in Crystals (J. Wiley and Sons, Inc. Chapman and Hall, Ltd, New York London, 1945;vi: 1 l 255 p.

High-Resolution X-Ray Diffraction

High-Resolution X-Ray Diffraction of III–V Semiconductor Thin Films

Hédi Fitouri, Mohamed Mourad Habchi and Ahmed Rebey

Additional information is available at the end of the chapter

Abstract

In this chapter, we will address the structural characterization of III–V semiconductor thin films by means of HRXRD. We first give an overview on the basic experimental apparatus and theory element of this method. Subsequently, we treat several examples in order to determine the effect of doping, composition and strain on structural properties of crystal. Analysed layers were grown by metal organic vapour phase epitaxy (MOVPE). Films treated as examples are selected in order to bring the utility of characterization technique. Here, we investigate GaAs/GaAs(001), GaAs:C/GaAs(001), GaN/Si(111), GaN:Si/Al$_2$O$_3$(001), GaAsBi/GaAs(001) and InGaAs/GaAs(001) heterostructures by using different scans for studying numerous structural layers and substrate parameters. Different scan geometries, such as ω-scan, $\omega/2\theta$-scan and map cartography, are manipulated to determine tilt, deformation and dislocation density induced by mismatch between layer and substrate. This mismatch is originated from the difference between the chemical properties of two materials generated by doping or alloying. Such HRXRD measurements are explored through the angular spacing between peaks of the substrate and layer. The half of full width maximum (HFWM) of peak layer intensity is a crucial qualitative parameter giving information on defect density in the layer.

Keywords: HRXRD, thin films, III–V semiconductors, alloys, stress, reciprocal map

1. Introduction

Over the past decade, the epitaxy of structures based on III–V materials has emerge to become of vital commercial importance within the electronics, optoelectronics and telecommunication industries. With rapid developments of epitaxy apparatus (such as molecular beam epitaxy or metal organic chemical vapour epitaxy) and *in situ* diagnostics (such as RHEED and

reflectometry), the elaborated active part of heterostructure has now come in the vicinity of idealism. However, such deviation from ideal properties (structural, optical or electrical) can reduce the device response. In this way and for economical reasons, it is desirable to characterize the as-grown layers prior to further processing. Indeed, high-resolution of X-ray diffraction (HRXRD) is now one of the widely used tools for non-invasive determination of the composition, thickness and perfection of the epitaxial layers of compound semiconductors. Recently, there had been great interest in the use of this technique with different scan geometries.

In this chapter, we will address the structural characterization of III–V semiconductor thin films by means of HRXRD. We first give an overview on the basic experimental apparatus of this method. Subsequently, we treat several examples in order to determine the effect of doping, composition and strain on structural properties of crystal.

2. Experimental details and theory element

All layers investigated in this work are elaborated by metal organic vapour phase epitaxy (MOVPE) technique [1–8].

For arsenide layers, we use a Bruker D8 diffractometer. An X-ray tube with a copper cathode generates the incident beam (1.54056 Å). In order to obtain highly monochromatic incident beam, we use a monochromator constituted by four Ge(022) crystals which gave a resolution of $\frac{\Delta\lambda}{\lambda} < 1.5\times10^{-4}$. The scattered beam can be detected by a scintillation point detector as reported in the left of **Figure 1**. The layer, that shall be examined, is mounted on the sample holder. As shown in the right of **Figure 1**, we denote ω as the angle between X-ray beam and the crystal surface, 2θ, the detector position, φ, the rotation angle around the normal of crystal and τ (or χ), the inclination angle of crystal in a perpendicular plane to the surface. This configuration gives a coupled and uncoupled scans, such as ω-scan (or rocking curve scan) and $\omega/2\theta$ scan.

For nitride layer, HRXRD measurements have been performed with a Bede 200 diffractometer equipped with a four-crystal monochromator in Si[220] mode.
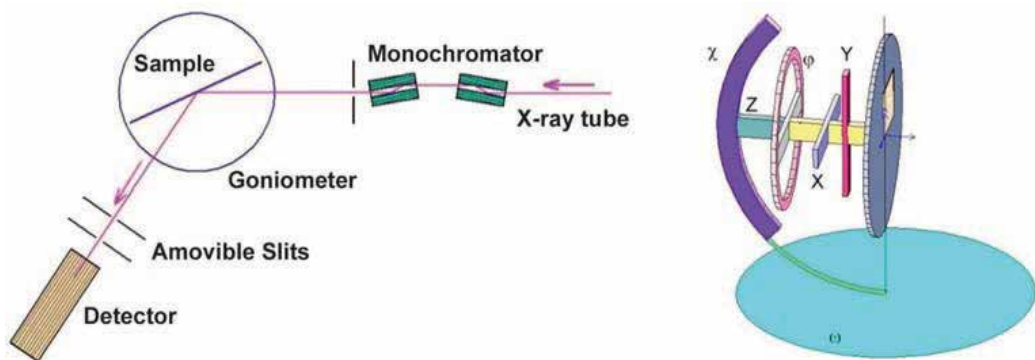

Figure 1. In the left, optical path of X-ray beam for the used goniometer. In the right, goniometer axes.

The simple form of Bragg equation for the lattice planes with Miller indices (*hkl*) and the distance d_{hkl} between two such adjacent planes is given by

$$2d_{hkl} \sin \theta = n\lambda \qquad (1)$$

where:

- For cubic lattice with lattice constant $a, d_{hkl} = \frac{a}{\sqrt{h^2+k^2+l^2}}$,

- For hexagonal lattice with lattice constant a and c, $d_{hkl} = \frac{a}{\sqrt{\frac{4}{3}(h^2+k^2+hk)+(\frac{a}{c})l^2}}$.

Differentiation of Bragg equation and subsequent division of the result by the same equation yields the differential Bragg equation

$$\frac{\Delta d_{hkl}}{d_{hkl}} + \Delta\theta . \cot(\theta) = \frac{\Delta\lambda}{\lambda} \qquad (2)$$

In our case, the spectral width of the incident beam is neglected ($\frac{\Delta\lambda}{\lambda} \sim 0$).

3. Application for thin films

3.1. Bulk films and substrates

Bulk substrates are characterized by a perfect crystallographic structure with an insignificant defect density. In HRXRD measurements, they have been used as a reference for Bragg angular measurements. But it is vital to minimize intrinsic and extrinsic effects, such as tilt substrate or tilt substrate-to-holder sample (due to inaccurate sample mounting).

As an example, in order to determine the disorientation of GaAs substrate, the (004) rocking curves peak angles (ω_S) were taken for some azimuthal angle φ as shown in **Figure 2**. As mentioned earlier, ω_S variation follows the relation: $\omega_s(004) = \langle \omega_s \rangle + A\cos(\varphi - \varphi_0)$.

where A is the tilt or the disorientation to the absolute crystallographic substrate orientation.

Similarly, $\chi(004) = \langle \chi \rangle + A\sin(\varphi - \varphi_0)$ or $\chi(004) = \langle \chi \rangle - A\sin(\varphi - \varphi_0)$.

The best fit of experimental data by expression reported below allows the values of $\langle \omega_s \rangle = 33.0308°$ and $A = 0.472°$. By using Bragg's law, we can measure the lattice parameter of GaAs substrate $a_s = \frac{2\lambda_{CuK\alpha1}}{\sin\langle\omega_s\rangle} = 5.6526\mathring{A}$. The manufacturer indicates that this commercial substrate is exactly orientated to (001) with a tolerance of ±0.5° and the lattice parameter is of $5.6533\mathring{A}$ corresponding to a Bragg angle of 33.028°. The difference between the two Bragg angles represents an error of about 0.003°. Also, the value of tilt A is in the same order of the tolerance given by the substrate producer.

3.2. Homoepitaxy

Homoepitaxy is the growth of a layer on the substrate where the two materials have the same physical characteristics (Si/Si, GaAs/GaAs, etc.). Such a structure is characterized by small full-

width at half-maxima (FWHMs) of measured peaks when growth is perfectly optimized and no supplementary information is given about the layer properties.
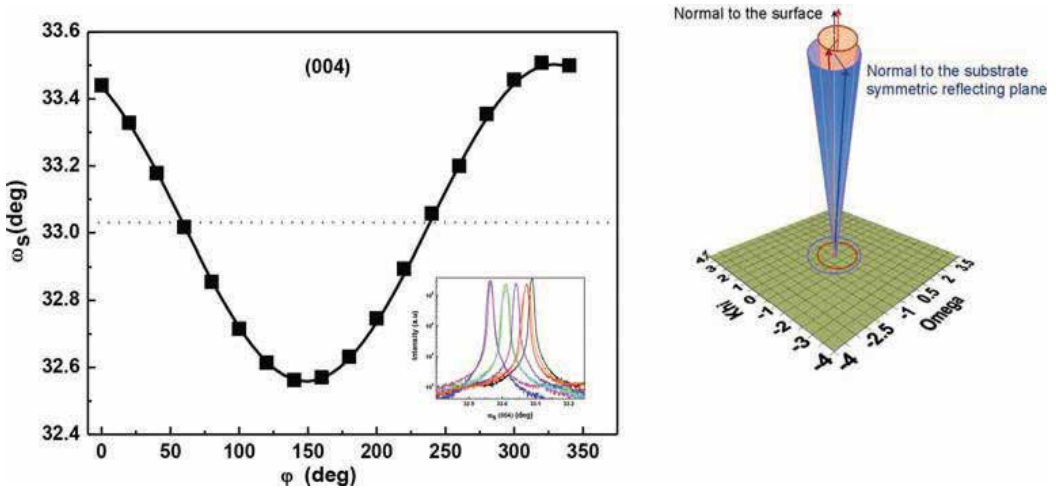

Figure 2. In the left, measured Bragg angle GaAs substrate of (004) rocking curves as a function of the azimuthal angle φ fitted by (the solid line) a sinusoidal equation. In the inset a series of rocking curves are shown. In the right, illustration of ω-scan around the normal to the substrate.

Doping of semiconductors is required to improve the electrical properties of material. In numerous applications, it is necessary to dope strongly n+ or p+ any part of the structure. Indeed, for tunnel effect or to obtain ohmic contact in GaAs, doping levels above 10^{19} cm^{-3} were needed. This requirement gives rise to a modification in structural properties of the doped layer. Yet, this deviation to ideal structure is clearly observed when atomic covalent radius of impurity is smaller or higher compared to atomic radius of matrix constituents. As an example, the doping of GaAs by carbon (C) gives rise to tetragonal distortion of GaAs caused by smaller covalent radius of C (r_c = 0.77 Å) compared to those of gallium (r_{Ga} = 1.26 Å) and arsenic (r_{As} = 1.20 Å). HRXRD is sensitive to this smaller deviation and will be used to determine the doping concentration.

The perpendicular lattice mismatch of C-doped GaAs was investigated by measuring (004) reflection and according to the following relation:

$$\varepsilon^{\perp} = \left(\frac{\Delta a}{a}\right)^{\perp} = -\Delta\theta_B\cot(\theta_B) \tag{3}$$

where $\theta_B = 33.028°$ is the Bragg angle for (004) reflection.

On the other hand, in order to investigate the conditions of strain relaxation we have measured the parallel lattice mismatch $\Delta a_{//}$. Indeed, to find the in-plane lattice mismatch, an asymmetric (±1, ±1, ±5) reflection should be determined. The inclination angle φ is between a reflection from a lattice plane and the surface. The measurement of a reflection can be carried out at high

angle $\theta_B + \varphi$ or at a low angle $\theta_B - \varphi$. We can calculate the components of lattice mismatch from the measured differences in Bragg angle and lattice-plane orientation with regard to the substrate according to [9]:

$$\varepsilon^{\perp} = \frac{\Delta a^{\perp}}{a_{GaAs}} = \Delta\varphi tg\varphi - \Delta\theta \cot\theta_B \tag{4}$$

$$\varepsilon^{//} = \frac{\Delta a^{//}}{a_{GaAs}} = -\Delta\varphi \cot\varphi - \Delta\theta \cot\theta_B \tag{5}$$

In our case $\theta_B = 45.064°$ and $\varphi = 15.791°$.

For more details, let $\Delta\omega_a$ be the angular spacing between peaks of the substrate and of C-doped GaAs layer in $\omega/2\theta$ curve, and $\Delta\omega_b$ the same quantity measured after rotating the crystal by 180° around the normal to the wafer surface. Then, for (115) reflection

$$\Delta\varphi = \frac{1}{2}(\Delta\omega_a - \Delta\omega_b), \tag{6}$$

$$\Delta\theta_B = \frac{1}{2}(\Delta\omega_a + \Delta\omega_b). \tag{7}$$

The double determination of $\varepsilon^{\perp}$ from (004) and (115) reflections gives a more precision on its values than that of $\varepsilon^{//}$.

Based on this result, it is possible to determine the compensation ratio θ of our films using the Vegard's law in the strained form [10, 11].

$$\left(\frac{\Delta a^{\perp}}{a_{GaAs}}\right)_{strained} = \left(\frac{1+\upsilon}{1-\upsilon}\right)\left(\frac{\Delta a\perp}{a_{GaAs}}\right)_{relaxed} = 1.9\left(\frac{\Delta a\perp}{a_{GaAs}}\right)_{relaxed}. \tag{8}$$

We assume that the substituted carbon in the gallium site (C_{Ga} usually used to estimate the compensation) is the dominant cause of the compensation described by [12, 13]

$$\left(\frac{\Delta a^{\perp}}{a_{GaAs}}\right)_{relaxed} = \frac{4}{\sqrt{3}a_{GaAs}N}(\Delta r_{As} + \Theta\Delta r_{Ga})\frac{p_H}{(1-\Theta)} \tag{9}$$

where $\Delta r_{As} = -0.43$ Å and $\Delta r_{Ga} = -0.49$ Å are the difference between the covalent radii of C and As and Ga, respectively. $N = 2.22 \times 10^{22}$ cm^{-3} is the number of gallium or arsenic atoms per cm^3 in pure GaAs crystal and $\upsilon = 0.31$ is the Poisson's ratio.

Figure 3 illustrates a comparison between experimental data results and curves calculated for strained or relaxed states and with different compensation ratios. Using this dependence between $\frac{\Delta a^{\perp}}{a_{GaAs}}$ and p$_H$, we extrapolate the compensation ratio for any layer. We remark that the values deduced, using this consideration, are in the same order than that deduced by Hall Effect or SIMS measurements.
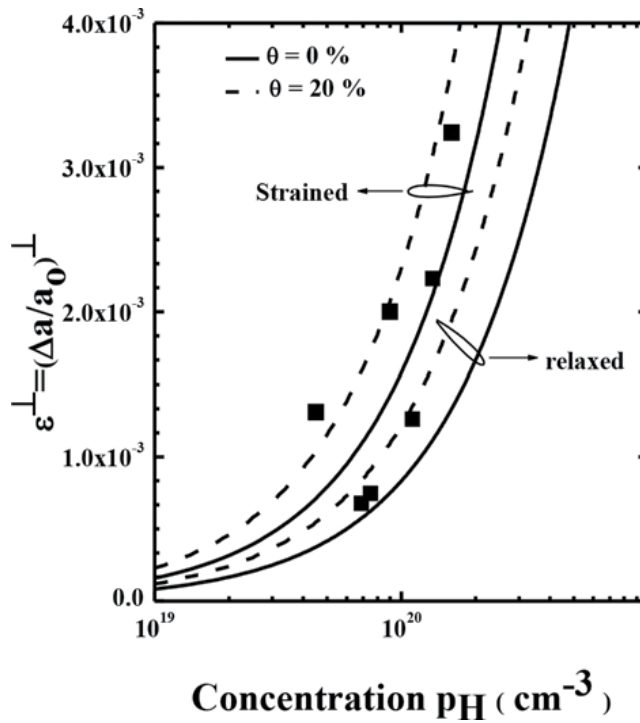
Figure 3. Perpendicular lattice mismatch ($\varepsilon^{\perp}$) of GaAs:C epilayers on GaAs substrates as a function of hole concentration p_H. The lines represent the predicted contraction based on Vegard's law for two values of compensation ratios $\theta = 0$ and $\theta = 0.25$.

3.3. Heteroepitaxy

Heteroepitaxy is the growth of a layer on the substrate where the two materials have different physical characteristics such as GaAs/Si, GaAs/Ge, GaN/Al$_2$O$_3$, etc. This means that the under-lying substrate and the epitaxial layer are different materials with typically different lattice constants and perhaps even different crystal symmetry. Generally, this structure is character-ized by misfit mismatch which generates stress and structural defects. In order to be accom-modating to the substrate, the layer stays at less energetic equilibrium state which gives rise to appearance of tilt, twist and curvature of the system {layer + substrate}. HRXRD technique is able to determine these parameters.

3.3.1. Undoped GaN

III-Nitrides and related alloys cover a wide wavelength domain ranging from the red to the ultraviolet. Their interesting properties such as large and direct band gap make them attractive for the development of optoelectronic devices as well as high temperature and high power electronic applications. The MOVE growth of these materials is completed by using various substrates. However, the lack of suitable lattice matched substrate constitutes the major obsta-cle for further improvement in GaN material properties. Several attempts have been achieved for GaN growth on silicon substrate. Indeed, this choice is motivated by the availability with

low cost, the large size and high electrical and thermal conductivities of silicon. But, the success of GaN layer epitaxy requires a special growth procedure by using different processes (buffer layer, SiN treatment, etc.) in order to reduce the damage effects.

In this section, we focus on GaN layer grown on silicon substrate Si(111) where mismatch is of about 17%. This difference leads to the formation of a large number of defects (dislocations, cracks, etc.) and gives rise to layer mosaicity.

The GaN mosaicity can be usually described by two components of the misorientation: one is the tilt of c-axis with respect to the growth direction and the other is the twist of the columns orientation about the c-axis. GaN (00.l) ω-scans reflect the mosaic structure of the tilt among the crystallites. GaN (h0.l) ω-scans reflect the mosaic structure of twist between the crystallites. For symmetric (00.l) reflections, the full-width at half-maximum (FWHM) of the X-ray rocking curve (XRC) which characterize the tilt, was found to be around 1800 arcs. Note that both tilt and twist mosaics contribute to the rocking curve width of asymmetric (h0.l) reflections. For twist measurement, it is necessary to measure a series of reflections and extrapolate to an inclination angle χ of 90°. The plot of FWHM versus sin (χ) gives rise to an average twist of about 1.9° (**Figure 4**). The average twist was determined as half FWHM extrapolated to sin (χ) = 1. This high value of the twist can be explained by the interaction between hillocks of GaN during the nucleation process or dislocations which lead to a broad rocking curve width of GaN reflections.
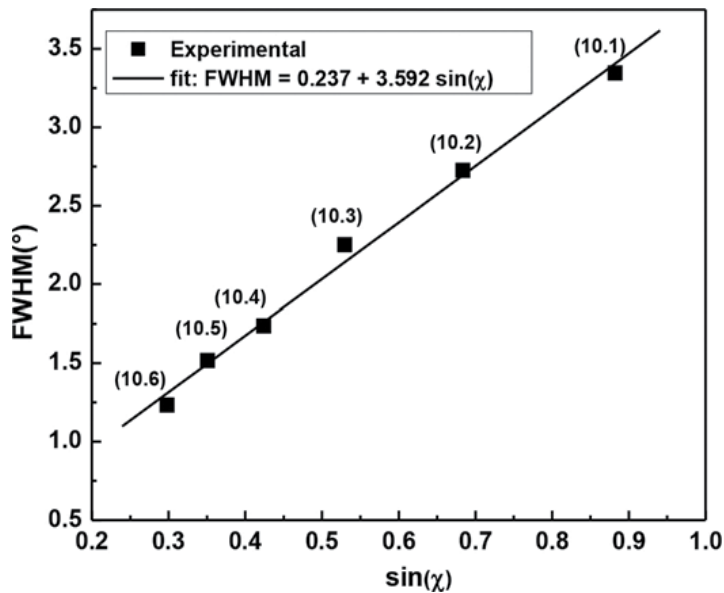

Figure 4. Evolution of FWHM (h0.l) plane reflections as a function of inclinations (χ) referring to (00.l) plane. The solid line represents the best linear fit of experimental data.

3.3.2. Si doped GaN

In order to study the effect of Si-doping on stress in GaN layers, HRXRD and Raman spectra measurements were carried out. **Figure 5** shows HRXRD patterns measured in $\theta/2\theta$ scan mode.
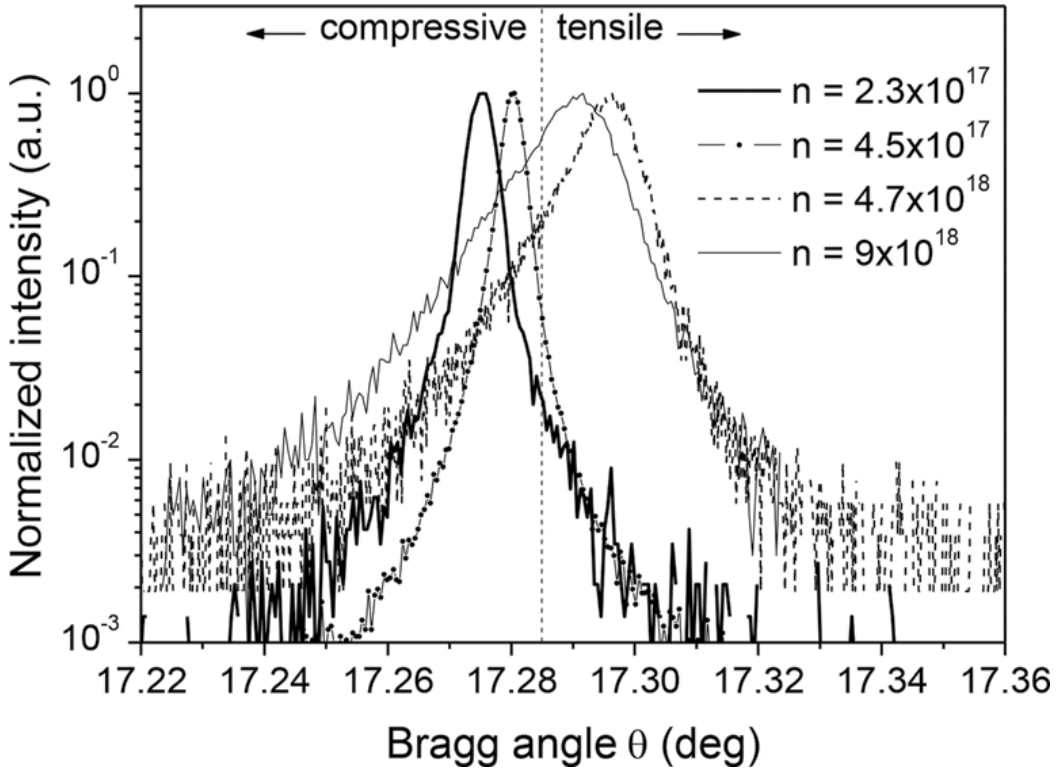
Figure 5. ω-scans of the Si-doped GaN samples.

The θ position shifts to the higher angle corresponding to smaller c lattice constant when Si concentration increases. The asymmetric shape of the ω-scan for high doping levels can be attributed to a stress gradient normal to the sample surface [14]. The in-plane stress $\sigma_{//}$ can be roughly determined from the relationships [15].

$$\sigma_{//} = \frac{a-a_0}{a_0} \left(C_{11} + C_{12} - 2 \frac{C_{13}^2}{C_{33}} \right), \tag{10}$$

where C_{ij} are the elastic constants of GaN (C_{11} = 390 GPa, C_{12} = 145 GPa, C_{13} = 106 GPa, C_{33} = 398 GPa) [16]. a_0 is the lattice constant for strain-free bulk GaN (a_0 = 3.189 Å). The values of the a lattice parameter, measured by HRXRD, and the corresponding stress values $\sigma_{//}$ show that the incorporation of silicon not only leads to stress relaxation in GaN layers, but also induces tensile stress ($\sigma_{//} > 0$) for doping levels higher than 1.6×10^{18} cm^{-3}. According to our PL data analysis (not shown here), we attribute the strong band gap reduction in the Si-doped GaN layers is essentially due to the relaxation of stress in these layers.

The effect of silicon doping on the mechanism of stress relaxation and defect formation in GaN is still under discussion. One plausible explanation is that the relaxation increases with Si-induced defects formed during the cool-down process [17, 18]. Thus, we can assume that the incorporation of silicon leads to increase of the dislocation density in the GaN epilayer. Note that the dislocation densities in GaN-based materials have been generally measured by

transmission electron microscopy (TEM) and etch pit densities (EPDs). However, as non-destructive method, X-ray rocking curves (ω-scans) can be used to measure the dislocation densities with accuracy equal to TEM and EPDs. The theory elements of this technique are described by Gay et al. [19] and Hordon and Averbach [20], for the case of highly dislocated metal crystals and extended by Ayers [21] to the case of zinc-blende semiconductors.

The model developed by Ayers uses the rocking curve line width broadening owing to threading dislocations for calculation of their densities. Then, the square of the measured rocking curve line width β_m for the (hkl) reflection can be written as [21]:

$$\beta_m^2(hkl) = K_\alpha + K_\varepsilon \tan^2\theta \tag{11}$$

where $K_\alpha = 2\pi\ln(2b^2D)$, $K_\varepsilon = 0.09\,b^2D\,|\ln(210^{-7}cm\sqrt{D}|$, b is the length of the burgers vector and D is the dislocation density. K_α is the rocking curve broadening owing to angular rotation at dislocations. K_ε is the broadening produced by strain surrounding dislocations.

The plot of β_m^2 versus $\tan^2\theta$ should give rise to a straight line. The dislocation densities can be independently calculated from the slope (K_ε) as well as the intercept (K_α). The obtained results based on the two ways should be identical. A plot according to last equation for various X-ray peaks is shown in **Figure 6**. As predicted by the model, the symmetric and asymmetric reflections are on a single straight line. Dislocation densities calculated according the Ayers model from the slopes and intercepts of these linear fits are shown in **Figure 7**.

AFM data corresponding to the densities of surface depressions and pinned steps are also given for comparison. It is well known that the surfaces of GaN layers grown by MOVPE are typically dominated by these two kinds of dislocation mediated surface structures [22]. So, as seen in **Figure 7**, the dislocation densities calculated from the slopes ($D_\varepsilon = 8.4 \times 10^8$ to 7.1×10^9 cm^{-2}) are in same order of magnitude with that obtained by AFM measurements ($D_{AFM}=1.3 \times 10^9$ to 8×10^9 cm^{-2}). The lack of internal consistency (D_ε slightly different from D_α) may be explained by the existence of sources of rocking curve broadening other than dislocations that give rise to different relative amounts of rotational and strain broadening [21].

3.4. Alloys

The III–V materials have raised a fundamental attention in the field of optoelectronics and rapid electronics. Particularly, the alloy semiconductors have an exceptional amount of interests owing to the possible adjustment of band gap and lattice parameter by changing chemical composition. Recently, the technological progress of elaboration and process techniques provides a great opportunity to design new structure architecture and quantum nanostructure based on non-conventional semiconductor materials. This fact requires a suitability of characterization tools adapted to this advance.

3.4.1. GaAsBi alloy as a new material

Owing to the large size and core electronic structure of Bi atom, Bi-containing semiconductor alloy materials exhibit a small or negative band gap. The interesting properties of III–V-Bi alloy offer a great opportunity for possible design in optoelectronic application devices. Recent

results from various groups demonstrated that GaAs$_{1-x}$Bi$_x$ thin films can be produced by molecular beam epitaxy (MBE) [23–25] or by MOVPE [1, 2, 26–28]. Further, GaAs$_{1-x}$Bi$_x$ alloy presents temperature insensitivity of band gap required in the resolution of problems of the lasing wavelength fluctuations. The quality of epitaxial compound film is governed by thickness uniformity, degree of alloying and substrate temperature. Precisely, the growth behaviour of GaAs$_{1-x}$Bi$_x$ was quite different from that of usual ternary semiconductor alloys such as GaInAs and AlGaAs. A very narrow growth conditions are reported by comparison between structural and optical characterizations. In this way, HRXRD is comely tool to investigate the structural properties of this material.
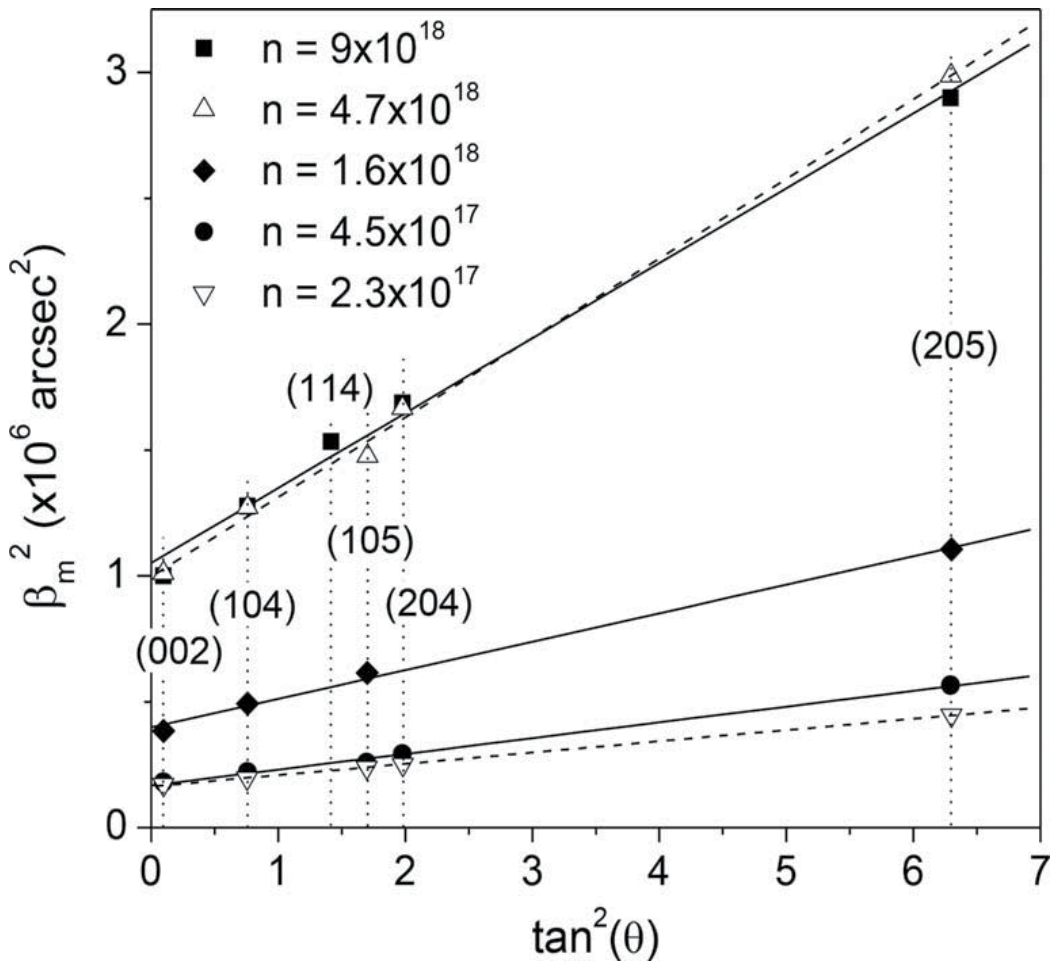

Figure 6. Square of rocking curve line width β_m (*hkl*) versus tan$^2\theta$ for Si-doped GaN samples.

Figure 8 shows the diffraction pattern in the θ –2θ scan of X-ray diffraction measurement for a GaAs$_{1-x}$Bi$_x$ layer grown on p-type GaAs substrate. The spectrum shows three resolved peaks located at 31.627, 66.048 and 65.528° which are associated with the plane diffraction of (002)

and (004) GaAs and (004) GaAs$_{1-x}$Bi$_x$, respectively (detail is shown in the inset figure). No other phases were identified.
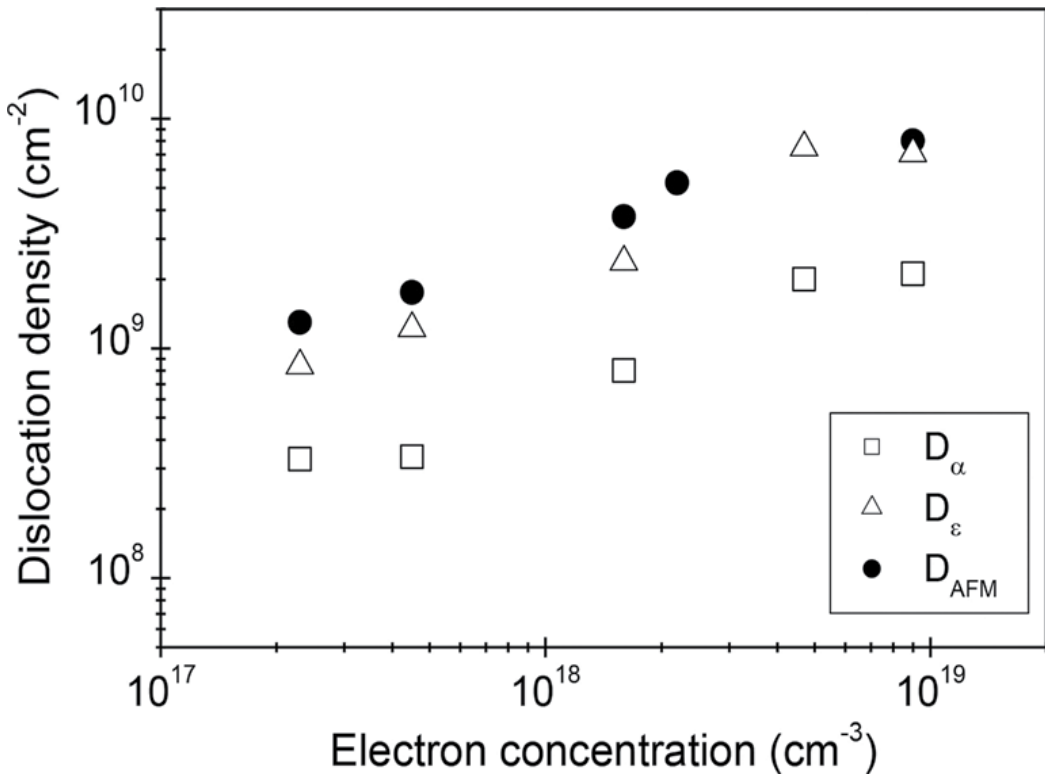

Figure 7. Dislocation densities calculated according to Ayers model from slopes (D_ε) and intercepts (D_α). AFM data are given for comparison.

HRXRD measurements of symmetric (004) and asymmetric (115) plane diffractions were carried out in order to determine the lattice parameter of GaAs$_{1-x}$Bi$_x$ and then Bi composition, as shown in **Figure 9**. In fact, the presence of two peaks relative to the layer and substrate diffractions, Pendellösung oscillations, seen in the wings of peaks, reveals a smooth and coherent interface. From these oscillations, we can calculate the layer thickness from Bragg's law: $t = \frac{\lambda \gamma_H}{\Delta \omega \sin(2\theta_B)}$. The period ($\Delta \omega$) is independent of scattering power of layer composition. $2\theta_B$ is the scattering angle, λ is the wavelength of the X-ray radiation and $\gamma_H = \sin(\theta_B + \varphi)$. φ is the angle between the diffraction planes and the surface.

The lattice constants in growth direction ($a_\perp$) and in the plane ($a_{//}$) of GaAs$_{1-x}$Bi$_x$ layer were calculated from the peak separation ($\Delta \theta_B$) between GaAs and GaAs$_{1-x}$Bi$_x$. $a_\perp$ is deduced from the spacing of the layer (004) plane (d_{004}) in the form of $a_\perp = 4\,d_{004}$ using a symmetric reflection (004). From asymmetric reflection (115), $a_{//}$ is deduced from the spacing of the layer (115) plane (d_{115}), in the form of $a_{//} = \sqrt{2}\left[\frac{1}{d_{115}^2} - \frac{25}{a_\perp^2}\right]^{\left(-\frac{1}{2}\right)}$.
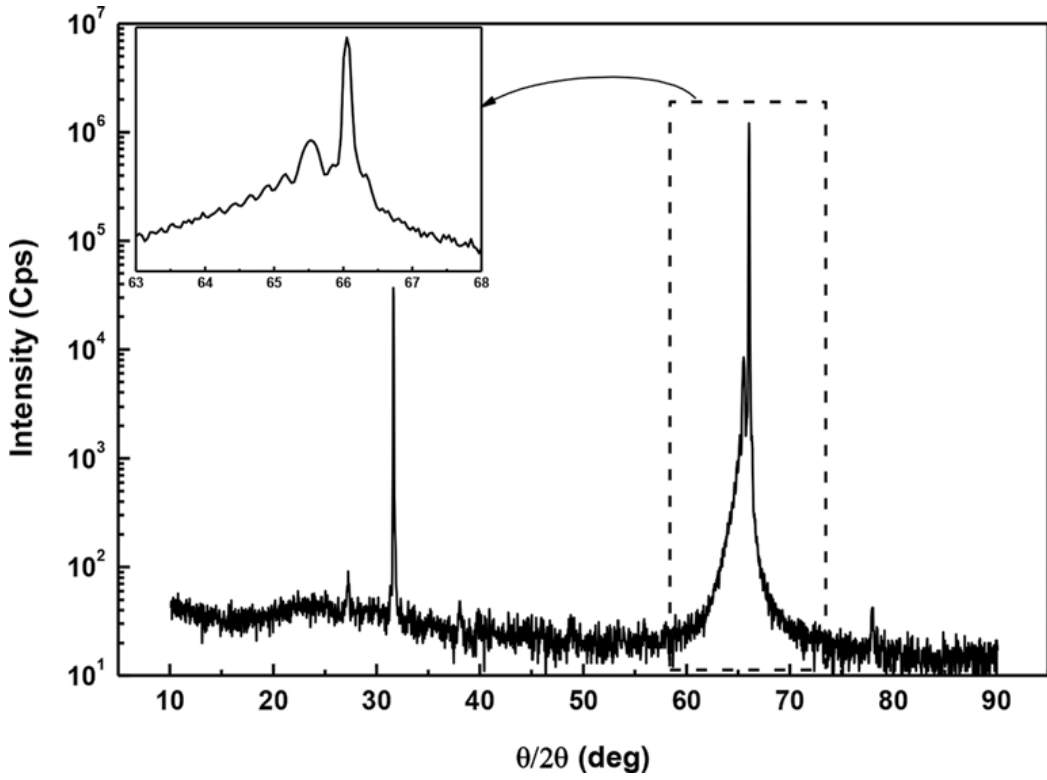
Figure 8. Diffraction pattern in the $\theta - 2\theta$ scan of X-ray diffraction measurement for a GaAs$_{1-x}$Bi$_x$ layer grown on (100) Zn doped GaAs substrate. The inset shows a zoom between $2\theta = 63°$ and $68°$.

The lattice constant (a_0) of unstrained cubic GaAs$_{1-x}$Bi$_x$ is assumed from

$$a_\perp = a_{//} + (a_0 - a_{//})\frac{(C_{11} + 2C_{12})}{C_{11}} \tag{12}$$

where $C_{11} = 11.92$ and $C_{12} = 5.99$ are the elastic constants for GaAs$_{1-x}$Bi$_x$ which are supposed to be equal to those of GaAs. The Bi composition x, is calculated from a_0 using Vegard's law:

$$a_0 = xa_{GaBi} + (1-x)a_{GaAs} \tag{13}$$

where a_{GaBi} is the lattice constant of hypothetical zinc-blend GaBi and assumed to be 6.324 Å [29]. $a_{GaAs} = 5.653$ Å is the lattice constant of GaAs.

Thickness homogeneity and layer composition were characterized by recording (004) X-ray $\omega/2\theta$ curves for several positions in the layer surface. Small changes of 0.001 and 0.002° mm^{-1} have been detected for $\Delta\omega$ and $\Delta\theta_B$, respectively. Bi composition is estimated to 3.7% with a relative change of about 0.05% per mm. The layer thickness is about 50 nm. These values were also compared to those deduced from simulated X-ray patterns using the dynamical theory

shown as dotted lines in **Figure 9**. The tetragonal distortion induced by the epitaxy is taken into account using the elastic constants of GaAs.
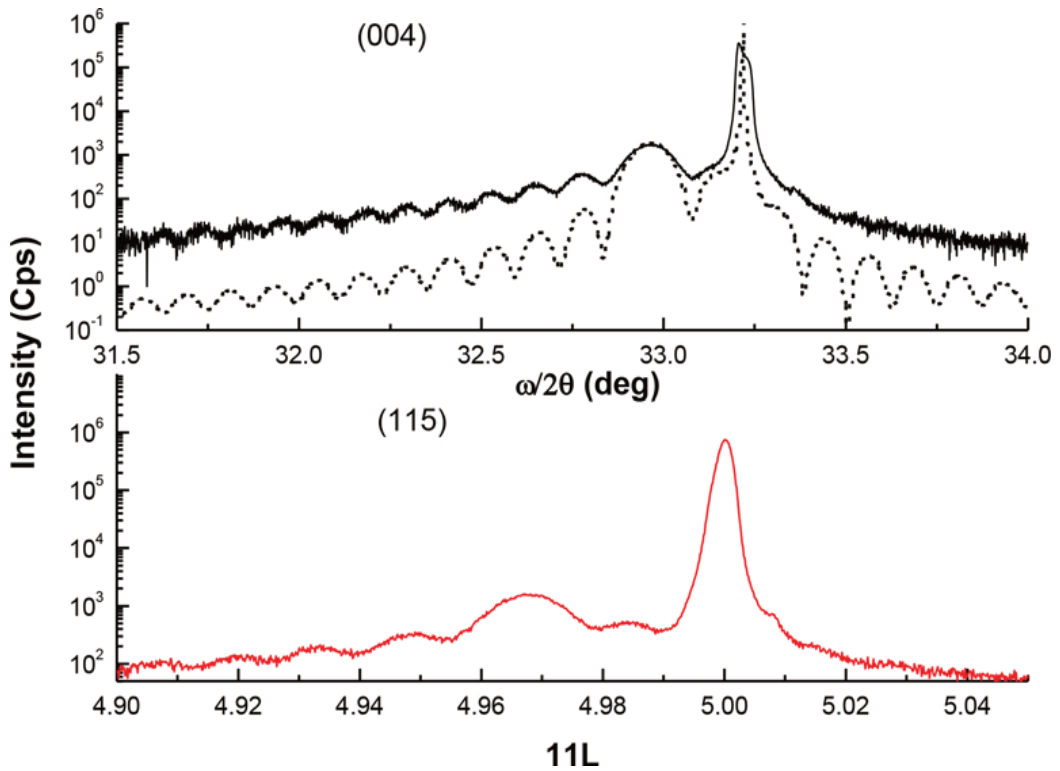

Figure 9. In the top: HRXRD (004) experimental $\omega/2\theta$ curve (solid line) and simulated curve (dotted line) of $GaAs_{0.963}Bi_{0.37}$ layer grown on (100) Zn doped GaAs substrate. In the bottom: optimized scan of HRXRD (11L) reflection plane. L is changed around 5.

The optimization of GaAsBi MOVPE growth conditions was detailed in our previous works [1, 2]. A good crystalline quality was obtained using a V/III ratio of about 9.5, trimethylbismuth (TMBi) flow of 0.2 µmol min^{-1} and a growth temperature of 420°C. The measured Bi content value is around 3.7%. The epitaxial layers show a low Bi island density on the surface [2]. It should be noted that small deviations from optimal growth conditions may give rise to a surface formation of big Bi droplets. The latter appear with a higher density and different shapes for high TMBi flow (~3 µmol min^{-1}).

As a demonstrative example, **Figure 10** illustrates the diffraction patterns of symmetric (004) and asymmetric (115) reflections for the as-grown and annealed GaAsBi layers grown with high TMBi flow. To check thermal stability, GaAsBi layer was annealed at 750°C for 15 min under AsH$_3$ flow. These curves present more diffraction peaks, other than that of the GaAs substrate, located at 32.8, 32.5 and 32.12° in the left side of the substrate peak, and denoted as GaAsBi(1), GaAsBi(2) and GaAsBi(3), respectively. The same diffraction peaks have been detected in the (115) asymmetric configuration, but more shifted with respect to GaAs

substrate peak. It seems that these three peaks are linked to different Bi contents in GaAsBi layer. Based on the Vegard's law we have found: $x_{\text{GaAsBi(1)}} = 3.7\%$, $x_{\text{GaAsBi(2)}} = 8\%$ and $x_{\text{GaAsBi(3)}} = 14\%$. The obtained Bi contents are calculated after the determination of the lattice constants perpendicular and parallel to GaAsBi surface using HRXRD measurements for the (004) and (115) planes, respectively. For hypothetical zinc blend GaBi, the lattice constant is estimated to be 6.324 Å [29]. More calculations details of Bi content are reported in the following Ref. [1]. We have also investigated the structural properties of the annealed layer at 750°C using HRXRD. The measured diffraction curves show a remarkable stability versus thermal annealing. In fact, the same curve shape was obtained for annealed sample (**Figure 10**). Bi droplets are entirely removed from GaAsBi layer after annealing. This behaviour shows that the existence of these droplets is not responsible of diffraction peaks appearance and confirms the structural thermal stability of GaAsBi alloy (**Figure 10**).
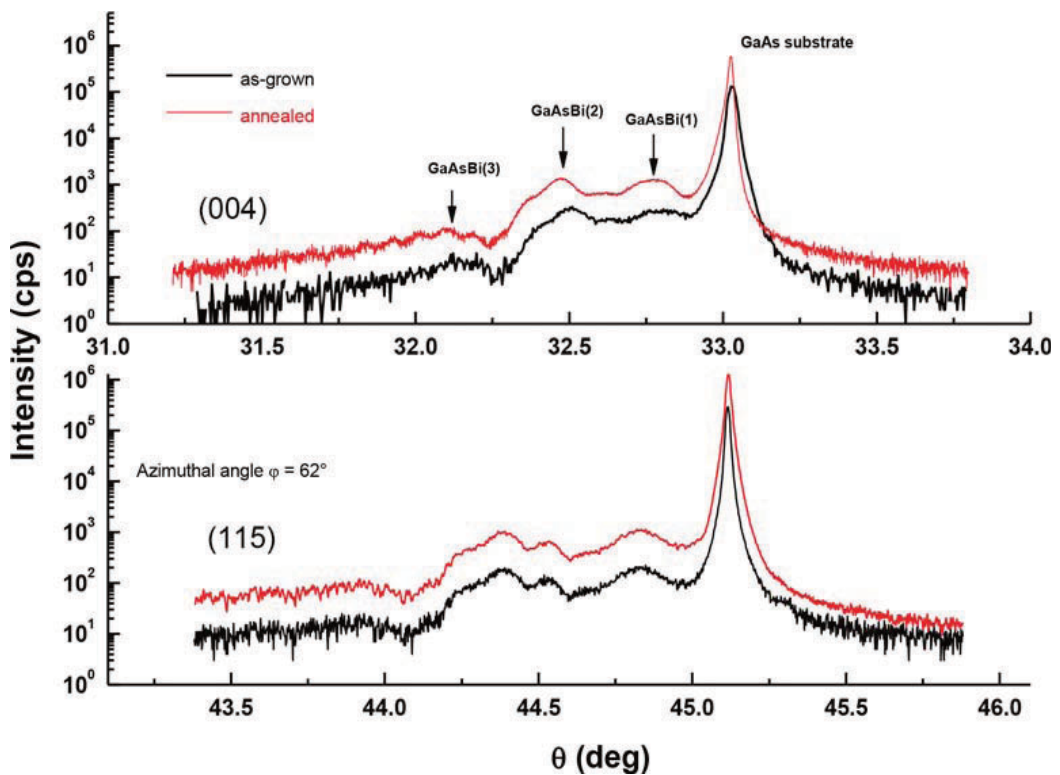

Figure 10. HRXRD (004) and (115) experimental $\omega/2\theta$ patterns of as-grown and annealed GaAsBi layers grown on GaAs substrate at 420°C under 3 μmol min⁻¹ of TMBi flow.

To find out an eventual crystallographic tilting of this sample, we have achieved several ω scans for different azimuthal angles φ for each resolved peak indicated by arrows and shown in **Figure 11**. We report in **Figure 11**, for different azimuthal angles, the diffraction angles variation of the substrate $\omega_{\text{Substrate}}$ and the layer ω_{GaAsBi} for the three aforementioned peaks (GaAsBi(1), GaAsBi(2) and GaAsBi(3)). All the measured amplitudes of the cosine variation of

$\omega_{Substrate}$ and ω_{GaAsBi} are about 1.18°. Note that the given incertitude on GaAs substrate off cut angle is about 1°, and then the GaAsBi layer is not tilted with respect to the substrate. The splitting between the farthest GaAsBi(004) multiple diffraction peaks is about 0.68°. This value is probably corresponding to a maximum tilt between GaAsBi grains which can be present in the layer.
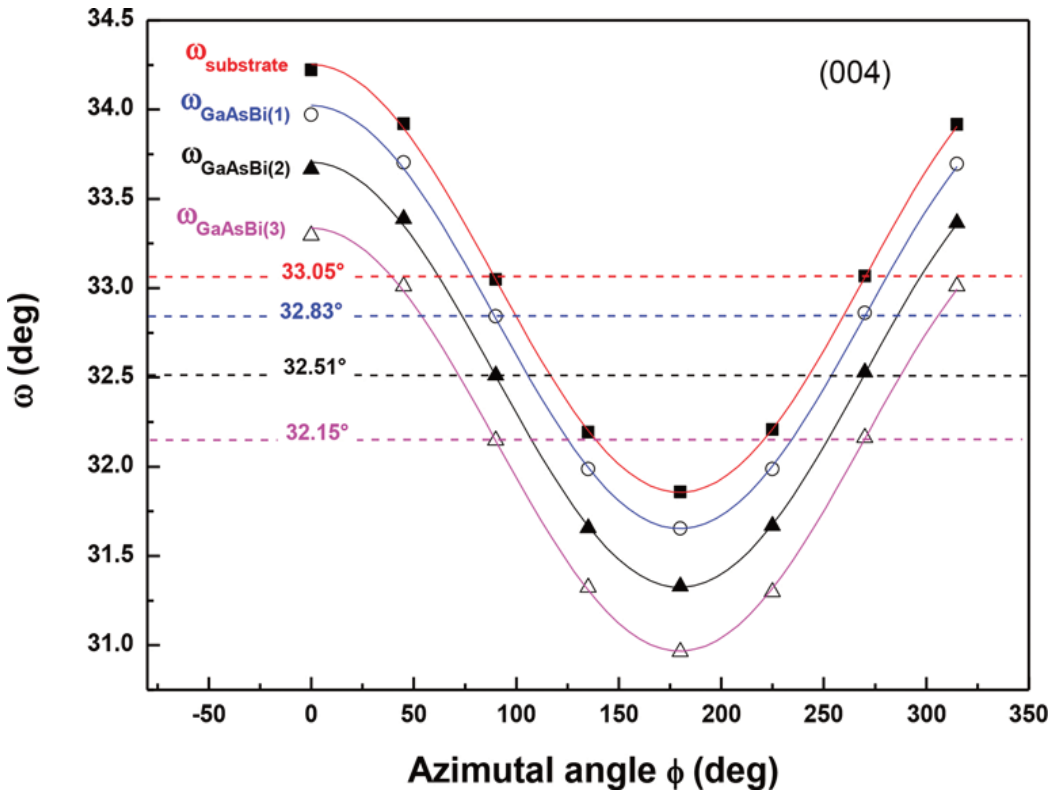

Figure 11. Diffraction angles variation of GaAs substrate (ω_S) and GaAsBi layer (ω_L) for the three aforementioned peaks versus azimuthal angles φ.

Ciatto et al. [30] have investigated the local structure around Bi atoms in GaAsBi layers. Their X-ray absorption spectrometry results show that at 1.2% Bi content, Bi atoms are randomly distributed. At 1.9%, Bi atoms tend to form next-nearest-neighbour pairs, and at 2.4% Bi aggregates appear. In our work, the lowest Bi content in GaAsBi layer is around 3.7%, showing that necessarily Bi aggregates are already formed in the layer.

X-ray diffraction measurements exhibit that growth under high TMBi flow leads to a compositional inhomogeneity, as well as the presence of liquid can affect the Bi incorporation. This fact may be responsible of the XRD pendellösung fringes vanishing, and it was clearly seen when growing GaAsBi under optimized conditions [1, 2]. Some caution is required when interpreting X-ray profile of GaAsBi layers. The confusion can arise from metallic Bi diffraction peak, which can appear in layers having Bi droplet on the surface. Since thermal annealing at

750°C have completely removed Bi islands from the surface, and diffraction curve are exactly the same as before annealing, so this confirms that metallic Bi does not contribute to the diffraction curve.

On interpreting our X-ray profile, the probable assumption is the presence of atomic disorder created by Bi during its incorporation in GaAs matrix. Indeed, the disorder becomes more significant with increasing Bi content. In our case, this content is higher than 3.7% which explains the important disorder and the appearance of several diffraction peaks. There are some assumptions, like support phase separation in GaAsBi alloy [27], the presence of 'micro regions' with different Bi contents [31] or a difference in the strain state at different depths [32].

3.4.2. InGaAs alloys

The lattice mismatch between GaAs and InGaAs alloy layers is relatively small which allows pseudomorphic growth to take place. But uppermost layer can also be partially relaxed or completely relaxed depending on the layer thickness and the indium composition. For a quantitative analysis, the degree of relaxation is given by

$$R = \frac{a_{\text{film}} - a_{\text{substrate}}}{a_{\text{film}}^{\text{relax}} - a_{\text{substrate}}} \tag{14}$$

where a_{film} denotes the measured lattice constant of the film and the totally relaxed lattice constant. R is equal to 1 for fully relaxed films and equal to 0 for pseudomorphic growth.

In this part, we explore a reciprocal space map (RSM) in order to investigate some structural properties of prototype InGaAs alloys in relaxed or strained states.

The Bragg equation relates every X-ray reflex that can be detected with a set of parallel lattice plane (hkl). However, the Laue condition attributes every X-ray reflex to reciprocal lattice point which makes it appropriate to label the reflexes with the indices of their corresponding reciprocal lattice points HKL. The maximum length of the scattering vector in the case of backscattering ($\theta_B = 90°$) is given by $Q_{\max} = 2|k| = \frac{4\pi}{\lambda}$.

Whenever the scattering vector is equal to reciprocal lattice vector, an X-ray reflex is observed. As a result, all reflexes which for a given wavelength λ are accessible for diffraction experiments are situated within the hemisphere with radius equal to $\frac{4\pi}{\lambda}$ (in right of **Figure 12**).

Such a scan can be carried out by combining the $\omega/2\theta$-scan with ω-scan mode in the following way: first for a given length of the scattering angle a ω-scan is accomplished, then the $\omega/2\theta$-scan mode is employed to change the length of the scattering vector by a small amount and then again a ω-scan is performed and shown as reported in left of the **Figure 12**. With RSM measurement, the graph can be presented either in angular coordinates or in reciprocal lattice coordinates. Angular coordinates RSM is the x- and z-axes can be ω, 2θ, $\omega/2\theta$, or $2\theta/\omega$. Reciprocal coordinates RSM shows the graph in reciprocal lattice unit Q_x and Q_z, where can be defined with the following equations [33]:

$$Q_Z = \frac{2}{\lambda} \sin\theta \cos(\omega-\theta)$$
$$Q_X = \frac{2}{\lambda} \sin\theta \sin(\omega-\theta)$$

$$(15)$$

where $\lambda = 1.5406$ Å is the wavelength of CuK$_{\alpha 1}$ radiation, $\theta = 2\theta/2$ the angular position of the detector and ω is the experimental Bragg angle for considered reflection.
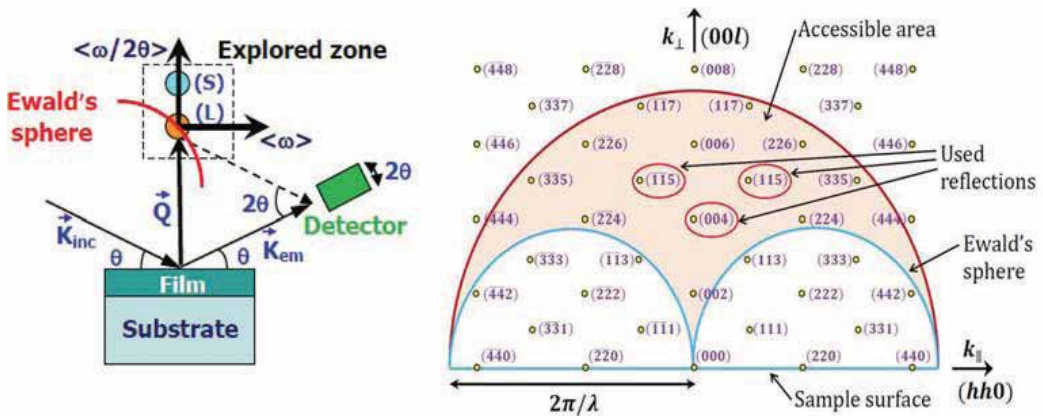

Figure 12. Ewald construction illustrating the scattering geometry in the cases of symmetrical and asymmetrical reflexes. The grey arrows show the scan directions for $\omega/2\theta$-scan and a ω-scan. The accessible reflections in conventional scattering geometry are shown.

ΔQ_Z and ΔQ_X are determined from the difference between measured angles for the substrate and the layer. For (115) reflection on (001) substrate, the perpendicular lattice parameter of the layer is obtained from $\Delta Q_Z = \frac{5}{a_\perp} - \frac{5}{a_s}$

where a_{GaAs}=5.6325 Å is the lattice parameter of the GaAs substrate.

Other possible equivalent representations of reciprocal map are accessible, such as by that representing the Bragg angle change by changing (*hkl*) indices.

Generally, the reciprocal maps show two intense peaks localized in $\Delta Q_X = \Delta Q_Z = 0$ relative to the GaAs substrate and the in $\Delta Q_X \neq \Delta Q_Z \neq 0$ relative to the layer.

3.4.2.1. InGaAs/GaAs relaxed layer

Figure 13 illustrates an example of 2D and 3D map representations for a sample InGaAs/GaAs. In order to analyse maps topography with more facility, pedagogic representation as contour curves of iso-intensity is reported in the same figure.

Using RSM, the analysis of material properties can be completed both qualitatively and quantitatively. The last figure shows the illustration of a qualitative description of the change of the layer peak position with respect to the substrate peak. Qualitatively, a symmetric RSM scan can confirm that our sample is tilted or not. However, to determine whether our sample is strained or relaxed, an asymmetric scan is needed.
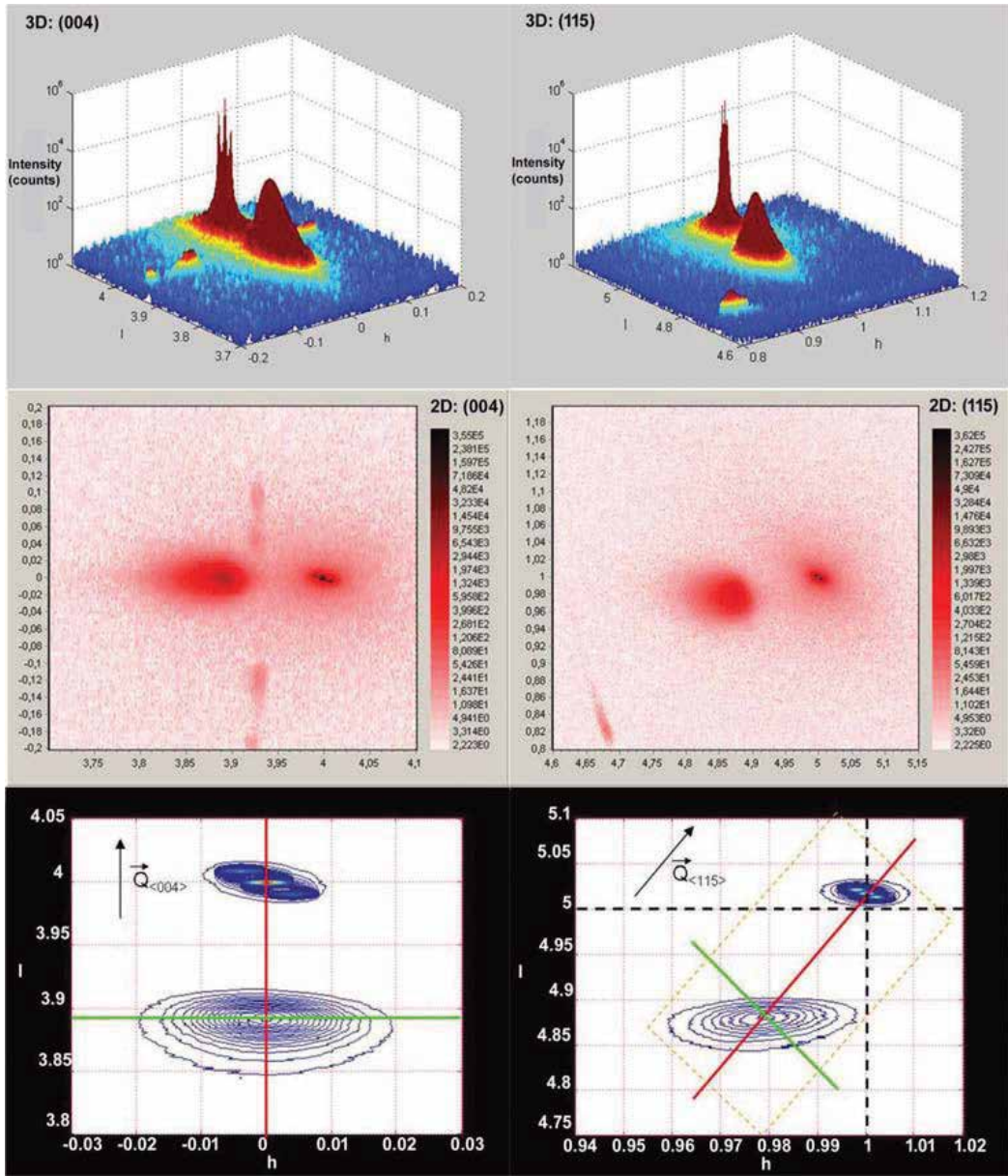
Figure 13. 3D and 2D reciprocal space maps of In$_{.08}$Ga$_{.92}$As/GaAs structure, recorded around (004) and (115) nodes. In the bottom, contour curves of iso-intensity are drawn. Diffusion vectors $\vec{Q}_{(004)}$ and $\vec{Q}_{(115)}$ were added to corresponding RSM.

3.4.2.2. InGaAs/GaAs strained layer

InGaAs epitaxial layer on GaAs(100) substrate was investigated by HRXRD in order to determine the structural properties of this strained structure. **Figure 14** shows reciprocal space
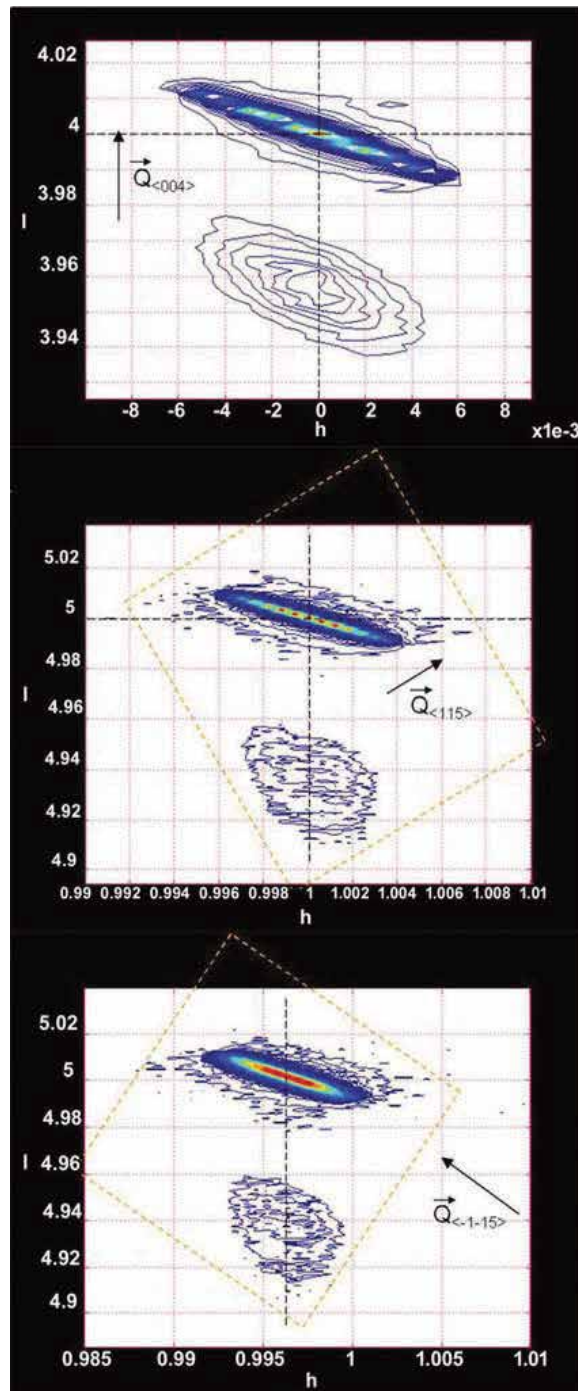
Figure 14. Reciprocal space mapping of In$_{.08}$Ga$_{.92}$As/GaAs structure, recorded around (004), (115) and ($\overline{1}\overline{15}$) nodes. Diffusion vector $\vec{Q}_{(hhl)}$ was added to the corresponding RSM.

maps (RSM) of an InGaAs/GaAs sample in two-dimensional representation of iso-intensity curves around (004), (115) and $(\overline{11}5)$ nodes. Note that both spots of InGaAs active layer and GaAs substrate, relative to (004) symmetric reflection, were aligned along <001> direction. The obtained result confirms the absence of tilt between the active layer and the substrate. In addition, diffraction spots from (115) and $(\overline{11}5)$ asymmetric reflections were also aligned along the growth direction, which was different from that of scattering vector $\vec{Q}$. Sample was then strained and pseudomorphed. A fully strained epilayer adapts its planar lattice fully with the planar lattice of the substrate (**Figure 14**).

4. Conclusions

This chapter has covered a range of applications of HRXRD technique from simple rocking curve scans (ω and $\omega/2\theta$) to space mapping cartography. Routine measurements applied to particular heterostructures such as GaAs/GaAs(001), GaN/Si(111), GaAsBi/GaAs(001) and InGaAs/GaAs(001) are reported in order to bring the capability of analysis of this technique. The former is a powerful tool that can provide accurate information on the structural properties of the analysed material. Indeed, the method is sensitive enough to determine the composition, thickness and perfection of the epitaxial layers of compound semiconductors.

The application of high-resolution diffraction space mapping is more prevalent since it is now possible to obtain a whole wealth of structural parameters other than just the thickness or composition. This is a developing field and this technique can be considered to determine the deviation from perfection.

Acknowledgements

Author details

Hédi Fitouri, Mohamed Mourad Habchi and Ahmed Rebey*

*Address all correspondence to: ahmed.rebey@fsm.rnu.tn

Faculty of Sciences, Research Unit on Hetero-Epitaxy and Applications, University of Monastir, Monastir, Tunisia

References

[1] H. Fitouri, I. Moussa, A. Rebey, A. Fouzri, B. El Jani, J. Cryst. Growth 295 (2006), 114–118.

[2] I. Moussa, H. Fitouri, A. Rebey, B. El Jani, Thin Solid Films 516 (2008), 8372–8376.

[3] M. M. Habchi, A. Rebey, B. El Jani, J. Cryst. Growth 310 (2008), 5259–5265.

[4] M. M. Habchi, A. Rebey, B. El Jani, Microelect. J. 39 (2008), 1587–1593.

[5] A. Rebey, L. Béji, B. El Jani, P. Gibart, J. Cryst. Growth 191 (1998), 734–739.

[6] A. Rebey, B. El Jani, A. Leycuras, S. Laugt, P. Gibart, Appl. Phys. 68 (1999), 349–352.

[7] A. Bchetnia, A. Touré, T.A. Lafford, Z. Benzarti, I. Halidou, M.M. Habchi, B. El Jani, J. Cryst. Growth 310 (2008), 5259–5265.

[8] N. Chaaben, T. Boufaden, A. Fouzri, M.S. Bergaoui, B. El Jani, Appl. Surf. Sci. 253 (2006), 241–245.

[9] X. R. Wang, X. Y. Chi, H. Zheng, Z. L. Miao, J. Wang, Z. S. Zhang, Y. S. Jin. J, Vac. Sci. Technol. B 6(1) (1988), 34.

[10] N. Chen, Y. Wang, H. He, L. Lin, Phys. Rev. B. 54(12) (1996), 8516.

[11] W. Lei, M. Pessa, Phys. Rev. B 57(23) (1997), 14627.

[12] A. Rebey, W. Fathallah, B. El Jani, Microelect. J. 37 (2006), 158–166.

[13] A. Rebey, Z. Chine, W. Fathallah, B. El Jani, E. Goovaerts, S. Laugt, Microelect. J. 35 (2004), 875–880.

[14] A. Cremades, L. Görgens, O. Ambacher, M. Stutzmann F. Scholz, Phys. Rev. B 61 (2000), 2812.

[15] V. S. Harutyunyan, A. P. Aivazyan, E. R. Weber, Y. Kim, Y. Park S. G. Subramanya, J. Phys. D: Appl. Phys. 34 (2001), A35–A39.

[16] A. Polian, M. Grimsditcv, I. G. Grzegory, J. Appl. Phys. 79 (1996), 3343.

[17] Z. Chine, A. Rebey, H. Touati, E. Goovaerts, M. Oueslati, B. El Jani, S. Laugt, Phys. Stat. Sol. (A) 203(8) (2006), 1954–1961.

[18] I. H. Lee, I. H. Choi, C. R. Lee, S. K. Noh, Appl. Phys. Lett. 71 (1997), 1359.

[19] P. Gay, P. B. Hirsch, A. Kelly, Acta Met. 1 (1953), 315.

[20] M. J. Hordon, B. L. Averbach, Acta Met. 9 (1961), 237.

[21] J. E. Ayers, J, Cryst. Growth, 135 (1994), 71.

[22] B. Heying, E. J. Tarsa, C. R. Elsass, P. Fini, S. P. DenBaars, J. S. Speck, J. Appl. Phys. 85 (1999), 6470.

[23] Y. Takehara, M. Yoshimoto, W. Huang, J. Saraie, K. Oe, A. Chayahara, Y. Horino, Jpn. J. Appl. Phys. 45 (2006), 67.

[24] S. Tixier, M. Adamcyk, T. Tiedje, S. Francoeur, A. Mascarenhas, P. Wei, F. Schiettekatte, Appl. Phys. Lett. 82 (2003), 2245.

[25] M. Yoshimoto, S. Murata, A. Chayahara, Y. Horino, J. Saraie, K. Oe, Jpn. J. Appl. Phys. 42 (2003), L1235.

[26] K. Oe, J. Cryst. Growth 237–239 (2002), 1481.

[27] K. Oe, Jpn. J. Appl. Phys. 41 (2002), 2801.

[28] K. Oe, H. Okamoto, Jpn. J. Appl. Phys. 37 (1998), L1283.

[29] A. Janotti, S. -H. Wei, S. B. Zhang, Phys. Rev. B 65 (2002), 115203.

[30] G. Ciatto, E. C. Young, F. Glas, J. Chen, R. A. Mori, T. Tiedje, Phy. Rev. B, 78 (2008), 35325.

[31] N. A. El-Masry, E. L. Piner, S. X. Liu, S. M. Bedair, Appl. Phys. Lett. 72 (1998), 40.

[32] S. Pereira, M. R. Correia, E. Pereira, P. O'Donnell, E. Aves, A. D. Sequeira, N. Franco, Appl. Phys. Lett. 79 (2001), 1432.

[33] P. Van der Sluis, J. Phys. D: Appl. Phys. 26 (1993), A188–A191.

Applications of X-ray Spectroscopy to Study Different Biological Systems

X-Ray Spectroscopy on Biological Systems

Joanna Czapla-Masztafiak, Wojciech M. Kwiatek,

Jacinto Sá and Jakub Szlachetko

Additional information is available at the end of the chapter

Abstract

In the field of biological studies, next to the standard methods, new tools are offered by contemporary physics. X-ray spectroscopic techniques enable probing electronic structure of occupied and unoccupied states of studied atom and distinguish the oxidation state, local geometry, and ligand type of elements that occur in biological material. Direct analysis using X-ray spectroscopy avoids many chemical preparation steps that might modify biological samples. The information obtained gives us insight into important biochemical processes all under physiological conditions. In this chapter we focus our attention to the application of X-ray spectroscopy to the study of biological samples, with special emphasis on mechanisms revealing interaction between DNA and different cytotoxic agents and in the determination of changes in oxidation state of different elements in pathologically altered human cells and tissue.

Keywords: X-ray spectroscopy, XAS, XES, DNA, chemical speciation

1. Introduction

X-ray spectroscopy is a powerful method giving the insight into the chemical and electronic structure of studied samples. Since twentieth century, it has been extensively used in a plethora or research fields starting from solid-state physics [1, 2] and followed by chemical [3] and environmental sciences [4], archeological and art research [5], as well as biological and health studies [6]. The advantages of this technique is its elemental specificity and high penetration depth of probe X-rays resulting in the possibility to undertake *in situ* experiments that provide information about the sample under ambient/operational conditions, that is, direct observation of species at the molecular level in low (biological) concentrations without the need for

preconcentration, extraction, or crystallization [7, 8]. For these reasons, X-ray spectroscopy has been recognized as the valuable addition to classical methods used in biological sciences and many improvements have been made in the experimental techniques as well as data analysis and interpretation. Research includes the simplest systems, such as single compounds, as well as more complex and heterogeneous structures such as cells and tissues. The examples of applications are, among others, the structural characterization of chloroperoxidase compound I [9], the determination of ligand environment of zinc in different tissues of Zn-hyperaccumulating plants [10] and chemical structure of metalloproteins [11]. A lot of researches concern changes in oxidation states of trace elements in case of different pathologically altered cells and tissues, for example the studies of differences in iron and zinc oxidation state contained in healthy and neoplastic tissues of the human brain [12], iron in normal and stenotic human aortic valves [13] or copper inside single neurons from Parkinson's disease and control substantia nigra [14]. Another group of application is identification of elements' chemical species in biological systems, like sulfur in erythrocytes and blood plasma [15], selenium in human cancer cells [16], as well as arsenic in various cell structures [17]. X-ray spectroscopy gives also the opportunity to follow biologically relevant processes in time-resolved experiments including the ultrafast time domain. The processes studied are for example excitation of Mn cluster in photosystem II [18] and recombination of myoglobin following the photolysis of NO [19]. The development of new X-ray sources and X-ray free electron lasers (XFELs) will make possible to study the dynamics of biological systems with femtosecond time resolution, which will elucidate the mechanisms of many important bioprocesses.

The need for more sensitive research methods in medical sciences is forced mostly by the increasing incidence rate of the diseases of affluence, primarily cancer and cardiovascular diseases [20]. These types of studies are focused on two main goals—effective diagnosis on the early stage of the disease and design of efficient therapy. This can be reached, for example, by the discovery and validation of new biomarkers to understand the etiopathology of diseases and by studying new, alternative treatment methods like, for example, novel potential drugs and their interaction with the components of living cells. This review summarizes our latest efforts in applying X-ray spectroscopy to study different biological systems starting from the impact of different damaging agents on the model of DNA molecule and followed by the chemical speciation in the studies of cancerous cell lines and human tissues. Chosen topics show the variety of medically important subjects that can be studied with X-ray spectroscopy and its undeniable role as a technique complementary to classical methods.

2. Principals of X-ray spectroscopy techniques

X-ray spectroscopic methods are atom-specific techniques, using X-ray excitation to gather information about the electronic and geometric structure of the studied system. X-rays in the range from several to few tens of keVs are absorbed by matter mainly through the photoelectric effect. In this process, an X-ray photon with sufficient energy is absorbed by an electron in a tightly bound quantum core level (such as the 1s, 2s or 2p) of an atom. A core electron is promoted to higher, unoccupied state or to the continuum. Following an absorption event, the

atom is in an excited state, with one of the core electron levels left empty (a core hole). During the decay of this intermediate excited state, the core hole is filled by another inner- or valence-shell electron. The decay from the excited to the final state is accompanied by the emission of an X-ray photon, which energy depends on electronic levels involved in the process or by the emission of an Auger electron or Coster-Kroning electron. But the latter phenomenon will not be discussed in this chapter. X-ray absorption and X-ray emission spectroscopy (XAS and XES, respectively) are devoted to the study aforementioned processes. XAS provides information about the unoccupied electronic density of states of an atom whereas XES reflects occupied density of states, and when applied together, providing the detailed picture of the molecular orbitals [21].

The absorption process is described by the absorption coefficient μ in the function of incidence energy, where we can distinguish two regions—a sharp rise in absorption (an absorption edge corresponding to the promotion of the core level electron to the higher state) and the region above absorption edge, characterized by the rich structure. Therefore, XAS spectrum is divided into two parts: the X-ray absorption near-edge structure (XANES)—typically within 30 eV of the main absorption edge, and the extended X-ray absorption fine-structure (EXAFS). XAS spectra are sensitive to the formal oxidation state, coordination chemistry, and the distances, coordination number, and species of the atoms surrounding the selected element. K- and L-level X-ray emission spectra, reflecting the energy distribution of photons emitted by the atoms, can be divided into α and β regions. α lines are characterized by high transition yields but provide little direct chemical information. On the other hand, β lines associated with satellites are being sensitive to chemical environment of the atom, but are much weaker in intensity. For example, two ranges may be recognized around X-ray emission spectrum of Kβ line: Kβ mainline consisting of metal 3p to metal 1s transitions and the valence-to-core (V2C K$\beta_{2,5}$) region comprised of transitions from valence, ligand-localized orbitals to the metal 1s. Both have been shown to contain valuable chemical information—the Kβ mainline is sensitive to the metal spin state as well as the metal-ligand covalence [22] while the V2C region contains information about ligand identity, electronic structure, and metal-ligand bond length [23].

The more detailed information about the electronic structure of studied systems can be obtained by the use of resonant X-ray emission spectroscopy (RXES, also called resonant inelastic X-ray scattering (RIXS)) that is characterized by high sensitivity. RXES, which is photon-in photon-out spectroscopy, combines X-ray absorption and X-ray emission information. RXES experiments can be performed with the use of high-energy resolution X-ray spectrometers, the powerful instruments used to determine the electronic structure of matter that have found many applications in a variety of scientific areas [24–28]. In general, X-ray spectrometers rely on the X-ray dispersion by a crystal providing high-energy resolution for X-ray detection. In order to access detailed information about the electronic structure of matter, the energy resolution has to be around 0.1–5 eV in order to be comparable with the natural lifetimes of studied electronic states of an atom [29, 30]. There are three relevant X-ray emission spectrometer geometries: von Hamos [31, 32], Johannson [33], and Johann [34]. In the RXES studies presented in this review, the von Hamos-type spectrometer has been used with segmented analyzer crystal which disperses the photon energy along one axis and focuses the

X-ray photons along the other axis [35]. Setup scheme for typical RXES experiment under physiological conditions is presented in **Figure 1**.
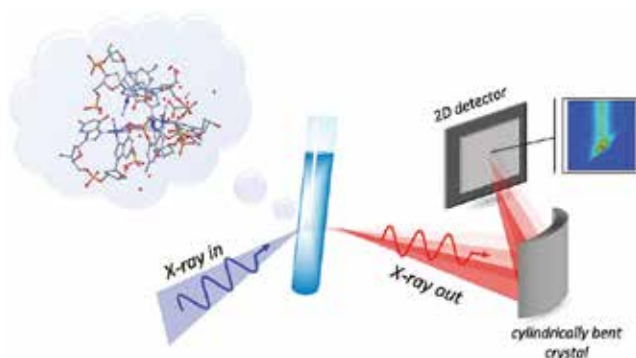

Figure 1. Schematic representation of the experimental setup used in *in situ* RXES experiment [7]. Reproduced by permission of The Royal Society of Chemistry.

The sample is placed at the center of the crystal curvature, and the X-rays are imaged on either a 1D strip detector or a 2D detector. This generates an emission spectrum in a single measurement without any detector or crystal motion. By scanning the incidence energy, one can obtain full RXES plane. A cut in the plane performed at maximum emission energy results in high-resolution X-ray absorption spectrum (HR-XAS) that, due to reduced lifetime broadening, provides detailed information about very small variations in the unoccupied electronic states. The example of RXES plane measured for cisplatin compound is presented in **Figure 2**. It shows the states generated by the resonant excitation of a $2p_{3/2}$ electron into the Pt 5d orbitals (L_3-edge transition). Schematically shown horizontal and vertical cuts along the RXES plane correspond to the $L\alpha_1$ lines of the X-ray emission spectrum (XES) and high-resolution X-ray absorption spectrum (HR-XAS) profiles, which provide information on occupied and unoccupied electronic states of the metal, respectively.
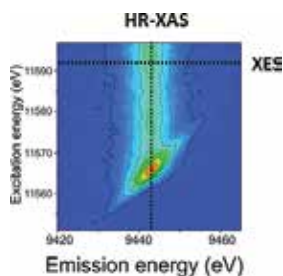

Figure 2. Pt L_3-edge RXES map of cisplatin compound [7]. Reproduced by permission of The Royal Society of Chemistry.

In parallel to the development of the experimental aspects of X-ray spectroscopy, the significant progress has been done in the theory and ab initio calculations of XAS and XES spectra that

enables detailed qualitative and quantitative analysis of experiment. Among others, two representatives of ab initio codes are FEFF9.0 [36] and FDMNES [37]. FEFF9.0, based on Green's Function, is automated software for ab initio multiple scattering calculations of X-ray absorption and X-ray emission signals and various other signals for solids, clusters, or molecules. The code provides yields for X-ray scattering amplitudes that may be directly compared to measured RXES signals. Recently, code was upgraded with several new features for more precise and more realistic calculations, which include ab initio Debye-Waller factors, improved treatment of inelastic loses and core-hole interaction as well as more accurate treatment of crystalline systems with k-space calculations of the Green's function. Similarly, to FEFF software, FDMNES provides yields for X-ray scattering amplitudes that may be directly compared to measured experimental spectra. Nevertheless, unlike FEFF, which is based on self-consistent spherical muffin-tin scattering potentials, the FDMNES employs the finite difference method (FDM) based on density functional theory (DFT) with a potential exchange correlation depending on the local electron density. Therefore, FDMNES may provide more accurate density of states calculations, especially for surface states, but at cost of much longer computation times.

3. Chemical analysis of antitumor compounds

It is beyond doubt that, in case of cancerous diseases, the effective therapy is needed. The majority of drugs used in cancer treatments are cytotoxic (cell killing) and interfere with the cells' DNA. Consequently, the DNA-drug interaction mechanism is of the primary interest when new antitumor compounds are studied. The development of new anticancer drugs is forced by the strong side effects and chemoresistance, both being induced when commonly used platinum-based chemotherapeutics are applied. The binding mechanism of newly synthesized complexes to DNA is one of the most important characteristics to be determined for identification of drug–DNA activity. This can be probed with direct techniques, like nuclear magnetic resonance (NMR) or crystallography. However, these approaches very often require harsh sample preparation that may lead to difficulties in the interpretation of the results. Therefore, simultaneously to the development of new routes of drug synthesis and studying drug-DNA interaction, further development of experimental techniques is necessary. Most importantly, detailed structural and electronic information of the samples has to be retrieved under *in situ* conditions with the ability to control the sample environment and mimicking real physiological conditions.

3.1. Chemical speciation

During the phase of designing new potential antitumor compound, it is important to understand how its structure influences its activity. Especially, it is essential to apprehend why different diastereomers of metal compounds are showing differences in reactivity that sometimes cannot be justified by simple steric effects. In order to study the effect of stereochemistry on the electronic structure around the metal center, RXES technique was used [38]. Two chiral platinum (II) compounds [39], namely (1S,2S)- and (1R,2R)-1-(4-fluorophenyl)-3-

isopropyl-1,2-diaminedichloro platinum(II) (*trans* and *cis*, respectively), were studied. *Cis* isomer exhibits 50-times higher anticancer activity than the *trans* one [39]. Pt L$_3$-edge RXES spectra of the studied samples were collected with the use of wavelength-dispersive X-ray spectrometer in von Hamos geometry. The experimental setup allows the simultaneous detection of Lα_1 and valence-to-core (V2C) signals and therefore from obtained maps, HR-XAS and V2C spectra were extracted by performing cuts at RXES plane. Experimental data were complemented with theoretical FEFF9.0 calculations of orbital contribution to the measured signals. This approach gave us the information about the density of occupied and unoccupied electronic states. **Figure 3** presents the comparison of experimental results obtained for *trans* and *cis* compounds.
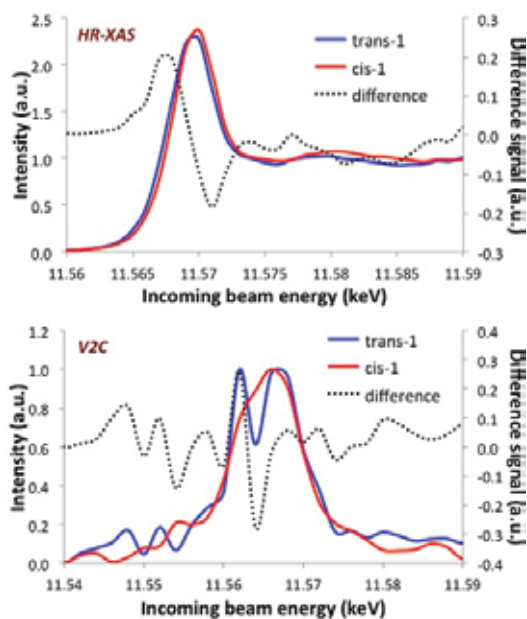

Figure 3. Comparison of the measured HR-XAS (top) and V2C emission (bottom) spectra between *trans* and *cis* Pt-derivatives. Difference profile is the result of subtracting *trans* profile from the *cis* profile [38]. Reproduced by permission of The Royal Society of Chemistry.

Calculated differential signal for both HR-XAS and V2C spectra reveals significant differences that can be associated with the increase of anticancer activity upon configuration inversion from *trans* to *cis*. In case of HR-XAS, the configuration change from *trans* to *cis* shifts the position of the white line to higher energies and increases its intensity, which is caused by increase in empty electronic states. This is related with the increase in the ability to form new bonds and strengthening the formed ones. More pronounced differences can be observed in case of V2C spectra. By analyzing the calculated orbital contributions (**Figure 4**), one can notice that two distinct peaks in V2C *trans* spectrum are resulting from the overlap of filled states of Pt-5d and Cl-2p with F-2p states forming a shoulder. In contrast, in *cis* spectrum, Pt-5d and Cl-2p do not overlap significantly and F-2p orbital is shifted toward higher energy, which results in a loss

of the shoulder and overlap of the two peaks, resolvable in case of *trans* spectrum. The same analysis was performed in order to compare the effect of substitution of various ligands in the studied compounds, and the differences in HR-XAS and V2C spectra were also observed [38] showing that changes in R^1 and R^2 positions influence Pt electronic configuration.
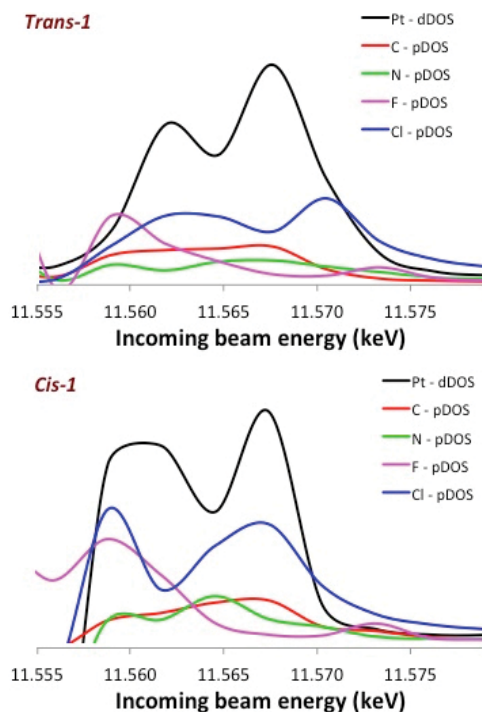

Figure 4. Orbital contribution for V2C emission spectra for *trans* and *cis* Pt-derivatives [38]. Reproduced by permission of The Royal Society of Chemistry.

As it was shown, the RXES technique is sensitive to changes of electronic structure of metallodrugs that arise not only from the changes in the structure of ligands bonded directly to the studied atom but also from the stereochemistry of further neighbors. Therefore, high chemical sensitivity of this method makes it ideal for the studies of anticancer drug mechanism in *in situ/in vivo* conditions.

3.2. The mechanism of action of chemotherapeutic drugs

In further studies, RXES method was also used to disentangle the DNA-drug interaction mechanism [7]. The studies focused on well-known cisplatin (*cis*-diamminedichloroplatinum(II)) compound that is widely used in treating a variety of cancers such as testicular, ovarian, head, and neck tumors [40]. Although very efficient, the use of cisplatin is still dose-limited by side effects and inherited or acquired resistance phenomena, only partially amended by employment of new platinum drugs [41]. Cisplatin action mechanism was only confirmed

190 X-ray Scattering

via X-ray structural analysis to lead to the formation of intrastrand cross-links (*cis*-[Pt(NH$_3$)$_2${d(GpG)-N7(1),-N7(2)}]) with DNA 20 years after its implementation [42, 43].

RXES experiment was performed on cisplatin samples incubated for 24 h with calf thymus DNA. In order to follow the full mechanism of cisplatin binding, aqueous and buffer solution (physiological serum) of the drug was also studied. The intensity of the main resonance in the measured RXES Pt L$_3$-edge map depends directly on the unoccupancy values in the 5d orbitals, which are sensitive to the type of coordinating ligand, bonding strength and angle. Thus, changes in the structure around platinum atom can be easily detected by measuring its density of states in the 5d orbital. *In situ* RXES experiment was combined with theoretical calculations performed with FEFF9.0 code. The differential RXES maps (ΔRXES) resulting from experimental data obtained for cisplatin in aqueous and buffer solution and cisplatin incubated with DNA are presented in **Figure 5(a** and **b**). The results are compared with theoretically calculated spectra for different reaction pathways.

The analysis showed that the hydration of cisplatin in a buffer solution leads to the formation of a mono- and a diaqua complexes (*cis*-[PtCl(NH$_3$)$_2$(H$_2$O)]$^+$ and *cis*-[Pt(NH$_3$)$_2$(H$_2$O)$_2$]$^{2+}$, respectively). Since both complexes induce similar changes in RXES spectra, it is difficult to judge which of the structures is predominant. Nevertheless, other studies [44, 45] revealed that both structures are likely to play a role in the reaction with DNA. Further, we compare the differential RXES map resulting from the addition of calf thymus DNA to the aquated cisplatin with calculated differences. Calculations were performed for both hydration products and revealed that the final structure of cisplatin–DNA adduct is *cis*-[Pt(NH$_3$)$_2$-{d(GpG)-N7(1),-N7(2)}], which means that cisplatin bonds to N(7) atoms of adjacent guanines in DNA strand, which is consistent with X-ray crystallography results [42, 43]. Following step in data analysis was the extraction of HR-XAS spectra from RXES maps at constant emission energy of ~9443 eV along with FEFF9.0 calculations of orbital contributions for obtained signals (see **Figure 6**).
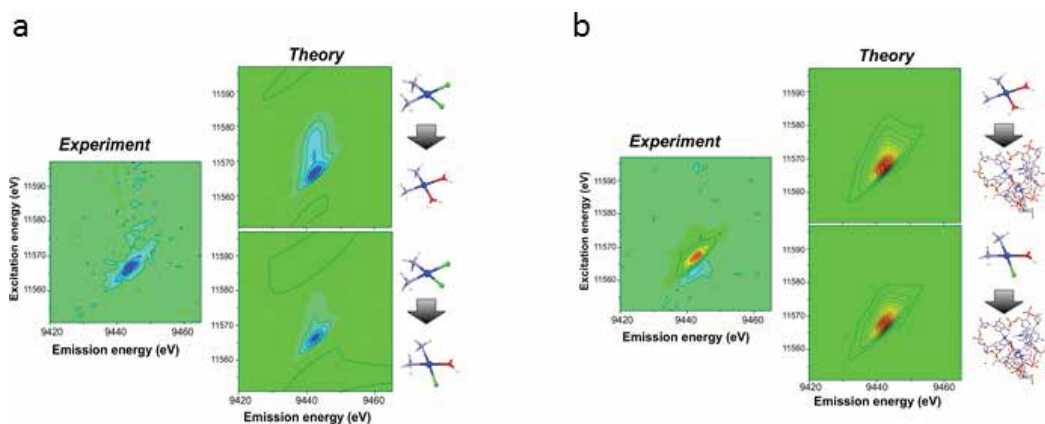

Figure 5. ΔRXES maps resulting from (a) cisplatin hydration in buffer solution. The result is compared with theoretical predictions (top) loss of two chloride ions; and (bottom) loss of a chloride ion, (b) resulting from the bonding of the aquated cisplatin with DNA. The result is compared with theoretical predictions (top) diaqua complex + DNA; and (bottom) monoaqua complex + DNA [7]. Reproduced by permission of The Royal Society of Chemistry.
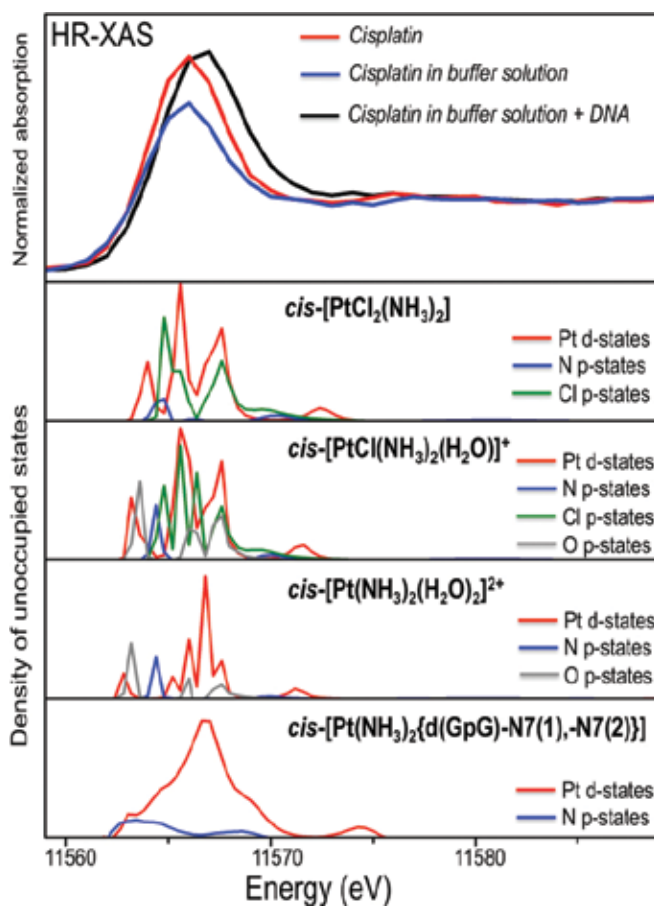
Figure 6. HR-XAS extracted from the RXES maps of (top panel) cisplatin in deionized water (red); cisplatin in buffer solution (blue); and cisplatin in buffer solution + DNA. (black). Pt 5d-density of states orbital contribution computed with FEFF9.0 (subsequent panels) [7]. Reproduced by permission of The Royal Society of Chemistry.

Changes in HR-XAS signal are clearly visible and can be interpreted by the changes in the electronic density of states of platinum and neighboring atoms. In case of hydration products, changes are associated with the substitution of Cl ligands with water molecules that lead to the removal of Cl p-orbital contribution and the appearance of a contribution due to the O p-orbitals from the water molecules that overlap less with Pt d-orbitals indicating weaker bonding. In case of cisplatin-DNA complex, HR-XAS is reflecting strong hybridization of Pt d-orbitals and p-orbitals of N(7) atoms of guanines indicating that the formed bonds are significantly stronger than Pt-Cl (cisplatin) and Pt-O (mono- and diaqua complexes).

The presented methodology has the potential to shorten the time from drug development to drug application by decades because the process is very sensitive and fairly quick, since it does not require extraction and/or preconcentration. The measurements yield direct information of bonding motifs under relevant conditions and in a time-resolved fashion. Furthermore, the

studies can be coupled with the most recent advance in theoretical calculations, which brings an even further dimension when talking about drug action mechanism understanding. RXES provides both basis and confirmation of theoretical study findings, which decreases the computational time tremendously.

We foresee this technique applied to all sorts of systems, and cells as the targets, which is enabled by X-ray probe of high penetration depth and high chemical speciation. The advent of von Hamos dispersive-type spectrometer to follow the system and improved sample delivery systems, such as liquid jet [46], ensures measurements under beam damage-free conditions.

4. Investigating DNA radiation damage

Since many years, more effort is put into the studies of the impact of radiation on human organism. Such research is carried out both in the context of radiation protection and therapy purposes. One of the most important biomolecules being strongly linked to biological radio-sensitivity is DNA, which damage may trigger cell death or genomic instability. Common damage types caused by radiation are as follows: single-strand breaks (SSB) and double-strand breaks (DSB), base damage, and DNA-DNA and DNA-protein cross-links. The type and energy of radiation determine the probability of particular kinds of DNA damage production. The interactions of various kinds of radiation with DNA are complex, providing a spectrum of changes that vary in number and distribution. The molecular lesions are caused by either direct ionization/excitation of DNA or indirectly, for example, through the ionization of water and the formation of damaging-reactive hydroxyl radicals. Nevertheless, there are still unanswered questions concerning the detailed mechanism of DNA damage. For instance, the influence of low radiation doses, UV radiation, and the aspect of indirect effects is of particular interest. The biochemical and spectroscopic methods that are commonly used in these kinds of studies can identify the possible damage types and provide information about the timescale for lesion formation, but they are not directly sensitive to the lesion structure. Moreover, these methods typically involve DNA degradation, processing, staining, or labeling procedures, which by themselves may alter the DNA damage [47]. Therefore, a new experimental approach was proposed by us [48] in order to study changes in the molecular structure of the DNA backbone due to the interaction with various radiation types. Using X-ray absorption spectroscopy (XAS) at the phosphorus K-edge, the influence of radiation on both the local geometric and electronic structure around the sugar phosphate backbone was probed. The local structure around the P atoms in DNA is sensitive to the different forms of damage. The DNA strand breaks are linked to bond cleavage in the DNA backbone that can produce 5'-phosphate (5'-PO_4), 3'-phosphate (3'-PO_4), and 3'-phosphoglycolate (3'-PG) termini. Further, the formation of photolesions such as the cyclobutane pyrimidine dimer (CPD) changes the molecular conformation resulting in a distortion around the P atom. In **Figure 7**, the structure of different damage sites is presented.
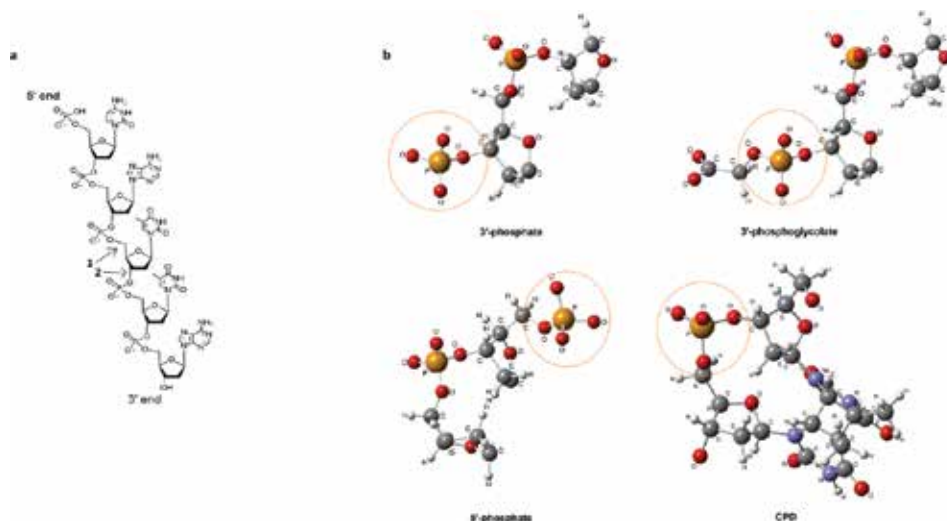
Figure 7. (a) Chemical structure of the fragment of DNA strand. Arrows indicate the bonds that can be broken and lead to 1: 3'-termini; 2: 5'-termini. (b) Structures of the four lesion types: 3'-phosphate, 3'-phosphoglycolate, 5'-phosphate, and CPD. Distorted PO_4 groups are highlighted with orange circles, reproduced from elsewhere with permission [48].

It is expected that various geometries are obtained depending on the form and energy of the radiation used. In our studies, we focused on two different radiation types, namely UV-A and proton radiation. UV-A (315–400 nm) is a main part of UV solar light that is considered as most serious environmental carcinogen. Although its absorption in DNA is rather small, it penetrates our skin very efficiently and can reach its deeper layers [49]. UV-A can cause several damage types and among them the most pronounced are single- and double-strand breaks and CPDs [50], which are produced only by UV radiation. In contrast, proton radiation produces DNA strand breaks but no CPDs. Proton radiation is the most common particle radiation used in cancer therapy of a variety of tumors, including those of the central nervous system, eye, lung, breast, prostate, head, and neck, as well as sarcomas and many pediatric cancers [51]; therefore, its detailed interaction with biomolecules has to be known.

The concept of presented studies [48] was to combine XAS experiment with theoretical calculations in order to identify the damage types and their structure. As a model sample, calf thymus DNA was used because its structure is almost identical with human DNA [52]. X-ray absorption spectra were collected for aqueous solutions of DNA irradiated with UV-A and protons, as well as for non-irradiated DNA that was used as a reference sample. Next, the spectral differences were calculated for P K-edge spectra obtained for irradiated and non-irradiated DNA (**Figure 8(a)**).

Simultaneously, P K-edge XAS spectra were calculated theoretically for each possible damage type (see structures in **Figure 7**), using FDMNES code, and the same procedure, as in case of experimental data, to obtain spectral differences was applied. Among others, the differences showed changes in the intensity of main peak in case of 3'- and 5'-phosphate that can be

associated with the break in one of the C-O bonds around PO_4 group, and a shift toward higher energies in case of CPD structure, associated with decreasing bond angle in O-P-O bond. Next, experimental differences were fitted with theoretical ones. The results of the fit for UV-A irradiated DNA are shown in **Figure 8(b)**. It was shown that the experimental difference can be reconstructed by the combination of theoretical spectra of 3′-phosphate, CPD, and 5′-phosphate with relative ratios 56% (±6.2%), 32% (±12%), and 12% (±6.8%), respectively. It indicates that the major damage types are strand breaks with predominant 3′-phosphate termini structure. Second group of damage is the formation of CPDs, which presence confirms direct absorption of UV-A radiation by DNA molecule. In case of the spectra obtained for proton-irradiated DNA, the same analysis was performed and it revealed that protons produce mainly 3′-phosphate (74% ± 17.6%) and 5′-phosphate (26% ± 19.6%) lesions. No CPDs were detected, supportive with the fact that they are only produced by UV radiation. The results for both irradiation types show that the bond between 5′-carbon atom of deoxyribose and oxygen in the phosphate group is most likely to be broken in the DNA backbone.
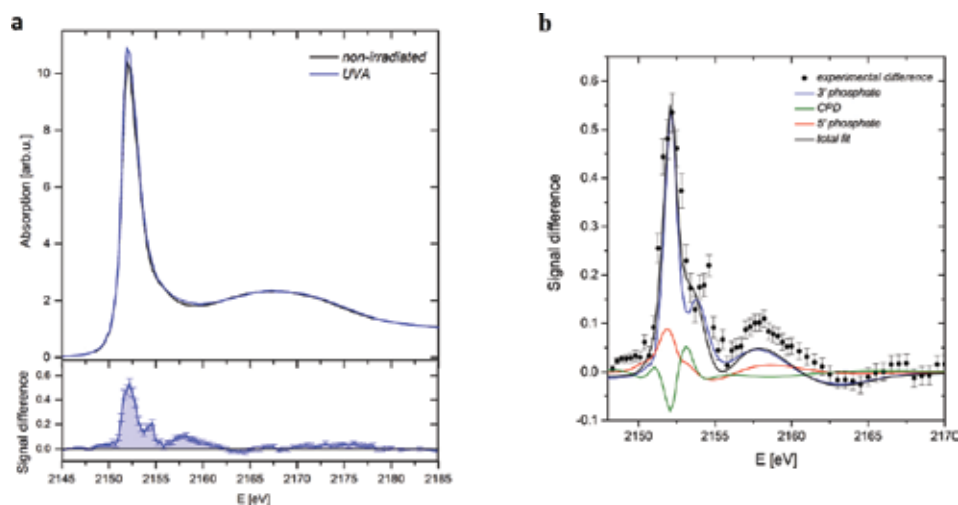

Figure 8. (a) (top) Phosphorus K-edge x-ray absorption spectra of intact and UVA-irradiated aqueous DNA samples; (bottom) P K-edge XAS difference signal between the spectrum of damaged and reference DNA sample. (b) The experimental difference of P K-edge XAS obtained for UVA-irradiated DNA sample fitted with the theoretical spectra. Reproduced from elsewhere with permission [48].

The foregoing approach of determining DNA damage can be easily implemented to study the effect of any damaging agents like various radiation types and chemical compounds. As it was shown, XAS is sensitive to the structure of the produced damage and can provide information about their relative ratios; therefore, it can be used in studies revealing the mechanism of damage development. Especially, it is important to study first stages of damage formation, since, as Boudaïffa et al. [53] suggested, "it is only through a complete understanding of such early events in the generation of genotoxic damage that we may hope to eventually manipulate the effects of ionizing radiation at a molecular level." It is foreseen that the developed methodology can be used in the time-resolved experiments on lesion formation at the X-ray free

electron lasers (XFELs), which give the opportunity to perform X-ray spectroscopy studies with ultrafast timescales.

5. Studies of changes in chemical forms of sulfur in case of prostate cancer

According to the World Health Organization, "cancer is the uncontrolled growth of cells, which can invade and spread to distant sites of the body. Cancer can have severe health consequences and is a leading cause of death" [20]. It comprises 13% of all deaths worldwide and among more than 100 types of cancerous diseases, each requiring unique diagnostic and treatment; prostate cancer is the second most common type in men [20]. As in the case of other cancerous diseases, one of the main issues in prostate cancer research is represented by the discovery and validation of new cancer biomarkers to understand its etiopathology for both diagnosis and new therapies design. A biomarker of cancer can be any structural and/or functional detectable change connected with a cancer disease in human individuals, for example, in genes, proteins, or metabolites [54]. Ideal experimental method to identify such changes should be highly sensitive, specific, and characterized by as minimal as possible sample manipulation. The studies presented in this section take advantage of X-ray spectroscopy to study sulfur species in prostate cancer cell lines and tissue [6, 8, 55, 56]. Sulfur is a key element in human organism. In biological systems, sulfur is present in all of its oxidation state from the reduced one (-2) to the most oxidized one (+6). First of all, it is a part of two amino acids—cysteine and methionine —and their derivatives, which are building blocks of many important proteins. Further, another important compound is the major low-molecular-weight thiol glutathione (GSH), which is involved in the defense against reactive oxygen species that disrupts homeostasis as observed in several pathological conditions [57]. In its oxidized form, sulfur is present for example in sulfates, like chondroitin sulfate, the glucosaminoglycan (GAG) occurring in extracellular matrix that affects proliferation and cell division during growth and differentiation of tissues. Increased expression of chondroitin sulfate is associated with the development of malignant lesions in various tissues, and it was shown that in case of prostate cancer, it indicates high tumor malignancy [58, 59]. Additionally, sulfenic, sulfinic, and sulfonic derivatives may be formed during severe oxidation stress that is strongly associated with cancerogenesis and their presence in prostate cells or their surrounding may indicate dysregulated redox balance [60]. Because of its sensitivity, X-ray absorption spectroscopy accompanied by careful data analysis was applied to such a complex and heterogenic samples.

5.1. Sulfur speciation in prostate cancer cell lines

Commercially available cell lines are often used as a model sample in different cancer research. In the first part of our experiment, three commercial prostate cancer cell lines and one non-cancerous cell lines were used. They were as follows: PC-3 cell line, derived from advanced androgen independent bone metastasized prostate cancer; DU145 cell line, derived from brain metastasis; LNCaP (androgen-sensitive human prostate adenocarcinoma cells), derived from the left supraclavicular lymph node metastasis; and PZ-HPV-7, derived from epithelial cells cultured from normal tissue obtained from the peripheral zone of the prostate. Sulfur K-edge

X-ray absorption spectra were acquired on the paraffin-fixed, dried layer of cells, placed on Mylar foil. Typical spectra obtained for each cell type are presented in **Figure 9(a)**.

All of the spectra are characterized by two strong features at energies 2472.4 and 2480.0 eV that, after the comparison with the spectra of reference compounds [6], were identified as the signature of reduced and oxidized forms of sulfur. Although the positions of the main features are identical in all spectra, they differ by the intensity. Preliminary analysis performed with the use of peak fitting method to determine the area under the peaks showed that the content of reduced sulfur forms does not vary much between cell lines but significant differences are present in the content of oxidized sulfur forms between cancerous and non-cancerous cells [6, 8]. These preliminary results suggested that there might be changes in redox balance, and therefore, the detailed analysis by linear combination fit method was performed with the use of ATHENA software [61]. The method was used before, for example, to establish sulfur forms in erythrocytes and plasma [15]. Experimental S K-edge XAS spectra of prostate cells were fitted with spectra of model sulfur-bearing compounds that are likely to be present in human cells. The chosen groups were as follows: amino acids, thiols, disulfides, sulfonates, and sulfates. In case of sulfonates, two model compounds were used: taurine and cysteic acid. The representative result of fitting procedure is shown in **Figures 9(b)** and **10** presents the results of the fitting for all cell line types in the form of bar graphs together with standard deviation.
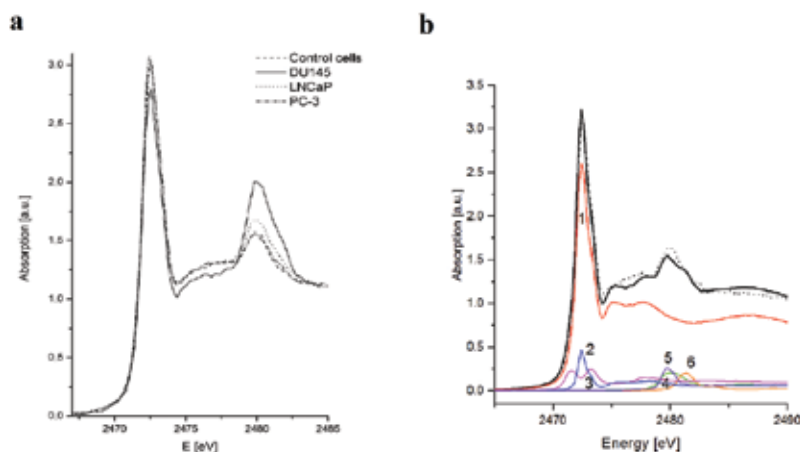

Figure 9. (a) The comparison of experimental S K-edge XANES spectra of four different cell lines. (b) Example of experimental sulfur K-edge XANES spectrum (PC3 cells, dotted line) with a linear combination (solid thick line) of: 1. amino acid, 2. thiol, 3. disulfide, 4. sulfonate (cysteic acid), 5. sulfonate (taurine), and 6. sulfate. Reproduced from elsewhere with permission [8].

In case of disulfide group, no differences were observed. There were very slight changes in amino acids and sulfates content, and the most pronounced differences were shown in case of thiols and sulfonates, especially between DU-145 cells and control cells. Thiols group may be associated mainly with reduced glutathione (GSH) and presented results for this group are consistent with the studies of Canada et al. [62] in which it was shown that DU-145 cells, in

comparison with other prostate cancer cells, are characterized by the highest level of GSH. GSH is known as a neutralizing agent of oxidizing species, produced during severe oxidative stress that is considered as one of the major factors in development and progression of prostate cancer [63]. The higher content might be also the indicator of active cell proliferation as it is observed in cells with aggressive phenotype [64]. The sulfonates group consists mainly of the metabolic products generated during the oxidation of cysteine. The other example is gluta-thione sulfonate (GSA) that is formed as a result of the interaction between reduced glutathione and free radicals [65].
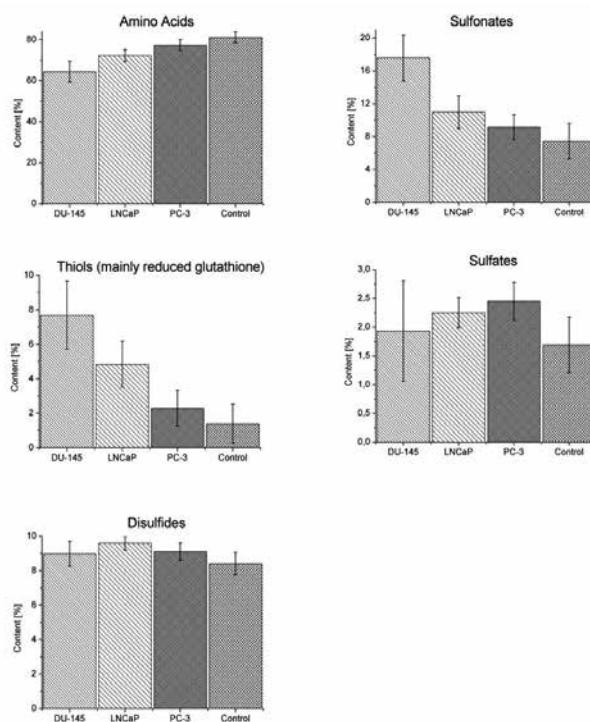

Figure 10. The content of the model groups of compounds in different cell lines obtained from linear combination fit. The sulfonate content represents both cysteic acid and taurine content. The error bars were calculated as the standard deviation of the determined mean values. Reproduced from elsewhere with permission [8].

The results obtained during the analysis of S K-edge XAS spectra of prostate cell lines gave insights into the potential biochemical changes that occur in cancer cells. The differences in the content of thiols between various cancerous cell lines and non-cancerous one may indicate a greater free radical production in cancer cells and their increased proliferative activity. Clearly visible is also the increase in the content of oxidized sulfur forms in case of cancer cells that indicates the unbalanced redox status. Although it is not clear whether these differences are a cause or consequence of malignant transformation, however, the results point out that this process influences strongly the biochemistry of sulfur-bearing compounds inside the cell.

5.2. Distribution of different forms of sulfur in prostate cancer tissue

In prostate tissue, as in other tissues in human organism, we can find different types of cells accompanied by extracellular matrix. Typical prostate is built of two main parts: prostatic glands and stroma composed from smooth muscle cells and connective tissue. Therefore, such a structure is far more complex than cell lines, in which all cells are of the same phenotype. To analyze the distribution of different forms of the element of interest in tissue, XAS imaging can be used and data need to be collected from the tissue area that covers different histological parts. The method is based on the fact that different oxidation states of the same element can be selectively excited by tuning the incidence energy. The generated fluorescence signal is collected in point-by-point mode in the chosen sample area for each of the incidence energy. The fraction of individual forms of the element can be extracted for each pixel by applying the procedure described by Pickering et al. [66, 67]. The calculated relative concentrations can then be used to generate 2D maps of the distribution of each form and compared with microscopic image.

Our experiment [56] was performed on the tissue sections obtained during routine prostatectomies that were in a form of 15-μm-thick air-dried slices placed on Mylar foil. The first step was to measure full XAS spectra in few different points on the tissue in order to establish the value of incidence energies that should be used in XAS imaging. The examples of spectra are presented in **Figure 11**.
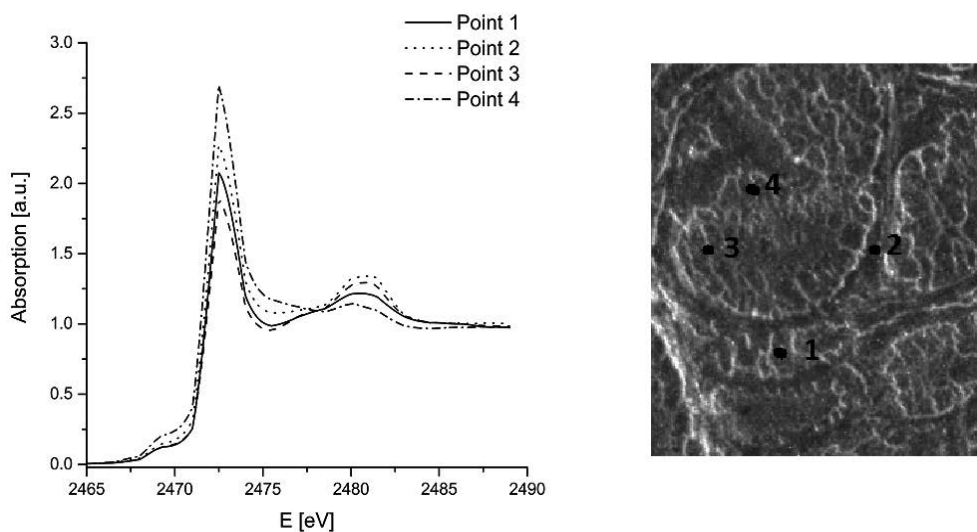

Figure 11. Sulfur K-edge μ-XANES spectra collected at different points in prostate tissue (left) together with the microscopic image of the tissue with marked measurements points (right). Spectra 1, 3, and 4 are measured in nodular part while spectrum 2 in stroma. Reproduced from elsewhere with permission [56].

The two main features have the same energy position as the ones in prostate cancer cells. Therefore, the scanning energies were set above these features (2473 and 2482 eV) to image

reduced and oxidized forms of sulfur in the tissue. Additionally, scans were also performed with energy 2477 eV, which is exciting energy of sulfur with intermediate oxidation state and 2500 eV, which excites total sulfur in the sample. The latter was used to normalize measured fluorescence intensities for different pixels. The data for prostate cancer tissue were collected with 10-μm spatial resolution that was enough to analyze different histological parts. 2D distribution maps of individual chemical forms of sulfur in three prostate cancer tissue samples obtained from three different patients are presented in **Figure 12**. Maps are accompanied by the microscopic image of the studied area.
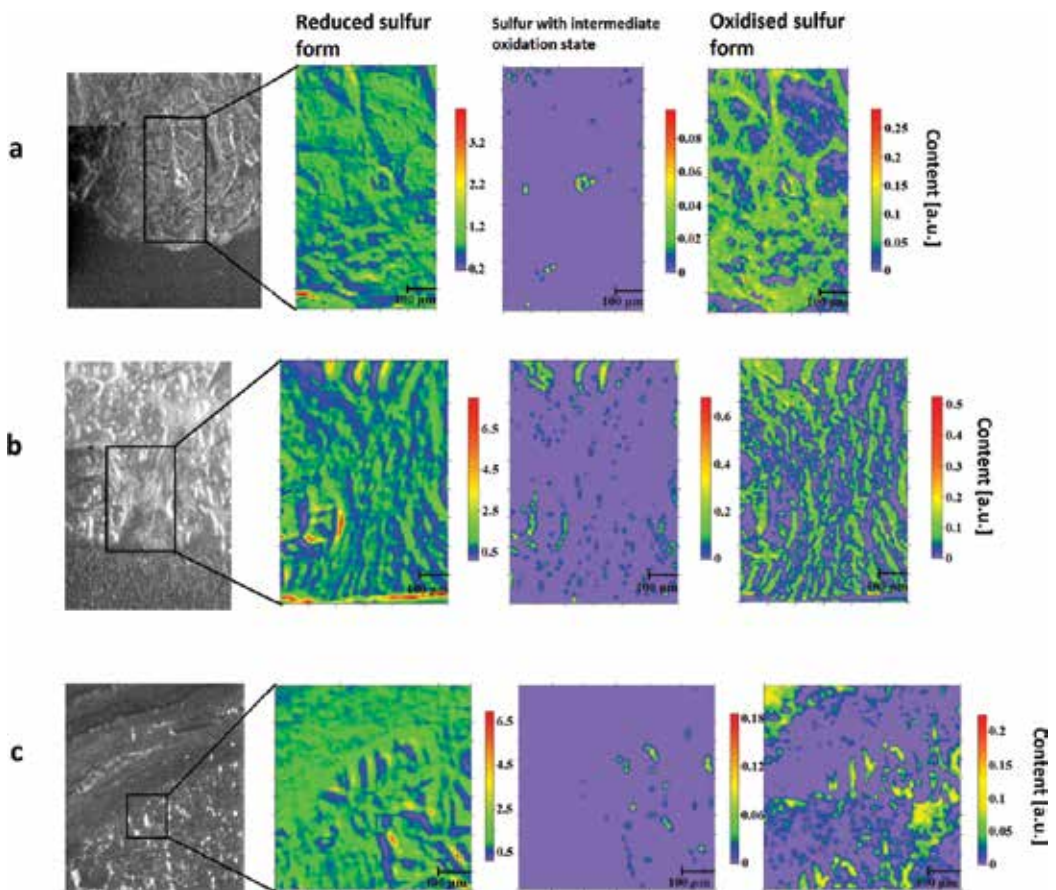

Figure 12. Two-dimensional maps of the distribution of individual chemical forms of sulfur in the selected areas of three different prostate cancer tissue slices together with microscopic image with marked area of scanning. (a–c) Samples derived from three different patients diagnosed with prostate cancer undergoing prostatectomy. Reproduced from elsewhere with permission [56].

Based on the results, we observed that the majority of sulfur located in prostate tissue occurs in reduced form, which is consistent with the results obtained for cell lines. This form is present

in all histological structures but predominantly in glandular part of the tissue. In contrast, the compounds containing sulfur with intermediate oxidation state occur in very small quantities in studied samples and they are not correlated with the specific histological structures. Sulfur with highest oxidation state is distributed unevenly, with higher content present in prostate stroma. As in case of prostate cancer cells, the occurrence of highly oxidized forms of sulfur may be the indicator of the production of oxidative derivatives of sulfur-bearing compounds resulting from the interaction with reactive oxygen species activity due to oxidative stress [60]. But in case of tissue structure, another source of sulfur with high oxidation state may be the elevated concentration of chondroitin sulfate in extracellular matrix, the compound that plays a potential role in aggressiveness of a tumor [58, 59].

Conclusions drawn from this experiment confirmed the results obtained for cell lines and extended them with information about spatial distribution of the various forms of sulfur in different histological parts of tissue. In case of heterogenous samples like human tissue, the methodology applied here allows to study the distribution of various chemical species of the same element without any chemical manipulation. In case of biologically essential elements, the detection of changes in their biochemistry can help to elucidate the possible mechanism of cancer development and progression.

Acknowledgements

Author details

Joanna Czapla-Masztafiak[1,2*], Wojciech M. Kwiatek[1], Jacinto Sá[3,4] and Jakub Szlachetko[2,5]

*Address all correspondence to: joanna.czapla@ifj.pan.pl

1 Institute of Nuclear Physics, Polish Academy of Sciences, Krakow, Poland

2 Paul Scherrer Institut, Villigen, Switzerland

3 Department of Chemistry, Ångström Laboratory, Uppsala University, Uppsala, Sweden

4 Institute of Physical Chemistry, Polish Academy of Sciences, Warsaw, Poland

5 Institute of Physics, Jan Kochanowski University in Kielce, Kielce, Poland

References

[1] Szlachetko J, Sá J. Rational design of oxynitride materials: from theory to experiment. CrystEngComm. 2013;15:2583–2587. doi:10.1039/c3ce26909d

[2] Glatzel P, Bergmann U. High resolution 1s core hole X-ray spectroscopy in 3d transition metal complexes—electronic and structural information. Coord. Chem. Rev. 2005;249:65–95. doi:10.1016/j.ccr.2004.04.011

[3] Szlachetko J, Sá J, Nachtegaal M, Hartfelder U, Dousse J-C, Hoszowska J et al. Real time determination of the electronic structure of unstable reaction intermediates during Au_2O_3 reduction. J. Phys. Chem. Lett. 2014;5:80–84. doi:10.1021/jz402309s

[4] Schäfer T, Buckau G, Artinger R, Kim JI, Geyer S, Wolf M et al. Origin and mobility of fulvic acids in the Gorleben aquifer system: implications from isotopic data and carbon/sulfur XANES. Org. Geochem. 2005;36:567–582. doi:10.1016/j.orggeochem.2004.10.011

[5] Nakai I, Matsunaga M, Adachi M, Hidaka K-I. Application of XAFS in archaeology. Journal de Physique IV Colloque. 1997;7:pp. C2-1033 – C2-1034. doi:10.1051/jp4:19972131

[6] Czapla J, Kwiatek WM, Lekki J, Steininger R, Göttlicher J. Determination of changes in sulphur oxidation states in prostate cancer cells. Acta Phys. Pol. A. 2012;121:497–501. doi:10.12693/APhysPolA.121.497

[7] Lipiec E, Czapla J, Szlachetko J, Kayser Y, Kwiatek W, Wood B, et al. Novel *in situ* methodology to observe the interactions of chemotherapeutical Pt drugs with DNA under physiological conditions. Dalton Trans. 2014;43:13839–44. doi:10.1039/c4dt00861h

[8] Czapla J, Kwiatek WM, Lekki J, Dulińska-Litewka J, Steininger R, Göttlicher J. Chemical species of sulfur in prostate cancer cells studied by XANES spectroscopy. Rad. Phys. Chem. 2013;93:154–159. doi:10.1016/j.radphyschem.2013.05.021

[9] Stone KL, Behan RK, Green MT. X-ray absorption spectroscopy of chloroperoxidase compound I: insight into the reactive intermediate of P450 chemistry. Proc. Natl. Acad. Sci. U.S.A. 2005;102:16563–16565. doi:10.1073/pnas.0507069102

[10] Salt DE, Prince RC, Baker AJM, Raskin I, Pickering IJ. Zinc ligands in the metal hyperaccumulator Thlaspi caerulescens as determined using X-ray absorption spectroscopy. Environ. Sci. Technol. 1999;33:713–717. doi:10.1021/es980825x

[11] Arcovito A, Benfatto M, Cianci M, Hasnain SS, Nienhaus K, Nienhaus GU, et al. X-ray structure analysis of a metalloprotein with enhanced active-site resolution using *in situ* X-ray absorption near edge structure spectroscopy. Proc. Natl. Acad. Sci. U. S. A. 2007;104:6211–6216. doi:10.1073/pnas.0608411104

[12] Wandzilak A, Czyzycki M, Wrobel P, Szczerbowska-Boruchowska M, Radwanska E, Adamek D, et al. The oxidation states and chemical environments of iron and zinc as

potential indicators of brain tumour malignancy grade—preliminary results. Metallo-mics. 2013;5:1547–1553. doi:10.1039/c3mt00158j

[13] Czapla-Masztafiak J, Lis GJ, Gajda M, Jasek E, Czubek U, Bolechała F, et al. Determi-nation of oxidation state of iron in normal and pathologically altered human aortic valves. Nucl. Instruments Methods Phys. Res. Sect. B. 2015;364:70–75. doi:10.1016/j.nimb.2015.04.026

[14] Chwiej J, Adamek D, Szczerbowska-Boruchowska M, Krygowska-Wajs A, Bohic S, Lankosz M. Study of Cu chemical state inside single neurons from Parkinson's disease and control substantia nigra using the micro-XANES technique. J. Trace Elem. Med. Biol. 2008;22:183–188. doi:10.1016/j.jtemb.2008.03.006

[15] Pickering IJ, Prince RC, Divers T, George GN. Sulfur K-edge X-ray absorption spectro-scopy for determining the chemical speciation of sulfur in biological systems. FEBS Lett. 1998;441:11–14. doi:10.1016/S0014-5793(98)01402-1

[16] Weekley CM, Aitken JB, Vogt S, Finney L a., Paterson DJ, De Jonge MD, et al. Uptake, distribution, and speciation of selenoamino acids by human cancer cells: X-ray absorption and fluorescence methods. Biochemistry. 2011;50:1641–1650. doi:10.1021/bi101678a

[17] Bacquart T, Deves G, Ortega R. Direct speciation analysis of arsenic in sub-cellular compartments using micro-X-ray absorption spectroscopy. Environ. Red. 2010;110:413–416. doi:10.1016/j.envres.2009.09.006

[18] Dau H, Haumann M. Time-resolved X-ray spectroscopy leads to an extension of the classical S-state cycle model of photosynthetic oxygen evolution. Photosynth. Res. 2007;92:327–343. doi:10.1007/s11120-007-9141-9

[19] Lima FA, Milne CJ, Amarasinghe DC V, Rittmann-Frank MH, Veen RM Van Der, Reinhard M, et al. A high-repetition rate scheme for synchrotron-based picosecond laser pump X-ray probe experiments on chemical and biological systems in solution. Rev. Sci. Instrum. 2011;82:063111. doi:10.1063/1.3600616

[20] Available from: http://www.who.int/cancer/en/ [Accessed: 11.07.2016]

[21] Sá J. High-resolution XAS/XES: analyzing electronic strudtures of catalysis. CRC Press: Taylor and Francis Group; 2014.

[22] Lundberg M, Kroll T, DeBeer S, Bergmann U, Wilson S, Glatzel P, et al. Metal-ligand covalency of iron complexes from high-resolution resonant inelastic X-ray scattering. J. Am. Chem. Soc. 2013;135:17121–17134. doi:10.1021/ja408072q

[23] Pollock CJ, DeBeer S. Valence-to-core X-ray emission spectroscopy: a sensitive probe of the nature of a bound ligand. J. Am. Chem. Soc. 2011;133:5594–5601. doi:10.1021/ja200560z

[24] Vankó G, Renz F, Molnár G, Neisius T, Kárpáti S. Hard-X-ray-induced excited-spin-state trapping. Angew. Chemie Int. Ed. 2007;46:5306–5309. doi:10.1002/anie.200604432

[25] Bergmann U, Glatzel P. X-ray emission spectroscopy. Photosynth. Res. 2009;102:255–266. doi:10.1007/s11120-009-9483-6

[26] Sikora M, Juhin A, Weng T-C, Sainctavit P, Detlefs C, de Groot F, et al. Strong K-edge magnetic circular dichroism observed in photon-in-photon-out spectroscopy. Phys. Rev. Lett. 2010;105:037202. doi:10.1103/PhysRevLett.105.037202

[27] Singh J, Lamberti C, van Bokhoven J. Advanced X-ray absorption and emission spectroscopy: *in situ* catalytic studies. Chem. Soc. Rev. 2010;39:4754–4766. doi:10.1039/c0cs00054j

[28] Lancaster KM, Roemelt M, Ettenhuber P, Hu Y, Ribbe MW, Neese F, et al. X-ray emission spectroscopy evidences a central carbon in the nitrogenase iron-molybdenum cofactor. Science. 2011;334:974–977. doi:10.5061/dryad.6m0f6870

[29] Campbell JL, Papp T. Atomic level widths for X-ray spectrometry. X-ray Spetrom. 1995;24:307–319. doi:10.1002/xrs.1300240606

[30] Campbell JL, Papp T. Widths of the atomic K-N7 levels. At. Data Nucl. Data Tables. 2001;77:1–56. doi:10.1006/adnd.2000.0848

[31] von Hámos L. X-ray spectroscopy and imaging by means of a curved crystal reflectors. Naturwissenschaften. 1932;20:705.

[32] Hoszowska J, Dousse JC, Kern J, Rheme C. High-resolution von Hamos crystal X-ray spectrometer. Nucl. Instrum. Methods Phys. Res. Sect. A. 1996;376:129–138. doi:10.1016/0168-9002(96)00262-8

[33] Johannson T. On a novel, exactly focusing X-ray spectrometer. Zeitschrift Für Phys. 1931;82:507.

[34] Johann HH. Obtaining intense X-ray spectra by means of concave crystals. Zeitschrift Für Phys. 1931;69:185.

[35] Szlachetko J, Nachtegaal M, De Boni E, Willimann M, Safonova O, Sà J, et al. A von Hamos X-ray spectrometer based on a segmented-type diffraction crystal for single-shot X-ray emission spectroscopy and time-resolved resonant inelastic X-ray scattering studies. Rev. Sci. Instrum. 2012;83:103105. doi:10.1063/1.4756691

[36] Rehr JJ, Kas JJ, Vila FD, Prange MP, Jorissen K. Parameter-free calculations of X-ray spectra with FEFF9. Phys. Chem. Chem. Phys. 2010;12:5503–5513. doi:10.1039/b926434e

[37] Bunău O, Joly Y. Self-consistent aspects of X-ray absorption calculations. J. Phys. Condens. Matter. 2009;21:345501. doi:10.1088/0953-8984/21/34/345501

[38] Sá J, Czapla-Masztafiak J, Lipiec E, Kayser Y, Fernandes DLA, Szlachetko J, et al. Resonant X-ray emission spectroscopy of platinum(ii) anticancer complexes. Analyst. 2016;141:1226–1232. doi:10.1039/C5AN02490K

[39] Berger G, Leclercqz H, Derenne A, Gelbcke M, Goormaghtigh E, Nève J, et al. Synthesis and in vitro characterization of platinum(II) anticancer coordinates using FTIR spectroscopy and NCI COMPARE: a fast method for new compound discovery. Bioorg. Med. Chem. 2014;22:3527–3536. doi:10.1016/j.bmc.2014.04.017

[40] Tisato F, Marzano C, Porchia M, Pellei M, Santini C. Copper in diseases and treatments, and copper-based anticancer strategies. Med. Res. Rev. 2010;30:708–749. doi:10.1002/med.20174

[41] Santini C, Pellei M, Gandin V, Porchia M, Tisato F, Marzano C. Advances in copper complexes as anticancer agents. Chem. Rev. 2014;114:815–862. doi:10.1021/cr400135x

[42] Sherman SE, Gibson D, Wang AH-J, Lippard SJ. X-ray structure of the major adduct of the anticancer drug cisplatin with DNA: cis-[Pt(NH3)2(d(pGpG))]. Science. 1985;230:412–417. doi:10.1126/science.4048939

[43] Takahara P, Rosenzweig A, Frederick C, Lippard S. Crystal structure of double-stranded DNA containing the major adduct of the anticancer drug cisplatin. Nature. 1995;377:649–652. doi:10.1038/377649a0

[44] Baik MH, Friesner RA, Lippard SJ. Theoretical study of cisplatin binding to purine bases: why does cisplatin prefer guanine over adenine? J. Am. Chem. Soc. 2003;125:14082–14092. doi:10.1021/ja036960d

[45] Cepeda V, Fuertes M, Castilla J, Alonso C, Quevedo C, Pérez JM. Biochemical mechanisms of cisplatin cytotoxicity. Anticancer. Agents Med. Chem. 2007;7:3–18. doi:10.2174/187152007779314044

[46] Fernandes DLA, Pavliuk MV, Sá J. A 3D printed microliquid jet with an adjustable nozzle diameter. Analyst. 2015;140:6234–6238. doi:10.1039/C5AN01329A

[47] Jiang Y, Rabbi M, Kim M, Ke C, Lee W, Clark RL, et al. UVA generates pyrimidine dimers in DNA directly. Biophys. J. 2009;96:1151–1158. doi:10.1016/j.bpj.2008.10.030

[48] Czapla-Masztafiak J, Szlachetko J, Milne CJ, Lipiec E, Sá J, Penfold TJ, et al. Investigating DNA radiation damage using X-ray Absorption Spectroscopy (XAS). Biophys. J. 2016;110:1304–1311. doi:10.1016/j.bpj.2016.01.031

[49] Osipov AN, Smetanina NM, Pustovalova MV, Arkhangelskaya E, Klokov D. The formation of DNA single-strand breaks and alkali-labile sites in human blood lymphocytes exposed to 365-nm UVA radiation. Free Radic. Biol. Med. 2014;73:34–40. doi:10.1016/j.freeradbiomed.2014.04.027

[50] Kielbassa C, Roza L, Epe B. Wavelength dependence of oxidative DNA damage induced by UV and visible light. Carcinogenesis. 1997;18:811–816. doi:10.1093/carcin/18.4.811

[51] Foote RL, Stafford SL, Petersen IA, Pulido JS, Clarke MJ, Schild SE, et al. The clinical case for proton beam therapy. Radiat. Oncol. 2012;7:174–183. doi:10.1186/1748-717X-7-174

[52] Mouret S, Philippe C, Gracia-Chantegrel J, Banyasz A, Karpati S, Markovitsi D, et al. UVA-induced cyclobutane pyrimidine dimers in DNA: a direct photochemical mechanism? Org. Biomol. Chem. 2010;8:1706–1711. doi:10.1039/b924712b

[53] Boudaïffa B, Cloutier P, Hunting D, Huels M a, Sanche L. Resonant formation of DNA strand breaks by low-energy (3 to 20 eV) electrons. Science. 2000;287:1658–1660. doi:10.1126/science.287.5458.1658

[54] Bellisola G, Sorio C. Infrared spectroscopy and microscopy in cancer research and diagnosis. Am. J. Cancer Res. 2012;2:1–21.

[55] Kwiatek WM, Czapla J, Podgórczyk M, Kisiel A, Konior J, Balerna A. First approach to studies of sulphur electron DOS in prostate cancer cell lines and tissues studied by XANES. Rad. Phys. Chem. 2011;80:1104–1108. doi:10.1016/j.radphyschem.2011.05.005

[56] Czapla-Masztafiak J, Okoń K, Gałka M, Huthwelker T, Kwiatek WM. Investigating the distribution of chemical forms of sulfur in prostate cancer tissue using X-ray absorption spectroscopy. Appl. Spectrosc. 2016;70:264–271. doi:10.1177/0003702815620128

[57] Matés JM, Segura JA, Alonso FJ, Márquez J. Pathways from glutamine to apoptosis. Front. Biosci. 2006;11:3164–3180.

[58] Ricciardelli C, Mayne K, Sykes PJ, Raymond WA, McCaul K, Marshall VR, et al. Elevated stromal chondroitin sulfate glycosaminoglycan predicts progression in early-stage prostate cancer. Clin. Cancer Res. 1997;3:983–992.

[59] Ricciardelli C, Quinn DI, Raymond WA, McCaul K, Sutherland PD, Stricker PD, et al. Elevated levels of peritumoral chondroitin sulfate are predictive of poor prognosis in patients treated by radical prostatectomy for early-stage prostate cancer. Cancer Res. 1999;59:2324–2328.

[60] Paschos A, Pandya R, Duivenvoorden WCM, Pinthus JH. Oxidative stress in prostate cancer: changing research concepts towards a novel paradigm for prevention and therapeutics. Prostate Cancer Prostatic Dis. 2013;16:217–225. doi:10.1038/pcan.2013.13

[61] Ravel B, Newville M. ATHENA, ARTEMIS, HEPHAESTUS: data analysis for X-ray absorption spectroscopy using IFEFFIT. J. Synchrotron Radiat. 2005;12:537–541. doi:10.1107/S0909049505012719

[62] Canada AT, Roberson KM, Vessella RL, Trump DL, Robertson CN, Fine RL. Glutathione and glutathione S-transferase in benign and malignant prostate cell lines and prostate tissues. Biochem. Pharmacol. 1996;51:87–90. doi:10.1016/0006-2952(95)02157-4

[63] Khandrika L, Kumar B, Koul S, Maroni P, Koul HK. Oxidative stress in prostate cancer. Cancer Lett. 2009;282:125–136. doi:10.1016/j.canlet.2008.12.011

[64] Matés JM, Pérez-Gómez C, De Castro IN, Asenjo M, Márquez J. Glutamine and its relationship with intracellular redox status, oxidative stress and cell proliferation/death. Int. J. Biochem. Cell Biol. 2002;34:439–458. doi:10.1016/S1357-2725(01)00143-1

[65] Wefers H, Sies H. Oxidation of glutathione by the superoxide radical to the disulfide and the sulfonate yielding singlet oxygen. Eur. J. Biochem. 1983;137:29–36.

[66] Pickering IJ, Sneeden EY, Prince RC, Block E, Harris HH, Hirsch G, et al. Localizing the chemical forms of sulfur in vivo using X-ray fluorescence spectroscopic imaging: application to onion (*Allium cepa*) tissues. Biochemistry. 2009;48:6846–6853. doi:10.1021/bi900368x

[67] Pickering IJ, George GN. X-ray absorption spectroscopy imagin of biological tissues. AIP Conf. Proc. 2007;882:311–315. doi:10.1063/1.2644509

X-Ray Diffraction in Biology: How Can We See DNA and Proteins in Three Dimensions?

Claudine Mayer

Additional information is available at the end of the chapter

http://dx.doi.org/10.5772/64999

Abstract

Knowing the three-dimensional structure of biological macromolecules, such as proteins and DNA, is crucial for understanding the functioning of life. Biological crystallography, the main method of structural biology, which is the branch of biology that studies the structure and spatial organization in biological macromolecules, is based on the study of X-ray diffraction by crystals of macromolecules. This article will present the principle, methodology and limitations of solving biological structures by crystallography.

Keywords: biological macromolecules, X-ray diffraction, monocristal, tridimensional structure

1. Introduction

In 1953, James Watson and Francis Crick revealed the double helical structure of DNA using the results of Rosalyn Franklin obtained by X-ray scattering on natural filaments formed by DNA molecules [1]. Proteins, the nanomachines essential to living organisms, have their "manufacturing plan" encoded in their DNA gene sequence [2]. During their synthesis, proteins adopt a specific three-dimensional structure that allows them to perform their functions within the cell. "Seeing" the structure of biological macromolecules, such as proteins or nucleic acids (RNA or DNA), allows researchers to elucidate the mechanisms of live in all organisms, and among many other applications, allows them to design new drugs [3].

"Seeing" proteins or nucleic acids in three dimensions, a dream or a reality? Could microscopy, a technic known since more than 350 years that allows to visualize biological cells, be the right

approach? Of course, the dimensions of these two objects, macromolecules and cells are very different: The cell size ranges generally from 10 to 100 microns (10^{-6} m), the dimensions of biological macromolecules, proteins or nucleic acids, are of the order of tens of angstroms (10^{-10} m) (**Figure 1**). To reach atomic details, the method of choice is crystallography, whose principle is based on the bombardment by X-ray of crystals composed of biological macromolecules [4].
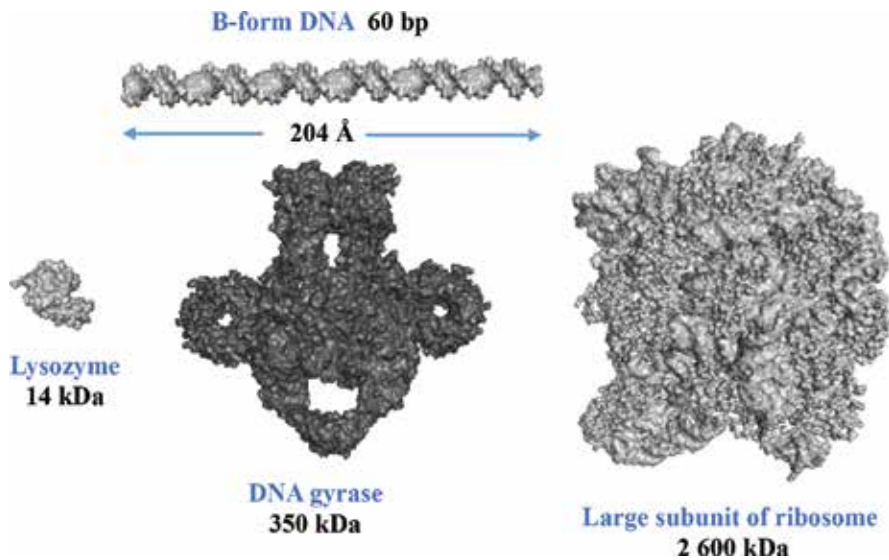

Figure 1. Dimension of biological macromolecules represented at the same scale (picture provided by Dr Jérémie Piton). The length of a 60 base pairs DNA double helix is 204 Å.

Why using X-rays? Their wavelength is of the order of the angström and thus corresponds to the distance between two bound atoms. **Why using a crystal**? To date, the conception of an X-ray microscope encounters two obstacles. First, the signal from a single macromolecule is too low, second, a device, such as lenses, generating a direct image of a macromolecules, does not exist for X-rays. Using a crystal, that contains about 10^{15} identical macromolecules periodically arranged in the three directions of space, overcomes these obstacles.

In only 50 years, crystallography has become the technique of choice for the determination of structures of biological macromolecules at atomic scale, taking advantage of the major advances in the scientific fields as diverse as molecular biology, biochemistry, computer science, physics and more recently robotics. Today, crystallography is able to address the determination of three-dimensional structures of macromolecules more and more complex, more and more quickly. Currently, more than 25 crystal structures are deposited daily in the Protein Data Bank (http://www.rcsb.org)[1] [5].

---

[1] The protein Data Bank (PDB) is a databank that contains 120,262 entries of macromolecules structures (protein, nucleic acids, complexes), 107,455 have been solved by X-ray crystallography (July 2016).

The physical principle of crystallography is based on X-ray diffraction by all the electrons constituting the atoms of all the macromolecules contained in the crystal (**Figure 2**). The analysis of these diffraction data then allows the crystallographer to calculate the electron density, which is the distribution of the electron cloud of the macromolecule in the crystal. This electron density provided it is sufficiently precise—this preciseness depends on the resolution of the diffraction data—allows the localization of each atom of the molecule, and thus the determination of its coordinates in the three-dimensional space [6].
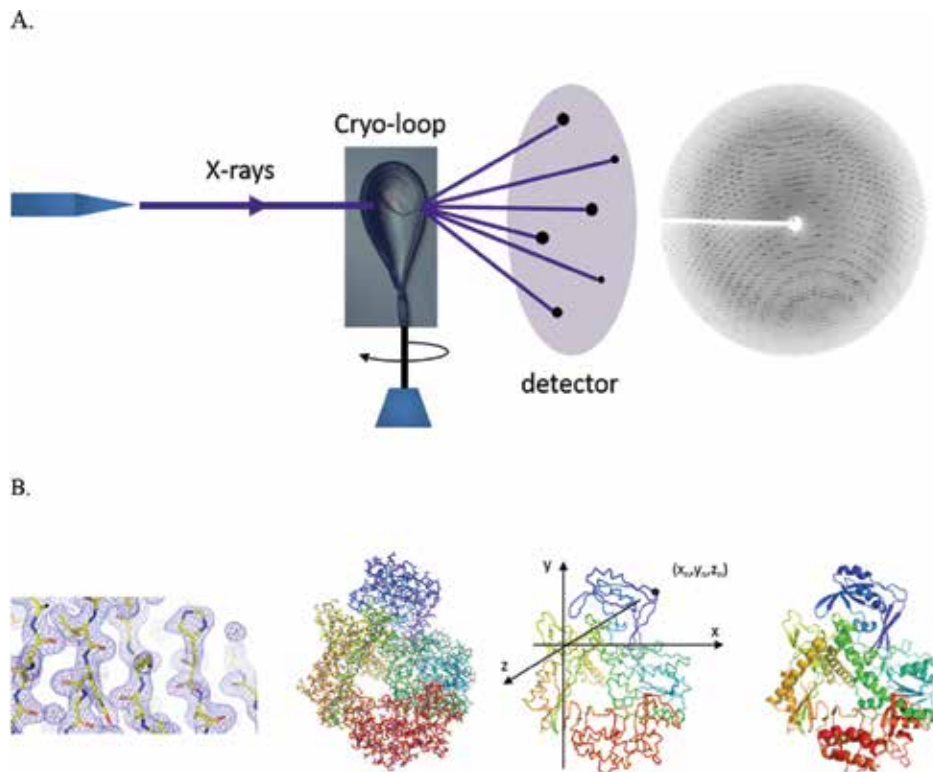

Figure 2. The principle of crystallography. (A) A monochromatic X-ray beam bombards a crystal frozen in a cryo-loop that rotates on itself. The observed diffraction spots are the result of the impact on the detector of the wave diffracted by the electrons in the crystal. (B) Electron density map of a fragment of a macromolecule is represented (left). The three-dimensional structure of a macromolecule (here a protein) is represented in three ways: all-atoms, backbone and cartoon representation (see **Figure 9**).

To get this three-dimensional structure, several steps that falls within multiple disciplines are required (**Figure 3**). Each of these steps represents potential bottlenecks that need to be overcome. These are the production and the purification of the macromolecule, its crystallization, diffraction data collection and processing. Another crucial step is the determination of the phases of the measured signal, absolutely required to calculate the electron density. The last step is the refinement of the built structure, called the model, which will then be interpreted in the context of its biological function. The analysis of the model will thus raise new questions

leading to the resolution of other crystal structures, such as structure of a complex between the studied protein and its partners [7]. We will in the following sections describe each of these steps.
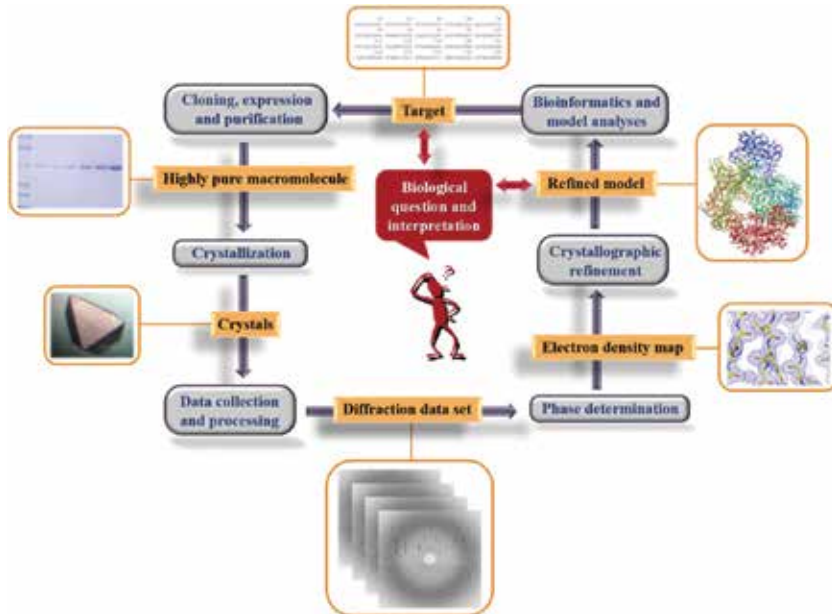

Figure 3. The main steps of the three-dimensional structure determination of biological macromolecules by crystallography.

2. Steps upstream the structure determination

The first step, a step that falls within biology and includes molecular biology and biochemistry techniques, is the production of highly pure macromolecule in large quantity. Once the sequence of the macromolecule to be studied has been identified and characterized by bioinformatics analyses, the sequence corresponding to the gene of the macromolecule is cloned in an expression vector and produced classically in a bacterial organism (typically *Escherichia coli*). The macromolecule is then extracted from the bacterial cells and purified using chromatographic techniques. The prerequisite for the next step is to obtain a concentrated[2] (of the order of tens of grams per liter) and highly pure sample (greater than 98%) of the macromolecule.

The next bottleneck is based on physical chemistry, specifically crystallization which addresses concepts such as solubility of molecules and their transition from soluble state to a solid

_____
[2] In a aqueous solution containing a buffer, salt and various additives.

crystalline ordered state [8]. This step, built on statistical screenings plays with the variation of parameters such as temperature, pH, concentrations of biological macromolecules, as well as nature and concentration of crystallizing agents and various additives [9]. Obtaining a single homogeneous crystal, that result to high quality diffraction data, represents a crucial step in the process of determining a macromolecular structure. In order to increase the success rate, crystallization robots are used today to screen more than several thousands of parameters. The size (from tens to hundreds of microns) and the morphology of the crystals are highly variable (**Figure 4**) and are not necessarily related to their diffracting power and quality.
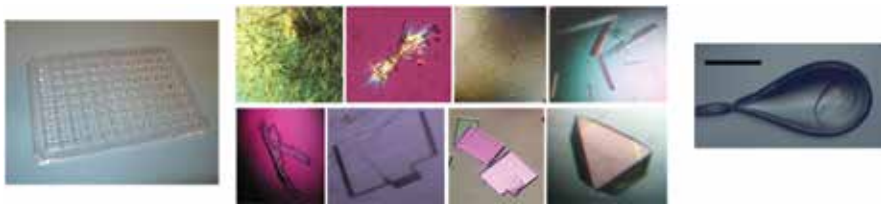

Figure 4. Crystals of biological macromolecules. Left, a typical crystallization plate used in crystallization robots that allows to screen 96 crystallization conditions. Middle, different crystals of macromolecule. Right, the crystal is shown in its cryo-loop (see Section 2.). The black bar is 100 microns.

3. The diffraction data

The crystals obtained during the previous step are fished using a small loop (**Figure 4**), cryo-cooled to protect them from radiation damage [10], and then placed into a monochromatic X-ray beam produced by an appropriate source, either a rotating anode generator available in crystallography laboratories or a synchrotron radiation, the latter producing significantly more intense beams [11]. Under these conditions, the waves scattered by the electrons of the macromolecules that are three-dimensionally ordered in the crystal add up in given directions (the diffracted beam is characterized by a structure factor, **Figure 7**) and generate a diffraction spot on the screen of the detector (**Figure 5A**). All the spots, regularly spaced, form the diffraction pattern (**Figure 5A**). This diffraction pattern is reconstituted by using several hundreds of images, each corresponding to an orientation of the crystal that rotates on itself during the measurement of the diffraction data (**Figure 2** and **Figure 5B**). The information contained in each diffraction spot is characterized by the amplitude and the phase of the structure factor characterizing the corresponding scattered wave.

The three-dimensional distribution of the spots is directly related to the cell parameters, e.g. the three lengths of the parallelepiped that constitutes the volume element (the cell), which is regularly repeated in space (**Figure 6**) and allows to describe the crystal. The distribution of the spot intensities is directly related to the electron density distribution (the macromolecules) in the cell. Mathematically, this means that the diffraction pattern is the Fourier transform of the electron density (**Figure 7**).
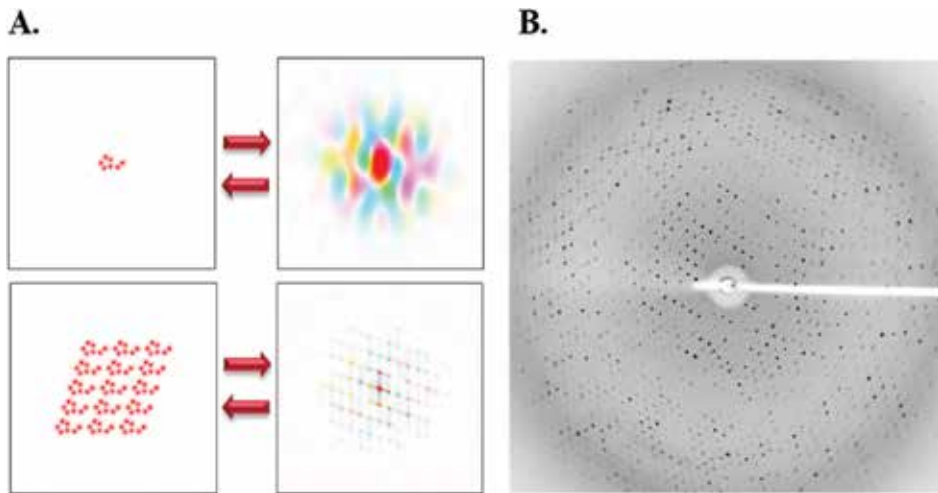
Figure 5. (A) The diffraction pattern (or Fourier transform) of a crystallized molecule generates a three-dimensional spot lattice (bottom), whose background image corresponds to the Fourier transform of a single molecule (top). The amplitude and phase of the diffracted beams are represented by the color brightness and the color hue, respectively (Kevin Cowtan's Picture Book of Fourier Transforms (http://www.ysbl.york.ac.uk/~cowtan/fourier/fourier.html). (B) Example of detector image constituting the diffraction pattern. Hundreds of images are usually recorded. The spots at the image edge are high resolution spots, providing the most detailed information.
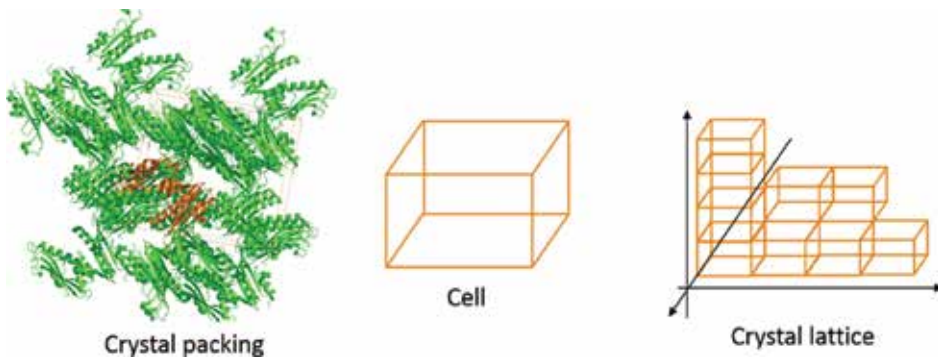

Figure 6. The macromolecules are ordered in the three directions of space and form the crystal packing (left). The smallest volume that is repeated by translation in all directions of space is the cell (middle and right). It forms a parallelepiped characterized by three vectors named a, b and c.

The electron density contained in one cell can thus be calculated by inverse Fourier transform, a mathematical property of this transformation, provided the amplitude and the phase of all the diffracted beams are known (**Figure 7**). Whereas the amplitude is directly proportional to the intensity of the diffracted spots, the phase information is not experimentally measurable.

In summary, the crystal "realizes" a Fourier analysis producing diffraction data, and the crystallographer will calculate a Fourier synthesis to get the electron density contained in one cell (**Figure 7**).

$$\rho(xyz) = \frac{1}{V} \sum_{\substack{hkl \\ -\infty}}^{+\infty} |F(hkl)| \cdot e^{-2\pi i[hx+ky+lz-\phi(hkl)]} \qquad F(hkl) = \sum_j f_j e^{2\pi i(hx_j+ky_j+lz_j)}$$
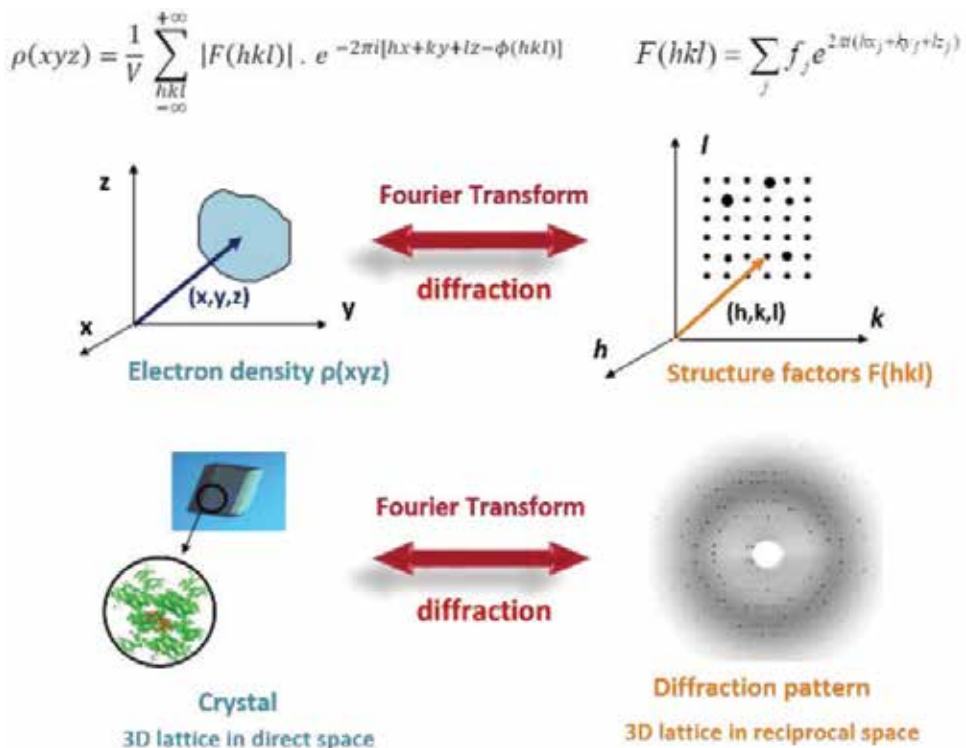

Figure 7. Schematic summary of the relationship between the diffraction (structure factors and diffraction spots) and the electron density of the structure three-dimensionally packed in the crystal.

4. From the diffraction data to the electron density

Three main methods exist for the estimation of the phases [12]. We have to remember here that the number of phases to be estimated is typically several tens to hundreds of thousands (the phase of each spot for which the intensity has been measured has to be estimated).

The first method is *molecular replacement*. It uses the known structure of a homologous protein. To date, approximately 60% of the structures found in the PDB were solved by this method [5]. It consists of constructing a virtual crystal by placing the homologous structure in the cell of the crystal studied using mathematical translation and rotation functions and comparing the diffraction pattern calculated from this virtual crystal and the measured diffraction data. Since the Fourier transforms of two homologous molecules placed in the same crystal are similar, the calculated phases are an excellent approximation of the phases of the measured signal [13–15].

The second method is *multiple isomorphous replacement*, which consists in diffusing heavy atoms (electron-rich) in the crystal [16]. In the first protein structure determination, the phase problem was solved using this method, those of the myoglobin and the hemoglobin [17, 18], by John

Kendrew and Max Perutz in 1960. The presence of the heavy element slightly modifies the diffraction intensities and the comparison of the diffraction pattern in the presence and absence of these heavy elements allows the estimation of the phases by triangulation, after having positioned the heavy atoms in the crystal lattice using methods known as Patterson functions [19].

The third method is *anomalous dispersion*, a specific property of the diffraction pattern when absorption of X-radiation is no longer negligible [20, 21]. This method consists in varying the incident beam wavelength around the absorption edge of one of the atom type contained in the molecule. Comparing the diffraction pattern at different wavelengths will allow the estimation of the phases using methods similar to that of the isomorphous replacement [22]. Selenium is often used because it has an absorption edge near to the wavelengths used (e.g. 1 Å). For proteins, selenomethionine, an amino acid for which the sulfur is replaced by selenium, is generally introduced biosynthetically [23]. In the case of nucleic acids, modified bases containing bromine are frequently used [24].

5. From the electron density to the structural model

Once a first set of phases is estimated, a first electron density map is calculated. If this map is sufficiently interpretable, the macromolecule can be built step by step in this map (**Figure 8**). A combination of automated algorithm and manual method available through interactive graphics softwares are used [25], leading to a final model composed of the three-dimensional coordinates of each atom of the cell content constituted by one or several macromolecules.

From that first built model, the diffraction intensities are calculated by Fourier transform and compared to the intensities experimentally measured. This comparison allows the step by step improvement of the model. This cyclical process is called the crystallographic refinement, alternating the search for global minimum of energy functions and manual reconstruction of the model [26].
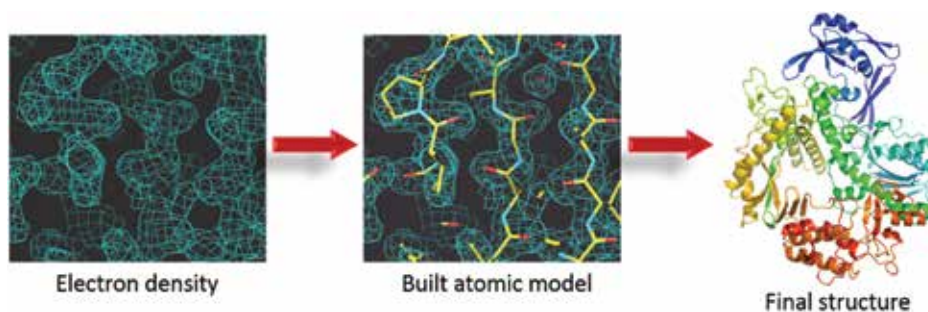

Electron density   Built atomic model   Final structure

Figure 8. The calculation of the electron density map (left) allows the building of the atomic model step by step (middle) and leads to the three-dimensional model of the structure (right).

6. Steps downstream the structure determination

The final step, downstream the structure determination by X-ray diffraction, concerns the interpretation of the structure and its integration into the biological context [27–29]. It consists in the understanding of the structural result as a three-dimensional object and the appreciation of its function at the cellular or evolution level. The description of the interatomic interactions, the secondary structures (**Figure 9**), the domains and their arrangement that defines the fold or the tertiary structure (**Figure 9**), as well as the characterization of the shape, the electrostatic properties and the quaternary structure based on the content of the cell in the crystal packing, are often complemented by the study of the macromolecule in solution, to better characterize its oligomeric (**Figure 9**) and its dynamic behavior, alone or in the presence of interactors, if known. These studies use a variety of biophysical methods, such as mass spectrometry, analytical ultracentrifugation, light scattering, microcalorimetry or surface plasmon resonance
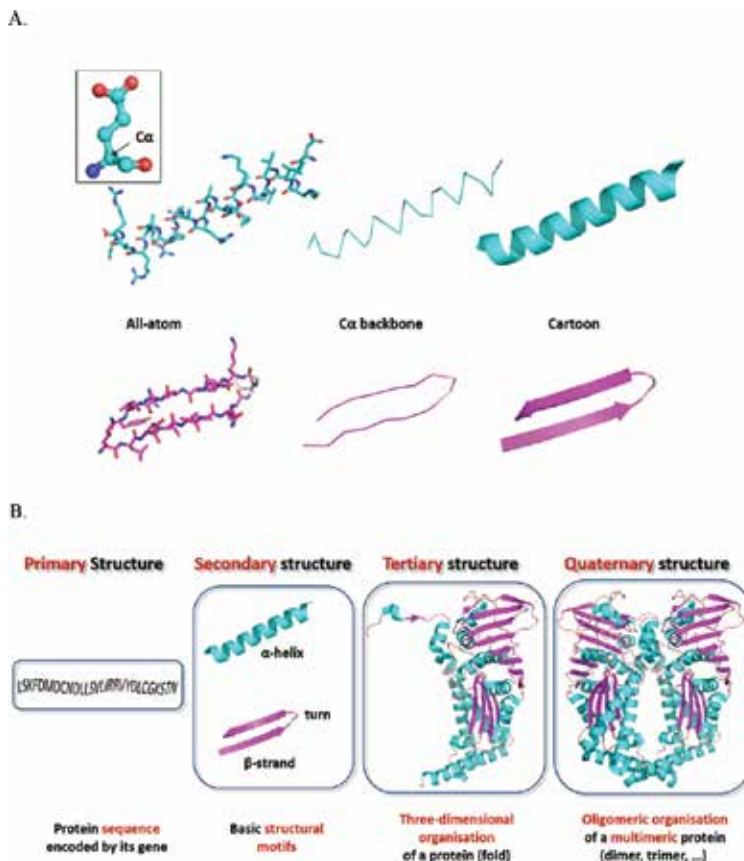

Figure 9. (A) The protein structures are represented by three modes of representation (see also **Figure 2**). The "all-atom" representation shows all the atoms in the protein, the representation "Cα backbone" shows only one atom of each amino acid, the Cα carbon atom, and cartoon representation shows the secondary structures in the shape of a helix for α-helices and in the form of arrows for β-strands. (B) Protein structures are described in four levels, from primary to quaternary structure.

(Biacore® technology), etc … [30]. In the case of enzymes, these studies will be coupled with enzymological approaches to determine the activity and the catalytic constants.

An analysis based on bioinformatics tools will allow to place the structure determined in the context of structural and evolutionary knowledge at a given time [31]. The lessons learned from these studies, often of primary importance, provide information including the classification of the structure and its sequence within a family counterparts, on the distribution and evolution of folding in the different domains of life (viruses, bacteria, archaea, eukaryotes), on the possible function when it is unknown, on the catalytic site and its spatial conservation and sequence, on the degree of oligomerization or on the existence of interaction with other partners, proteins, nucleic acids or ligands. A final type of study seeks to place the three-dimensional object into the context of the knowledge on the major biological mechanisms of live, such as knowledge on gene expression with transcriptomics, on complex formation with interactomics, etc … This information will include the characterization of the partners of the studied macromolecule at the scale of the cell or the whole organism.

All these steps, from the structure determination to the biological interpretation, far from being the end of the story, are often the beginnings of new structural studies (**Figure 3**). These can be articulated around analyses of the relative importance of the components of the macromolecule, the aminoacids, by determining the structure of mutants, or the studies of the interactions with partners by determining the structure of macromolecular complexes.

Author details

Claudine Mayer[1,2,3*]

Address all correspondence to: mayer@pasteur.fr

1 Department of Structural Biology and Chemistry – Institut Pasteur, Paris, France

2 CNRS UMR 3528, Paris, France

3 Paris Diderot University, Sorbonne Paris Cité, Paris, France

References

[1]   Watson J.D., Crick F.H.C., Molecular structure of nucleic acids: a structure for deoxyribose nucleic acid. Nature, 1953, 171, p. 737-738.

[2]   Anfinsen C., The formation and stabilization of protein structure. Biochem. J., 1972, 128, p. 737–749.

[3]   Scapin G., Structural biology and drug discovery. Curr. Pharm. Des., 2006, 12, p. 2087–2097.

[4]   Blundell T.L., Johnson L.N., Protein Crystallography. Academic Press, New York, 1976.

[5]   Berman H.M., Westbrook J., Feng Z., Gilliland G., Bhat T.N., Weissig H., Shindyalov I.N., Bourne P.E., The Protein Data Bank. Nucl. Acids Res., 2000, 28, p. 235-242.

[6]   Wlodawer A., Minor W., Dauter Z., Jaskolski M., Protein crystallography for non-crystallographers, or how to get the best (but not more) from published macromolecular structures. FEBS J., 2008, 275, p. 1-21. Review.

[7]   Wlodawer A., Minor W., Dauter Z., Jaskolski M., Protein crystallography for aspiring crystallographers or how to avoid pitfalls and traps in macromolecular structure determination. FEBS J., 2013, 280, p. 5705–5736. Review.

[8]   Chernov A.A. Protein crystals and their growth. J. Struct. Biol., 2003, 142, p. 3–21.

[9]   Luft J.R., Collins R.J., Fehrman N.A., Lauricella A.M., Veatch C.K., DeTitta G.T. A deliberate approach to screening for initial crystallization conditions of biological macromolecules. J. Struct. Biol., 2003, 142, p. 170-179.

[10]   Garman E.F., Schneider T.R. Macromolecular cryocrystallography. J. Appl. Crystallogr., 1997, 30, p. 211-237.

[11]   Moffat K, Ren Z., Synchrotron radiation applications to macromolecular crystallography. Curr. Opin. Struct. Biol., 1997, 7, p. 689–696.

[12]   Taylor G., The phase problem. Acta crystallogr. D., 2003, 59, p. 1881-1890.

[13]   Rossmann M.G. The molecular replacement method. Acta Crystallogr. A., 1990, 46, p. 73-82.

[14]   Tickle I.J., Driessen H.P., Molecular replacement using known structural information. Methods Mol. Biol., 1996, 56, p. 173-203. Review.

[15]   Abergel C., Molecular replacement: tricks and treats. Acta Crystallogr. D Biol. Crystallogr., 2013, 69, p. 2167-2173. Review.

[16]   Perutz, M.F., Isomorphous replacement and phase determination in non-centrosymmetric space groups. Acta Cryst. 1956, 9, p. 867–873.

[17]   Perutz M. F., Rossmann M. G., Cullis A. F., Muirhead H., Will G., North A. C., Structure of hemoglobin: a three-dimensional Fourier synthesis at 5.5 A resolution, therefore obtained by X-ray analysis. Nature, 1960, 185, p. 416-422.

[18]   Kendrew J.C., Bodo G., Dintzis H.M., Parrish R.G., Wyckoff H., Phillipps D.C., A three-dimensional model of the myoglobin molecule obtained by X-ray analysis. Nature, 1958, 181, p. 662-666.

[19]   Patterson A.L., A direct method for the determination of the components of interatomic distances in crystals. Zeitschrift für Kristallographie, 1935, 90, p. 517-542.

[20]   Read R.J., As MAD as can be. Structure, 1996, 4, p. 11-14. Review.

[21]   Blow D.M., How Bijvoet made the difference: the growing power of anomalous scattering. Methods Enzymol., 2003, 374, p. 3–22.

[22]   Ealick S.E., Advances in multiple wavelength anomalous diffraction crystallography. Curr. Opin. Chem. Biol., 2000, 4, p. 495–499.

[23]   Doublie S., Preparation of selenomethionyl proteins for phase determination. Methods Enzymol., 1997, 276, p. 523–530.

[24]   Anderson A.C., O'Neil R.H., Filman D.J., Frederick C.A., Crystal structure of a brominated RNA helix with four mismatched base pairs: an investigation into RNA conformational variability. Biochemistry, 1999, 38, p. 12577-12585.

[25]   Emsley P., Debreczeni J.E., The use of molecular graphics in structure-based drug design. Methods Mol. Biol., 2012, 841, p. 143-159.

[26]   Tronrud, D.E., Introduction to macromolecular refinement. Methods in molecular biology series, 2007, vol. 364: macromolecular crystallography protocols: vol. 2: 34 structure determination. p. 231–253, Humana Press Inc, Totowa, NJ.

[27]   Baker E.N., Seeing atoms: the rise and rise of crystallography in chemistry and biology, chemistry in New Zealand, January 2011, (New Zealand Institute of Chemistry), New Zealand.

[28]   Shi Y., A glimpse of structural biology through X-ray crystallography. Cell, 2014, 159, p. 995-1014.

[29]   Yonath A., X-ray crystallography at the heart of life science. Curr. Opin. Struct. Biol., 2011, 21, p. 622–626.

[30]   Malik S.S., Shrivastava T., Protein characterization using modern biophysical techniques. Advances in Protein Chemistry, 2013, OMICS Group eBooks. (http://www.esciencecentral.org/ebooks/ebooks-about.php)

[31]   Lecompte O., Thompson J.D., Plewniak F., Thierry J., Poch O., Multiple alignment of complete sequences (MACS) in the post-genomic era. Gene, 2001, 270, p. 17. Review.

Edited by Alicia Esther Ares

X-ray scattering techniques are a family of nondestructive analytical techniques. Using these techniques, scientists obtain information about the crystal structure and chemical and physical properties of materials. Nowadays, different techniques are based on observing the scattered intensity of an X-ray beam hitting a sample as a function of incident and scattered angle, polarization, and wavelength.

IntechOpen